

Technical University of Denmark



Synthetic Aperture Compound Imaging

Hansen, Jens Munk; Jensen, Jørgen Arendt

Publication date:
2012

Document Version
Publisher's PDF, also known as Version of record

[Link back to DTU Orbit](#)

Citation (APA):
Hansen, J. M., & Jensen, J. A. (2012). Synthetic Aperture Compound Imaging. Technical University of Denmark (DTU).

DTU Library

Technical Information Center of Denmark

General rights

Copyright and moral rights for the publications made accessible in the public portal are retained by the authors and/or other copyright owners and it is a condition of accessing publications that users recognise and abide by the legal requirements associated with these rights.

- Users may download and print one copy of any publication from the public portal for the purpose of private study or research.
- You may not further distribute the material or use it for any profit-making activity or commercial gain
- You may freely distribute the URL identifying the publication in the public portal

If you believe that this document breaches copyright please contact us providing details, and we will remove access to the work immediately and investigate your claim.

Synthetic Aperture Compound Imaging

Jens Munk Hansen

July 1st, 2012

SUBMITTED IN PARTIAL FULFILLMENT OF THE
REQUIREMENTS FOR THE DEGREE OF
DOCTOR OF PHILOSOPHY
AT
THE TECHNICAL UNIVERSITY OF DENMARK
SEPTEMBER 2012

Signature of Author

THE AUTHOR RESERVES OTHER PUBLICATION RIGHTS, AND NEITHER THE THESIS NOR EXTENSIVE EXTRACTS FROM IT MAY BE PRINTED OR OTHERWISE REPRODUCED WITHOUT THE AUTHOR'S WRITTEN PERMISSION.

THE AUTHOR ATTESTS THAT PERMISSION HAS BEEN OBTAINED FOR THE USE OF ANY COPYRIGHTED MATERIAL APPEARING IN THIS THESIS (OTHER THAN BRIEF EXCERPTS REQUIRING ONLY PROPER ACKNOWLEDGEMENT IN SCHOLARLY WRITING) AND THAT ALL SUCH USE IS CLEARLY ACKNOWLEDGED.

© Copyright by Jens Munk Hansen 2013
All Rights Reserved

CONTENTS

Contents	i
Preface	iii
Acknowledgements	v
Abstract	vii
Resumé på dansk	ix
1 Introduction	1
1.1 Speckle and anatomy	1
1.2 Origins of speckle	2
1.2.1 Resolution Limit	2
1.2.2 Speckle interference	2
1.2.3 Speckle Pattern	3
1.2.4 Speckle Image	3
1.3 Compounding	4
1.4 Spatial compounding	5
1.4.1 Early <i>in-vitro</i> Results	5
1.4.2 Scan-line conversion	6
1.4.3 Results	6
1.5 Synthetic Aperture Focusing	7
1.6 Virtual Sources	8
1.6.1 Acceptance Angle	9
1.7 Effective Aperture	9
2 Synthetic Aperture Compounding	13
2.1 Purpose	13
2.2 Contribution	13
2.2.1 Synthetic Aperture - Angle Compounding	14
2.2.2 Validation	15
2.2.3 Simulation Study	16
2.3 Discussion	18
3 Synthetic Aperture Compounding using a Convex Array	21
3.1 Purpose	21
3.2 Contribution	21
3.2.1 Synthetic Aperture Compounding - Revisited	22
3.2.2 Validation	24

3.2.3	Results	25
3.3	Discussion	32
4	Synthetic Aperture Compounding using a Phased Array	35
4.1	Purpose	35
4.2	Contribution	35
4.2.1	Figure of merit	36
4.2.2	Synthetic Aperture Compounding - Done Right	39
4.2.3	Measurements	40
4.2.4	Real-time implementations	45
4.2.5	Synthetic Aperture Imaging using the GPU	45
4.3	Discussion	47
	References	48
A	Papers	53
A.1	A Method for Synthetic Aperture Compounding	53
A.2	An Object-oriented Multi-threaded Software Beamformation Toolbox	59
A.3	Methods and Systems for Producing Compounded Ultrasound Images	71
A.4	Performance of Synthetic Aperture Compounding for <i>in-vivo</i> Imaging	125
A.5	Compounding in Synthetic Aperture Imaging	131
A.6	Synthetic Aperture Compounding using a Phased-array Transducer	143
A.7	Synthetic Aperture Beamformation using the GPU	155
B	Technical Details	161
B.1	Derivation of the coherence function	161

PREFACE

I have spent three years on doing research at the *Center for Fast Ultrasound Imaging* (CFU) at DTU Elektro. Time has been spent on obtaining knowledge within inverse problems, statistics, digital design techniques, medical imaging, and ultrasound signal processing. Time has been spent on helping students in laboratory sessions, correcting student reports, developing software for ultrasound signal processing for myself and other people to use, and assisting my colleagues with their research. More time has been spent on reading books, articles, and patents within the field of ultrasound imaging. The majority of my time, I have spent with many different and exciting subjects of which the most interesting are covered in this dissertation.

The research, development, and writing has been carried out under supervision of Professor Jørgen Arent Jensen and with support from BK Medical. The main area of my interest and the goal of this dissertation is to improve image quality by developing spatial compounding for synthetic aperture imaging.

Jens Munk Hansen
July, 2012

ACKNOWLEDGEMENTS

I would like to dedicate this project to my family and friends, who have supported me and dealt with all of my mental and physical absence during the writing of this dissertation.

My supervisor Professor Jørgen Arendt Jensen from *Center for Fast Ultrasound Imaging* (CFU) has contributed with an exceptional guidance and has been a tremendous source of knowledge and insight, and is the motivator for implementing spatial compounding for synthetic aperture imaging.

At BK Medical, I would like to thank Jakob Kortbek and Svetoslav Ivanov Nikolov for the work they have put into the patent application. In particular, I would like to thank Svetoslav for being the corresponding author for the patent application.

During my stay at Northeastern University in Boston, I had the pleasure of working with David R. Kaeli and his student Dana Schaa. I would like to thank them both for welcoming me into their group and for their assistance and guidance for realizing real-time synthetic aperture beamformation using the GPU.

Martin Christian Hemmsen for many discussions and for testing some of the software that I have developed at CFU.

Michael Johannes Pihl for invaluable discussions in the office.

Henrik Laursen and Elna Sørensen have helped me with innumerable IT and administrative problems. A great help, I could not have done without.

All the PhD students at CFU, past and present. They have created a great working environment, which allows for sparring of new ideas and projects for research within the field of ultrasound. They have always been available for help and discussions on ultrasound and on life in general.

My parents for helping me with all manner of problems during the last 35 years, for always supporting me and always being there.

The PhD project was supported by grant 024-2008-3 from the Danish Science Foundation and by BK Medical Aps, Denmark.

ABSTRACT

Medical ultrasound imaging is used for many purposes, e.g. for localizing and classifying cysts, lesions, and other processes. Almost any mass is first observed using B-mode imaging and later classified using e.g. color flow, strain, or attenuation imaging. It is therefore important that the B-mode images have high contrast. Like all imaging modalities, ultrasound is subject to a number of inherent artifacts that compromise image quality. The most prominent artifact is the degradation by coherent wave interference, known as “speckle”, which gives a granular appearance to an otherwise homogeneous region of parenchyma.

A successful approach to reduce the speckle artifacts is spatial compounding, where images are acquired from a number of directions and combined after envelope-detection. Today, spatial compounding is implemented in all high-end ultrasound systems and available when using a low pitch transducer with a fairly high number of independent channels. A drawback of conventional compounding is a reduction of the frame rate.

In this dissertation, a method for obtaining compound images using synthetic aperture data is proposed and investigated. The new approach allows spatial compounding to be performed for any number of angles without reducing the frame rate or temporal resolution. This important feature is an intrinsic property of how the compound images are constructed using synthetic aperture data and an improvement compared to how spatial compounding is obtained using conventional methods.

The method is investigated using simulations and through measurements using both phased array and convex array transducers. The images all show an improved contrast compared to images without compounding, and by construction, imaging using an improved frame rate is possible. Using a phased array transducer, it is demonstrated through theoretical considerations that the compound effect achieved is close to a theoretical maximum for the amount of compounding attainable and using a λ -pitch convex array transducer, the first *in-vivo* images are created.

The computational demands for an implementation are massive and the limiting factor is the amount of memory IO resources available. An equally high demand for memory throughput is found in the computer gaming industry, where a large part of the processing takes place on the graphics processing unit (GPU). Using the GPU, a framework for synthetic aperture imaging is implemented providing proof-of-concept for real-time implementations of synthetic aperture imaging.

RESUMÉ PÅ DANSK

Medicinsk ultralydsskanning bruges til mange formål, eksempelvis til lokalisering og klassificering af cyster, læsioner og andre processer. Næsten alle masser observeres først ud fra et B-mode billede og bliver senere klassificeret ved anvendelse af eksempelvis *color flow mapping* eller ved at tage en biopsi. Det er derfor vigtigt at B-mode billeder fremstår med den bedst mulige kontrast og opløsning. Ligesom ved andre billedmodaliteter, så forekommer der artefakter i ultralydbilleder som kompromitterer billedkvaliteten. Den mest fremtrædende artefakt og skyldes et interferensfænomen, som får et ellers homogent område af parenkym til at fremstå med et granulært udseende. Dette fænomen går under navnet *speckle*.

En vellykket fremgangsmåde til at reducere speckle er *spatial compounding*, hvor billeder optages fra forskellige vinkler og lægges sammen. I dag er *spatial compounding* implementeret i alle *high-end* ultralydssystemer og tilgængelig når man anvender en transducer med et stor antal uafhængige kanaler. En ulempe ved den konventionelle implementation af *spatial compounding* er at der med den forbedrede kontrast følger en forringelse af systemets tidslige opløsning.

I denne afhandling præsenteres en ny metode, hvor *compound* billeder kan frembringes ved brug af syntetisk aperturbilleddannelse. Den nye metode tillader frembringelse af *compound* billeder svarende til at optage data fra et vilkårligt antal vinkler og samtidigt uden at gå på kompromis med systemets tidsopløsning. Denne egenskab er en medfødt egenskab ved metoden, hvorpå billeder frembringes ved brug af syntetisk apertur og en forbedring i forhold til hvordan *compound* billeder bliver lavet med konventionel billeddannelse.

Fremgangsmåden bliver undersøgt ved anvendelse af simuleringer og med målinger, hvor både *phased-array* og konvekse transducere anvendes. Alle billederne viser en forbedret kontrast sammenlignet med billeder lavet uden brug af *spatial compounding* og grundet metoden som billederne er fremstillet på, så er det muligt at få en bedre tidlig opløsning. Ved at bruge en *phased-array* transducer, så demonstreres at den opnåede effekt er tæt på hvad der teoretisk er muligt og med brug af en konveks transducer skabes de første *in-vivo compound* billeder med den nye fremgangsmåde.

Kravene til sand-tids behandling af de medicinske ultralydssignaler med den nye metode er meget store - specielt kravene til hurtig hukommelsestilgang. Lignende krav til hukommelsestilgang findes i spilbranchen, hvor en stor del af processeringen bliver udført på grafikprocessoren også kendt som GPU'en. Ved hjælp af en hurtig GPU, demonstreres det hvor hurtigt syntetisk aperturbilleddannelse kan afvikles og dette er hurtigt nok til at en sand-tids implementation.

INTRODUCTION

This chapter serves as an introduction to spatial compounding and synthetic aperture imaging. The reader is assumed to be familiar with ultrasound imaging using conventional focusing often referred to as dynamic receive focusing.

1.1 Speckle and anatomy

When improving the contrast of ultrasound images by removing speckle, it is important to understand what causes speckle and how it is related to the structure of tissue. In Fig. 1.1, two images of approximately the same cross-sectional view of the human liver are shown. An optical image and an ultrasound image. The optical image has great

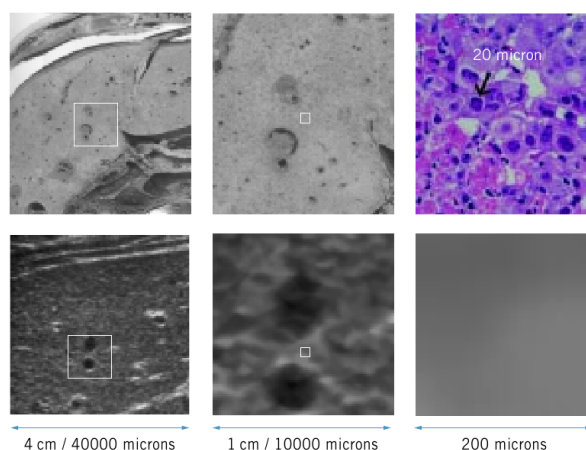


Figure 1.1: Magnification of optical and ultrasound images of the liver. Courtesy of GE Healthcare.

contrast and high detail resolution, whereas the ultrasound image has a granular appearance, which makes it quite hard to differentiate the different structures. Even though the granularities look like cellular structures, they are not. The cellular structures are typically two orders of magnitude smaller than what is resolvable by an ultrasound scanner.

By repeating a measurement or by comparing images frame by frame, one will discover that the speckle granularities are persistent and not the result of a random phenomena, which can be removed, e.g. like additive noise. This indicates that the speckle is fully deterministic, once the structure of the tissue is known.

1.2 Origins of speckle

To understand the origin and nature of speckle, it is necessary to recall how an image is processed in an ultrasound scanner.

1.2.1 Resolution Limit

As should be clear to the reader, images from an ultrasound imaging system are formed by envelope-detection of a sum of received signals delayed by focusing. After possibly a scan-line conversion, the images are logarithmically compressed to better visualize the large differences in intensity. Due to the simple image formation by envelope detection, the image of a single scatterer is represented by the received pulse and the axial resolution therefore depends on its length¹. The resolution in the lateral and elevation plane depend on the focusing used, which can be either geometric or electronic. In the next section, we will demonstrate what happens, when imaging scatterers that are separated by less than the resolution limit.

1.2.2 Speckle interference

To illustrate the origin of speckle, the pulse-echo fields from a pair of scatterer located symmetrically around the focus point of a 128-element, λ -pitch linear array were simulated using Field II [2, 3]. The excitation used was a two-cycle sine at 7 MHz and the electronic focus was at the depth of 40 mm. The signals were beamformed using the beamformation toolbox [4] and in Fig. 1.2, the images of the two scatterers are shown together with the sum of the received signals delayed by focusing and the result of the envelope-detection. The axial FWHM was measured to 0.27

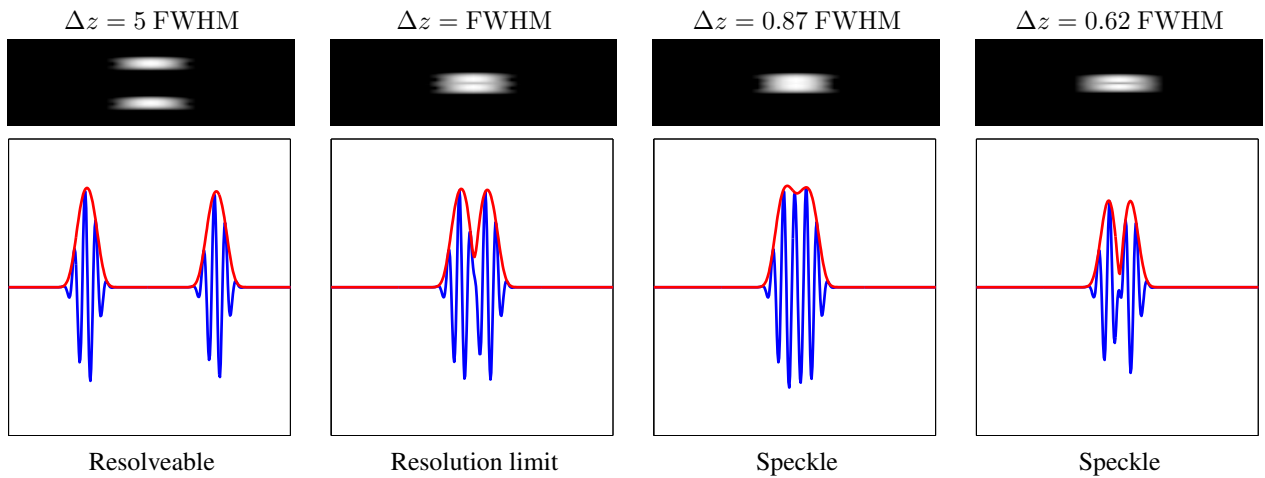


Figure 1.2: Two scatterers imaged using dynamic receive focusing.

mm, which is close to half the length of the excitation. Using $c = 1540 \text{ m/s}$, we have $\lambda = c/f_0 = 0.22 \text{ mm}$. In the first situation, the scatterers are separated axially by 5 times the FWHM, and they are clearly resolvable in the image. In the next image, the scatterers are separated by the FWHM, which can be seen by the envelope dropping to half of its full value. In the two last images, the scatterers are moved even closer together and complex interference causes the scatterers to first appear as a single scatterer and then again as multiple scatterers. It is this kind of interference that gives the granular appearance of ultrasound images. A similar situation occurs, when imaging scatterer separated laterally by less than the lateral FWHM.

¹The axial resolution can be shown to be inversely proportional to the bandwidth of the system, e.g. long chirps can be applied to achieve high penetration and maintain axial resolution [1].

1.2.3 Speckle Pattern

The situation illustrated in Fig. 1.2 does not fully explain the granular appearance of the ultrasound images in Fig. 1.1, but is an important ingredient for understanding the origin of speckle patterns. We will now extend the analysis to a situation with 10000 scatterers randomly positioned on a line and their amplitudes scaled to simulate a 2 mm water cyst at a depth of 41 mm. In Fig. 1.3, the image of this line is shown together with the sum of the received signals delayed by focusing and the result of the envelope-detection. Despite the high density of scatterers, different patterns

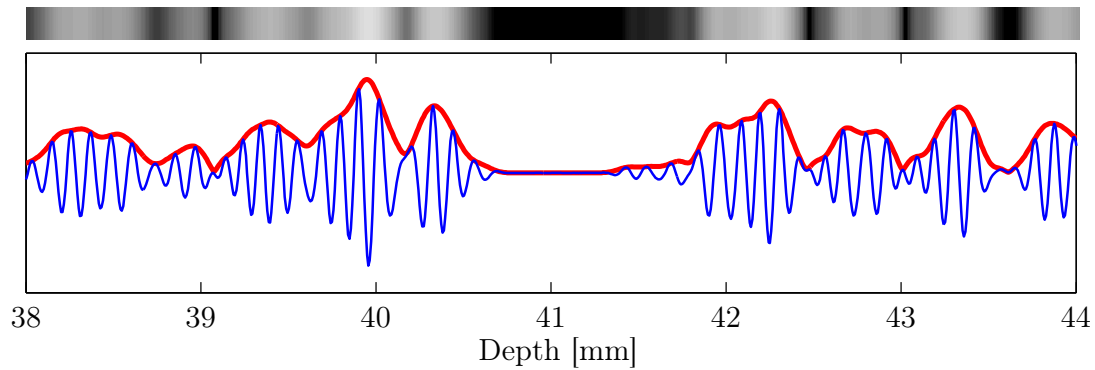


Figure 1.3: Simulated ultrasound image of 10000 scatterers randomly positioned on a line of length 10 mm. At a depth of 41 mm, a cyst of width 2 mm is represented by scaling the amplitudes of the scatterers. The dynamic range is 30 dB to clearly show the speckle pattern.

are appearing at multiple depths. Repeating the simulation using different realizations of the scatter positions or their amplitudes give different speckle patterns. For a comparison, in Fig. 1.4, an artificial intensity image is shown. The intensity image is obtained by a simple convolution of the scatter position map with a Gaussian kernel constructed using the FWHM obtained from the PSF. The intensity image thereby represents the density of the scatterers images. When comparing the two images, it is clear that the speckle represented by the light and dark areas outside the cyst in

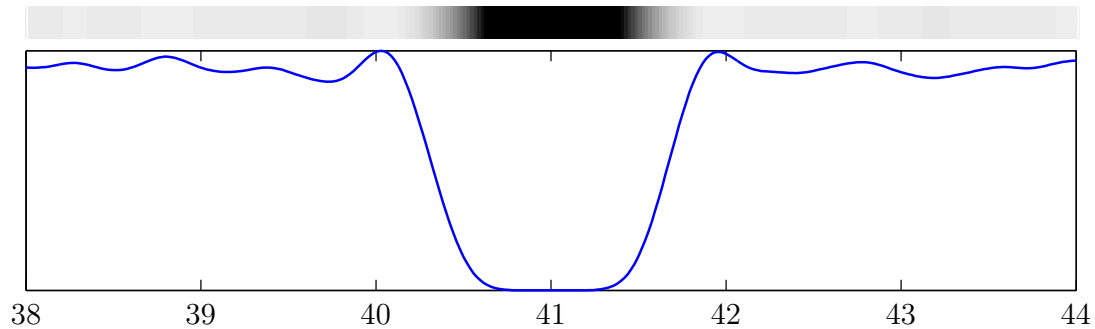


Figure 1.4: Artificial intensity image of the 10000 scatterers used for simulating the image in Fig. 1.3. The dynamic range is 30 dB.

Fig. 1.3 is not related to the density of the scatterers.

1.2.4 Speckle Image

The situation for the line in previous section can be extended to an image with scatterers distributed over a region. The distribution can be selected to represent structures found in human tissue using the program Field II. An interesting situation to simulate is the presence cysts with different diameters and different scattering levels relative to the background. In this way, the disturbance of speckle can be studied and algorithms for speckle reduction can be examined.

Proceeding in the same way as in the previous section, 100000 scatters were distributed uniformly and their amplitudes scaled to represent a cyst with a diameter of 5 mm. and a scattering level of -12 dB relative to the background.

Using a 192-element, λ -pitch linear array, the received signals from 192 focused emissions were simulated with Field II and the signals beamformed using dynamic receive apodization with a Hamming profile and an f-number, $f_{\text{rcv}} = 1.0$. In Fig. 1.5a, the image of a cyst simulated at a depth of 40 mm is shown. A two-dimensional pattern is seen, where

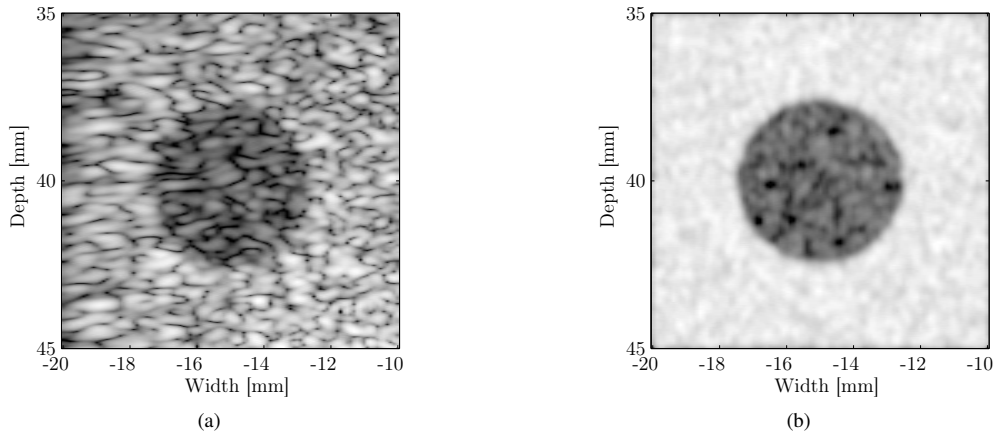


Figure 1.5: Simulated ultrasound image of a cyst at depth 40 mm (a). Artificial amplitude image obtained using the scatter distribution (b).

each of the dimensions have a distribution similar to that of the one-dimensional case. If an image is formed using instead the scatter position map convolved with a Gaussian kernel representing the axial and lateral resolution, the image in 1.5b is obtained after envelope detection. Again, it is evident, how the speckle degrades the contrast and detail resolution. The latter because structures appear, which do not directly represent the scatter distribution. The small fluctuations in Fig. 1.5b is due to the limited number of scatterers. The distribution of scatters can be viewed as binning in a multi-dimensional histogram with an average bin size equal to the resolution cell or to be introduced the later, the *speckle cell*. Such a binning process is a Poisson process and by requiring an average bin count of 10, we cover situations with bin counts 3 standard deviations below the mean.

1.3 Compounding

Many attempts have been made to reduce the speckle in ultrasound images. This includes the Lee and Frost filters [5, 6] and other adaptive methods [7]. Often these filters give a marginal reduction in speckle noise and do not preserve the resolution in the image. More successful approaches are based on averaging decorrelated frames. Independent frames have different speckle patterns, but share the same feature information. In relation to the discussion in the previous section, decorrelated images correspond to creating two images using two different sets of samples (scatter locations) from the same scatter distribution. The images produced will both represent the cyst, but the two speckle patterns will be different and when averaged, the speckle will be reduced. Averaging methods include temporal averaging, spatial compounding [8, 9], and frequency compounding [10]. They are all based on averaging multiple decorrelated frames [11] and decorrelation is obtained through tissue or probe motion in temporal averaging, by transmitting and receiving at different angles or using different subapertures in spatial compounding, and image formation at different frequencies in frequency compounding. Today, in addition to temporal averaging, spatial compounding is implemented in all state-of-the-art, high-end ultrasound systems and available when using a low pitch transducer with a fairly high number of independent channels [12]. The most successful approach due to its simple implementation is multi-angle compound imaging (MACI), which was investigated at CFU in 1997 by Søren Kragh Jespersen [13] and later adopted by Philips. A better approach, which is slightly more difficult to implement, is *aperture compounding*, where the compound effect is obtained by imaging the same line using different transmit apertures [14]. Siemens are holding this patent, so they are most likely using this approach for compound imaging. Another and more interesting

approach is compound imaging, where an adaptive synthesis selects, whether the final image point should be made by compounding or by coherently adding the images [15]. Siemens is also the holder of this patent.

A weakness of all the above methods for spatial compounding is a reduction of the frame rate or at least a reduction of the true temporal resolution. The latter occurs when a system is using a circular buffer for storing images and reusing old frames to achieve an apparently higher temporal resolution, a method sometimes referred to as recursive imaging. To remedy the drop in frame rate, methods have been developed, where only receive compounding is used [16] or where the number of scan-lines is reduced by using a more uniform scan-line density [17].

In the next section, spatial compounding will be described in more detail using the MACI approach investigated by Jespersen [13].

1.4 Spatial compounding

To obtain spatial compounding, a low-pitch transducer must be used. In the following, it will be assumed that a linear array is used, but the method can also be applied to convex arrays. Proceeding with a linear array, a subset of elements is selected as the active aperture and this aperture is used as a phased array to steer the beam making an angle θ with a normal to the transducer surface. The active aperture is slid across the transducer, until scan lines originating from the entire extent of the linear array are recorded. This procedure is repeated for a number of angles, θ_i , $i = 1, \dots, N_\theta$. In this way, N_θ images can be formed by envelope-detection. The N_θ images are afterwards added using scan-line conversion. In Fig. 1.6a, an illustration is given of how the scan lines are distributed for a situation with $N_\theta = 3$. An

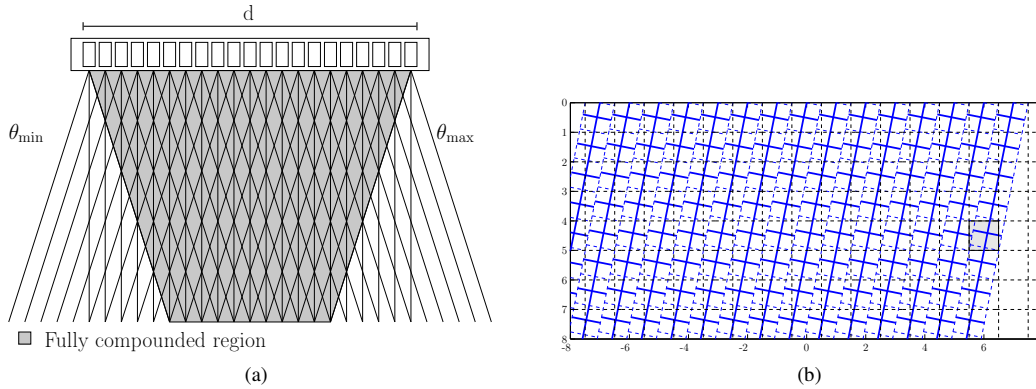


Figure 1.6: Illustration of scan line directions and origins used for spatial compounding for a setup with $N_\theta = 3$ (a). Sample strip-integral model used for interpolation among the lines and line samples (b).

alternative formulation will be given in Chapter 2, where the images are obtained by using scan lines always pointing in a direction normal to the transducer. The images are then created by using apertures, which are located such that the scan-line originates from their center or by using apertures that are displaced a certain fraction of their size to either left or right. The advantage with this approach is that there is no need for scan-line conversion and the degree of compounding can easily be estimated using a one-dimensional theory. This is the “better” approach mentioned in Section 1.4 and used by Siemens [14].

1.4.1 Early *in-vitro* Results

In this section, the first experiences I have made with spatial compounding are presented. The work was carried out at BK Medical and the idea was to get hands-on experience with compounding, and see how speckle can be reduced and more importantly isolate the speckle reduction caused by compounding. This last point is very important because in a commercial scanner many attempts are made for removing speckle and therefore it is necessary to isolate the speckle reduction caused by spatial compounding. I have used the results as a qualitative reference for what kind of speckle

reduction, I should expect or aim for, when implementing spatial compounding for synthetic aperture imaging. The results were presented at the Euroson conference in Copenhagen, March 2010 together with the very first simulations of synthetic aperture compounding.

From the previous section, it should be clear that removing speckle pattern can be achieved by filtering the images, e.g. by applying a low-pass filter. Applying a low-pass filter to Fig. 1.5a gives an image, which look a lot like Fig. 1.5b, with the possibility of hiding structures that should have been present either inside or outside the cyst. In ultrasound imaging, focusing is extremely important. Incorrect focusing causes blurring of the images, which may be confused with speckle reduction. To isolate the effect of compounding, a commercial scanner was used to record images for a number of angles. The task for compounding was then reduced to scan-line conversion.

1.4.2 Scan-line conversion

By looking at Fig. 1.6a, it should be clear that the scan-line conversion needed for spatial compounding using MACI is straightforward. None the less, I decided to spend some time on different algorithms for interpolating among the samples of the different scan lines. I developed a library, which facilitates nearest neighbor and bi-linear interpolation between the individual scan lines and line samples. In addition to the two well-known interpolation schemes, I implemented an interpolator based on a strip-integral model, which considers line samples to be rectangles and computes the overlap of the line samples and a given pixel. The value of the pixel is then computed as a sum of the line samples values weighted by their overlap. This interpolation scheme is illustrated in Fig. 1.6b, where the center of the scan lines are shown using thick solid lines (the long ones) and the line samples (their centre) are represented by thick solid lines arranged on the scan lines. For the pixel highlighted in the figure, it should be clear that four line samples are contributing. A simplification of this algorithm is also implemented, where the contribution is computed by the length of the lines crossing the pixel, which we will refer to as the line-integral model. The lines in question are the center lines of the scan lines and samples respectively.

1.4.3 Results

The images presented in this section were presented at the Euroson conference have not been published in any other way. A BK transducer Type 8811 with 192 elements operating at 9 MHz was used for scanning a rubber phantom with small water cysts. Images for 13 compound angles $\theta = -12^\circ, -10^\circ, \dots +12^\circ$ were acquired by steering the array. In Fig. 1.7, images of the rubber phantom are shown with and without compounding. The compound image is obtained

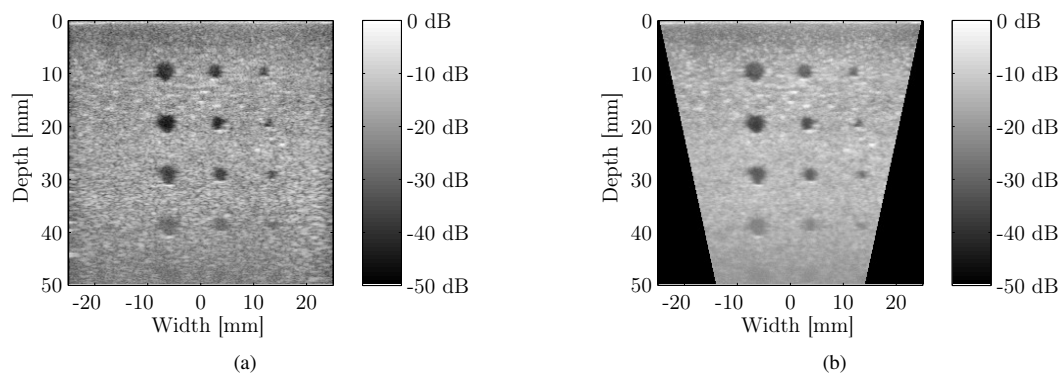


Figure 1.7: Ultrasound images of a cyst phantom. Fig. (a) is made without compounding and Fig. (b) is made with compounding using 13 angles.

by adding all 13 images using the strip-integral interpolation algorithm, which gave the most smooth image. Images created using linear interpolation and the line-integral model are very hard to distinguish from the image shown here. The choice for interpolation was based on wire-phantom simulations, which revealed the best detail resolution, when using the more expensive strip-integral approach for interpolation.

The speckle appearance in Fig. 1.7 is clearly reduced, when comparing the compound image to the image without compounding. However, it seems like the dynamic range is reduced. This could be explained by the many additions applied to already logarithmically compressed data with a limited dynamic range. To illustrate the effect of compounding using different numbers of angles, in Fig. 1.8, a smaller image of one of the water cyst is shown using compounding with 1, 5, and 9 angles. An increasing effect of speckle reduction is observed when using more angles

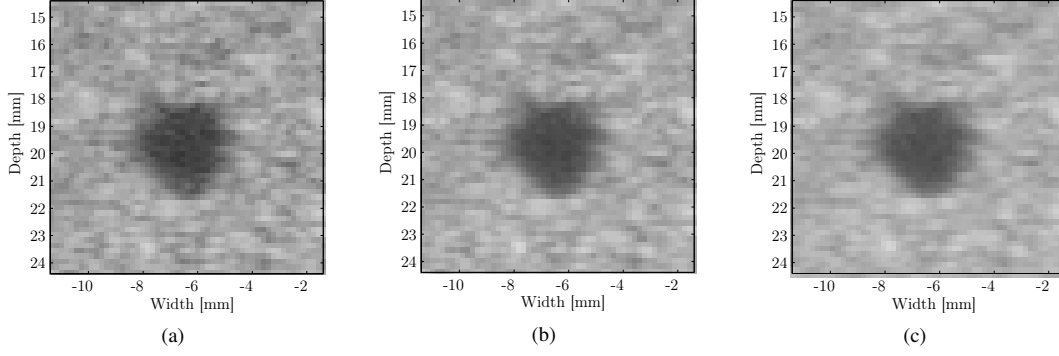


Figure 1.8: Compound images using 1 (a), 5 (b), and 9 (c) angles.

and it is this kind of effect, we would like to see when implementing compounding using synthetic aperture focusing, which will be introduced in the next section.

1.5 Synthetic Aperture Focusing

Synthetic aperture focusing was originally formulated for improving the spatial resolution of radar images back in the 1950s. The new focusing technique was used for increasing the size of the transmit aperture by repeatedly illuminating a scene with pulses of radio waves. The many echos were received successively at different antenna position and coherently detected and processed to better resolve objects in the target scene. The idea was in the late 1960s and early 1970s adopted to ultrasound imaging [18, 19].

In its simplest implementation, a single transducer element is emitting a signal, which is interpreted as a spherical wave. To coherently detect or focus the signal scattered at a point of interest and received with an element on the receiving aperture, the time-of-flight must be calculated. Assuming that the speed of sound, c , is constant, the time-of-flight, t_{TOF} , is given by

$$\begin{aligned} t_{\text{TOF}} &= t_{\text{TOF}_{\text{xmt}}} + t_{\text{TOF}_{\text{rcv}}} \\ &= \frac{|\vec{r}_{\text{fp}} - \vec{r}_{\text{xmt}}| + |\vec{r}_{\text{rcv}} - \vec{r}_{\text{fp}}|}{c}, \end{aligned} \quad (1.1)$$

where the location of the emitting element and receiving elements are given by \vec{r}_{xmt} and \vec{r}_{rcv} , respectively. The point of interest is referred to as the focal point, \vec{r}_{fp} . This procedure is repeated for each element of the transmit aperture and a weighted sum of contributions from each transmit-receive channel pair are computed. This is different from conventional focusing, in the sense that for each emission, an entire image is created instead of just a single image line. The image created from a single emission is often referred to as a low-resolution image, since it lacks transmit focusing. The transmit focusing is realized by coherently adding low-resolution images from different emissions.

In addition to focusing, the contributions are weighted to suppress side lobes and what we refer to as the beamformed image at the position \vec{r}_{fp} , can be computed according to

$$I(\vec{r}_{\text{fp}}) = \sum_{\text{xmt}=1}^{N_{\text{xmt}}} \mathcal{A}_{\text{xmt}}(\vec{r}_{\text{fp}}) \sum_{\text{rcv}=1}^{N_{\text{rcv}}} \mathcal{A}_{\text{rcv}}(\vec{r}_{\text{fp}}) s_{\text{xmt,rcv}}(t_{\text{TOF}}(\vec{r}_{\text{xmt}}, \vec{r}_{\text{fp}_{\text{xmt}}}, \vec{r}_{\text{fp}}, \vec{r}_{\text{rcv}})), \quad (1.2)$$

where N_{rcv} is the number of receiving elements, $\mathcal{A}_{\text{xmt}}(\vec{r}_{\text{fp}})$ and $\mathcal{A}_{\text{rcv}}(\vec{r}_{\text{fp}})$ are the apodization functions used for transmit and receive, respectively, and $s_{\text{xmt},\text{rcv}}(t)$ is the interpolated time-domain echo signal received at element rcv after the xmt'th emission. The outer sum is over the N_{xmt} emissions used to construct the final image point. Equation (1.2) is general in the sense that it covers all beamformation using delay-and-sum focusing. For focused emissions, one needs to modify the time-of-flight calculations using a virtual source located at the transmit focus, $\vec{r}_{\text{fp},\text{xmt}}$. This idea was used by Passmann and Ermert for single-element transducers [20, 21] and extensive work has been done in our group for focusing using multi-element transducers [22, 23]. For a conventional B-mode image, $N_{\text{xmt}} = 1$, and only a single emission contributes to a given line.

Synthetic aperture focusing has been applied to many different transducer geometries for both imaging and blood velocity estimation. The simple implementation just described, where only a single element is used for transmit and the transmit position is scanned across the aperture, is referred to as the multistatic approach and is illustrated in Fig. 1.9. The multistatic approach should be seen as a contrast to the monostatic approach, where a single element

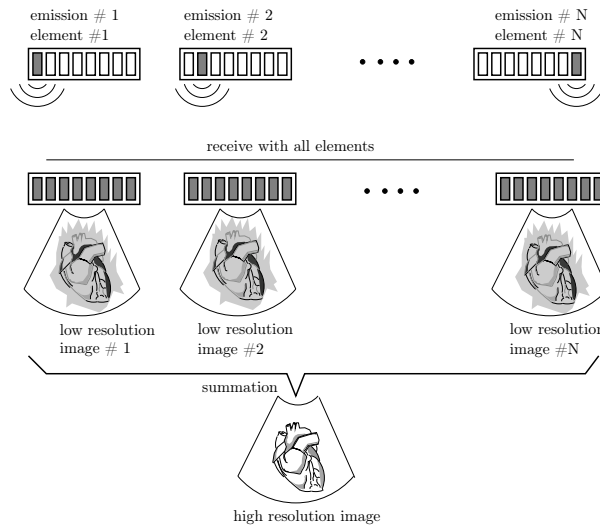


Figure 1.9: Simple model for synthetic transmit aperture ultrasound imaging [22].

is used for both transmit and receive, corresponding to moving a single-element transducer along a line [24]. The two-approaches together with a bi-static approach were investigated by Ermert and Lang [25].

1.6 Virtual Sources

The multistatic approach implemented directly using a phased-array or another low pitch transducer with a fairly high number of independent elements has an important disadvantage. Using single elements for emissions, limits the energy due to the small area of each element. The monostatic approach also has disadvantages, since the assumption of the emission of a spherical wave is obscured especially in the presence of a focusing lens.

The solution to this problem is to use multiple elements and with waveforms delayed to match a spherical wave emitted from a virtual source behind the transducer [26, 23]. If the virtual source is placed in front of the transducer for focused emissions, one needs to take into account a shift of the focus, which was explained by Li and Wolf [27]. This is only relevant for synthetic aperture imaging, since the time-of-flight calculation is unchanged for the line passing through the virtual source, cf. (2) in the conference paper.

1.6.1 Acceptance Angle

When using multiple elements for focused or defocused emission, the assumption of spherical wave propagation is not everywhere equally valid. In other words, when using the assumption of spherical propagation, there is a limit for where in the image, a given emission can improve on the focusing.

This relationship was studied by Oddershede et. al and they show that the geometric boundary approximation illustrated in Fig. 1.10 is a good approximation and the *acceptance angle* is given by [28]

$$\theta = \arctan\left(\frac{1}{2f_{\text{xmt}}}\right), \quad (1.3)$$

where f_{xmt} is the f-number derived from the width of the active aperture and the focus depth, $f_{\text{xmt}} = \frac{F}{D_{\text{act}}}$. The

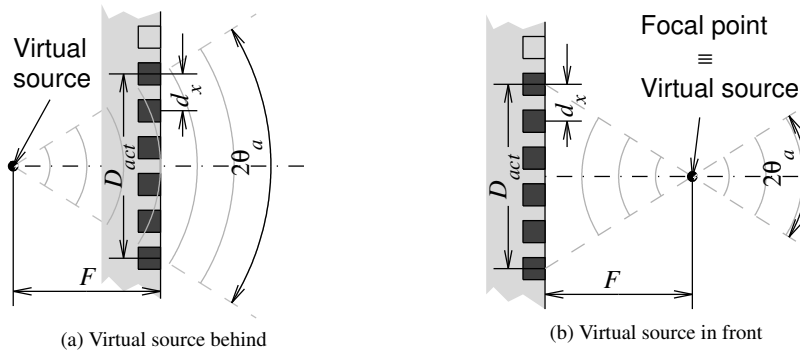


Figure 1.10: Virtual source for focused and defocused emissions [23].

focus depth D_{act} is often chosen such that the angle is at least as large as the 6 dB acceptance angle for the individual elements to get a fairly low f-number and thereby a high resolution. Ideally, experiments should be made using both different f-numbers for the focusing and different f-numbers for transmit and receive apodization in (1.2). For all measurements in this dissertation, an f-number of -0.5 is used for unfocused emissions. This has been used with success in our group for many publications [29, 30, 31].

1.7 Effective Aperture

As stated in the previous section, it is important to use a sufficiently low f-number to get a high resolution for synthetic aperture focusing. The reader may think that it is equally important to also use many unfocused emissions and preferably an amount equal to the number of receiving elements. This will work, but it can be shown that to achieve a resolution equal that of conventional focusing, the *effective aperture* of the two approaches must be the same. The effective aperture is related to the lateral resolution by a Fourier relation valid both in the far field and at the focal point. Using this relation, the continuous wave radiation pattern $P(\mu)$ is given by [32]

$$P(\mu) = \mathcal{F}\left[\mathcal{A}_{\text{xmt}}\left(\frac{x}{\lambda}\right) * \mathcal{A}_{\text{rcv}}\left(\frac{x}{\lambda}\right)\right], \quad (1.4)$$

where $\mu = \sin(\theta)$ is the direction sine of the steering angle, \mathcal{A}_{xmt} and \mathcal{A}_{rcv} are the apodization functions, $(\frac{x}{\lambda})$ is the element location in wavelengths, and \mathcal{F} denotes the Fourier transform.

Using (1.4), it can be shown that a sparse configuration of apertures can be used for achieving an effective aperture equal to what can be attained using a sequence of single-element emissions or a sequence with as many virtual sources as receiving elements [32]. It also follows that the effective aperture for a single-element emission is about half the size of that used for a conventional image - another reason for naming an image formed using a single emission a low-resolution image.

A disadvantage of using sparse sequences is a reduced signal-to-noise ratio resulting from coherent addition of fewer signals. The purpose of this dissertation is not to study sparse sequences and therefore to obtain sufficient penetration, an array of virtual sources equal to the size of the receiving aperture will be used for all simulations and measurements.

Contributions

The Majority of the work has been presented at conferences, published in journals, and a single patent has been filed for the method for producing compound images using synthetic aperture data. The patent and the papers can be found in Appendix A. In addition to the scientific publications, an amount software has been written, e.g. an offline beamformation toolbox [4] and a real-time beamformation framework for beamformation using the GPU [33].

Conference Papers

1. **J. M. Hansen** and J. A. Jensen: A Method for Synthetic Aperture Compounding. Proceedings of the IEEE Ultrasonics Symposium, October, 2010.
2. **J. M. Hansen**, M. C. Hemmsen and J. A. Jensen: An object-oriented multi-threaded software beamformation toolbox. Proceeding of SPIE, vol. 7968, article no. 79680Y, 2011.
3. **J. M. Hansen** and J. A. Jensen: Performance of Synthetic Aperture Compounding for *in-vivo* imaging. Proceedings of the IEEE Ultrasonics Symposium, October, 2011.
4. **J. M. Hansen**, D. Schaa and J. A. Jensen: Synthetic Aperture Beamformation using the GPU. Proceedings of the IEEE Ultrasonics Symposium, October, 2011.

Journal Papers

1. **J. M. Hansen** and J. A. Jensen: Compounding in Synthetic Aperture Imaging. IEEE Trans. Ultrason., Ferroelec. and Freq. Contr., 2012, *In press*.
2. **J. M. Hansen** and J. A. Jensen: Synthetic Aperture Compounding using a Phased-array Transducer. J. Acoust. Soc. Am., submitted

Patents

1. **Jens Munk Hansen**, Svetoslav Ivanov Nikolov, Jacob Kortbek and Jørgen Arendt Jensen. Methods and Systems for producing compounded ultrasound images, International Application Number PCT/P81007275/DK00.

Software

1. Beamformation toolbox. This is a multi-threading object-oriented C++ library implementing time-domain beamformation. The library interfaces to Matlab through Matlab objects.
2. Image inspection tools. A collection of tools for inspecting the resolution and contrast of ultrasound images. The library facilitates measurements of the full width at half maximum (FWHM), the cystic resolution, the signal-to-noise ratio at a point and other performance indicators.
3. C framework for beamformation on the GPU using OpenCL.

Organization of the Dissertation

The dissertation is divided into four chapters. The present chapter, which serves as a brief introduction to ultrasound imaging and a motivation for the project followed by three chapters, each containing a presentation of the results published in one or two papers. Following each presentation, a short discussion and summary is given.

Chapter 2:

In this chapter, the proposal for compounding using synthetic aperture is given and results are produced using simulations.

Chapter 3:

We generalize the idea for synthetic aperture compounding to be used for a convex array transducer and make the very first images using the suggested approach. The method is applied to clinical data acquired with the previous research scanner in our group.

Chapter 4:

Using the experiences gained from the research presented in Chapter 2 and 3, the method is refined and reformulated for improving the compound images. The modified approach is used for a phased array transducer and wire, speckle, and cyst images are presented.

SYNTHETIC APERTURE COMPOUNDING

This chapter contains a presentation of the conference papers

- **J. M. Hansen** and J. A. Jensen: A Method for Synthetic Aperture Compounding. Proceedings of the IEEE Ultrasonics Symposium, October, 2010.
- **J. M. Hansen**, M. C. Hemmsen and J. A. Jensen: An object-oriented multi-threaded software beamformation toolbox. Proceeding of SPIE, vol. 7968, article no. 79680Y, 2011,

which can be found in full length in Appendix [A.1](#) and [A.2](#), respectively. The first paper is the paper where synthetic aperture compounding was introduced and based on the research presented in the paper and in this chapter, a patent was filed together with BK Medical

- **Jens Munk Hansen**, Svetoslav Ivanov Nikolov, Jacob Kortbek and Jørgen Arendt Jensen. Methods and Systems for producing compounded ultrasound images, International Application Number PCT/P81007275/DK00.

The second paper is a presentation of yet another beamformation toolbox, written in C++ with a Matlab interface. The implementation of the toolbox was motivated by the need for alternative apodizations needed for synthetic aperture compounding and the possibility for beamforming low-resolution images much faster.

2.1 Purpose

As explained in the introduction, ultrasound images obtained using synthetic aperture focusing have higher detail resolution, but in the way it is formulated in the literature, the images still suffer from speckle artifacts. The purpose of this chapter and the first paper is to prototype an approach for spatial compounding using synthetic aperture focusing, which not only produces compound images with a higher resolution but at the same time, compounding can be obtained without reducing the frame rate.

2.2 Contribution

To understand how spatial compounding can be obtained using synthetic aperture focusing, it is instructive to rethink, how conventional spatial compounding can be obtained using a number of unfocused emissions. For conventional spatial compounding, where the active aperture is used as a phased array to steer the beam making an angle θ with a normal to the transducer surface, the steering amounts to changing the transmit focus. By steering the beam to either right or left, image points, which are not central to the active aperture, are beamformed. This is actually the most important part, but at the time of writing the first paper, I did not fully understand the consequences of the displacement of the apertures, and the approach for synthetic aperture compounding was formulated in terms of a steering angle, θ . Returning to conventional compounding, and how this can be achieved using a number of unfocused

emissions. The transmit focusing can be obtained by delaying the signals from all the unfocused emissions in such a way that they sum up coherently at the focus point and apply an apodization corresponding to the one used for a given focused transmission.

Next, the received signals for each channel are added across the emissions. The outcome is a data set, which under the assumptions of an isotropic medium with no second-order scattering is identical to a data set obtained using the focused emission. This is a good thought to have in mind, but by doing this, it is no longer possible to focus everywhere in the image, which is the primary reason for synthetic aperture imaging.

2.2.1 Synthetic Aperture - Angle Compounding

The approach that we decided to pursue was to do apply an apodization similar to what is used for conventional compounding and perform the focusing like it is done for synthetic aperture imaging. This implies that for each point in the image and for each steering angle, θ , apodizations must be computed for the given emission as well as for each receiving element. In Fig. 2.1, the time-of-flight and apodization calculations for an emission with origin \vec{r}_{xmt} and a receiving element positioned at \vec{r}_{rcv} is illustrated. In Fig. 2.1, the apodizations are computed using the distance

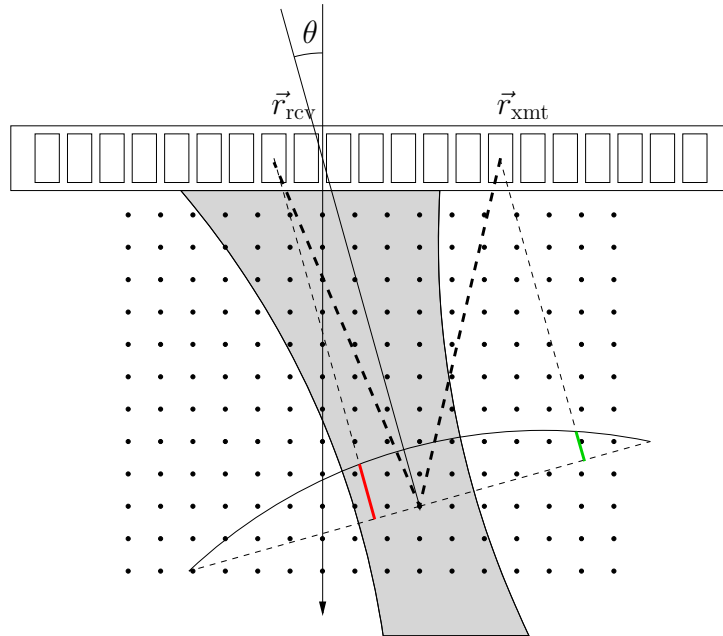


Figure 2.1: The example shows, how the time-of-flight and apodizations are calculated for a single emission with transmit origin \vec{r}_{xmt} and a selected receive element positioned at \vec{r}_{rcv} for a single direction θ . The length of the wave propagation path (thick dashed line) is used for calculating time-of-flight. The receive apodization is computed using the distance from the receive element to the “scan line” and the value (red line) can be read-off from the arc representing an apodization function. Similarly, a transmit apodization (green line) is computed using the distance from the origin of the transmission to the “scan line”. The grey area shows the “beam” that we are synthesizing by applying the given apodization.

from either the source (\vec{r}_{xmt}) or the sink (\vec{r}_{rcv}) to the “scan line”. Instead of beamforming lines and sampling the Nyquist criteria in all directions and afterwards struggling with scan line conversion, in-phase and quadrature data are beamformed on a grid of points, one point for each point in the final image. In this way, a complex image for each steering angle is computed, and the final image is obtained by adding their absolute values followed by logarithmic compression.

2.2.2 Validation

Development of new imaging methods includes several quality and performance assessment stages. For ultrasound imaging, a combination of water tank, phantom measurements, and extensive clinical evaluations are carried out to ensure that the desired clinical performance is met. The performance criteria are defined using measures for detail resolution, contrast, sensitivity, dynamic range, and temporal resolution. For the initial conference paper, “A Method for Synthetic Aperture Compounding”, attention was mistakenly given to contrast, only. Obviously, a study of the detail resolution should also have been included - in particular to demonstrate, how contrast comes at the cost of a reduced detail resolution.

The reason for forgetting the detail resolution in the paper was that it was so easy to do proper focusing using data simulated with Field II and the real challenge was to get an improved contrast due to compounding and not improper focusing. The detail resolution was studied at the time of submitting the first paper, and since it was omitted in the paper, the results will be presented here. We will get back to a more thorough evaluation of ultrasound images in the next chapter, where imaging is made using data acquired with our research scanner, SARUS [34]. For now, the attention will be given to the detail resolution and contrast assessed by simulating wires in a water tank and cysts at different scattering levels in a homogeneous backscattering medium. In the next few paragraphs, a number of measures used for evaluating the approach for compounding using synthetic aperture data, will be defined.

Detail resolution

The *detail resolution* is the separation at which identically point targets can be distinguished. It is distinguished by the main lobe width of the point-spread-function (PSF) and the 6 dB axial pulse length, i.e. the lateral and axial full width at half maximum (FWHM) of the PSF, cf. Chapter 1. The PSF can be found by scanning a water tank with wires and analyze the resulting image. Ideally, a point source should be scanned, but for practical reasons, wires are used and the dimensions of the PSF are studied two at a time. For simulations, a point source can easily be simulated using Field II and this is how the PSF is addressed in this chapter.

Contrast

Most commonly, contrast resolution refers to the ability to distinguish echogenicity differences between a region of interest (ROI) and the background (B). The contrast is quantified using a signal-to-noise ratio for contrast often referred to as the contrast-to-noise ratio or simply contrast [35]

$$C_{\Delta I} = \frac{|\mu_{I_{ROI}} - \mu_{I_B}|}{\sqrt{\sigma_{I_{ROI}}^2 + \sigma_{I_B}^2}} = \frac{\Delta I}{\sqrt{\sigma_{I_{ROI}}^2 + \sigma_{I_B}^2}}, \quad (2.1)$$

where $\mu_{I_{ROI}}$ and μ_{I_B} are the mean intensities of the ROI and the background, respectively, and $\sigma_{I_{ROI}}^2$ and $\sigma_{I_B}^2$ are their corresponding variances. The intensities are related to the magnitude, V , of the received signal, through $V^2 = I$. The contrast, $C_{\Delta I}$, is object dependent and is improved by increasing the object contrast, ΔI , as well as by lowering the variance inside the ROI or in the surrounding tissue. In (2.1), the mean intensities appear and the equation therefore only applies, when the regions are large compared to the speckle size. For compound imaging, the contrast is very interesting, since by averaging independent measurements, the variance of the mean scales inversely proportional to the number of measurements. Unfortunately, the images averaged for compound imaging are not completely independent, and the contrast is improved by less from the averaging process. Defining performance criteria using object dependent quantities is very unfortunate, and as just stated, the contrast (2.1) is object dependent. This implies, in principle that one needs to define standard phantoms for comparing the performance of different ultrasound imaging systems. Instead of studying the contrast, one therefore often studies the expectation value of V , in units of its standard deviation. In the literature, this quantity is referred to as the signal-to-noise ratio at a point [36]

$$\text{SNR}_0 = \frac{\mu_V}{\sigma_V}. \quad (2.2)$$

The envelope-detected signals, V , follow Rayleigh statistics and for a fully developed speckle, the theoretical value of SNR_0 is 1.91 and the number of independent images can be found using [36]

$$N_{\text{eff}} = \left(\frac{\text{SNR}_0}{1.91} \right)^2. \quad (2.3)$$

When measuring the contrast (2.1) or the signal-to-noise ratio at a point (2.2), the means and the standard deviations should be replaced by the sample means and sample standard deviations. The statistician may argue that the pooled variance should be used in (2.1) and an unbiased estimator should be used for the standard deviation in (2.2), but since we are averaging a high number of pixels, this doesn't really change the results. The name signal-to-noise ratio at a point has led to a lot of confusion, because noise in this context refers to speckle, and contrary to white noise (e.g. electronic noise), speckle is fully deterministic. Deterministic in the sense that if the fine structure of the tissue is known, the speckle pattern can be computed and for a fixed target, it is persistent. More confusingly, if the electronic noise is increased or the focusing is done incorrectly, the signal-to-noise ratio at a point will most likely increase. This is due to electronic noise or improper focusing leads to blurring of the images, which obviously lowers the variance. It is therefore very challenging to distinguish true speckle reduction and compute correctly the number of independent images.

2.2.3 Simulation Study

To prototype the approach for compound imaging using synthetic aperture data, a simulation study was initiated. The primary purpose was to show, how the contrast of cysts gets improved by compounding using the suggested approach and compare the results to compound images created using conventional focusing. The initial simulations were made to mimic the scattered signal from a grid of wires for single-element emissions with a 7 MHz, λ -pitch transducer with 192 elements. The parameters used for simulating the transducer using Field II are given in Table 2.1 Once, the

Parameter	Value
Elements	192
Active elements (transmit)	64
Center frequency	$f_0 = 7$ MHz
Pitch	0.208mm
Kerf	0.035mm
Element height	4.5 mm
Excitation	2 cycles at f_0
Elevation focus	20 mm
Electronic focus	25 mm
Compound angles	$-9^\circ, -7^\circ, \dots, 9^\circ$

Table 2.1: Simulation parameters for the initial prototyping of synthetic aperture compounding.

focusing was in place, a number of cysts with different scattering levels were simulated at depths ranging from 10 to 50 mm. In Fig. 2.2, images of the wires and cysts are shown. The images are created using 10 compound angles with an angular separation of 2° . For each angle, an aperture with a width equal to the width of 64 elements was synthesized for both transmit and receive. In Fig. 2.2a, the point spread function can be seen to widen across depth and when moving to either side. This is due to an increased depth and when moving to either side, a smaller effective aperture. The lateral FWHM is extracted and given in Table 2.2.

Grating lobes are also present, but they are very low due to the limited steering of the aperture. In Fig. 2.2b, 20 cyst are simulated with scattering levels of -12 , -9 , -6 , and -3 dB relative to the background. Only the most hypoechoic cysts are clearly visible, but they are all hard to distinguish from the background. The speckle reduction seems larger for cysts at larger depths, which may at first seem counterintuitive. The reason for this behavior is now fully understood, but at the time of writing the first paper, I was not aware of how to interpret this. The explanation for the increased speckle reduction is that the further we go down, the further apart the apertures are synthesized and the more decorrelated the speckle patterns become before the averaging. In Chapter 4, the theory needed for a quantitative understanding of this behavior is presented.

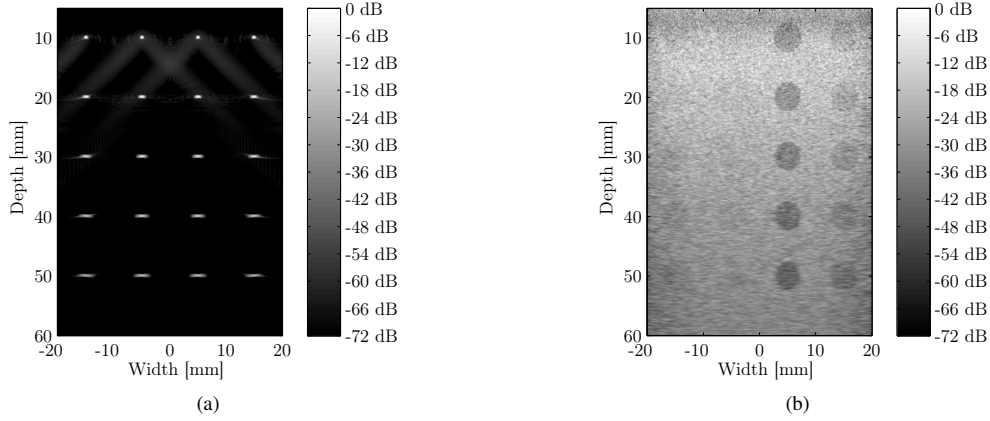

 Figure 2.2: Synthetic aperture compound images created using 10 angles with an angular separation of 2° .

Table 2.2: Lateral FWHM for simulations of synthetic aperture (SA), synthetic aperture compounding (SAC), dynamic receive focusing (DRF) and dynamic receive focusing with compounding (DRFC).

		SA		SAC		DRF		DRFC	
Lat. pos.		5 mm	15 mm	5 mm	15 mm	5 mm	15 mm	5 mm	15 mm
Depth	10 mm	0.28	0.29	0.30	0.31	0.52	0.57	0.52	0.63
	20 mm	0.36	0.39	0.48	0.50	0.67	0.72	0.65	0.73
	30 mm	0.40	0.46	0.68	0.73	0.88	0.83	0.86	0.94
	40 mm	0.42	0.51	0.88	0.95	1.29	1.24	1.17	1.19
	50 mm	0.44	0.57	1.06	1.15	1.65	1.50	1.47	1.49

To illustrate the effect of achieving compounding by adding images incoherently, the very same image data (IQ-data) were added coherently to create a synthetic aperture reference images. In Fig. 2.3, the images are shown and the lateral FWHM is extracted and given in Table 2.2. The resolution is improved, but the speckle is more dominating and the cysts are harder to localize. The speckle images in Fig. 2.2b and Fig. 2.4b are both too bright at depths around 15 mm. This happens because at this stage of the implementation, no attention was given to how many emissions were contributing to a given image point. In Chapter 4, a convenient method for dealing with this issue together with attenuation is used for creating the images. In Fig. 2.4, compound images created using dynamic receive focusing are shown. Similarly, to the compound images created using synthetic aperture, the compound images are created using 10 angles with an angular separation of 2° and for each image line, 64 channels are used for focusing in transmit and receive. The compound effect is surprisingly good, but part of the effect is due to a blurring caused by the lack of transmit focusing. The lateral FWHM for the images focused using dynamic receive focusing with and without compounding are extracted and shown in Table 2.2. The results show that within the fully compounded region, the resolution is improved upon compounding and a study of the axial resolution revealed that compounding has the effect of trading axial for lateral resolution. The reader may find it surprisingly that the resolution near the focus point at 25 mm is worse than what was obtained using synthetic aperture. The reason for this is that the synthetic aperture images are created using the same IQ-data used for creating the synthetic aperture compound images and therefore the effective aperture is larger.

For the simulation study used in the conference paper, “A Method for Synthetic Aperture Compounding”, the pitch was changed to $\lambda/2$ to avoid grating lobes, but all the remaining parameters are kept as those in Table 2.1. The cysts were simulated at a depth of 40 mm as shown in Fig. 2.5. Images were created using synthetic aperture with and without compounding like described in this chapter. The MACI approach for compound imaging were also studied, where compound images are created using 1, 3, and 5 angles with an angular separation of 2° . All the images can be found in the conference paper and will not be shown here. The signal-to-noise ratio at a point, SNR_0 and the contrast for the cysts were measured and for all cysts, an increased contrast was observed when applying either spatial

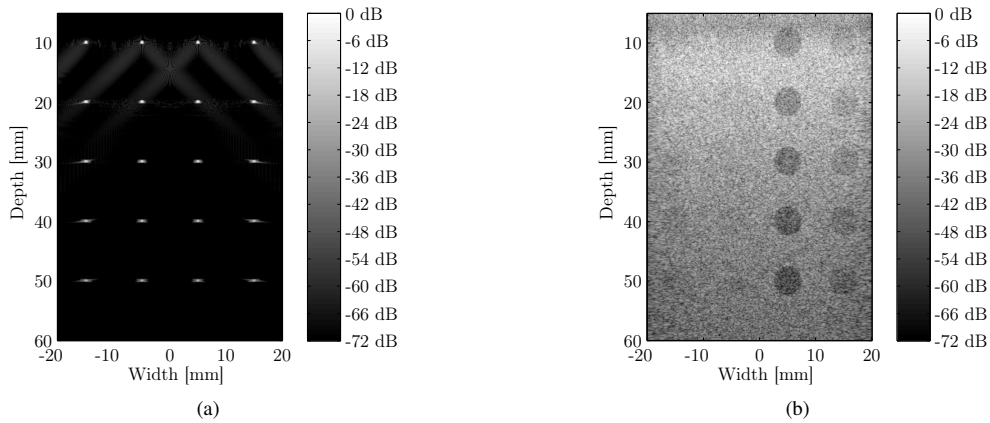


Figure 2.3: Synthetic aperture images created using the same IQ-data used for creating Fig. 2.2, but added coherently.

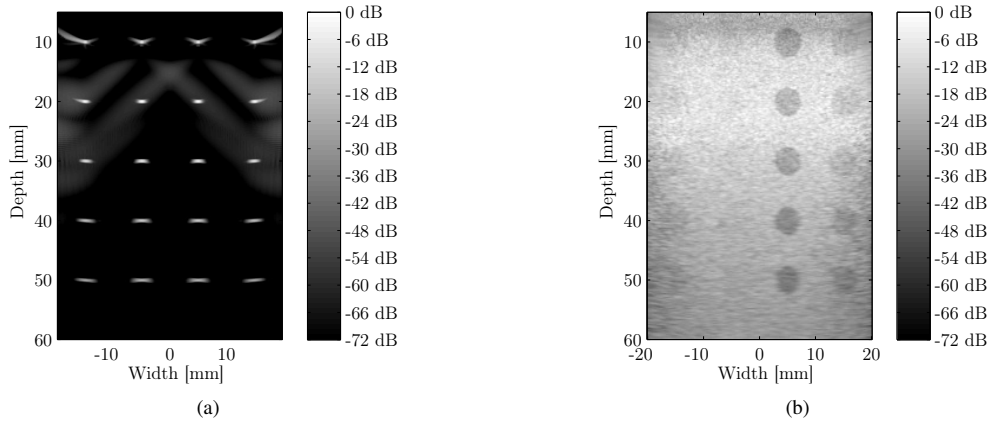


Figure 2.4: Images created using dynamic receive focusing and compounding using 10 angles with an angular separation of 2° . The transmit focusing was performed using a focus depth of 25 mm.

compounding or the new approach for compounding using synthetic aperture data.

2.3 Discussion

A method for synthetic aperture compounding has been formulated for synthetic aperture data acquired using single-element emissions. For all cysts imaged using conventional spatial compounding, an improved signal-to-noise ratio at a point is obtained, when increasing the number of compound images - this in agreement with the results of Jespersen [13].

Using instead synthetic aperture data, an increased resolution is obtained, which can be seen from the numbers in Table 2.2. The fact that speckle is reduced and contrast improved can be seen by comparing Fig. 2.2 and 2.3 or by inspecting the numbers of Table I and Table III in the conference paper. The success for simulating synthetic aperture compound images with an improved contrast opens for further applications of synthetic aperture imaging worth investigating. In particular, an even better contrast can easily be obtained by trading off resolution by using smaller transmit or receive apertures.

The next steps are to collect synthetic aperture data with our research scanner SARUS, validate the method using *in-vivo* data, and finally to implement synthetic aperture compounding for real-time *in-vivo* imaging.

If we were to repeat a simulation study for synthetic aperture compounding, we would most likely make a different

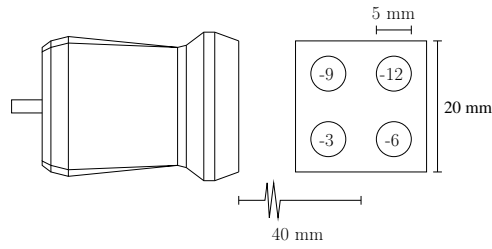


Figure 2.5: Simulation setup with a phased-array transducer and an image region of size (HWD) $5 \times 20 \times 20$ mm. containing 4 circular regions with a diameter of 5 mm and scattering levels ranging from -3 to -12 dB relative to the background.

choice with respect to the compound angles and synthesize apertures corresponding to steering the beam using larger angles.

SYNTHETIC APERTURE COMPOUNDING USING A CONVEX ARRAY

This chapter contains a presentation of the conference paper

- **J. M. Hansen**, and J. A. Jensen: Performance of Synthetic Aperture Compounding for *in-vivo* imaging. Proceedings of the IEEE Ultrasonics Symposium, October, 2011

and the journal paper

- **J. M. Hansen** and J. A. Jensen: Compounding in Synthetic Aperture Imaging. IEEE Trans. Ultrason., Ferroelec. and Freq. Contr., 2012,

which was accepted for publication, Tuesday, May 29th. after a minor revision. The papers can be found in full length in Appendix A.4 and A.5, respectively. The research for the journal paper were put on stand by due to reassembling of the research scanner, SARUS, and unfortunately, no clinical images were made. To test the performance of synthetic aperture compounding for *in-vivo* imaging, data recorded with our previous research scanner, RASMUS [37], were used for creating clinical synthetic aperture images with and without compounding. The clinical images are not presented in the journal paper, since they are collected using a difference probe and acquisition system and no interleaved data were acquired for conventional compounding suitable for comparison. The journal paper is an extended and more elaborated version of the conference paper and apart from the clinical images, no attention will be paid to the conference paper.

3.1 Purpose

The purpose of the study was to establish a setup, which could be used for clinical studies using the research scanner, SARUS. Setups for imaging using synthetic aperture with and without compounding as well as imaging using dynamic receive focusing with and without compounding should be established. The latter for comparison and ideally, they could be compared with state-of-the-art ultrasound imaging systems using dynamic receive focusing.

3.2 Contribution

In Section 2.2.1, the approach for spatial compounding using synthetic aperture data was presented and in Section 2.2.3, the use was demonstrated through simulations. The simulation results are very convincing, but at the same time counterintuitive, in particular, since the compound effect was largest far away from the transducer surface. In this chapter, this issue will be explained and synthetic aperture compounding will be reformulated to improve on the compound effect across depth. The new formulation also applies to a convex array transducer and a setup,

where virtual sources are used rather than single-element emissions. Using the research scanner SARUS under ongoing development, a setup is established for synthetic aperture compounding using a convex array transducer. The setup is optimized for proper focusing and different apodizations are studied to achieve the best detail resolution. Next, the contrast is optimized for lesion detection using an already established performance measure and a parameter derived from the method of the ideal observer [38]. Finally, clinical data recorded with our previous research scanner, RASMUS, are used for an *in-vivo* demonstration of how compounding can be achieved without reducing the frame rate or temporal resolution.

3.2.1 Synthetic Aperture Compounding - Revisited

The generalization of the method formulated in Section 2.2.1 to emissions involving multiple elements and a virtual source behind the aperture is in principle straight forward. The location of the emitting element, \vec{r}_{xmt} should simply be replaced with the location of the virtual source. However, an implementation of this revealed many complications of which some had been studied before. Creating a spherical wave by computing delays for a number of elements is quite challenging and it turned out to be a lot easier to do proper focusing using single-element emissions. Also, the fact that the sound does not cross the transducer lens and matching layers in a straight line needs to be considered to improve on the focusing. The initial transducer used for synthetic aperture compounding turned out to be slightly delaminated causing some signals to arrive later than what was expected and therefore, a setup for estimating phase errors was developed. Finally, the acceptance angle for the virtual source was studied to improve on the resolution - a study inspired from the work of Oddershede [28]. Before formulating the approach for synthetic aperture compounding using a convex array, we provide the details for how synthetic aperture (without compounding) can be formulated and applied to a convex array transducer.

Synthetic Aperture

Most often for synthetic aperture imaging, a full transmit aperture is synthesized by emitting spherical waves for a number of subapertures and receiving with all or part of the elements [39, 32, 40]. The positions of origins for the spherical waves are selected to make up a transmit aperture with the same pith as that for the receiving aperture. Using a complete data set acquired this way, any beam and focusing can be synthesized.

For synthesizing a transmit aperture, delays and apodization values are calculated for each point in the image to construct signals, which at each point sum up coherently. Many unfocused emissions contribute to synthesizing a transmit aperture, and in Fig. 3.1, the time-of-flight and apodization calculation involved for a single emission and a single focal point are shown. The transmit apodization can be read-off as the intersection of the Tukey profile (blue) and the line passing through the focal point, \vec{r}_{fp} , and parallel to the center line of the emission. For the transmit apodization, it is very important to take into account, the acceptance angle for the virtual source as stated by Oddershede [28], but also the acceptance angle for the individual elements needs to be considered. The shaded area in the figure represents the volume of insonification within the acceptance angle for the active elements. For the illustration in the figure, an acceptance angle of 22.5° is used. For receive focusing, another set of delays and apodizations are applied to the signals received from the individual transducer elements and then a weighted sum is performed. In Fig. 3.1, the receive apodization can be read-off as the intersection of the “scan line” and the Hamming profile (red). The apodizations can be adjusted to maintain a constant resolution over a range of depths using a fixed f-number for an expanding or contracting aperture for transmit and receive beamformation. At the end of Section 3.2.3, we demonstrate how the resolution at a fixed depth can be optimized by adjusting the f-number for transmit and receive apodization. In this way, the size of the apertures contributing to improving on the resolution can be computed, which can be used for estimating the effective aperture.

Synthetic Aperture - Angle Compounding

To perform compounding using synthetic aperture data, the linearity of delay-and-sum beamformation is exploited to synthesize multiple transmit and receive apertures using data from part or all of the unfocused emissions. The transmit apodizations are calculated like formulated in the previous chapter with the exception that the synthesized beam now

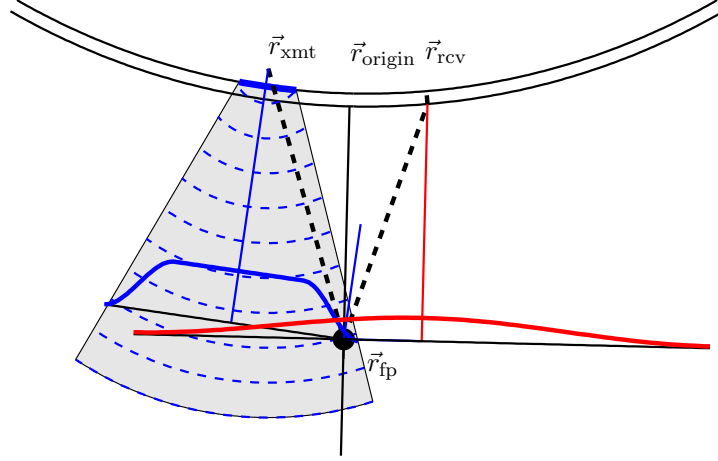


Figure 3.1: Wave propagation path (thick dashed line) for calculating time-of-flight for an emission with origin \vec{r}_{origin} and data acquired with the element positioned at \vec{r}_{rcv} .

make an angle θ with a normal to the transducer surface. In Fig. 3.2, it is shown for a single point in the image, how the transmit apodization for an emission with origin \vec{r}_{xmt} ¹ is calculated using the distance from the transmit origin to the “scan line”. The apodization value can be read-off from the figure as the intersection of the scan line and

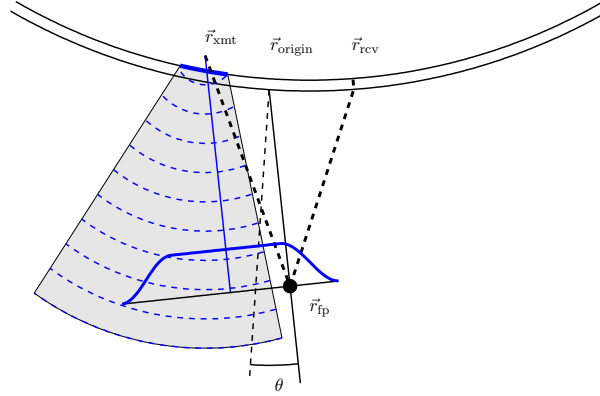


Figure 3.2: Transmit apodization calculation for a single image point \vec{r}_{fp} for an emission with origin \vec{r}_{xmt} .

the apodization profile. For the situation illustrated in the figure, the value is close to unity. Note here that steering the beam too heavily results in signals from emissions to contribute to the image outside the regioninsonified. The apodization calculated in Fig. 3.2 is an example of this.

The receive apodizations are calculated for each point and applied to the signals received from the individual receiving elements for each transmission. In Fig. 3.3, it is demonstrated how they are calculated using the distance from the “scan line” to the position of the receiving elements. The apodization values can be read-off the figure as the intersection of the “scan line” and the Hamming profile (red). Also in receive, signals may contribute to the image, where they should not. This happens when we are close to the transducer and the steering causes the angle of incidence for some elements to be larger than the acceptance angle.

In addition to the apodizations illustrated in the Figs. 3.2 and 3.3, transmit and receive apodizations were applied to ensure that no signals received or transmitted with an angle of incidence larger than 45° contributed to the image.

In Section 3.2.3, it will be demonstrated that a set of N_θ images, each optimized to give the best possible detail

¹In the conference paper, it is written that the emission is originating from \vec{r}_{origin} . This is a typo.

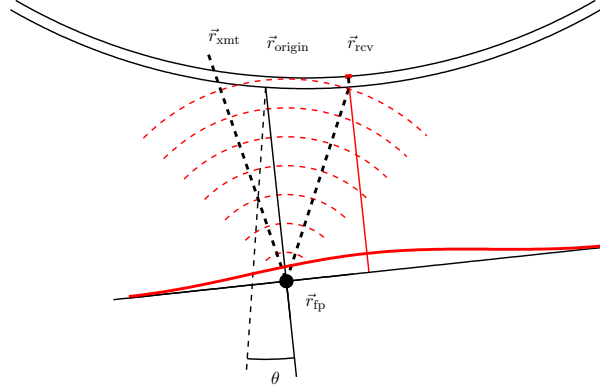


Figure 3.3: Receive apodization calculation for a single image point \vec{r}_{fp} for an image angle θ .

resolution, results in a synthetic aperture compound image with no speckle reduction and how compounding can be achieved only by sacrificing some of the detail resolution. The full explanation on this can be found in the two journal papers and will be given in Chapter 4 with more details.

3.2.2 Validation

After entering the laboratory and working with data collected with our research scanner, SARUS, it came clear that the detail resolution (FWHM) and contrast (2.1) defined in Chapter 2 were not by themselves adequate for optimizing the image quality. In particular, the detail resolution defined by the full width at half maximum ignores what is outside the main lobe and this has a significant impact on images of wide dynamic range systems. The signal outside the main lobe and clutter fill-in images of anechoic objects such as cysts, or weakly echogenic objects such as blood vessels, and reduces their detectability. It is therefore of great interest to improve on the ability to detect anechoic or weakly echogenic objects in the presence of strong surrounding objects. This ability is sometimes referred to as contrast resolution, but was first introduced as *cystic resolution* [41].

Cystic Resolution

The cystic resolution can be quantized by the clutter energy to total energy ratio (CTR). The CTR is defined as the ratio of the energy outside a circular region \mathfrak{R} with radius R centered at the peak of the PSF to the total PSF energy

$$\text{CTR}_R(\vec{r}_0) = 10 \log \left(\frac{\int_{\vec{r} \notin \mathfrak{R}} |h(\vec{r}, \vec{r}_0)|^2 dS}{\int |h(\vec{r}, \vec{r}_0)|^2 dS} \right) = 10 \log \left(1 - \frac{\int_{\vec{r} \in \mathfrak{R}} |h(\vec{r}, \vec{r}_0)|^2 dS}{\int |h(\vec{r}, \vec{r}_0)|^2 dS} \right),$$

where $|h(\vec{r}, \vec{r}_0)|$ is the PSF at \vec{r}_0 . Since the scattered signals from individual scatterers are statistical independent, for a large ensemble of measurements, the CTR is also a measure of the difference between the average level of an anechoic cyst's center and the background. To get a single measure, one either measures the drop in brightness for a fixed radius R or the radius for which a cyst can be observed at a fixed level. For improving the detail resolution of SAC, the latter was used with a scattering level of -20 dB, i.e. $R_{20\text{dB}} \equiv \{R | \text{CTR}_R = -20\text{dB}\}$. In the conference paper, the implementation of CTR was mistakenly implemented using the magnitude, V , instead of the intensity, $I = V^2$. All results reported for this quantity will therefore be taken from the journal paper.

Tissue contrast resolution

Similarly to how the FWHM can be replaced with an improved measure for detail resolution, the object contrast (2.1) defined in Chapter 2 can be replaced with a measure, which captures the ability to detect lesions or distinguish differences in echogenicity. Contrary to the object contrast, the improved measure is object independent and can be

measured by scanning a speckle phantom without cysts. The measure is derived from a theoretical model of an ideal observer for the task of identifying a lesion within a uniform background, where the model quantifies the expected trade-off between resolution loss and speckle reduction. It assumes Rayleigh statistics, an elliptical speckle cell shape, and that the lesion is large compared to the speckle size. Using this model, the signal-to-noise ratio for lesion detection is [35]

$$\text{SNR}_{\Delta I} = \frac{CdN_{\text{eff}}^{1/2}}{(S_{\text{lat}}S_{\text{ax}})^{1/2}}, \quad (3.1)$$

where C is the contrast of a circular lesion of diameter d , S_{lat} and S_{ax} are the lateral and axial speckle dimension, and N_{eff} is the number of independent images compounded. The contrast, C , in (3.1) should be thought of as the constant true contrast and to improve the detectability of cyst with a fixed diameter, it is therefore of great interest to maximize the density

$$\rho_{\text{SID}} = \frac{N_{\text{eff}}}{(S_{\text{lat}}S_{\text{ax}})}, \quad (3.2)$$

which we have baptized the *speckle information density* (SID). The speckle dimensions can be obtained from the auto-covariance function of the intensity as shown in the journal paper.

For a cyst with fixed radius and a given echogenicity, optimizing the SID improves on the detectability. Moreover the definition (3.2) states that an improvement followed by reducing the speckle size by a factor of 2 is equivalent to a compound image constructed using 2 independent images. The speckle information density (3.2) is related to the normalized information density (NID) introduced by Ustuner et al. [42] through

$$\rho_{\text{SID}} = \frac{\pi \text{NID}}{2 \cdot 1.91^2}.$$

The NID was used for the conference paper, but since the definition in the presentation by Ustuner was somewhat unclear, the SID defined using the original expression (3.1) was used for the journal paper.

3.2.3 Results

For both the conference and the journal paper, a SAC setup using a commercial 3.5 MHz, 192-element, λ -pitch convex array (BK Medical) was used for water tank and tissue phantom measurements. Data were collected using the experimental ultrasound scanner, SARUS, capable of storing 12-bit individual channel data at 70 MHz. For SA and SAC imaging, a 16-element subaperture was used for 192 unfocused emissions. For each emission, data from all 192 channels were stored. For all emissions, a two-cycle sinusoid was used for excitation together with a Hamming apodization on the active subaperture. Compounding was performed using 5 compound angles with an angular separation of 5° .

For conventional compounding using dynamic receive focusing, a 64-element subaperture was used for 192 focused emissions for each compound angle. The excitation used was the same as for the synthetic aperture setup. Compounding using dynamic receive focusing was similarly performed using 5 angles with an angular separation of 5° . The focused emissions for each subaperture were constructed using a focal distance of 42 mm and by steering the beam in directions relative to a normal on the active subaperture.

Wire Phantom Results

For compounding using both conventional and synthetic aperture focusing, the very limited angular span was used to avoid grating lobes. In the next sections, we will elaborate on how the focusing and apodization were optimized to improve on the detail resolution.

Phase Errors

As stated in Section 3.2.1, the initial measurements were made using a linear array, where phase errors were observed. The phase errors significantly degrade the focusing and this needs to be compensated for. We therefore established a

model, which by scanning a wire phantom could be used for estimating all phase errors resulting from the transducer or the acquisition system. The work has not been documented or published elsewhere, so the idea and results are presented in this section. For a transducer with N elements, a setup with N single-element emissions are used for scanning a wire phantom and data from all receiving elements are stored. Using synthetic aperture focusing, an initial image is created and used for locating the wire. Next, a line passing through the wire is beamformed using each single-element emission and instead of adding the signals, the beamformed signals for each receiving element are stored. In this way, we get $N \times N$ estimates for combinations of lengths of ray paths

$$\begin{pmatrix} l_1 \\ l_2 \\ \vdots \\ l_{N \times N} \end{pmatrix} = \begin{pmatrix} 2 & 0 & 0 & \dots & 0 \\ 1 & 1 & 0 & \dots & 0 \\ \vdots & & & & \\ 0 & 0 & 0 & \dots & 2 \end{pmatrix} \cdot \begin{pmatrix} d_1 \\ d_2 \\ \vdots \\ d_N \end{pmatrix}. \quad (3.3)$$

In (3.3) d_j is the length of the ray path from the j 'th element to the wire including a possible focusing error and l_i is the position of the wire on the line passing through the initial estimate for the position of the wire. The position l_i is thus determined using only a single receive channel and data from a single emission. This position can be determined by the peak of the envelope, but since we are only interested in the relative positioning, it is more accurate to determine the positions of the wire l_i by estimating lags using cross-correlation preferably combined with some upsampling of the signals. We next solve the linear system, $l = G \cdot d$ for d . This corresponds to finding the delays such that all elliptical arcs from element pairs coincide with the wire. The damped least squares (DLS) solution to the problem is the solution d_ϵ , which minimizes the following quantity

$$\|G \cdot d - l\|^2 + \epsilon^2 \|d\|^2 \quad (3.4)$$

Minimizing (3.4) is equivalent to minimizing

$$\left\| \begin{pmatrix} G \\ \epsilon \mathbb{1} \end{pmatrix} d - \begin{pmatrix} l \\ 0 \end{pmatrix} \right\|.$$

The corresponding normal equation is

$$\begin{pmatrix} G \\ \epsilon \mathbb{1} \end{pmatrix}^T \begin{pmatrix} G \\ \epsilon \mathbb{1} \end{pmatrix} d = \begin{pmatrix} G \\ \epsilon \mathbb{1} \end{pmatrix}^T \begin{pmatrix} l \\ 0 \end{pmatrix},$$

and for $G^T G + \epsilon^2 \mathbb{1}$ non-singular, we have $\hat{d}_\epsilon = (G^T G + \epsilon^2 \mathbb{1})^{-1} G^T l$. For fixing the regularization parameter, ϵ , we choose to fit the data barely within the noise and for Gaussian noise this corresponds to finding the ϵ , which minimizes

$$\left| \|G \cdot d_\epsilon - l\|^2 - (N \times N) \sigma_l^2 \right|, \quad (3.5)$$

where σ_l^2 is an estimate for the variance of the measurements l , which here is assumed to be the same for all $N \times N$ measurements. If this assumptions cannot be made, the last term can be replaced with the covariance matrix for the measurements.

In Fig. 3.4a, the initial image created using single-element emissions for the delaminated transducer is shown. After beamforming the first image, the line passing through the second wire was beamformed and in Fig. 3.4b, the up-sampled beamformed data are shown for the last single-element emission. The solid line represents the lags computed by cross-correlation, and it is clear that the signals do not add up coherently. The pooled standard deviation for l was computed by repeating the measurement 10 times to be about 0.1 samples at 70 MHz. Using the above procedure for estimating d by finding the ϵ , which minimizes (3.5), the phase errors were estimated and in Fig. 3.4c, the phase errors are shown as round-trip errors (multiply by two) to match the results published by Hemmsen [43]. The results agree within the uncertainty, which can be derived from the uncertainty of the measurements. For the convex transducer, a similar test setup was established and the errors computed were less than 0.01 μs , so there was no need for compensation to optimize on the resolution.

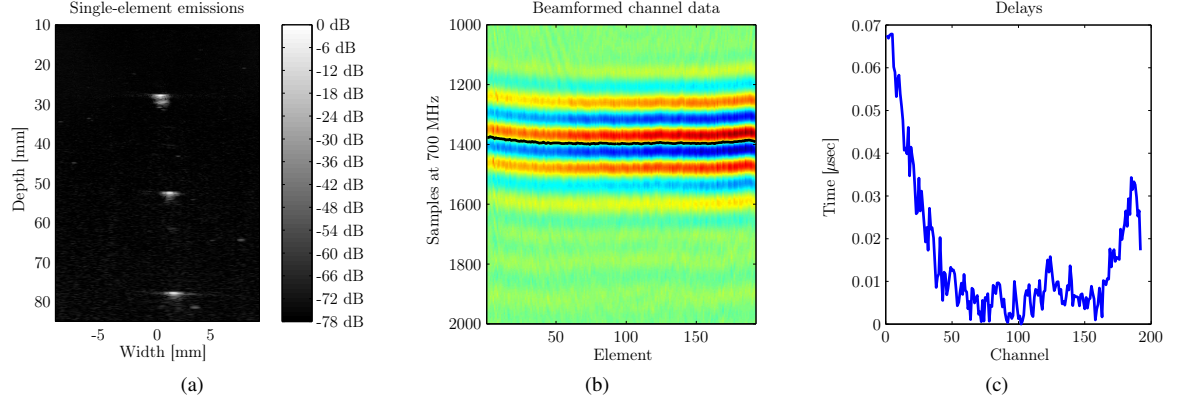


Figure 3.4: (a) image formed using 192 single-element emissions, (b) beamformed channel data for a single emission, and (c) estimated phase errors.

Apodization

To optimize the resolution for synthetic aperture compounding using the convex array, a simulation study using Field II was initiated. For a wire at a given depth, images were beamformed using different f-numbers for transmit and receive apodizations. The transmit f-number is related to the acceptance angle of the virtual source and the receive f-number is related to the acceptance angle of the receiving elements. The optimal image was found as the image with the best cystic resolution, represented by R_{20dB} . We decided to use the cystic resolution instead of the FWHM, since the latter was constant for a large range of f-numbers, while the value for R_{20dB} uniquely selected an optimal f-number for both transmit and receive apodization. If we try to maintain too low an f-number for receive apodization, too large an aperture is synthesized and edge artifacts appear. On the other hand, if we use too large an f-number, the width of the main lobe is increased. In both situations, the cystic resolution is degraded and the value for R_{20dB} increased.

A simulation setup was created, where a 16-element subaperture was used for 192 unfocused emissions, each with an origin behind the aperture corresponding to an f-number of -0.5 . The simulated data were beamformed using the beamformation toolbox [4] using dynamic apodization with a Hamming profile for a range of f-numbers for transmit and receive. In Fig. 3.5, the results are shown. The f-numbers uniquely picked out a global minimum for R_{20dB} , but

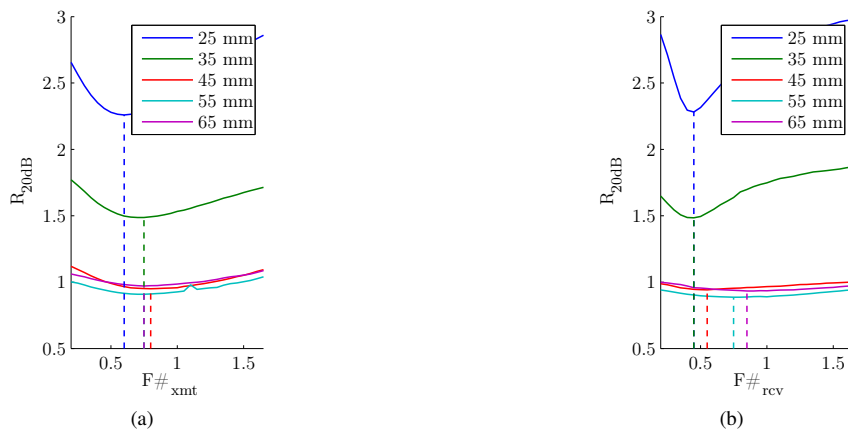


Figure 3.5: Field simulations to optimize the cystic resolution, R_{20dB} . In (a), the f-number used for receive apodization was 0.55 and in (b), the f-number used for transmit was 0.75.

unfortunately, the simulated images were worse than the measured ones and the optimal f-numbers found using Field II were not valuable for measurements. For investigating on this issue, a reference implementation was developed for

solving the Rayleigh integral (rigid baffle) using a plane-wave approximation similar to the default method used by Field II. The investigation revealed that the default method was not implemented correctly in Field II. In Fig. 3.6, the spatial impulse response (round trip) is shown for a scatterer at the position $(x, y, z) = (7, 0, 20)$ mm for a square element located at the origin and rotated 22.5° around the x-axis and 22.5° around the y-axis from an initial orientation in the xy-plane. It follows from the figure that the default method used by Field II results in a spatial impulse response equally offset to both the reference implementation and the more accurate method available, when switching on the `use_lines` option. When the `use_lines` method is used, the spatial impulse response is computed without any approximations. The output of the reference program was scaled to fit the amplitudes produced using Field II for a scatter located at $(0, 0, 40)$ mm. The error manifests itself as a phase error and has been observed, when an element

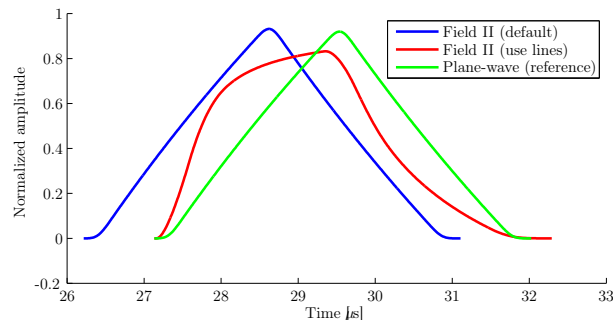


Figure 3.6: Spatial impulse response (round trip) for a scatterer computed using Field and a reference program.

is “double tilted” or the scatterer is located out-of-plane. When switching on the `use_lines` option using Field II, no errors have been observed. The author Jensen has concurred on this issue and the issue will be fixed for the next release of the program. Fig. 3.5 was made using the `use_lines` option, but still the measured images were better than the simulated ones.

To optimize on the cystic resolution, a parameter study was made using instead data measured with SARUS for SA, SAC, DRF, and DRFC. For SAC, the optimization is a bit more involved than stated in the journal paper. The optimization was done individually for each compound angle, but the results turned out to be almost identical for the different angles and the largest f-numbers were used. In Fig. 3.7, the cystic resolution represented by R_{20dB} is shown for a wire phantom measurement with wires at depths 41 and 66 mm for different f-numbers. The two graphs show

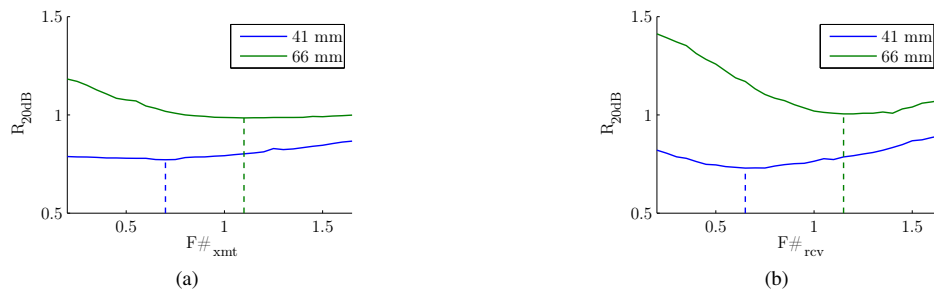


Figure 3.7: Measurements to optimize the cystic resolution, R_{20dB} . In (a), the f-number used for receive apodization was 1.15 and in (b), the f-number used for transmit was 1.10.

the value for R_{20dB} , when varying the f-numbers around a global minimum for the wire at the depth of 66 mm. A similar study was made to optimize the cystic resolution for a synthetic aperture setup without compounding and for a setup using dynamic receive focusing with and without compounding. The details can be found in the journal paper. In Fig. 3.8, the optimal PSFs are shown for the four imaging configurations. For both synthetic aperture and dynamic receive focusing, the PSFs are more round for the compounded images. For the images created using dynamic receive focusing, the clutter levels are quite high. Numbers for the FWHM, R_{20dB} , and the area of the 6 dB main lobe can be found in the journal paper.

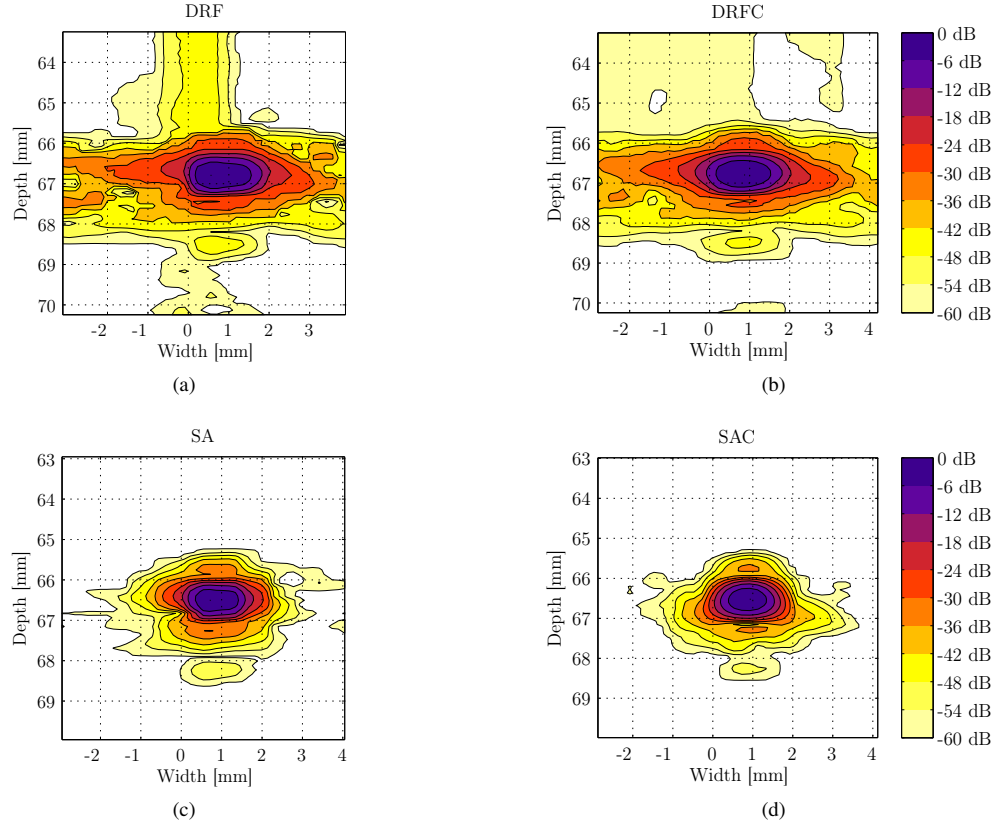


Figure 3.8: The PSF imaged at a depth of 66 mm obtained using a water tank phantom with wires. Figure (a) and (b) are made using dynamic receive focusing and figure (c) and (d) are made using synthetic aperture focusing. The figures to the right, (b) and (d) are compound images obtained using conventional compounding and synthetic aperture compounding, respectively.

We will end this section, by showing the clutter energy to total energy ratio and the clutter levels for the 4 PSFs in Fig. 3.8. It is very interesting to see, how synthetic aperture focusing outperforms the images made using dynamic receive focusing. The noise in the system was quite bad and a large amount of time was spent on optimizing the images created using dynamic receive focusing. From the experience I have working with a commercial scanner, I would say that we are missing about 10 dB for our images created using dynamic receive focusing to be as good as the images created using the commercial scanner from BK Medical available to our group. For the synthetic aperture imaging though, it is very interesting to see a clutter level of -70 dB or less, which implies that we should expect a dynamic range of similar magnitude.

Speckle Images

To investigate the performance for lesion detection, a tissue mimicking phantom was scanned using the same configurations as was used for scanning the wire phantom in the previous section. The images can be found in the journal paper and surprisingly, the image created using SAC is more grainy than the synthetic aperture image without compounding. At the time of writing the journal paper, this was fully understood, but in order not to complicate things too much, the approach for synthetic aperture compounding was formulated without considering the necessity for trading off detail resolution to achieve speckle reduction. In the journal paper, a theoretical model is presented, which states how much compounding in terms of the number of independent images, N_{eff} one gets by decreasing the size of the synthesized apertures. Unfortunately, when using angle compounding, the theory suggests an increased compound effect as a function of depth, which was also observed in Chapter 2. A long discussion on this can be found in the

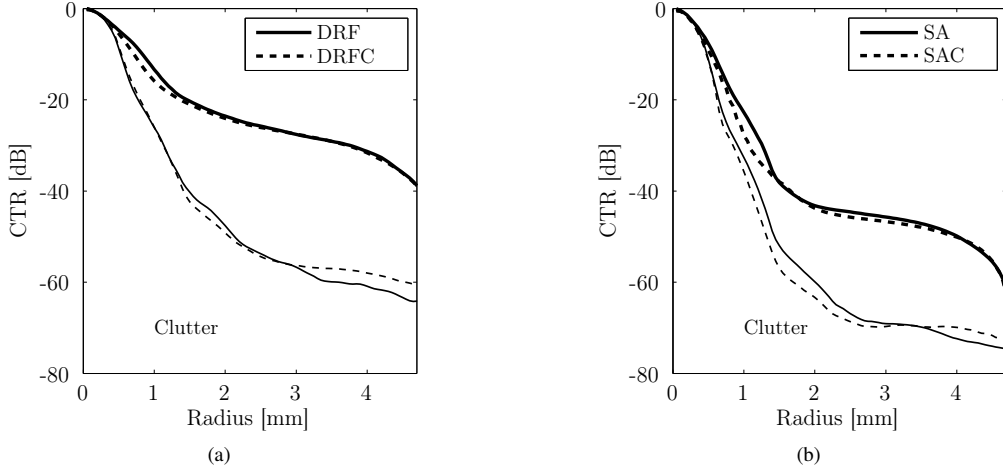


Figure 3.9: Clutter energy to total energy ratio (CTR) computed for the PSF at a depth of 66 mm. In (a), the CTR for DRF (thick solid line) and DRFC (thick dashed line) are shown and in (b), the CTR for SA (thick solid line) and SAC (thick dashed line) are shown. Clutter levels are shown below as thin dashed and solid lines for images with and without compounding, respectively.

journal paper and the discussion in this dissertation will be postponed to the next chapter, where a phased array transducer is employed for verifying the theory through measurements and compounding using synthetic aperture data will be formulated in a way, where the compound effect is independent of depth.

In this section, we simply show a number of speckle images created using the approach for synthetic aperture compounding described in Section 3.2.1, where the size of the synthesized aperture is scaled to achieve more or less compounding. The most interesting finding in the journal paper is the fact that using the speckle information density, (3.2), the size of the apertures can be scaled to a configuration, which is optimal for lesion detection. Using 5 compound angles separated by 5° , speckle images were created using different sizes of the synthesized apertures, the size determined by applying apodizations as shown in Fig. 3.2 and Fig. 3.3. In Fig. 3.10, the cystic resolution and the speckle information density is shown as a function of the size of the synthesized apertures. The cystic resolution

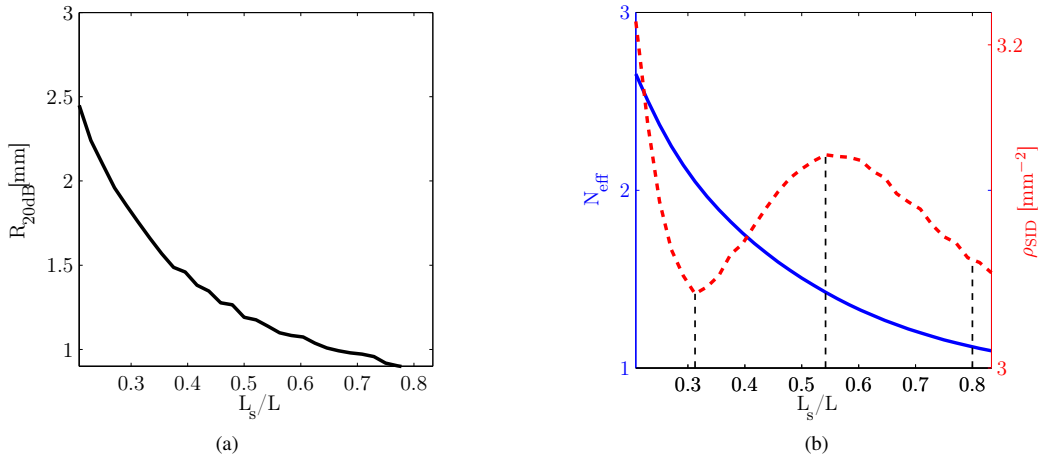


Figure 3.10: Cystic resolution, R_{20dB} , number of independent images, N_{eff} , and the speckle information density, ρ_{SID} for different sizes of the synthesized apertures.

is measured using the image of the wire at the depth of 41 mm, whereas the speckle information density is measured using a speckle image by computing SNR_0 inside a region of 20×20 mm at the same depth. The size of the synthesized aperture is shown as the fractional size of the total aperture (measured along the transducer surface).

It follows from Fig. 3.10 that by reducing the size of the synthesized apertures, the cystic resolution is degraded and the compound effect is increased. The speckle information on the other hand reaches a maximum, when the size of the synthesized apertures is about half the size of the full aperture.

In Fig. 3.11, three speckle images are shown constructed using the 3 different values for L_s/L corresponding to the dashed lines in Fig. 3.10b. Fig. 3.11a is created using the configuration, which gives the best cystic resolution,

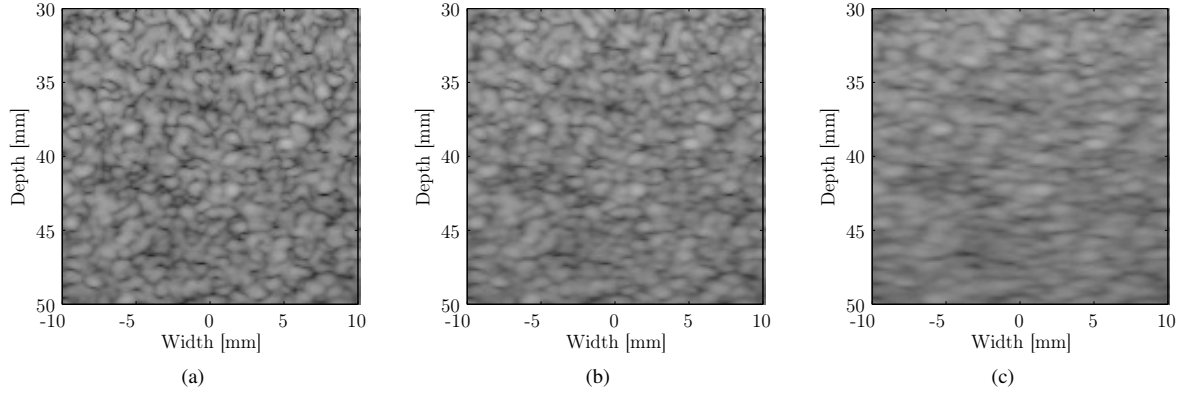


Figure 3.11: Speckle images created using the 3 different sizes of the synthesized apertures corresponding to the dashed lines in Fig. 3.10b: (a) $L_s/L = 0.81$, (b) $L_s/L = 0.54$, and (c) $L_s/L = 0.31$. The dynamic range used for all images is 60 dB.

Fig. 3.11b is created using the configuration, which gives the best value for the speckle information density, and Fig. 3.11c is created using a configuration with even smaller apertures. According to the theory of the ideal observer used by Smith [35], Fig. 3.11b and thereby the configuration used for constructing this image is superior to the configurations used for constructing Fig. 3.11a and 3.11c.

Similar results were found by studying other regions in the speckle image and we claim that this is not a coincidence. In the next chapter, a theoretical model will be presented, which states that the optimal compounding is achieved when synthesizing an aperture of about half the size of the full aperture - supporting the results and findings in this chapter and the journal paper.

Clinical Images

It has now been demonstrated, how synthetic aperture with and without compounding can be used for creating PSFs superior to what can be obtained using dynamic receive focusing using the same system for acquisition of data. Also, it has been shown how speckle reduction can be introduced by trading off resolution, by scaling the size of the synthesized apertures. The real game, however, is to take the approaches developed to the clinic and perform clinical trials. At the time of writing the journal paper, we were almost there, but I judged that there was too little time for completing a clinical study.

Luckily, in our research group, synthetic aperture data from the abdomen of a healthy 27 year old male have earlier been acquired using RASMUS, our previous research scanner. The data together with the script used for acquisition was backed up on our servers. It would have been ideal to have interleaved data from a compound acquisition sequence using dynamic receive focusing, but at least it was possible to make a shortcut for obtaining the very first *in-vivo* synthetic aperture compound images. In Fig. 3.12, the data is beamformed and the images are shown as they appear in the paper by Gammelmark [30].

By studying the scripts used for acquisition and creating the images, we were able to improve on the image quality. The following number of changes were made and the dynamic range of the image was increased from 40 to about 60 dB.

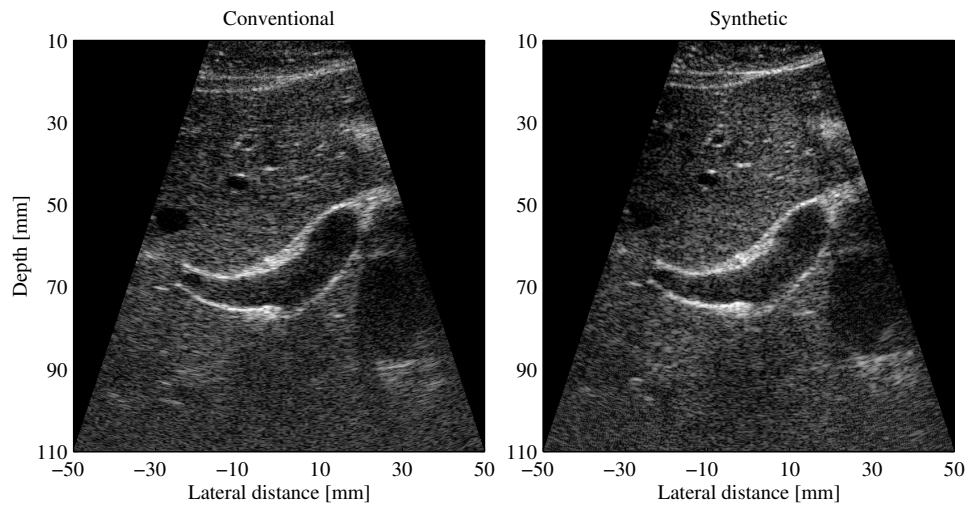


Figure 3.12: Images of the abdomen of a healthy 27 year old male. The portal vein branch is seen in the center of the images, and the hepatic and caval veins are located to the left and right of the portal vein, respectively. The conventional image is shown to the left, and the synthetic image is shown to the right. The dynamic range used for both images is 40 dB [30].

- When computing time-of-flight, one must take into account that match-filtering requires you to make your look-ups at a time corresponding to the time-of-flight plus about half the time of the excitation. For the original images, the time of the temporal round-trip impulse response convolved with the excitation was used.
- The origin for the time-of-flight should be at the virtual source and not at a point on the transducer surface. If this is done wrong, the low-resolution images will not add-up coherently.
- Interpolation among the samples should be done once and using preferably cubic-spline interpolation or a higher order interpolation routine - depending on how high a sampling rate is used. For the synthetic aperture image in Fig. 3.12 (right), the RF data were first resampled such that the time $t = 0$ corresponds to a point on the transducer surface (not the VS) and the beamformation was done in two steps, i.e. a total of three interpolations was used for the focusing.

In Fig. 3.13, the same data are used for beamforming a smaller part of the image using synthetic aperture imaging with and without compounding. Similarly to the images in the journal paper, the image created using compounding is more grainy, and it seems like compounding improves on the resolution. This is because the f-numbers used for transmit and receive beamformation have been optimized to give the best cystic resolution, similarly to Fig. 3.11a. The data used for the synthetic aperture images in the Figs. 3.12 and 3.13 were acquired using a 128-element, 5.5 MHz, convex array transducer (BK Medical) and a 20 μs FM chirp was used to improve on the signal-to-noise ratio [30]. For the synthetic aperture compound image, Fig. 3.13b, 5 angles with an angular separation of 5° was used together with dynamic transmit and receive apodization.

3.3 Discussion

A method for obtaining compound images using synthetic aperture data and a convex array has been presented. The suggested approach allows spatial compounding to be performed for any number of angles without reducing the frame rate or temporal resolution. Very importantly, it was demonstrated, how resolution must be sacrificed to achieve compounding and the compound effect can be adjusted by scaling the size of the synthesized apertures. More interestingly, it was demonstrated, how an optimal aperture size can be found by scanning a tissue-mimicking phantom and computing the speckle information density.

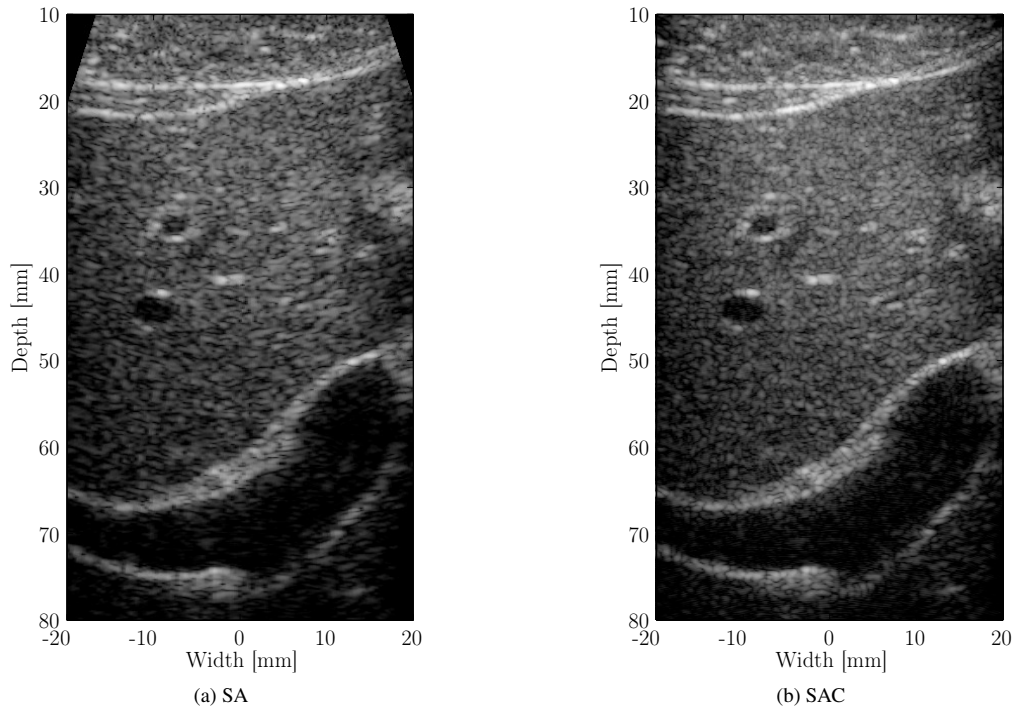


Figure 3.13: The images (a) and (b) show the abdomen of a healthy 27 year old male with and without compounding. The dynamic range is 60 dB.

In terms of the speckle information density, in the journal paper, it is shown how compound images obtained using synthetic aperture imaging are superior to images obtained using a similar setup using dynamic receive focusing. Also, it is shown that synthetic aperture compounding has an improved depth of field compared to that of conventional compounding.

The results and theory discussed in this chapter and in the journal paper state and suggest that compounding should be obtained from decorrelation of subapertures, which necessitates steering. Therefore, it will be very interesting to see how this method performs using a better transducer with $\lambda/2$ -pitch or a flat phased-array transducer, where the beam can be steered without having to worry about grating lobes. For *in-vivo* studies, a potential problem could be tissue motion corrupting the data resulting in lack of coherence of signals from different emissions. It is a problem, but it can successfully be compensated for using motion compensation as shown in [44].

SYNTHETIC APERTURE COMPOUNDING USING A PHASED ARRAY

This chapter contains a presentation of the journal paper

- **J. M. Hansen** and J. A. Jensen: Synthetic Aperture Compounding using a Phased-array Transducer. J. Acoust. Soc. Am.

and the conference paper

- **J. M. Hansen**, D. Schaa, and J. A. Jensen: Synthetic Aperture Beamformation using the GPU. Proceedings of the IEEE Ultrasonics Symposium, October, 2011.

The journal paper is the last and most successful paper written for this dissertation. It distinguishes itself from the other papers by successfully comparing measurement results with theory and the results very clearly demonstrate that compounding can be achieved using synthetic aperture data with no compromise on the frame rate. The paper can be found in full length in Appendix [A.6](#).

The conference paper was made during a short stay at Northeastern University in December 2010. In this paper, proof-of-concept is established for a real-time synthetic aperture beamformer running on the graphics processing unit (GPU) supporting dynamic transmit and receive apodization. The experiments show that using the OpenCL 1.0 framework, a naive beamformer performs much better on Nvidia Fermi GPUs than on the AMD Evergreen GPUs. Having studied the information the vendors reveal on their hardware, the better performance on the Nvidia GPUs for naive kernels is most likely due to their two-level thread hierarchy and a larger amount of L1 and L2 caches. The paper can be found in full length in Appendix [A.7](#).

4.1 Purpose

The purpose with the study was to use the experiences made for the previous study to implement compounding for synthetic aperture imaging in a way, where the compound effect as well as the resolution is uniform across depth.

4.2 Contribution

An intensive literature search was carried out for ultrasound imaging and compounding and it turns out that a theory has been established for computing the compound effect covering a wide range of aperture configurations. The theory

was derived for synthetic aperture radar imaging by Silverstein [45] and adapted to ultrasound imaging by O'Donnell and Silverstein [46]. The theory investigates the compound effect through a parameter baptized the *figure of merit* [35]

$$f_m = N_{\text{eff}} L_s / L, \quad (4.1)$$

where L and L_s are, respectively, the length of the aperture and the length of the subaperture(s) used for compounding. The thought behind the choice of this parameter is that in order to estimate the intensity inside a ROI, an image with twice the lateral resolution is equally good as an image compounded using two completely independent images made with apertures of half the size. At the focal point, the speckle size reflects the resolution, and the reader can think of each speckle cell as an estimate for the intensity and by increasing the resolution with a factor of two, twice as many speckle cells reside inside the ROI. Very interestingly, it turns out from measurement results by Trahey et al. [9] that in terms of the figure of merit, f_m , translating an aperture by half its length, results in about 3.2 independent images per aperture, i.e. $f_m = 3.2 \times 1/3 = 1.07$, which is better than using the full aperture [9]. A well established theory for computing N_{eff} for the purpose of optimizing f_m can be found in the literature [46]. The derivation is very elegant and since it is central to the research conducted in the journal paper, in the next section, it will be presented.

4.2.1 Figure of merit

The starting point of the analysis is to define the *normalized coherence function* between two measurements of the same object obtained using different aperture positions

$$\gamma_{ij} = \frac{\langle U_i U_j^* \rangle}{[\langle I_i I_j \rangle]^{1/2}}. \quad (4.2)$$

In (4.2), U is the focused complex zero mean echo signal, I represents the intensity, $I_i \equiv U_i U_i^*$, and the brackets denote ensemble averages (expectation values). The next ingredient needed is the *speckle contrast*, which is defined as the standard deviation for the speckle noise divided by the mean intensity and for N_s images, it is given by

$$C(N_s) = \frac{[\langle I^2(N_s) \rangle - \langle I(N_s) \rangle^2]^{1/2}}{\langle I(N_s) \rangle}. \quad (4.3)$$

In the literature, the inverse of the signal-to-noise ratio at a point (2.2) defined using the magnitude of the signals is sometimes also referred to as speckle contrast. The differences between the statistics obtained using magnitudes and intensities have been studied in great detail [35, 36] and an important difference is that for a fully-developed speckle, the speckle contrast defined using (4.3) is equal to unity, whereas defined using the magnitudes, it is equal to 1/1.91, cf. (2.2). To proceed, an assumption of equal intensities for the N_s images, makes it possible to express the speckle contrast (4.3) in terms of the normalized coherence function [45]

$$C(N_s) = \frac{1}{N_s} \left[\sum_{i,j=1}^{N_s} |\gamma_{ij}|^2 \right]^{1/2}. \quad (4.4)$$

At a sufficient distance, this assumption can always be made, e.g. by adjusting the gain. For a typical imaging setup, the subapertures used are of equal size and equally spaced to obtain a uniform lateral resolution and a homogeneous compound effect. In this case, the coherence matrix reduces to a Toeplitz matrix

$$\gamma_{ij} = \gamma(|i - j|x_0),$$

where x_0 is the displacement between neighbours. Using the Toeplitz assumption, the speckle contrast for an image compounded using N_s subapertures, each of size L_s and equally displaced simplifies to [46]

$$C(N_s, x) = \frac{1}{\sqrt{N_s}} \left[1 + \frac{2}{N_s} \sum_{i=1}^{N_s-1} (N_s - i) \gamma^2(i|x|)^{1/2} \right], \quad (4.5)$$

where we have introduced the relative aperture translation, $x = x_0/L_s$. Similarly to the signal-to-noise ratio at a point, the speckle contrast can be used for computing the equivalent number of independent images, according to

$$N_{\text{eff}} = [1/C(N_s, x)]^2. \quad (4.6)$$

Note the difference to the expression (2.3) in Chapter 2, where the magnitude is used instead of the intensity. With the equations, (4.5) and (4.6) at hand, we need to derive an expression for the normalized coherence function to compute, N_{eff} , and finally, the figure of merit, f_m .

The random fields $U_{i,j}$ appearing in (4.2) are formally time-dependent and the ensemble average can be thought of as averaging over many infinitesimal volumes that are small compared to the wavelength. The ensemble average can then be computed by integrating over space at the focus time. In Fig. 4.1, the synthetic aperture focusing for a continuous

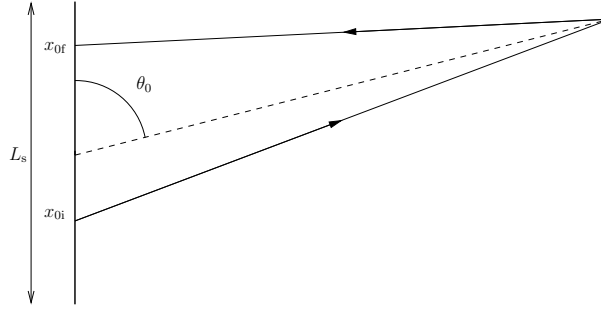


Figure 4.1: Continuum model of a linear array with a pulse emitted at x_{0i} and received at x_{0f} . The array is focused using $\mu_0 = \cos \theta_0$.

linear array is shown. The transmitted pulse is emitted from position x_{0i} and the scattered signal is received at position x_{0f} . The pulse-echo signal received at position x_{0f} is given by

$$U(x_{0i}, x_{0f}, t) = \int_0^\infty dr \int_0^{2\pi} d\phi \int_{-1}^1 d\mu \Lambda(\phi, \mu) a(t - 2r/c) \frac{\beta(r, \phi, \mu)}{r^2} \exp \{ik [ct - 2r + (x_{0i} + x_{0f}) \cdot (\mu - \mu_0)]\}, \quad (4.7)$$

where μ is the steering angle, $\mu = \cos \theta$, and $\mu_0 = \cos \theta$ is the coordinate representing the center focus, $\beta(r, \phi, \mu)$ is the complex scattering amplitude per unit volume, and $a(t - 2r/c)$ is the amplitude envelope, which can be assumed to be a rectangular pulse. In (4.7), we have used x_0 for positions on the array and $x = x_0/L_s$ will be used for relative positions. The beam-divergence function, $\Lambda(\phi, \mu)$, can be computed by requiring that it coincides with the Fraunhofer diffraction pattern in the far field. However, in order to derive the normalized coherence function, it is sufficient to use that the function can be extended to a holomorphic function in the complex plane and that it has a maximum at $\Lambda(\phi = 0, \mu = 0)$.

The focused signals $U(x, t)$ can now be obtained using (4.7) by summing or integrating over the transmitting and receiving array. For an array with center at $x_0 = 0$ and length L_s , the signal $U(x/2, t)$ focused at the polar angle $\mu_0 = \cos(\pi/2)$ is

$$U(x/2, t) = \int_{(x-1)L_s/2}^{(x+1)L_s/2} dx_{0i} \int_{(x-1)L_s/2}^{(x+1)L_s/2} dx_{0j} U(x_{0i}, x_{0j}, t, \mu_0 = 0).$$

From (4.2) we see that the coherence function $\gamma(x, t)$ relevant for two apertures each of length L_s with their centers separated by xL_s is given by

$$\gamma(x, t) = \frac{\langle U(x/2, t) U^*(-x/2, t) \rangle}{[\langle I(x/2, t) \rangle \langle I(-x/2, t) \rangle]^{1/2}}, \quad (4.8)$$

where the time variable, t , should be set to the value appropriate to the center focus, $t = 2R/c$. To perform the ensemble average, the complex scattering amplitudes $\beta(r, \phi, \mu)$ are treated as complex random variables for which the

amplitudes and phases are statistically independent. Accordingly, the averages over the ensemble of scatterers in (4.8) give

$$\langle \beta(r, \phi, \mu) \beta^*(r', \phi', \mu') \rangle = \sigma \delta(\vec{r} - \vec{r}'), \quad (4.9)$$

where $\delta(\vec{r} - \vec{r}')$ is the three-dimensional Dirac delta function and $\sigma(\vec{r})$ is the scattering intensity per unit volume. To perform the integrals involved, a number of assumptions are made: The scattering intensity per unit volume is slowly varying over the resolution cell, i.e. slowly varying within the main lobe and inside the range interval corresponding to the 6 dB axial pulse length. The integrals over the azimuthal angle, ϕ , and r can be performed independently of the μ integral. After performing the ϕ and r integrals, the normalized coherence function assumes the form [46]

$$\gamma(x) = \frac{\int_{-kL_s/2}^{kL_s/2} dz A(z^2) \exp(i4zx) \frac{\sin^4 z}{z^4}}{\int_{-kL_s/2}^{kL_s/2} dz A(z^2) \frac{\sin^4 z}{z^4}}, \quad (4.10)$$

where $z = \mu k L_s / 2$ and $A(z^2)$ represents the beam divergence function after the ϕ integration. The integrands in the above integrals are strongly peaked at $z = 0$, therefore for array lengths long compared to the wavelength, $kL_s \gg 1$, the integration limits can be extended to $\pm\infty$. The coherence function derived by Burckhardt [47] is not obtained by setting $A(z^2) = 1$ and with the limits at $\pm\infty$, which is stated by O'Donnell and Silverstein [46]. The coherence function used by Burckhardt, $\gamma(x) = 1 - |x|$, is obtained from an expression containing $\exp(i2zx)$ and the $\text{sinc}(z)$'s appearing as squares [47]. The integrals appearing in (4.10) with the limits taken at $\pm\infty$ can be solved very elegantly using Jordan's Lemma together with the Half-residue theorem as shown in Appendix B.1. The central part of the derivation uses that the beam divergence function $A(z^2)$ can be extended to a holomorphic function in the complex plane and has an extremum at $z = 0$, i.e.

$$\left(\frac{dA(z^2)}{dz} \right)_{z=0} = 0. \quad (4.11)$$

The resulting coherence function is [46]

$$\gamma(x) = \frac{\int_{-\infty}^{\infty} dz A(z^2) \exp(i4zx) \frac{\sin^4 z}{z^4}}{\int_{-\infty}^{\infty} dz A(z^2) \frac{\sin^4 z}{z^4}} \quad (4.12)$$

$$\begin{aligned} &= \begin{cases} 1 - 6x^2 + 6x^3 & 0 \leq x < 1/2 \\ 2(1 - x)^3 & 1/2 \leq x < 1 \\ 0 & 1 \leq x \end{cases} \\ &= \frac{1}{2} \left[-|1 - 2x|^3 + 2(|-1 + x|^3 + 6|x|^3 + |1 + x|^3) - |1 + 2x|^3 \right]. \end{aligned} \quad (4.13)$$

The details for why $\gamma(x)$ is independent of $A(z^2)$ can be found in Appendix B.1, and (4.13) is identical to the result one obtains by using the convolution theorem relating the Fourier transform of the product of two functions to the convolution of the individual Fourier transforms. The result (4.13) is simply the convolution of two triangles and the denominator of (4.12) is the DC component ensuring that $\gamma(0) = 1$. In Fig. 4.2a, the correlation function, defined as the square of the normalized coherence function is plotted as a function of the relative aperture displacement, x . With the correlation function at hand, the number of independent images, N_{eff} , can readily be computed using (4.5) and (4.6). To illustrate how the figure of merit, f_m , depends on the relative aperture displacement, x , and the fractional aperture size, L_s/L , we have done the following: For different numbers of subapertures, $N_s = 1, 2, \dots, 100$, and relative aperture displacements, x ranging from 0.1 to 1.0, the fractional aperture size, L_s/L , is calculated using

$$L_s/L = 1/(1 + x(N_s - 1)),$$

the number of independent images, N_{eff} , is computed for each combination of x and N_s , and finally the figure of merit, f_m , is computed using (4.1), (4.5), and (4.6). In Fig. 4.2b, contour lines for the figure of merit, f_m , are plotted as a function of the relative aperture displacement, x , and the fractional size of the subaperture(s), L_s/L . This result is most central to compound imaging and illustrates, how the figure of merit, f_m , reaches a maximum for a relative aperture displacement, x , somewhere between 0.4 and 0.5 for a wide range of fractional aperture sizes, L_s/L .

As a final remark, we mention that the established theory can easily be adapted to a setup, where compounding is achieved by translating the receive apertures only. As an example, consider the situation, where the transmit aperture

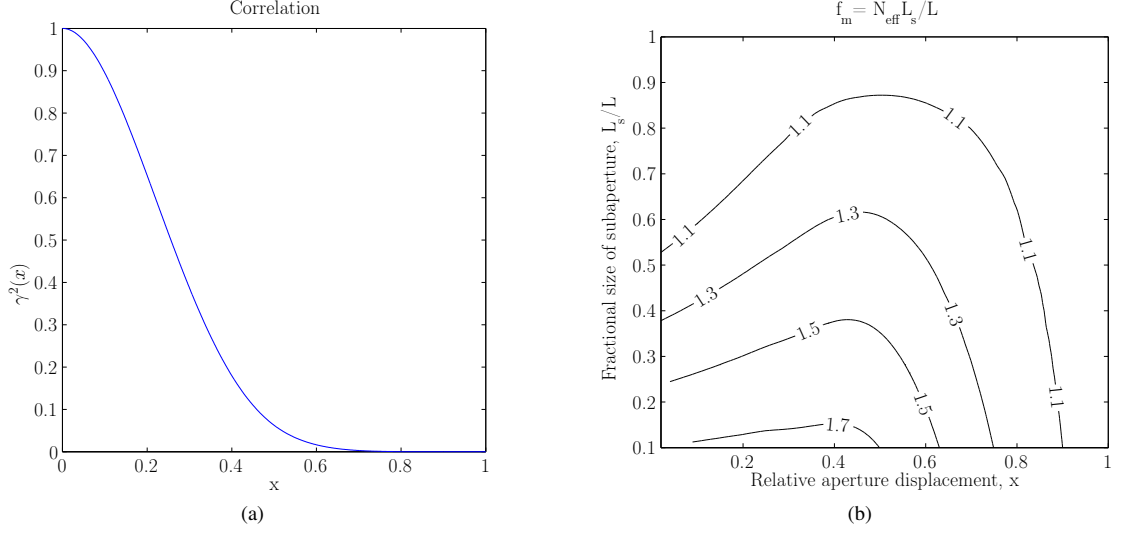


Figure 4.2: Intensity correlation as a function of the relative lateral displacement (a) and the figure of merit, f_m as a function of fractional aperture size, L_s/L , and relative lateral displacement, x .

is fixed at the origin, and the two receive apertures are located at $\pm x L_s/2$. In this case, the integrals appearing in (4.10) should be modified to contain $\exp(i2zx)$ and the resulting coherence function is a stretched version of (4.13) with a zero at $x = 2$ corresponding to the two receive apertures being separated such that neither of them overlap with the transmitting aperture.

4.2.2 Synthetic Aperture Compounding - Done Right

The theory described in the last section came clear to us during the writing of the journal paper of the previous chapter. In particular, how the theory for computing N_{eff} for a given aperture configuration supports the limited compound effect obtained, when synthesizing apertures too large. The theory also supports the initial findings of Chapter 2 revealing, how angle compounding results in an increased compound effect across depth, cf. Fig. 2.2. At the time of investigating the theory however, the acquisition setup was no longer available, and it was too late for changing the way the compound images were formed - at least the images obtained using conventional focusing. Having learned a lesson and understood the underlying theory, in this section a more ideal way for compounding using synthetic aperture data is formulated using aperture compounding. Using this formulation, a uniform compound effect can be obtained across depth, which can be combined with realizing a constant f-number to also ensure a constant resolution.

Synthetic Aperture - Aperture Compounding

Using the knowledge of the last section, for each point in the image, transmit apodization values are calculated corresponding to insonifying the point using focused beams from a number of synthetic apertures with different locations. In Fig. 4.3, it is shown for a single point, \vec{r}_{fp} , how the transmit apodization for an emission with origin \vec{r}_{xmt} is calculated using the distance from the transmit origin, \vec{r}_{xmt} to the “scan line” - the line connecting the point, \vec{r}_{fp} with the center of the synthetic aperture located at \vec{r}_3 . Similarly, receive apodizations are calculated for each point and applied to the signals received from the individual receiving elements for each transmission. The receive apodization values are likewise computed using the distance from the “scan line” to the position of the receiving elements as shown in Fig. 4.3. In addition to illustrating how the apodizations should be computed for a synthetic aperture located at \vec{r}_3 , Fig. 4.3 shows the locations of two other apertures located at \vec{r}_1 and \vec{r}_2 . The apertures are selected such that they overlap equally and are distributed symmetrically around the image point. Hence, in Fig. 4.3, three apertures are used,

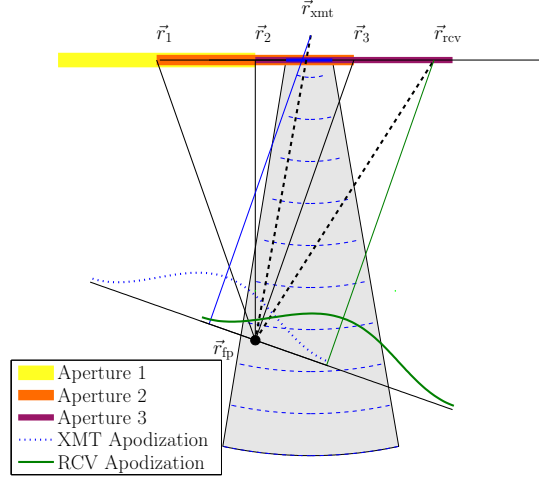


Figure 4.3: Transmit and receive apodization calculation for a single image point \vec{r}_{fp} for a sub-image using an aperture located at \vec{r}_3 . The apodization values can be read-off the figure as the intersection of the scan line and the apodization profiles. The shaded region is the region insonified by the active elements used for the unfocused emission with origin \vec{r}_{xmt} .

$N_s = 3$, and they are translated by half the aperture length and the apodizations for the situation in Fig. 4.3 are used for the third image.

The apodization calculations are carried out for a number of subapertures $i = 1, \dots, N_s$ to update N_s images used for compounding. To avoid the need for sampling according to the Nyquist criterion for the excitations used in all the directions of the scan lines, the RF data are beamformed as in-phase and quadrature components, and the envelope for each angular image is simply computed as the absolute value [48]. Finally, the compound image are constructed by adding the absolute images.

An implementation of this method uses a buffer for N_s images and calculates the delays and accesses the RF data for each pixel only once. In this way, a compound image is ready immediately after the last emission and only the processing resources limits the number of subapertures used. Since the RF data access is randomly shifted and image data access is contiguous, the amount of memory IO for data access is much larger than what is used for accessing the image. This means that the requirement for memory IO resources is comparable to what is required for synthetic aperture imaging without compounding. In Section 4.2.5, results will be given revealing that synthetic aperture imaging is extremely memory bound supporting that compounding can be implemented with almost no drop in performance.

4.2.3 Measurements

With the approach for compounding described in the last section in the journal paper, a commercial 128-element, 3.5 MHz linear phased-array transducer was used for investigating the performance of synthetic aperture compounding. Water tank measurements were used for measuring the detail resolution, a tissue-mimicking phantom was used for investigating the compound effect, and finally cyst phantom measurements were used for investigating the contrast. Sampling was done using the experimental ultrasound scanning system, SARUS, capable of storing 12-bit individual channel data at 70 MHz [49]. For synthetic aperture imaging, a 16 element subaperture was used for 128 unfocused emissions with an f-number of -0.5 . For all emissions, a two-cycle sinusoid was used for excitation together with a Hamming apodization on the active subaperture. A constant TGC was used for acquisition and to take into account that pixels at different locations may receive signal from a varying number of emissions apodized in different ways, a signal obtained by attenuating a constant signal with $0.5\text{dB}/(\text{cm} \cdot \text{MHz})$ was beamformed for normalization. Normalizing the images this way ensures that an object appears with equal brightness in the entire image region.

Tissue phantom measurements

To experimentally verify the theory of O’Donnell, a tissue-mimicking phantom was scanned and images were created by synthesizing $N_s = 2, \dots, 10$ transmit and receive apertures with relative aperture translations, $x = 0.10, 0.15, \dots, 0.90$ making a total of 153 different configurations for compounding. The transmit and receive apodizations were computed both to be of size L_s to experimentally investigate the theory of O’Donnell illustrated in Fig. 4.2b and again in Fig. 4.4a. The figure of merit was calculated using the signal-to-noise ratio at a point, SNR_0 and (2.3) and

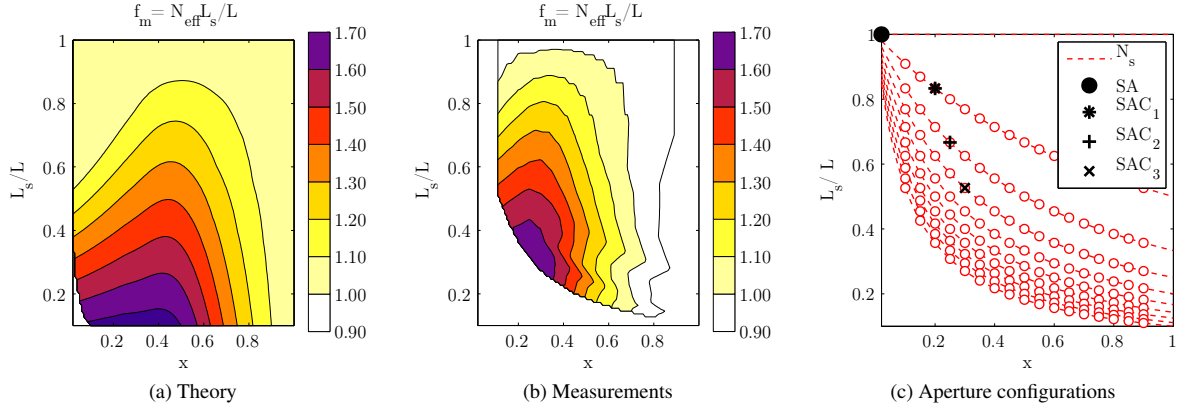


Figure 4.4: Theoretical and measured values for the figure of merit, f_m . In (a), the theoretical values are shown and in (b), the measured values are shown using a similar aperture configuration. In (c), the configurations used for computing f_m are marked with circular markers, where configurations on the same dashed line use the same number of subapertures.

the region used for extracting SNR_0 was directly in front of the transducer at a depth of 40 mm and 182x256 pixels corresponding to a region of 20x20 mm. In Fig. 4.4b, the measured values for f_m are shown. The measured values are a little smaller than the theoretical ones and the maximum is located at a position with larger and more overlapping subapertures. This can be explained by the fact that a necessary Hamming apodization was applied to the synthesized apertures to avoid edge artifacts, which otherwise give rise to higher values for N_{eff} . Then again, the theory of last section is inherently one-dimensional, and therefore only an approximate model. The Figs. 4.4a and 4.4b are both created by interpolating between the aperture configurations shown using circular markers in Fig. 4.4c. Among the aperture configurations, only a subset of four is used for the images displayed in this dissertation, and we will refer to them as SA, SAC_1 , SAC_2 , and SAC_3 . See Table 4.1.

Table 4.1: Selected aperture configurations: x is the relative aperture displacement, N is the number of subapertures, and L_s/L is the fractional size of a subaperture.

	x	N	L_s/L
SA	-	1	1.00
SAC_1	0.20	2	0.83
SAC_2	0.25	3	0.67
SAC_3	0.30	4	0.63

The 154 aperture configurations (including the SA configuration) used for creating Fig. 4.4b all suffer from a varying resolution across depth, since the aperture size(s) L_s are held fixed. We will refer to this initial setup as Setup I. To compensate for the varying resolution across depth, two other setups are investigated. A setup, where the locations of the subapertures are unchanged, but the individual apertures scaled to maintain a constant f-number across depth, Setup II, and finally, a setup where the apodization are designed to give apertures of size L_s for a certain depth, D_0 and then scaled using an f-number derived from L_s , i.e. $f = D_0/L_s$. In Table 4.2, the three setups are listed together with

the formulas for computing the size of the apodization windows. Apodizations for transmit and receive are handled in the same way. So far, only apertures of fixed size have been considered. In an imaging system, it is desirable to

Table 4.2: Synthetic aperture compound setups used.

Setup	Apodization	L_s
I	Hamming	$L_s = L/(1 + x(N_s - 1))$
II	Hamming	$L_s \mapsto D/f_{\text{xmt/rcv}}, \quad f_{\text{xmt/rcv}} = 2.0$
III	Hamming	$L_s \mapsto L_s D/D_0, \quad D_0 = 40\text{mm}$

maintain a constant resolution across depth and this can be achieved by using a constant f-number. In Fig. 4.5b, the value for the figure of merit, f_m , are calculated for a common f-number of 2.0 for transmit and receive. This translates

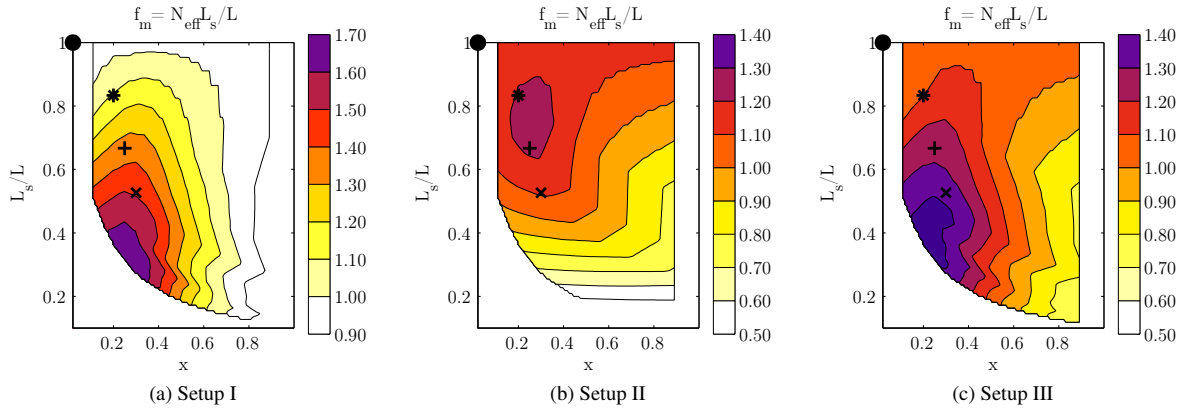


Figure 4.5: Measured values for the figure of merit, f_m . In (a), the measured values are shown using Setup I. In (c) and (b), values are measured when using Setup II and Setup III, respectively.

into that the size of the subapertures are changed according to, $L_s \mapsto D/2.0$. Fig. 4.5b shows that by maintaining the positions and number of apertures, but at the same time increasing their size, the effect of compounding is diminished for configuration with large values of N_s . The apertures become larger and less decorrelated and the maximum moves closer to the synthetic aperture configuration without compounding. In Fig. 4.5c, the size of the subapertures are tuned to be of their original size at a depth of 40 mm and using the f-number, $f = L_s/40\text{mm}$, they are scaled to maintain a constant resolution. In this way, the values for f_m are almost unchanged. This is the expected outcome, since the region examined is at a depth of 40 mm. If no requirement for detail resolution are given, the measurements in Fig. 4.5 show that a setup with many subapertures with a relative aperture translation of about 0.3 should be the ideal imaging configuration. However, in the next section we show that the detail resolution is quite poor for those configurations.

We end the tissue phantom study by computing the signal-to-noise ratio as a function of depth. The procedure is to acquire data for 10 images and treat the mean as the ground truth. To obtain a more smooth curve, the estimated noise and ground truth were both filtered using a mean filter with a length of 96 samples corresponding to 7.5 mm. In Fig. 4.6, the results are shown using Setup I and the configurations SA and SAC₂. The SNR is about 5 dB worse for the compound configuration, SAC₂, than what can be obtained using a setup without compounding. This is due to more data are added incoherently and is an unavoidable effect when doing compound imaging.

Water phantom measurements

To investigate on the resolution a water tank phantom was used with 4 wires at depths of 8, 34, 59, and 83 mm. The transducer was submerged into the water and data were collected using 128 unfocused emissions. The data were downsampled by the hardware to 35 MHz using a mean filter of width 2. The axial and lateral FWHM of

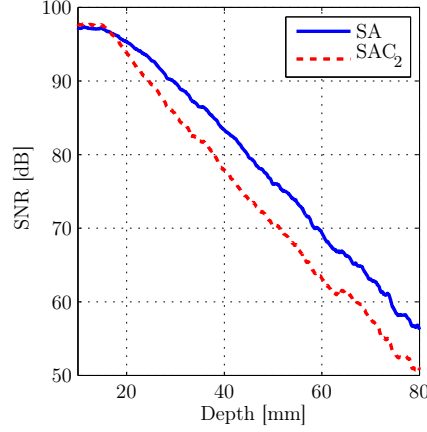


Figure 4.6: SNR as a function of depth for a synthetic aperture configuration with and without compounding.

the PSF together with the CTR, represented by $R_{20\text{dB}}$ were measured using the wire at the depth of 34 mm. In Fig. 4.7a, the CTR represented by $R_{20\text{dB}}$ is shown for all the configurations used. It clearly shows, how the introduction

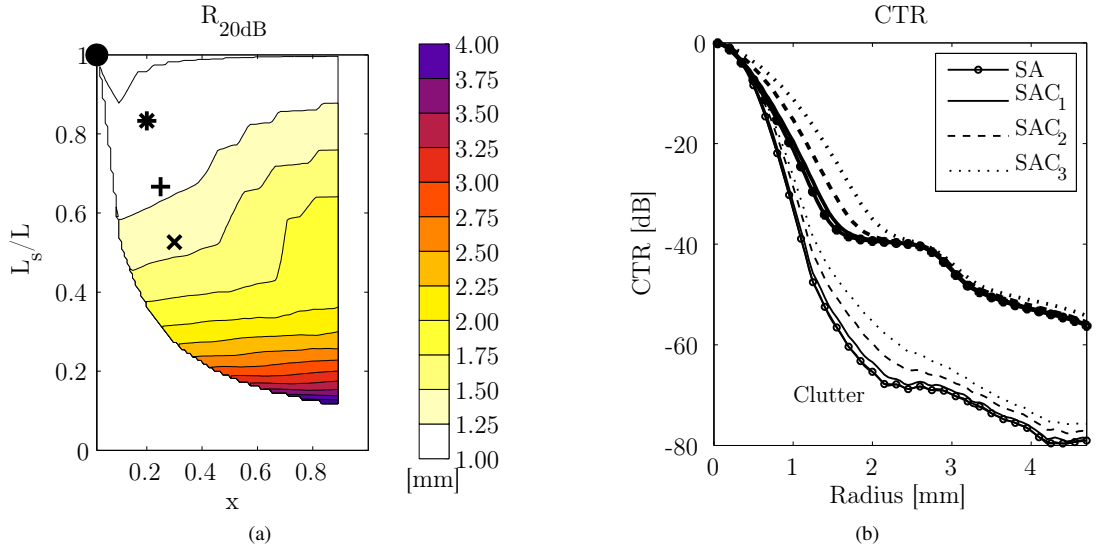


Figure 4.7: The CTR represented by $R_{20\text{dB}}$ is shown in (a), and in (b), the full CTR is plotted together with the clutter levels for the four the configurations, SA, SAC_1 , SAC_2 , and SAC_3 using Setup I.

of compounding requires a sacrifice of aperture and hence resolution. In a clinical setup, where the object is less homogeneous, one should expect that it is more difficult to do proper focusing, and if the inclusion of more elements by enlarging the aperture does not improve on the resolution, compounding should be used to increase the contrast. In Fig. 4.7b, the full CTR curves are plotted together with the clutter levels for the four configurations, SA, SAC_1 , SAC_2 , and SAC_3 . The CTR curves look like the integrals of Bessel functions. In fact, for a circular aperture, the CTR can be computed analytically and the result is the integral of a Bessel function [41]. The curves also nicely show, how the CTR is affected upon compounding, e.g. $R_{40\text{dB}}$ is unaffected, while $R_{20\text{dB}}$ is not. Contour plots of the PSFs can be found in the journal paper.

Cyst phantom measurements

In the last sections, it was demonstrated how compounding reduces speckle appearance at the cost of a reduced detail resolution. This is all very good, but it is more interesting to see the performance of compounding for detecting lesions and preferably in human tissue. In this section, the same aperture configurations and setups are applied for scanning a cyst-phantom with a speed-of-sound of 1540 m/s corresponding to human tissue. From Fig. 4.5, it follows that for the 3 setups investigated, images created using Setup I yield the highest value for the figure of merit, f_m , and should be the preferred solution for lesion detection. However, it is also desirable to have a constant resolution across depth and for this reason, we decided to image the cyst-phantom using Setup II, where a fixed f-number is realized for transmit and receive by scaling the apertures. In Fig. 4.8, images are created using Setup II, and 3 of the 4 aperture configurations in Table 4.1. It is quite clear to see, how compounding reduces the speckle and that the resolution is

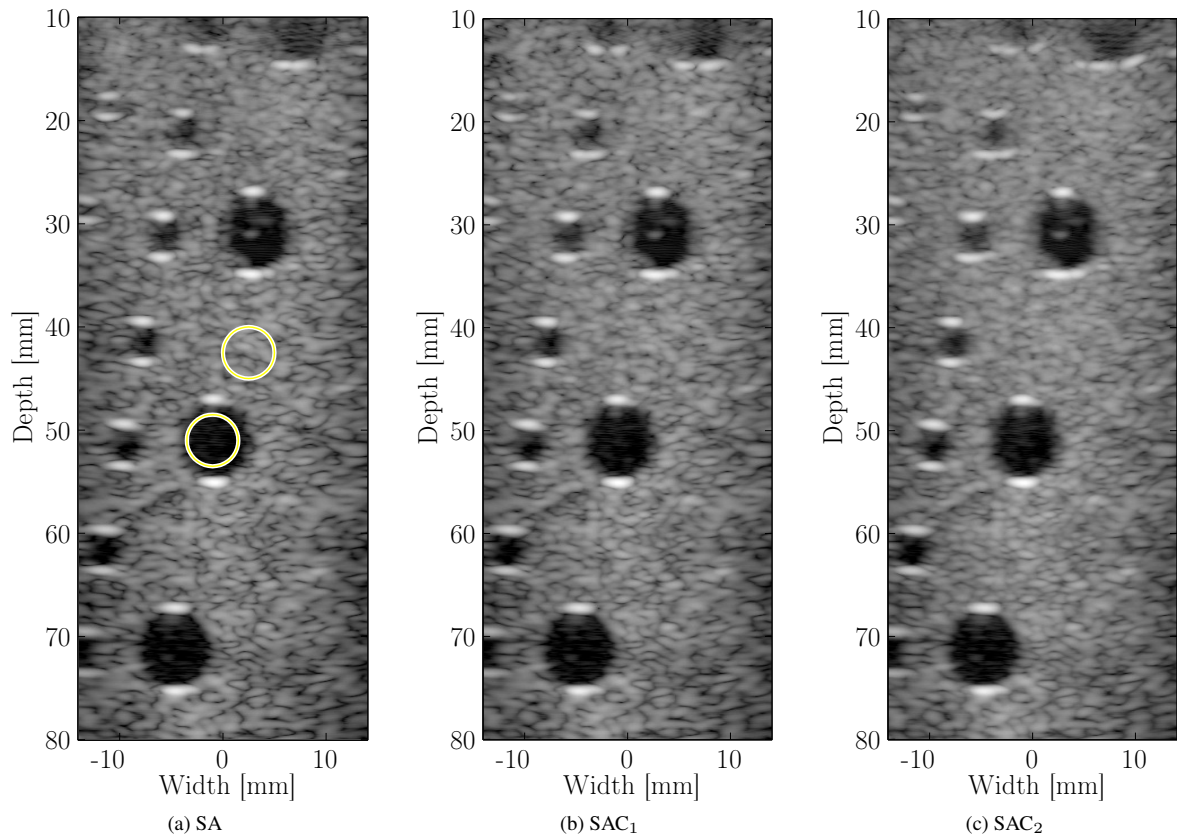


Figure 4.8: Synthetic aperture compound images created using Setup II. An image without compounding, (a), and two compound images, (b) and (c), created using aperture configuration SAC_1 and SAC_2 , respectively. All images are displayed using a dynamic range of 60 dB.

close to constant across depth. In the journal paper, the cyst at the depth of 50 mm is imaged using Setup I, where the compound effect is more profound, but where the resolution varies across depth. This is not a desirable setup for an ultrasound imaging system and simply serves to demonstrate, how resolution can be sacrificed to achieve better contrast. More interestingly, in the journal paper, it is demonstrated using Setup I, how the observed contrast of the cyst at the location shown in Fig. 4.8a is improved for a configuration, which gives a better value for the figure of merit. The latter is measured using a tissue mimicking phantom without cysts. The relation was investigated for all 154 configurations, and a correlation between the contrast of cyst and figure of merit was computed to be 0.81 with a p-value less than 0.0001. This suggests that the optimal compound configuration can be determined by scanning a tissue mimicking phantom without cysts. Following this idea, the tissue phantom measurements using Setup II

uniquely picks out a configuration, which yields the best value for the figure of merit, and the optimal configuration is somewhere between SAC_1 and SAC_2 , cf. Fig. 4.5b. A drawback of using the figure of merit and the reason for introducing the speckle information density in Chapter 2, is that the size of aperture is used as an estimate for the detail resolution. In the journal paper, the speckle information density, ρ_{SID} , is measured for the 3 setups and the 4 configurations and it is demonstrated, how an improved speckle information density is following by an improved contrast for the cyst.

4.2.4 Real-time implementations

Throughout the dissertation, almost no comments has been made on the possibilities for real-time implementations of synthetic aperture imaging with or without compounding. The primary reason is that the computational demands are about a factor of the number of lines heavier than what is required for conventional focusing. In other words, every time a line is processed for dynamic receive focusing, an entire low-resolution image needs to be processed for a synthetic aperture imaging setup. In our research group, we have developed a system capable of real-time synthetic aperture imaging using 256 channels. A setup using 32 emissions and an image with 136 lines, each with 1024 complex samples can be beamformed with a frame rate of 70 fps [50]. The data used for beamformation are 12-bit and sampled at 70 MHz and for each channel 8192 real samples are acquired. The system consists of 320 Virtex-IV FPGA distributed across 64 PCBs and the design is not only optimized for high throughput, but also accuracy has been highly prioritized, e.g. all RF data can be sampled and stored and 8192 point complex FFTs can be employed for advanced match-filtration. A commercial implementation can be created with less resources, but it is still a huge challenge and one of the limiting factors is the memory IO resources available.

4.2.5 Synthetic Aperture Imaging using the GPU

An equally high demand for memory throughput is found in the computer gaming industry, where hundreds of megabytes of data are processed every second for rendering a scene in a 3D computer game. The processing takes place on the graphics processing unit (GPU), which is a many-core massively parallel throughput-oriented execution unit. It contains a lot of arithmetic logic units (ALUs), and is suitable for single-instruction-multiple-data (SIMD) execution. The first four generations of GPUs were all fixed-function, but since then, the vendors have introduced vertex-level and pixel-level programmability and several high-level graphics languages have been released, which allow programs written in C/C++ to be executed by the GPU. In the conference paper, the most recent framework, OpenCL [51] is used for a kernel capable of SA beamformation using in-phase and quadrature data. The implementation was made to get hands-on experience using the GPU, and it is different from what has previously been published [52], since more advanced apodization can be applied, and the beamformer can be configured from within Matlab to experiment with different image and data dimensions.

GPU Hardware

The GPUs consist of several compute units, which each can be thought of as (a collection of) multi-core processors sharing some local memory and a common pipeline. This means in particular that the groups of cores read and write data simultaneously and this should be kept in mind when implementing programs for the GPU to execute. Further, no caching or very little caching is done by the hardware, so memory handling is more critical for GPU programs than for programs implemented for CPUs. The two manufacturers of GPUs, Nvidia and AMD/ATI have created two very different architectures for memory access on their devices. AMD operates with vectorized memory reads and writes and a uniform memory space exposition [53]. This is very similar to how SIMD is implemented on CPUs, and the programmer has to think of organizing data as 128-bit vectors (e.g. 4 floats) to achieve good performance. This makes the programming less flexible, but potentially speed-up calculations involving vectorized input and output. Nvidia work instead with a two-level thread hierarchy and scalar memory addressing and does not take advantage of instruction level parallelism to the same extent as their rival [54]. For synthetic aperture imaging, the memory access pattern is randomly shifted and very few arithmetic operations are performed compared to load and store operations. It is therefore an advantage to have a large amount of L1 cache available for each compute unit. At the time of conducting the research, the latest generation of GPUs from Nvidia had up to 48 kB of L1 cache available for each compute unit,

while the Evergreen family of their rival AMD, only had 8 kB. Further, since beamformation of a single pixel using linear interpolation involves only two consecutive values of RF data for each channel, you do not directly benefit from vectorized memory reads. These considerations together with some initial performance measurements using a number of GPUs, made us focus on the GTX-580 GPU from Nvidia. The initial performance results can be found in Table I in the conference paper.

Memory IO

As should be clear by now, beamformation comprises computation and application of channel delays and apodizations. The former also referred to as focusing amounts to massive distance calculations followed by memory look-ups. The amount of calculations involved in both distance and apodization calculated are massive, but the memory access pattern is randomly shifted. The latter is suboptimal for GPU architectures and the result is often a heavily memory bound application. To achieve a high performance, a high memory bandwidth as well as a low latency for access to the global memory is preferable. To improve on the latter, data are often copied to a faster internal memory on the chip. We used this approach with success for the AMD GPUs, but for the Fermi GPUs from Nvidia, it was faster to let the hardware perform the caching. The same strategy of copying memory to a faster location is also used for implementing SARUS.

The fastest GPU studied in the conference paper is the GTX-580, a member of the Fermi family, the latest generation of GPUs from Nvidia at the time of writing the paper. The main memory on the GTX-580 delivers 192 gigabytes per second (GB/s). This is six times the bandwidth of a Core-i7 with triple-channel DDR3-1333 memory, delivering 32 GB/s. The memory speedup is obtained using multiple 64-bits interfaces (6 instead of 3) and higher clock values. The latency for accessing the global memory is several hundred clock cycles, so a high bandwidth alone is not sufficient for a high performance. To hide the memory latency and keeping a high throughput, multithreading and caching is done explicitly by the programmer and/or implicitly by the hardware.

Design and Implementation

The GPU beamformer was designed to cover as many focusing strategies as possible and thereby be able to make important conclusions on processing capabilities and throughput. The initial beamformer implemented supports full synthetic aperture focusing with dynamic transmit and receive apodization with the possibilities for simplifications to improve on the performance or make conclusions about simpler focusing strategies, e.g. synthetic aperture sequential beamforming [55], where a lot research has been carried out in our research group [56, 57].

The implementation was made using the OpenCL framework by porting a very simple beamformer written in ANSI-C, which did not nothing but computing the time-of-flight and accessing the RF data using nearest neighbor interpolation. To validate the correctness and speed, data simulated using Field II was used as input. The data used for testing the speed was the same data used in Chapter 2 for the initial synthetic aperture compound images. After successfully reproducing the results using the GPU, the beamformer was modified to support linear interpolation and apodizations and no significant effect on the performance was observed demonstrating that the application is memory bound. In Fig. 4.9, the relevant parameters can be found together with an image beamformed using the GPU. Details about the implementation and the different strategies applied for optimization can be found in the conference paper. In the next section, the performance obtained for a number of synthetic aperture configurations will be presented together with a discussion of how the performance can be improved even further.

Results

After two weeks of playing around optimizing the kernels by precalculating delays or apodization values, removing branches, using different caching strategies, rearranging data to reduce the number of memory requests to the global memory, etc., we made some important conclusions: For all GPUs tested, no speed-up was obtained by precalculating delays or apodization values confirming that the application is indeed memory bound. Using the AMD HD 5870, we were able to speed up the calculation by explicitly using the local caches. Using the Nvidia GPUs on the other hand, it was faster to let the hardware do the caching. The most successful attempt for optimization was to use page-locked memory for the input data, which allowed us to do overlapped IO, such that while the GPU is busy beamforming data

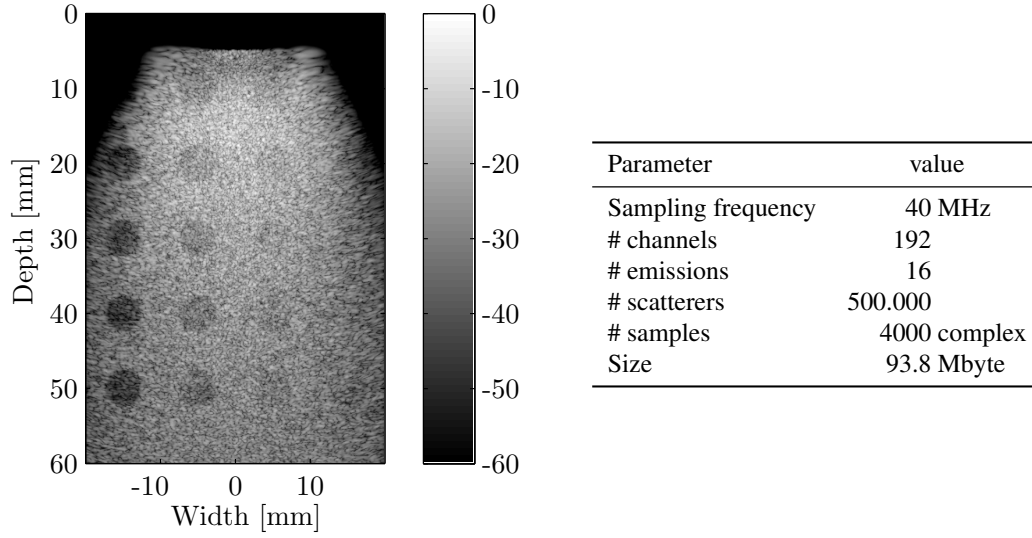


Figure 4.9: Cyst phantom image and parameters used for simulation. The image is beamformed using 512 lines, each with 512 complex samples.

from one emission, data for the next emission can be copied. Since, a sum of contributions is computed from a number of emissions, and the image is read back only once or continuously imaged on the screen, this application is ideal for overlapped IO. A 50% speed-up was achieved using overlapped IO. Using the GTX-580 GPU, the frame rates listed in Table 4.3 were obtained. The frame rates obtained clearly demonstrate real-time capabilities for beamformation

Table 4.3: Frame rates for an image size of 512x512 pixels beamformed using 4000 complex samples for each receive channel. The frame rates include reading back each frame to the CPU.

		# emissions			
		4	8	16	32
# channels	192	42.8	23.7	12.5	7.2
	128	70.4	39.9	20.0	11.2
	96	77.6	44.8	23.8	13.3
	64	137.3	75.4	39.7	21.1
	48	171.3	80.5	49.7	26.2
	24	226.2	143.7	86.1	44.2

using the GPU. Later experiments, where 16-bit input data was used instead of 32-bit floating point data, revealed an additional speed-up of close to a factor of two. Another way of speeding up the beamformation is to use multiple GPUs[52] and this will obviously work, since the PCI-X 2.0 x16 delivers easily 5 GB/s and the data rate for the fastest setup in the conference paper is at least a factor of ten below this value.

4.3 Discussion

In this final chapter, it was demonstrated how the compound effect achieved using a phased array transducer was close to the theoretical maximum for the amount of compounding attainable. Aspects of the necessary tradeoff between contrast and resolution was demonstrated by studying different aperture configurations with more or less compounding. By requiring a fixed resolution across depth, it was demonstrated how the apertures should be configured to achieve the best compound images. The quantitative results together with the proof-of-concept for a real-time implementation using the GPU suggest that further research should be conducted on this exciting topic.

REFERENCES

- [1] A. W. Rihaczek. *Principles of high-resolution radar*. McGraw-Hill, New York, 1969. 2
- [2] J. A. Jensen and N. B. Svendsen. Calculation of Pressure Fields from Arbitrarily Shaped, Apodized, and Excited Ultrasound Transducers. *IEEE Trans. Ultrason., Ferroelec., Freq. Contr.*, 39:262–267, 1992. 2
- [3] J. A. Jensen. Field: A Program for Simulating Ultrasound Systems. *Med. Biol. Eng. Comp.*, 10th Nordic-Baltic Conference on Biomedical Imaging, Vol. 4, Supplement 1, Part 1:351–353, 1996b. 2
- [4] J. M. Hansen, M. C. Hemmsen, and J. A. Jensen. An object-oriented multi-threaded software beam formation toolbox. In *Proc. SPIE - Medical Imaging - Ultrasonic Imaging and Signal Processing*, volume 7968, page 79680Y, 2011. 2, 10, 27
- [5] V. A. Frost, J. A. Stiles, K. S. Shanmugan, and J. C. Holtzman. Model for radar images and its application to adaptive digital filtering of multiplicative noise. *IEEE Transactions on Pattern Analysis and Machine Intelligence*, PAMI-4(2):157–166, 1982. 4
- [6] A. Lopes, R. Touzi, and E. Nezry. Adaptive speckle filters and scene heterogeneity. *IEEE Transactions on Geoscience and Remote Sensing*, 28(6):992–1000, 1990. 4
- [7] O. Lankoande, M. M. Hayat, and B. Santhanam. A markov-random-field based filter for speckle reduction in ultrasound imagery. In *Progress in Biomedical Optics and Imaging - Proceedings of SPIE*, volume 7265, 2009. 4
- [8] D. P. Shattuck and O. T. von Ramm. Compounding scanning with a phased array. *Ultrason. Imaging*, 4:93–107, 1982. 4
- [9] G. E. Trahey, S. W. Smith, and O. T. von Ramm. Speckle pattern correlation with lateral aperture translation: Experimental results and implications for spatial compounding. *IEEE Trans. Ultrason., Ferroelec., Freq. Contr.*, UFFC-33:257–264, 1986. 4, 36
- [10] P. A. Magnin, O. T. von Ramm, and F. L. Thurstone. Frequency compounding for speckle contrast reduction in phased array images. *Ultrason. Imaging*, 4(3):267 – 281, 1982. 4
- [11] R. F. Wagner, Michael F. Insana, and S. W. Smith. Fundamental correlation lengths of coherent speckle in medical ultrasonic images. *IEEE Trans. Ultrason., Ferroelec., Freq. Contr.*, 35:34–44, 1988. 4
- [12] R. Entekin, P. Jackson, and B.A. Porter. Real time spatial compound imaging in breast ultrasound: technology and early clinical experience. *medicamundi*, 43:35–43, September 1999. 4
- [13] S. K. Jespersen, J. E. Wilhjelm, and H. Sillesen. Multi-angle compound imaging. *Ultrason. Imaging*, 20:81–102, 1998. 4, 5, 18
- [14] San Jose CA Anming He Cai. Aperture compounding for medical imaging. Patent, 01 2003. US 6508770. 4, 5
- [15] Mountain View CA Kutay F. Ustuner, Portola Valley CA Mirsaid S. Bolorforosh, and Los Altos CA Albert Gee. Medical ultrasonic imaging with adaptive synthesis and compounding. Patent, 08 2002. US 6432054. 5
- [16] Mountain View CA Kutay F. Ustuner, Burlingame CA Charles E. Bradley, and Mountain View CA Daniel E. Need. Medical ultrasonic imaging method and system for spatial compounding. Patent, 03 2003. US 6527720. 5
- [17] San Jose CA Anming He Cai and Mountain View CA Rickard C. Loftman. Overlapped scanning for multi-directional compounding of ultrasound images. Patent, 09 2004. US 6790181. 5
- [18] J. J. Flaherty, K. R. Erikson, and V. M. Lund. Synthetic aperture ultrasound imaging systems. Patent, 12 1970. US 3548642. 7

- [19] C. B. Burckhardt, P-A. Grandchamp, and H. Hoffmann. An experimental 2 MHz synthetic aperture sonar system intended for medical use. *IEEE Trans. Son. Ultrason.*, 21(1):1–6, January 1974. 7
- [20] C. Passmann and H. Ermert. Adaptive 150 MHz ultrasound imaging of the skin and the eye using an optimal combination of short pulse mode and pulse compression mode. In *Proc. IEEE Ultrason. Symp.*, pages 1291–1294, 1995. 8
- [21] C. Passmann and H. Ermert. A 100-MHz ultrasound imaging system for dermatologic and ophthalmologic diagnostics. *IEEE Trans. Ultrason., Ferroelec., Freq. Contr.*, 43:545–552, 1996. 8
- [22] S. I. Nikolov. *Synthetic Aperture Tissue and Flow Ultrasound Imaging*. PhD thesis, Ørsted•DTU, Technical University of Denmark, 2800, Lyngby, Denmark, 2001. 8
- [23] S. I. Nikolov and J. A. Jensen. Virtual ultrasound sources in high-resolution ultrasound imaging. In *Proc. SPIE - Progress in biomedical optics and imaging*, volume 3, pages 395–405, 2002. 8, 9
- [24] J. T. Ylitalo and H. Ermert. Ultrasound synthetic aperture imaging: monostatic approach. *IEEE Trans. Ultrason., Ferroelec., Freq. Contr.*, 41:333–339, 1994. 8
- [25] M. Lang and H. Ermert. Linear synthetic aperture modes for ultrasonic pulse-echo imaging. *Biomedizinische Technik*, 42(5):108–115, 1997. 8
- [26] M. Karaman, P. C. Li, and M. O'Donnell. Synthetic aperture imaging for small scale systems. *IEEE Trans. Ultrason., Ferroelec., Freq. Contr.*, 42:429–442, 1995. 8
- [27] Y. Li and E. Wolf. Focal shifts in diffracted converging spherical waves. *Optics Communications*, 39(4):211–215, 1981. 8
- [28] N. Oddershede and J. A. Jensen. Effects influencing focusing in synthetic aperture vector flow imaging. *IEEE Trans. Ultrason., Ferroelec., Freq. Contr.*, 54(9):1811–1825, 2007. 9, 22
- [29] K. Gammelmark. Multi-element synthetic transmit aperture imaging using temporal encoding. Master's thesis, Ørsted•DTU, Technical University of Denmark, Lyngby, Denmark, 2001. 9
- [30] K. L. Gammelmark and J. A. Jensen. Experimental study of convex coded synthetic transmit aperture imaging. In *Proc. IEEE Ultrason. Symp.*, pages 1573–1576, 2002. 9, 31, 32
- [31] M. H. Pedersen, K. L. Gammelmark, and J. A. Jensen. In-vivo evaluation of convex array synthetic aperture imaging. *Ultrasound Med. Biol.*, page Submitted, 2006. 9
- [32] G. R. Lockwood, J. R. Talman, and S. S. Brunke. Real-time 3-D ultrasound imaging using sparse synthetic aperture beamforming. *IEEE Trans. Ultrason., Ferroelec., Freq. Contr.*, 45:980–988, 1998. 9, 22
- [33] J. M. Hansen, D. Schaa, and J. A. Jensen. Synthetic aperture beamformation using the GPU. In *Proc. IEEE Ultrason. Symp.*, pages 373–376, 2011. 10
- [34] J. A. Jensen, M. Hansen, B. G. Tomov, S. I. Nikolov, and H. Holten-Lund. System architecture of an experimental synthetic aperture real time ultrasound system. In *Proc. IEEE Ultrason. Symp.*, pages 636–640, Oct. 2007. 15
- [35] S. W. Smith, R. F. Wagner, J. M. Sandrik, and H. Lopez. Low contrast detectability and contrast/detail analysis in medical ultrasound. *IEEE Trans. Son. Ultrason.*, 30:164–173, 1983. 15, 25, 31, 36
- [36] R. F. Wagner, S. W. Smith, J. M. Sandrick, and H. Lopez. Statistics of speckle in ultrasound B-scans. *IEEE Trans. Son. Ultrason.*, 30:156–163, 1983. 15, 16, 36
- [37] J. A. Jensen, O. Holm, L. J. Jensen, H. Bendsen, S. I. Nikolov, B. G. Tomov, P. Munk, M. Hansen, K. Salomonsen, J. Hansen, K. Gormsen, H. M. Pedersen, and K. L. Gammelmark. Ultrasound Research Scanner for Real-time Synthetic Aperture Image Acquisition. *IEEE Trans. Ultrason., Ferroelec., Freq. Contr.*, 52 (5):881–891, May 2005. 21
- [38] W. P. Tanner and T. G. Birdsall. Definitions of d' and η as psychophysical measures. *JASA*, 30:922–928, 1958. 22
- [39] L. F. Nock and G. E. Trahey. Synthetic aperture imaging in medical ultrasound with correction for motion artifacts. In *Proc. IEEE Ultrason. Symp.*, pages 1597–1601, 1990. 22
- [40] C. R. Hazard and G. R. Lockwood. Theoretical assessment of a synthetic aperture beamformer for real-time 3-D imaging. *IEEE Trans. Ultrason., Ferroelec., Freq. Contr.*, 46:972–980, 1999. 22
- [41] D. Vilkomerson, J. Greenleaf, and V. Dutt. Towards a Resolution Metric for Medical Ultrasound Imaging. In *Proc. IEEE Ultrason. Symp.*, pages 1405–1410, 1995. 24, 43
- [42] K. F. Ustuner and G. L. Holley. Ultrasound imaging system performance assessment. Presented at 2003 AAPM Annual Meeting, 2003. 25
- [43] M. C. Hemmsen, J. Kortbek, S. I. Nikolov, and J. A. Jensen. Simulation of high quality ultrasound imaging. In *Proc. IEEE Ultrason. Symp.*, page Accepted for publication, Oct. 2010. 26
- [44] K. L. Gammelmark and J. A. Jensen. Duplex synthetic aperture imaging with tissue motion compensation. In

- Proc. IEEE Ultrason. Symp.*, pages 1569–1573, 2003. 33
- [45] S. D. Silverstein. Coherence and speckle reduction in compounded correlated phased arrays - Synthetic aperture radar. *J. Opt. Soc. Am.*, 3:1925–1934, November 1986. 36
- [46] M. O'Donnell and S. D. Silverstein. Optimum displacement for compound image generation in medical ultrasound. *IEEE Trans. Ultrason., Ferroelec., Freq. Contr.*, 35(4):470–476, 1988. 36, 38
- [47] C.B. Burckhardt. Speckle in ultrasound b-mode scans. *IEEE Trans. Son. Ultrason.*, SU-25(1):1–6, Jan. 1978. 38
- [48] J. S. Hwang and T. K. Song. A study of the display pixel-based focusing method in ultrasound imaging. *Ultrason. Imaging*, 23:1–18, 2001. 40
- [49] J. A. Jensen, H. Holten-Lund, R. T. Nielson, B. G. Tomov, M. B. Stuart, S. I. Nikolov, M. Hansen, and U. D. Larsen. Performance of SARUS: A Synthetic Aperture Real-time Ultrasound System. In *Proc. IEEE Ultrason. Symp.*, pages 305–309, Oct. 2010. 40
- [50] M. B. Stuart and J. A. Jensen. An Architecture and Implementation of Real-time Synthetic Aperture Compounding with SARUS. In *Proc. IEEE Ultrason. Symp.*, Oct. 2011. 45
- [51] Khronos OpenCL Working Group. *The OpenCL Specification, version 1.0.29*, 8 December 2008. 45
- [52] B. Y. S. Yiu, I. K. H. Tsang, and A. C. H. Yu. Real-time GPU-based software beamformer designed for advanced imaging methods research. In *Proc. IEEE Ultrason. Symp.*, pages 1920–1923, 2010. 45, 47
- [53] Advanced Micro Devices. Heterogeneous computing. OpenCL™ and the ATI Radeon™ HD 5870 ("Evergreen") architecture, 2010. 45
- [54] NVIDIA. *Whitepaper NVIDIA's Next Generation CUDA Compute Architecture: Fermi, v 1.1*, 2009. 45
- [55] J. Kortbek, J. A. Jensen, and K. L. Gammelmark. Synthetic aperture sequential beamforming. In *Proc. IEEE Ultrason. Symp.*, pages 966–969, 2008. 46
- [56] J. Kortbek, J. A. Jensen, and K. L. Gammelmark. Synthetic aperture sequential beamforming. *J. Acoust. Soc. Am.*, page Submitted, 2009. 46
- [57] M. C. Hemmsen, P. M. Hansen, T. Lange, J. M. Hansen, M. B. Nielsen, , and J. A. Jensen. Preliminary In-Vivo evaluation of Synthetic Aperture Sequential Beamformation using a multielement convex array. In *Proc. IEEE Ultrason. Symp.*, pages 1131–1134, 2011. 46
- [58] J. B. Reade. *Calculus with Complex Numbers*. Taylor & Francis, 2003. 162

PAPERS

A.1 A Method for Synthetic Aperture Compounding

- **J. M. Hansen**, and J. A. Jensen: A Method for Synthetic Aperture Compounding. Proceedings of the IEEE Ultrasonics Symposium, October, 2010.

A Method for Synthetic Aperture Compounding

Jens Munk Hansen and Jørgen Arendt Jensen

Center for Fast Ultrasound Imaging, Dept. of Elec. Eng. Bldg. 349,
Technical University of Denmark, DK-2800 Kgs. Lyngby, Denmark

Abstract—An approach to perform ultrasound spatial compounding using synthetic aperture data is proposed. The approach allows compounding to be performed for any number of directions without reducing the frame rate or temporal resolution. It is demonstrated how the contrast is improved by compounding and the effect is quantized by speckle statistics and by computing contrast-to-noise ratios (CNR) from the resulting images. The method is validated using Field II simulations for a 7 MHz, $\lambda/2$ -pitch transducer with 192 elements with 64 elements active for each scan line. Circular regions (cysts) with a diameter of 5 mm and scattering levels ranging from -3 to -12 dB relative to the background are imaged at 2 depths. Compound images composed of 1-5 images with an angular separation of 2 degrees are constructed and for the cysts at -3, -6, -9, and -12 dB, a CNR of -0.43, -1.11, -1.44, and -1.91 dB are obtained when using 5 images. Using the same RF data, a synthetic aperture image without compounding reveals a CNR of -0.36, -0.93, -1.23, and -1.61 dB for the four cysts, respectively.

I. INTRODUCTION

Medical ultrasound imaging is used for many purposes, e.g. for localizing and classifying cysts, lesions, and other processes. Almost any mass is first observed using B-mode imaging and later classified using e.g. color flow, strain, or attenuation imaging. It is therefore important that the B-mode images have high contrast. Like all imaging modalities, ultrasound is subject to a number of inherent artifacts that compromise image quality. The most prominent artifact is the degradation by coherent wave interference, known as 'speckle', which gives a granular appearance to an otherwise homogeneous region of parenchyma [1], [2]. The speckle reduces image contrast and diminishes the possibilities for detection of low-contrast regions.

A successful approach to remedy the speckle artifacts is spatial compounding [3], [4], where images are acquired from a number of directions and combined after envelope-detection. Today, spatial compounding is implemented in all state of the art, high-end ultrasound systems and available when using a low pitch transducer with a fairly high number of independent channels [5]. Inherent in all compounding techniques is a loss in frame rate due to acquisition at multiple angles. This paper suggests an approach based on synthetic aperture imaging, where this can be avoided.

The organization of this paper is as follows: First, spatial compounding is described in more detail and some properties are introduced for measuring speckle statistics and contrast. Next, synthetic aperture imaging is explained and the proposal for using synthetic aperture data for compounding is presented.

In the results section, simulation results for a cyst phantom are presented together with speckle statistics and contrast-to-noise ratios for cysts with scattering levels, ΔV ranging from -3 to -12 dB relative to the background. Finally, a discussion of the results is presented together with some future steps for further investigation of the proposed method.

II. METHODS

A. Compounding

For conventional spatial compounding, a low-pitch linear array is used. A subset of the elements is selected as the current active aperture, and this aperture is used as a phased array to steer the beam in a direction making an angle θ with a normal to the transducer surface. The active aperture is then moved, until scan lines originating from the entire extent of the linear array are recorded. This procedure is repeated for angles θ_i , $i = 1, \dots, N_\theta$, where N_θ is the number of angles to be used for compounding. Next, the N_θ images are envelope-detected and added using scan-line conversion. An illustration of the scan line positions for $N_\theta = 3$ is given in Fig. 1. Note that the effective region of the image is reduced to the

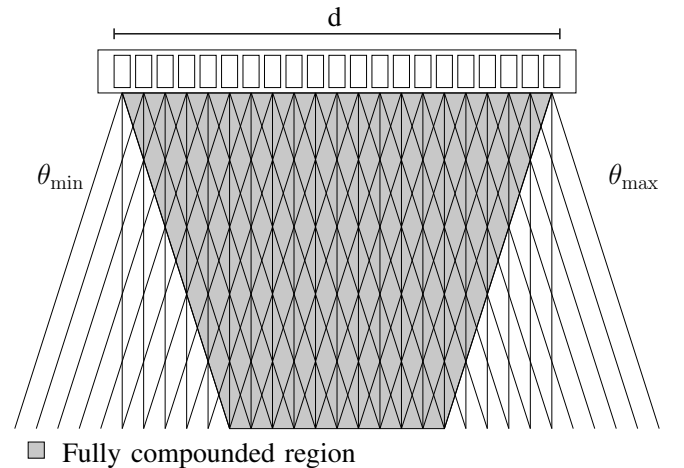


Figure 1: Illustration of scan line directions and origins used for spatial compounding. The example shows an image consisting of scan lines obtained using $N_\theta = 3$ directions.

fully compounded image region determined by the length of the array d and the beam angle extrema, θ_{\min} and θ_{\max} . The resulting image has a reduced speckle appearance, a lower

noise floor, boundaries subject to non-normal incidence are more visible, and image shadowing is confined to a smaller triangular region behind the attenuating masses or boundaries. For this study, only first order effects are considered, hence only the speckle pattern is analyzed.

To evaluate the image quality, one studies the magnitude V of the received signal (found by envelope-detection). For first order statistics, the parameter of interest is the expectation value of V , $\mu_V = \mathbb{E}(V)$, in units of its standard deviation, σ_V . In the literature, this is referred to as the speckle signal-to-noise ratio at a point,

$$\text{SNR}_0 = \frac{\mu_V}{\sigma_V},$$

and its inverse as the speckle contrast. The envelope-detected signals, V follow Rayleigh statistics and for a fully developed speckle, the theoretical value of SNR_0 is 1.91 [2], and if the N_θ images are uncorrelated, it is $1.91\sqrt{N_\theta}$. Images used for compounding are not uncorrelated and therefore a smaller improvement of the signal-to-noise is obtained [6].

Another parameter of interest is the contrast-to-noise ratio for a region-of-interest (ROI) with a scattering level different from the background:

$$\text{CNR} = \frac{\mu_{V_{\text{ROI}}} - \mu_{V_B}}{\sqrt{\sigma_{V_{\text{ROI}}}^2 + \sigma_{V_B}^2}},$$

where V_{ROI} and V_B are the envelope-detected signals from the ROI and background, respectively.

A drawback of conventional compounding is either a reduction of the frame rate or a reduction of the true temporal resolution. In the case of the latter, the temporal resolution is reduced due to images being buffered to achieve an apparent high frame rate.

B. Synthetic Aperture

Synthetic aperture imaging can synthesize the transmit aperture [7], the receive aperture [8], or both [9]. A typical setup for doing both, is to acquire data by emitting with a single transducer element and receiving with all or a subset of the elements. This procedure is then repeated for all emissions and a complete data set is acquired. Using this data set, any beam and focusing can be synthesized.

For transmit focusing, delays and apodizations are calculated for each point in the image to construct signals, which at each point sum up coherently. For receive focusing, another set of delays and apodizations are applied to the signals received from the individual transducer elements and then a weighted sum is performed. In addition, the apodization can be adjusted to even out the resolution over a range of depths to maintain a constant resolution by realizing a fixed F-number using an expanding or contracting aperture for transmit and receive beamformation, respectively. A major advantage of synthetic aperture imaging is the possibility to focus everywhere in the image resulting in a better resolution. Further, this can be achieved using the same amount of time for data acquisition as for conventional imaging. The price for the resolution though, is a huge increase in RF data processing - an increase by the number of lines to beamform for each pulse emission.

C. Synthetic Aperture Compounding

To perform compounding using synthetic aperture data, apodizations are calculated for each image point corresponding to imaging the point using a focused beam centered around the point and making an angle θ with a normal to the transducer surface. In Fig. 2, it is shown for a single point, how the transmit apodization for an emission with transmit origin \vec{r}_{xmt} are calculated using the orthogonal distance from the transmit origin to the “scan-line”. Similarly, receive apodizations are

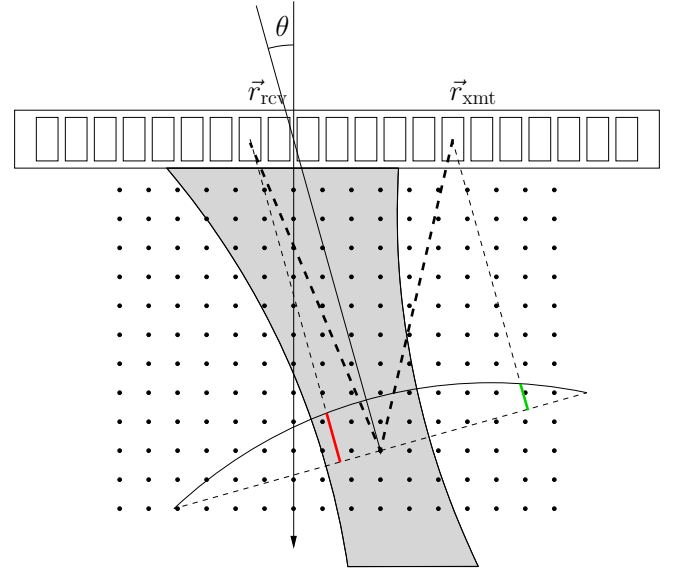


Figure 2: The example shows how the time-of-flight and apodizations are calculated for a single emission with transmit origin \vec{r}_{xmt} and a selected receive element positioned at \vec{r}_{rcv} for a single direction θ . The length of the wave propagation path (thick dashed line) is used for calculating time-of-flight. The receive apodization is computed using the orthogonal distance from the receive element to the “scan line” and the value (red line) can be read-off from the arc representing an apodization function. Similarly, a transmit apodization (green line) is computed using the orthogonal distance from the origin of the transmission to the scan line. The grey area shows the “beam” that we are synthesizing by making the given apodization.

calculated for each point and applied to the signals received from the individual receiving elements of each transmission. The receive apodization values are likewise computed using the orthogonal distance from the “scan-line” to now the position of the receiving element. The delay calculation are identical to what is used for synthetic aperture imaging without compounding. The RF data are beamformed as in-phase and quadrature components, and the envelope computed as the absolute value. This rather complex procedure is repeated for angles θ_i , $i = 1, \dots, N_\theta$, where N_θ is the number of angles to be used for compounding. Finally, the compound image are constructed by addition or multiplication of the enveloped images. An implementation of this method uses a buffer for N_θ images and calculates the delays for each pixel only once.

Further, the envelope can be computed for a pixel as soon as the RF data for the relevant emissions are processed to achieve the best possible temporal resolution.

III. RESULTS

A. Simulation

The proposed method for synthetic aperture compounding is implemented using a new software beamformation toolbox [10] and validated using Field II - a program for simulating ultrasound systems [11], [12]. A setup with a 7 MHz, $\lambda/2$ -pitch linear-array transducer with 192 elements are used for simulation. The emitted pulse is a single-cycle sinusoid and the temporal impulse response is modelled as a two-cycle sinusoid for both the transmitting and receiving aperture. The speckle pattern is modeled as the signal from a large collection of randomly placed scatterers with Gaussian amplitudes residing in a volume with dimensions (height-width-depth) $5 \times 20 \times 20$ mm. Circular (cylindrical) regions with a diameter of 5 mm and scattering levels ranging from -3 to -12 dB relative to the background are simulated at four positions by scaling the amplitudes accordingly. The random selection of point scatterers are chosen to have a density of at least 10 scatterers per resolution cell for any point in the image. The setup is shown in Fig. 3. Single-element emissions are simulated using

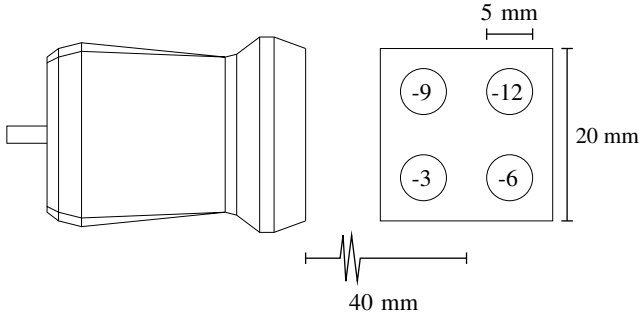


Figure 3: Simulation setup with a phased-array transducer and an image region of size (HWD) $5 \times 20 \times 20$ mm. containing 4 circular regions with a diameter of 5 mm and scattering levels ranging from -3 to -12 dB relative to the background.

a sampling frequency of 120 MHz and RF data are stored for all 192 elements, and all 192 elements are used for emission.

B. Compounding

For reference, a conventional compound image is created using 64 elements active for each scan line, dynamic receive focusing, and a Hamming apodization. Using random amplitudes for the scatter map, SNR_0 values are computed for images using 1, 3, and 5 angles for compounding. The results are shown in Table I. The values increase when using an increasing number of angles for compounding.

In Fig. 4, images of the cyst phantom are constructed using 1, 3, and 5 angles for compounding. The CNR values for the

# of images	1	3	5
Compounding	1.92	2.80	3.51
SA Compounding	1.87	1.92	2.00

Table I: SNR_0 for conv. and synthetic aperture compounding for images compounded of 1,3, and 5 angles. The compounding is made using addition of the envelope-detected signals.

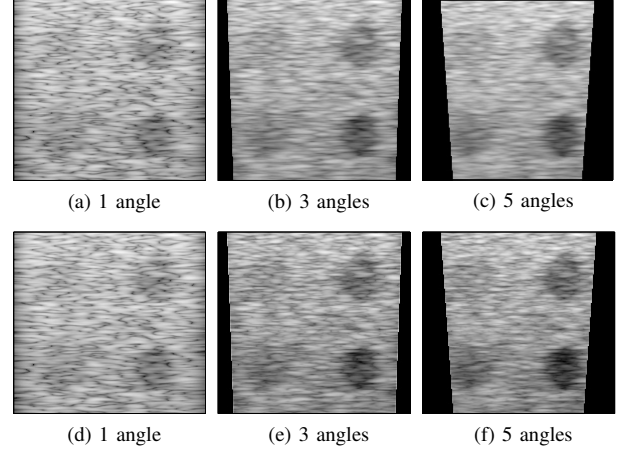


Figure 4: Convention spatial compound images. The images (a) - (c) and (d) - (f) are compounded using addition and multiplication respectively. For all the images, only the fully compounded region is shown.

four cysts are computed in Table II. The values are increasing for an increasing number of images for all the cysts. It is worth noticing that the CNR is worse when compounding using multiplication.

C. Synthetic Aperture Compounding

Synthetic aperture compounding as described in Section II-C is applied to the simulated data using a Hamming window as the apodization function represented by the arc in Fig. 2. Following the same approach as for conventional compounding, SNR_0 values are computed using random amplitudes for compounding using 1, 3, and 5 angles. The results are given in Table I. Note that the values are lower than the values obtained using conventional compounding. This can

Mode		Addition			Multiplication		
# of images		1	3	5	1	3	5
ΔV [dB]	-3	-0.48	-0.73	-0.83	-0.48	-0.67	-0.78
	-6	-0.67	-1.21	-1.65	-0.67	-1.15	-1.51
	-9	-0.99	-1.63	-2.15	-0.99	-1.51	-2.04
	-12	-1.50	-2.63	-3.34	-1.50	-2.42	-3.03

Table II: Contrast-to-noise ratios for cysts at scattering levels, ΔV , equal to -3, -6, -9, and -12 computed from conventional compound images constructed by addition respectively multiplication of 1, 3, and 5 images.

be explained by the blurring lowering the variance of images obtained using conventional compounding.

In Fig. 5, synthetic aperture compound images of the cyst phantom are created using 1, 3, and 5 angles for compounding. The CNR values for the four cysts are computed in Table III. The values are increasing for an increasing number of images for all the cysts. Again, it is worth noticing that the CNR is worse when compounding using multiplication.

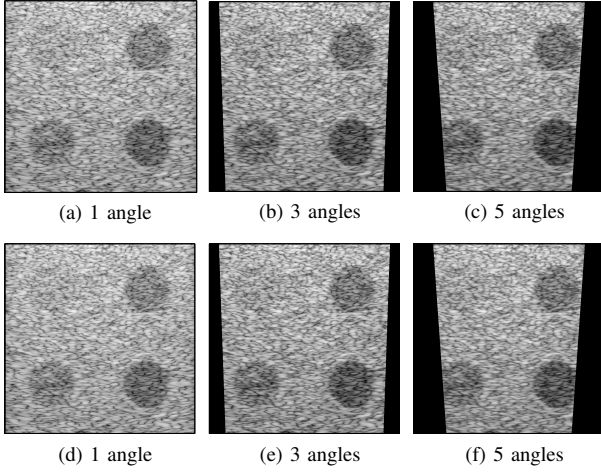


Figure 5: Synthetic aperture compound images. The images (a) - (c) and (d) - (f) are compounded using addition and multiplication respectively. For all the images, only the fully compounded region is shown.

Mode	# of images	Addition			Multiplication		
		1	3	5	1	3	5
ΔV [dB]	-3	-0.36	-0.40	-0.43	-0.36	-0.38	-0.40
	-6	-0.93	-1.02	-1.11	-0.93	-0.98	-1.05
	-9	-1.23	-1.34	-1.44	-1.23	-1.29	-1.36
	-12	-1.61	-1.76	-1.91	-1.61	-1.69	-1.80

Table III: Contrast-to-noise ratios for cysts at scattering levels, ΔV , equal to -3, -6, -9, and -12 computed from synthetic aperture compound images constructed by addition respectively multiplication of 1, 3, and 5 images.

IV. CONCLUSION

For all cysts imaged using spatial compounding, an improved speckle signal-to-noise ratio is obtained, when increasing the number of images and this is in agreement

with the results of [6]. As a consequence, the contrast is improved and low-contrast regions are easier to detect. Using synthetic aperture, an increased resolution is obtained, which is evident from Fig. 5. The fact that using the proposal for synthetic aperture compounding, the speckle is reduced and the contrast improved is evident from the results of Table I and Table III and this opens for further applications of synthetic aperture imaging worth investigating. In particular, better contrast can easily be obtained by trading off resolution by using a smaller transmit or receive aperture. For an implementation, the obvious choice is to use fewer emissions to also obtain a higher temporal resolution.

Next steps are to collect synthetic aperture data with our new research scanner SARUS [13], validate the method on *in-vivo* data, investigate the resolution trade-off when using fewer transmissions, and finally to implement synthetic aperture compounding for real-time *in-vivo* imaging to validate the method using pre-clinical trials.

REFERENCES

- [1] C. Burckhardt, "Speckle in ultrasound b-mode scans," *IEEE Trans. Son. Ultrason.*, vol. SU-25, no. 1, pp. 1–6, Jan. 1978.
- [2] R. F. Wagner, S. W. Smith, J. M. Sandrick, and H. Lopez, "Statistics of speckle in ultrasound B-scans," *IEEE Trans. Son. Ultrason.*, vol. 30, pp. 156–163, 1983.
- [3] D. Shattuck and O. von Ramm, "Compounding scanning with a phased array," *Ultrason. Imaging*, vol. 4, pp. 93–107, 1982.
- [4] G. E. Trahey, S. W. Smith, and O. T. von Ramm, "Speckle pattern correlation with lateral aperture translation: Experimental results and implications for spatial compounding," *IEEE Trans. Ultrason., Ferroelec., Freq. Contr.*, vol. UFFC-33, pp. 257–264, 1986.
- [5] R. Entekin, P. Jackson, and B. Porter, "Real time spatial compound imaging in breast ultrasound: technology and early clinical experience," *medicamundi*, vol. 43, pp. 35–43, September 1999.
- [6] S. K. Jespersen, J. E. Wilhjelm, and H. Sillesen, "Multi-angle compound imaging," *Ultrason. Imaging*, vol. 20, pp. 81–102, 1998.
- [7] C. R. Hazard and G. R. Lockwood, "Theoretical assessment of a synthetic aperture beamformer for real-time 3-D imaging," *IEEE Trans. Ultrason., Ferroelec., Freq. Contr.*, vol. 46, pp. 972–980, 1999.
- [8] L. F. Nock and G. E. Trahey, "Synthetic aperture imaging in medical ultrasound with correction for motion artifacts," in *Proc. IEEE Ultrason. Symp.*, 1990, pp. 1597–1601.
- [9] G. R. Lockwood, J. R. Talman, and S. S. Brunke, "Real-time 3-D ultrasound imaging using sparse synthetic aperture beamforming," *IEEE Trans. Ultrason., Ferroelec., Freq. Contr.*, vol. 45, pp. 980–988, 1998.
- [10] J. M. Hansen and J. A. Jensen, "An object-oriented multi-threaded software beam formation toolbox," in *Proc. SPIE - Medical Imaging - Ultrasonic Imaging and Signal Processing*, 2011, submitted.
- [11] J. A. Jensen and N. B. Svendsen, "Calculation of Pressure Fields from Arbitrarily Shaped, Apodized, and Excited Ultrasound Transducers," *IEEE Trans. Ultrason., Ferroelec., Freq. Contr.*, vol. 39, pp. 262–267, 1992.
- [12] J. A. Jensen, "Field: A Program for Simulating Ultrasound Systems," *Med. Biol. Eng. Comp.*, vol. 10th Nordic-Baltic Conference on Biomedical Imaging, Vol. 4, Supplement 1, Part 1, pp. 351–353, 1996b.
- [13] J. A. Jensen, M. Hansen, B. G. Tomov, S. I. Nikolov, and H. Holten-Lund, "System architecture of an experimental synthetic aperture real time ultrasound system," in *Proc. IEEE Ultrason. Symp.*, Oct. 2007, pp. 636–640.

A.2 An Object-oriented Multi-threaded Software Beamformation Toolbox

- **J. M. Hansen**, M. C. Hemmsen, and J. A. Jensen: An Object-oriented Multi-threaded Software Beamformation Toolbox. Proceeding of SPIE, vol. 7968, article no. 79680Y, 2011,

An object-oriented multi-threaded software beamformation toolbox

Jens Munk Hansen¹, Martin Christian Hemmsen^{1,2} and Jørgen Arendt Jensen¹

1) Center for Fast Ultrasound Imaging, Dept. of Elec. Eng. Bldg. 349,
Technical University of Denmark, DK-2800 Kgs. Lyngby, Denmark

2) BK Medical Aps, Mileparken 34, DK-2730 Herlev, Denmark

ABSTRACT

Focusing and apodization are an essential part of signal processing in ultrasound imaging. Although the fundamental principles are simple, the dramatic increase in computational power of CPUs, GPUs, and FPGAs motivates the development of software based beamformers, which further improves image quality (and the accuracy of velocity estimation). For developing new imaging methods, it is important to establish proof-of-concept before using resources on real-time implementations. With this in mind, an effective and versatile Matlab toolbox written in C++ has been developed to assist in developing new beam formation strategies. It is a general 3D implementation capable of handling a multitude of focusing methods, interpolation schemes, and parametric and dynamic apodization. Despite being flexible, it is capable of exploiting parallelization on a single computer, on a cluster, or on both. On a single computer, it mimics the parallelization in a scanner containing multiple beamformers. The focusing is determined using the positions of the transducer elements, presence of virtual sources, and the focus points. For interpolation, a number of interpolation schemes can be chosen, e.g. linear, polynomial, or cubic splines. Apodization can be specified by a number of window functions of fixed size applied on the individual elements as a function of distance to a reference point, or it can be dynamic with an expanding or contracting aperture to obtain a constant F-number, or both. On a standard PC with an Intel Quad-Core Xeon E5520 processor running at 2.26 GHz, the toolbox can beamform 300.000 points using 700.000 data samples in 3 seconds using a transducer with 192 elements, dynamic apodization in transmit and receive, and cubic splines for interpolation. This is 19 times faster than our previous toolbox.

Keywords: medical ultrasound, software, beamformation, toolbox, high-performance computing

1. INTRODUCTION

Image quality and diagnostic capabilities of medical imaging depend on the inversion of the measured data for the given modality. For ultrasound imaging, the inversion is primarily made by delay-and-sum beamformation. This comprises computation and application of channel delays and apodization for both transmit and receive elements. It sounds simple, but ideally, one would like the result of the beamformation to approximate the true inverse of the forward model, which itself is a complex model of both time and space. A forward model or simulation model is described by the ultrasound simulation program Field II.^{1,2} This may sound like elements of the future, but the evolution of ultrasound beamformers moving from analog into digital implementations, described by Thomenius,³ has made it possible to implement more advanced beamformers and new and improved methods of beamformation are still emerging. The resulting beamformer is designed for the desired application, quality demands, transducer type, and not to forget processing resources available. The latter is still the limiting factor for an ultrasound imaging system.

Many commercial and non-commercial toolboxes have been developed for different purposes within array signal processing,^{4,5} in particularly our previous toolbox BFT2 for off-line beamformation of ultrasound array signals.^{6,7} This paper presents a new toolbox, named BFT3. The development was motivated by requests for fast software beamformation of data collected with our new research scanner SARUS⁸ and requests for a number of advanced features for apodization for convex phased-array imaging and velocity estimation. The toolbox is now used intensively in several projects at *Center for Fast Ultrasound Imaging* (CFU).

When comparing features with features supported by our previous toolbox, the new toolbox outperforms the old by up-to a factor of 19 on a Quad-Core Xeon processor E5520 running at 2.26 GHz. In addition to this

dramatic speedup, it offers more flexibility with respect to convex and phased-array imaging. The speedup is primarily obtained from a better software pipelining and a multithreaded approach for beamformation.

It is designed to operate on real RF signals or on complex base band signals obtained from any application and any acquisition sequence. It supports parametric and dynamic apodization and a number of interpolation schemes including cubic spline interpolation using Neville's algorithm [9, §3.1] .

The toolbox has been developed using CPPUnit¹⁰ - a unit testing framework module for C++. Further, automated test have been implemented to ensure a consistency of output for a number of scenarios covering many existing beamformers such that the toolbox can serve as reference for implementation of new beamformers as well as for testing the precision of existing ones. The input data can originate from either a simulation program such as Field II, from an experimental setup, or from *in-vivo* measurements. The scenarios tested cover directional velocity estimation,¹¹ synthetic aperture (SA) imaging,¹² and variations hereof, e.g. synthetic transmit aperture (STA),¹³ synthetic receive aperture (SRA),¹⁴ synthetic aperture sequential beamformation (SASB).¹⁵ For all these cases, one can benefit from using multiple beamformers and the toolbox therefore facilitates multithreading.

The organization of this paper is as follows: First, beamformation is described and the principles used for time-of-flight calculations and apodization of elements are discussed. Next, the software design is presented and how the user can interact with the toolbox. In the results section, some examples of use are given together with some measures of performance. Finally, some concluding remarks are given.

2. BEAM FORMATION

Beamformation without apodization is all about phase computation for a group of signals exploiting that the sum of these signals can be either constructive or destructive. In medical ultrasound imaging, this is done for both the transmitted and the received field. The type of beamformation varies with the geometry of the transducer and the position of the focal points.

For the transmitted field, appropriate delays and possibly an apodization are applied to the transducer elements to construct a number of signals, which sum up constructively at a single focal point. Receive beamformation is similar in the sense that appropriate delays are applied to the signals received from the individual transducer elements and then a weighted sum is performed. Contrary to transmit focusing, when receiving, one can apply a number of delays corresponding to an equal number of focus points. In addition, an apodization can be applied to even out the resolution over a range of depths.

The first challenge is to compute appropriate delays, hence one needs to compute the time-of-flight t_{TOF} for the sound propagating from the transmit origin, \vec{r}_{xmt} to the focal point \vec{r}_{fp} and return to one of the receiving elements, \vec{r}_{rcv} . This task can be split into computing a transmit and a receive time corresponding to a transmit and a receive focus, $t_{\text{TOF}} = t_{\text{TOF}_{\text{xmt}}} + t_{\text{TOF}_{\text{rcv}}}$. Assuming the speed of sound, c is constant, we get

$$\begin{aligned} t_{\text{TOF}} &= t_{\text{TOF}_{\text{xmt}}} + t_{\text{TOF}_{\text{rcv}}} \\ &= \frac{|\vec{r}_{\text{fp}} - \vec{r}_{\text{xmt}}| + |\vec{r}_{\text{rcv}} - \vec{r}_{\text{fp}}|}{c}. \end{aligned} \quad (1)$$

If secondary scattering is neglected, the receive path is a straight line and the receive time is uniquely determined. The transmit path however is not well defined, since the emitted pressure wave does not emanate from a point source $\vec{r}_{\text{fp}_{\text{xmt}}}$ as indicated in Fig. 1b but rather from a complicated pattern resulting from numerous waves emitted from different elements at different times obeying Huygens' principle. For an unfocused beam though, (1) is close to correct. For a focused beam, the transmit time can be approximated by considering the transmit focal point $\vec{r}_{\text{fp}_{\text{xmt}}}$ as a virtual point source emitting a spherical wave.¹⁶⁻²⁰ By using this approximation, the t_{TOF} becomes

$$t_{\text{TOF}} = \frac{|\vec{r}_{\text{fp}_{\text{xmt}}} - \vec{r}_{\text{xmt}}| \pm |\vec{r}_{\text{fp}} - \vec{r}_{\text{fp}_{\text{xmt}}}| + |\vec{r}_{\text{rcv}} - \vec{r}_{\text{fp}}|}{c}, \quad (2)$$

where the \pm in (2) refers to whether the focal point is above or below a plane orthogonal to the center line of the beam. In Fig. 1, this plane is the plane containing the dashed line passing through the transmit focal point, $\vec{r}_{\text{fp}_{\text{xmt}}}$. For a beam perpendicular to the aperture, the plane deciding the sign in (2) is parallel to the aperture.

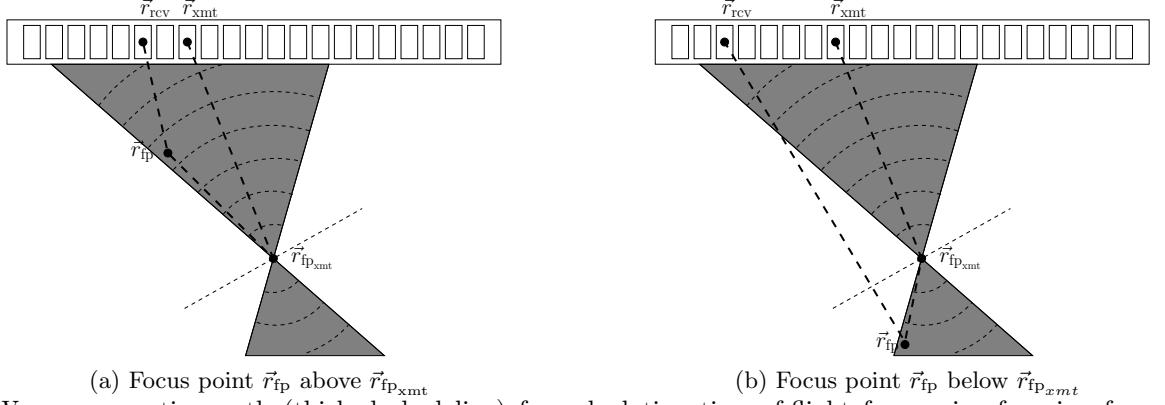


Figure 1: Wave propagation path (thick dashed line) for calculating time-of-flight for receive focusing for a phased array emission. The transmit origin \vec{r}_{xmt} and receiving position \vec{r}_{rcv} are coinciding with two different elements of the array as shown on the figure.

The result of beamforming a single point is a weighted sum of contributions for each transmit-receive channel pair. For imaging, we are interested in the absolute values and typically, we would either beamform complex data and compute the absolute or beamform a scan line of points and compute the envelope. For velocity estimation, we are interested in the phase and would therefore beamform densely sampled lines and possibly also in multiple directions, the latter for directional velocity estimation.

In general, a beamformed image point at position \vec{r}_{fp} can be computed according to

$$I(\vec{r}_{fp}) = \sum_{xmt=1}^{N_{xmt}} \mathcal{A}_{xmt}(\vec{r}_{fp}) \sum_{rcv=1}^{N_{rcv}} \mathcal{A}_{rcv}(\vec{r}_{fp}) s_{xmt,rcv}(t_{TOF}(\vec{r}_{xmt}, \vec{r}_{fp_{xmt}}, \vec{r}_{fp}, \vec{r}_{rcv})), \quad (3)$$

where N_{rcv} is the number of receiving elements, $\mathcal{A}(\vec{r}_{fp})$ is the apodization function in transmit and receive, and $s_{xmt,rcv}(t)$ is the interpolated time-domain echo signal received at element xmt after the rcv'th emission. N_{xmt} is the number of emissions used to construct the image point, where the origin of the emissions are spatially different, which is used in STA. For a conventional B-mode image, $N_{xmt} = 1$.

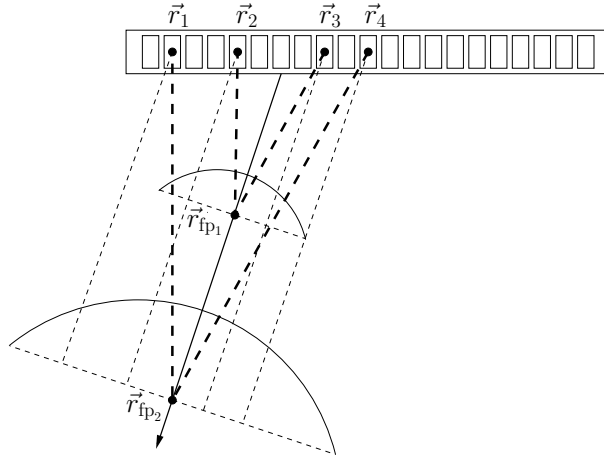


Figure 2: Wave propagation paths for calculating time-of-flight for transmit-receive element pairs for two different focal points. Apodization profiles are calculated for the two depths corresponding to a common F-number in transmit and receive.

With a finite aperture size, edge waves will affect the beam pattern by increasing the side lobes. To suppress

the edge-waves and lower the side lobes, apodization can be applied in both transmit and receive at the cost of lateral resolution, since the aperture width is inversely proportional to the width of the main lobe of the beam pattern. An apodization can therefore also be used to obtain a constant lateral resolution across depth by using an expanding and contracting aperture corresponding to a constant F-number. In the case of directional beamformation, apodization can be used to direct the beam and thereby control the coherence along a line so the beamformed RF data can be used for velocity estimation.

In Fig. 2, the wave propagation paths for transmit-receive element pairs for two different focal points are shown. In addition, an apodization profile is calculated corresponding to a common F-number for the two depths*. The apodization values for the elements is determined by the orthogonal distance from their positions to the apodization line as indicated by the intersections between the dashed lines and the two apodization profiles. Note that for the focal point \vec{r}_{fp_2} , we are running out of aperture and an edge-wave will most likely appear in the image. In the results section, we demonstrate how to deal with such edge-waves for dynamic apodization.

3. SOFTWARE DESIGN

The toolbox is object-oriented and written C++ conforming with the latest C++0x standard.²¹ Reference semantics is used for all objects to minimize memory consumption and improve consistency of calculations. Expression templates are used whenever their use were justified by an increased performance or to take advantage of generic programming using the *Standard Template Library*.²² A UML class diagram for the C++ part is shown in Fig. 3. This shows how a Base class handles reference semantics for the classes: Aperture, Apodization, and Line. Further, it shows that an Image consist of a number of Lines, each Line associated with two instances of the Apodization class, associated with an Aperture for transmit and receive respectively. We will elaborate on the individual classes in the next paragraphs. The toolbox has a Matlab MEX-interface^{23,24} that exposes five

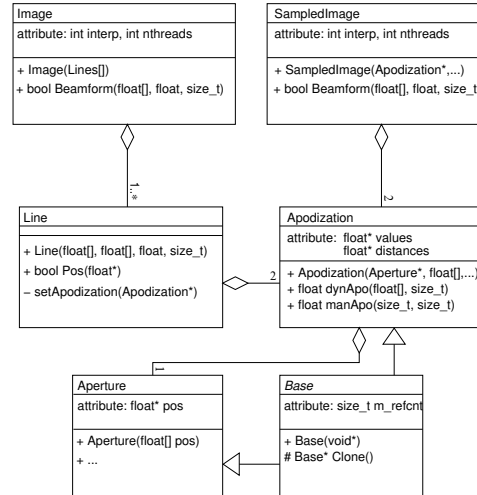


Figure 3: UML state diagram.

C++ classes to the user through five Matlab classes. The constructors, destructors, and a number of member functions of each class are then dynamically linked and can be invoked from Matlab just like general built-in functions except that they are encapsulated in Matlab classes.²⁵ Class instances are constructed in Matlab like in C# or Java and when destroyed, the Matlab classes invokes the respective destructors in C++ through the MEX-interface. In a similar way, all properties of the classes can be accessed and modified from within Matlab.

The Aperture class holds the spatial coordinates of the transducer elements, a focus point (for transmit or receive focusing), a delay profile, and a reference position for time-of-flight calculations. This class is used for defining both the transmit and receive aperture. For a receive aperture, the coordinates of the transducer elements are used for calculating $t_{\text{TOF}_{\text{rcv}}}$, the focus point is used for the possibility of fixed receive-focusing, the

*The F-numbers used for transmit and receive can of course also be different as well as the window functions

delay profile is to compensate for fixed delays in the system, and the reference position is ignored. The transmit aperture however uses this reference for calculating $t_{\text{TOF}_{\text{xmt}}}$, the coordinates of the transducer elements are used for transmit apodization for synthetic aperture beamformation, the focus point for fixed transmit-focusing and the delay profile is the delay of each transmission.

The Apodization class holds the defining properties of the tapering of the individual receive channels and a possible overall scaling for an emission used for synthetic aperture imaging. For scan-lines, the apodization can be defined in two ways and the resulting apodization is the product thereof. It can be defined completely in the sense that the user can define a number of windows to be applied for a number of range intervals, the range being defined as the distance from an apodization reference point to the focus point. This makes it possible to apply simple apodization or extraordinary apodization functions, like the ones investigated by Jensen and Munk for vector velocity estimation.²⁶ The second possibility is dynamic apodization with an expanding and contracting aperture defined by an F-number, an analytical window function, and the apodization reference to compute the width of an active sub-aperture for a given focus point. If the active sub-aperture extends outside the physical aperture, then only an inner fraction of the apodization window are applied as illustrated in Fig. 2.

The Line class holds the positions of the focus points. The points are parametrized using a reference point, a direction, a number of samples, and a spatial separation. The points are beamformed using a plurality of methods depending on distances to reference points, window functions, and possible F-numbers. To speed up calculations and remove unnecessary branches, the line class contains logic for determining which apodization that should be applied to which points on the line. To do this, intersections between the line and a number of sphere and cones need to be computed. This is all handled by the Line class.

The Image class is responsible for interpolation among the RF or complex samples. When using Neville's algorithm for spline interpolation, the second-order derivatives are cached for fast computation of the interpolated values. The parallization is made using pthreads on *nix and Win32 API on Microsoft Windows. Threads are spawned each time a line or image is beamformed. If more than line is beamformed using the same data, the toolbox exploits multithreading. The class is also responsible for initiating the beamformation process by calling the member function **Beamform**.

The SampledImage class is used for beamforming an image specified by a grid rather than by a number of scan lines, see Fig. 4.

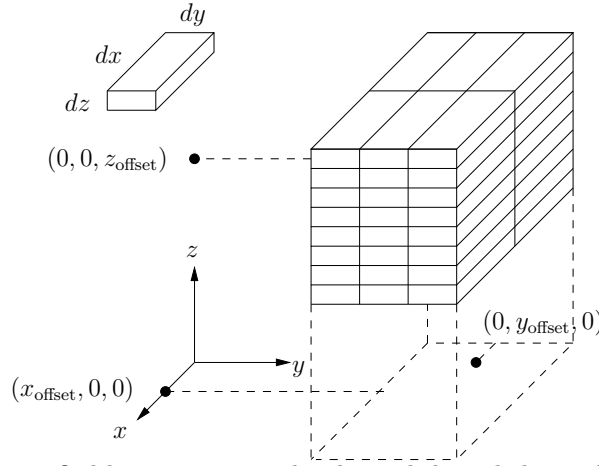


Figure 4: Points on a 3D grid specified by separations dx , dy , and dz and three offsets x_{offset} , y_{offset} , and z_{offset} . The offsets specify the coordinates of centermost position on the grid.

The class is primarily used for beamforming complex data but can also be used for directional beamformation for velocity estimation.¹¹ A method for synthetic aperture compound²⁷ was implemented using this feature.

4. EXAMPLES OF USE

When using the toolbox, first the sampling frequency and speed of sound are set as common parameters for all objects. Next, at least two Aperture instances and a number of scan lines are defined. For each line, two apodizations must be defined, one used for transmit and one for receive. When beamforming instead a grid of points using an SampledImage object, only two apodizations need to be defined. If lines are beamformed, an Image object must be created. Data from a single or a number of emissions can now be beamformed using either an Image or a SampledImage object.

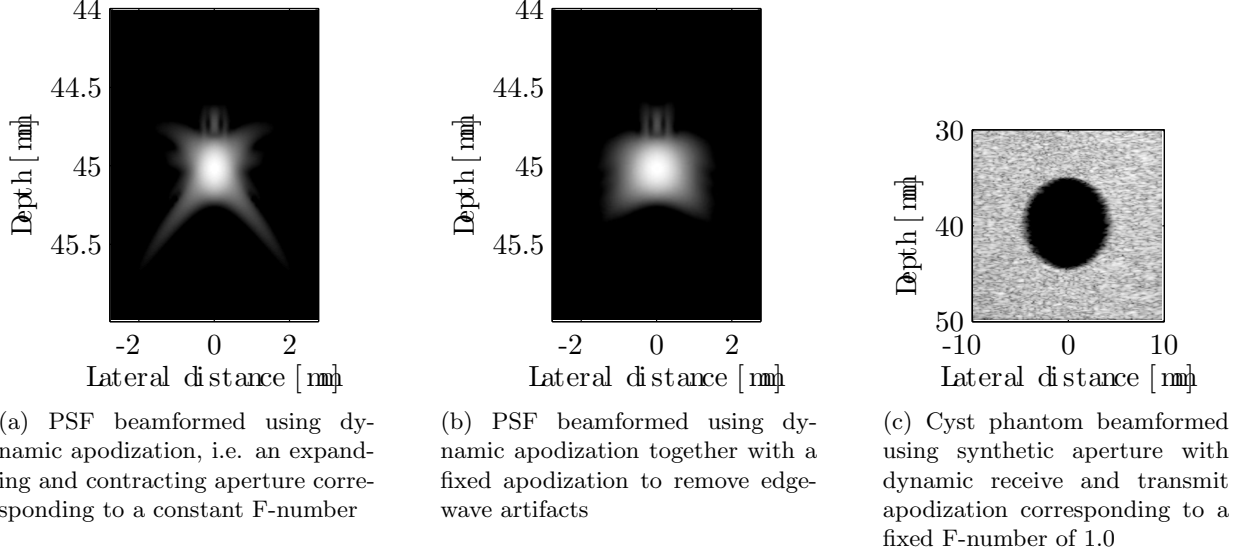


Figure 5: Data simulated with Field II are beamformed using the toolbox. The images show the envelope of the field with a dynamic range of 60 dB.

In Fig. 5a, the field from a point scatterer is beamformed using dynamic apodization and the resulting point-spread-function (PSF) is shown. In Fig. 5b, the same field is beamformed with an additional fixed apodization to remove edge-wave artifacts emerging since we are running out of aperture. Finally, in Fig. 5c, we have beamformed a cyst image using synthetic aperture imaging using 192 single-element emissions, 192 channels, and dynamic apodization in both transmit and receive.

5. RESULTS

In this section, the toolbox is profiled on a standard PC with a Quad-Core Xeon E5520 processors running at 2.26 GHz and on a workstation with two Quad-Core Xeon E5520 processors. To test the performance, data were simulated using Field II and images beamformed using dynamic receive focusing (DRF), synthetic aperture sequential beamformation (SASB), and synthetic aperture (SA) imaging. The details are listed in Table 1.

Table 1: Beamformation scenarios tested with the toolbox. For the SASB beamforming, the 1st stage corresponds to DRF but with a fixed focus, whereas the 2nd stage is a synthetic aperture stage, where a single image line is used for all receive channels to form each low resolution image. See¹⁵ for more details.

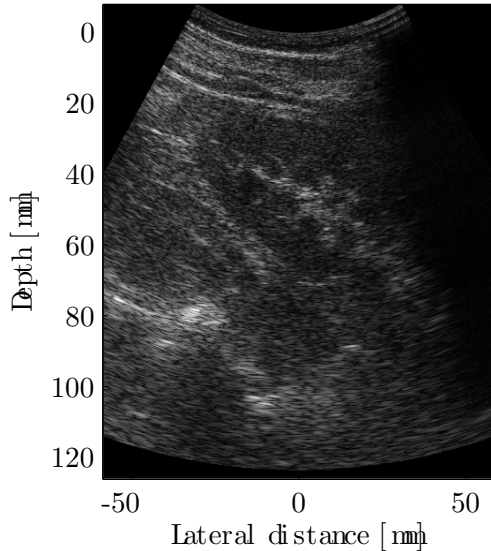
	# of lines	# of samples	# of emissions	# of rcv. channels	# of real RF samples
DRF	384	3116	384	64	3743
SASB 1st	384	3116	384	64	3743
SASB 2nd	384	3116	384	64	3116
SA	128	1038	192	192	1482

The number of line samples and RF samples, for all the scenarios in Table 1, are chosen such that all data are accessed. In Table 2, the run times of the toolbox are listed together with standard deviations obtained using a sample of 10 measurements.

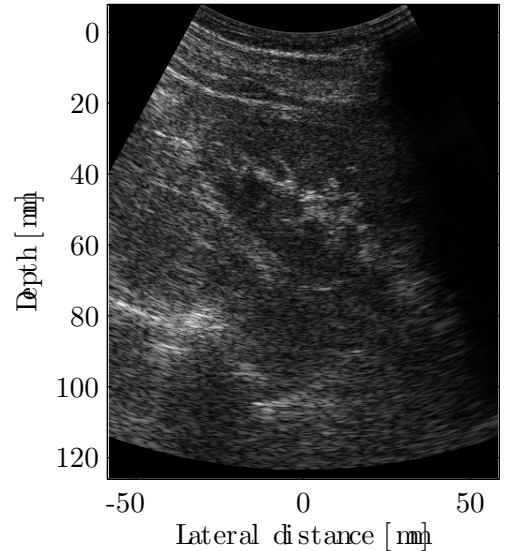
Table 2: Run times of the toolbox for beamforming images using dynamic receive focus (DRF), synthetic aperture sequential beamformation (SASB), and synthetic aperture (SA) on a workstation with Intel Quad-Core Xeon E5520 processors.

Hardware	1 CPU			2 CPU	
Threads	1	2	4	8	16
DRF	5.65 ± 0.062	5.65 ± 0.077	5.66 ± 0.072	5.64 ± 0.061	5.68 ± 0.081
SASB 1st	6.08 ± 0.012	6.08 ± 0.005	6.12 ± 0.076	6.17 ± 0.064	6.18 ± 0.045
SASB 2nd	105.58 ± 0.555	63.09 ± 0.577	37.32 ± 0.458	21.49 ± 0.605	17.57 ± 0.581
SA	1202.07 ± 9.82	616.35 ± 6.71	324.52 ± 5.24	165.75 ± 2.78	143.16 ± 2.49

To obtain the results in Table 2, the library was loaded and the data read into memory before starting the profiler. Simultaneous multithreading (SMT) was enabled and when using 1, 2, 4, and 8 threads, the threads were running on the non-hyper-threaded cores. When using 16 threads, half the threads were running on hyper-threaded cores. It is evident that for this particular application, the enabling of hyper-threading does give a small speedup. It should also be noted that only the SASB 2nd stage and the SA example benefit from multiple cores, since here multiple lines can be beamformed simultaneously. The large standard errors are due to the scheduler spawning threads for each emission. In the next version, worker threads will be waiting for signals in between emissions to lower the standard deviations and consequently also lower the run times for the toolbox.



(a) Liver image beamformed using dynamic receive focusing, a transmit focus in 40 mm depth, and an F-number of 2. The data are obtained with a convex transducer with 192 elements



(b) Liver image beamformed using SASB. The image is beamformed using data interleaved with those used for Fig. 6a.

Figure 6: Liver images beamformed using the toolbox for an ongoing research study at CFU.

At the moment, the toolbox is used for a number of research studies at CFU. One study using a convex transducer and data collected with a 2202 ProFocus ultrasound scanner (BK Medical, Herlev, Denmark). In Fig. 6, an *in-vivo* Liver image is beamformed using the toolbox.

6. CONCLUSION

A general 3D software toolbox for off-line beamformation has been developed. It is capable of handling a multitude of focusing methods, interpolation schemes and parametric and dynamic apodization. Further, it is capable of exploiting parallelization on a single computer, on a cluster, or on both. For synthetic aperture imaging, it is 19 times faster than our previous toolbox. The toolbox is now being used for a number of ongoing research projects at CFU and will be central for many to come.

REFERENCES

- [1] J. A. Jensen and N. B. Svendsen. Calculation of Pressure Fields from Arbitrarily Shaped, Apodized, and Excited Ultrasound Transducers. *IEEE Trans. Ultrason., Ferroelec., Freq. Contr.*, 39:262–267, 1992.
- [2] J. A. Jensen. Field: A Program for Simulating Ultrasound Systems. *Med. Biol. Eng. Comp.*, 4, Supplement 1, Part 1(1):351–353, 1996.
- [3] K. E. Thomenius. Evolution of ultrasound beamformers. In *Proc. IEEE Ultrason. Symp.*, volume 2, pages 1615–1621, 1996.
- [4] Tien Pham and T Whipps. Acoustic signal processing toolbox for array processing. *Proceedings of SPIE - The International Society for Optical Engineering*, 5096:597–606, 2003.
- [5] S. Sabchevski, I. Zhelyazkov, E. Benova, V. Atanassov, P. Dankov, M. Thumm, G. Dammertz., B. Piosczyk3, S. Illy, M. Q. Tran, S. Alberti5, and J-Ph. Hogge. Development of new generation software tools for simulation of electron beam formation in novel high power gyrotrons. *Journal of Physics: Conference Series*, 44:96–100, 2006.
- [6] S. Gustavsson. Parallel algorithms for ultrasound beamformation. Master’s thesis, Ørsted•DTU, Technical University of Denmark, Lyngby, Denmark, 2002.
- [7] J. Kortbek, S. I. Nikolov, and J. A. Jensen. Effective and Versatile software Beamformation Toolbox. In *Proc. SPIE - Medical Imaging - Ultrasonic Imaging and Signal Processing*, pages 651319,1–10, 2007.
- [8] J. A. Jensen, M. Hansen, B. G. Tomov, S. I. Nikolov, and H. Holten-Lund. System architecture of an experimental synthetic aperture real time ultrasound system. In *Proc. IEEE Ultrason. Symp.*, pages 636–640, Oct. 2007.
- [9] W. H. Press, B. P. Flannery, S. A. Teukolsky, and W. T. Vetterling. *Numerical recipes in C. The art of scientific computing*. Cambridge University Press, Cambridge, 2nd edition, 1992.
- [10] Blake Madden. Using cppunit to implement unit testing. In Mike Dickheiser, editor, *Game Programming Gems 6*, 2006.
- [11] J. A. Jensen. Directional velocity estimation using focusing along the flow direction: I: Theory and simulation. *IEEE Trans. Ultrason., Ferroelec., Freq. Contr.*, pages 857–872, 2003.
- [12] G. R. Lockwood, J. R. Talman, and S. S. Brunke. Real-time 3-D ultrasound imaging using sparse synthetic aperture beamforming. *IEEE Trans. Ultrason., Ferroelec., Freq. Contr.*, 45:980–988, 1998.
- [13] C. R. Hazard and G. R. Lockwood. Theoretical assessment of a synthetic aperture beamformer for real-time 3-D imaging. *IEEE Trans. Ultrason., Ferroelec., Freq. Contr.*, 46:972–980, 1999.
- [14] L. F. Nock and G. E. Trahey. Synthetic aperture imaging in medical ultrasound with correction for motion artifacts. In *Proc. IEEE Ultrason. Symp.*, pages 1597–1601, 1990.
- [15] J. Kortbek, J. A. Jensen, and K. L. Gammelmark. Synthetic aperture sequential beamforming. In *Proc. IEEE Ultrason. Symp.*, pages 966–969, 2008.
- [16] C. Passmann and H. Ermert. Adaptive 150 MHz ultrasound imaging of the skin and the eye using an optimal combination of short pulse mode and pulse compression mode. In *Proc. IEEE Ultrason. Symp.*, pages 1291–1294, 1995.
- [17] C. Passmann and H. Ermert. A 100-MHz ultrasound imaging system for dermatologic and ophthalmologic diagnostics. *IEEE Trans. Ultrason., Ferroelec., Freq. Contr.*, 43:545–552, 1996.
- [18] C. H. Frazier and W. D. O’Brien. Synthetic aperture techniques with a virtual source element. *IEEE Trans. Ultrason., Ferroelec., Freq. Contr.*, 45:196–207, 1998.
- [19] S. I. Nikolov and J. A. Jensen. Virtual ultrasound sources in high-resolution ultrasound imaging. In *Proc. SPIE - Progress in biomedical optics and imaging*, volume 3, pages 395–405, 2002.

- [20] S. I. Nikolov and J. A. Jensen. Comparison between different encoding schemes for synthetic aperture imaging. In *Proc. SPIE - Progress in biomedical optics and imaging*, volume 3, pages 1–12, 2002.
- [21] ISO/IEC. Dtr 19769, standard for programming language C++. Working Draft 3092, ANSI, 26. March 2010.
- [22] Alexander Stepanov and Meng Lee. The standard template library. Technical report, Hewlett-Packard Company, 1994.
- [23] The MathWorks Inc. *MATLAB Application Program Interface Guide*. The MathWorks Inc., 1998.
- [24] The MathWorks Inc. *External Interfaces/API*. The MathWorks Inc., 2002.
- [25] The MathWorks Inc. *A Guide to MATLAB Object-Oriented Programming*. The MathWorks Inc., 2007.
- [26] J. A. Jensen and P. Munk. A New Method for Estimation of Velocity Vectors. *IEEE Trans. Ultrason., Ferroelec., Freq. Contr.*, 45:837–851, 1998.
- [27] J. M. Hansen and J. A. Jensen. A method for synthetic aperture compounding. In *Proc. IEEE Ultrason. Symp.*, 2010.

A.3 Methods and Systems for Producing Compounded Ultrasound Images

- **Jens Munk Hansen**, Svetoslav Ivanov Nikolov, Jacob Kortbek, and Jørgen Arendt Jensen. Methods and Systems for producing compounded ultrasound images, International Application Number PCT/P81007275/DK00.

(43) International Publication Date
19 April 2012 (19.04.2012)(10) International Publication Number
WO 2012/049124 A2

(51) International Patent Classification:

A61B 8/14 (2006.01) G10K 11/34 (2006.01)
G01S 7/52 (2006.01) G01N 29/06 (2006.01)
G01S 15/89 (2006.01)

(21) International Application Number:

PCT/EP2011/067648

(22) International Filing Date:

10 October 2011 (10.10.2011)

(25) Filing Language:

English

(26) Publication Language:

English

(30) Priority Data:

PA 2010 00924 11 October 2010 (11.10.2010) DK
61/393,196 14 October 2010 (14.10.2010) US

(71) Applicant (for all designated States except US): **B-K MEDICAL APS** [DK/DK]; Mileparken 34, DK-2730 Herlev (DK).

(72) Inventors; and

(75) Inventors/Applicants (for US only): **HANSEN, Jens, Munk** [DK/DK]; Heinesgade 13, 4 th, DK-2200 Copenhagen N (DK). **NIKOLOV, Svetoslav, Ivanov** [BG/DK]; Ryttergårdsvej 18, lejl 203, DK-3520 Farum (DK). **KO-**

RTBEK, Jacob [DK/DK]; Guldæble Have 2, DK-5210 Odense NV (DK). **JENSEN, Jørgen, Arendt** [DK/DK]; Klørvang 35, DK-2970 Hørsholm (DK).

(74) Agent: **BOESEN, Johnny, P.**; Zacco Denmark A/S, Hans Bekkevolds Allé 7, DK-2900 Hellerup (DK).

(81) Designated States (unless otherwise indicated, for every kind of national protection available): AE, AG, AL, AM, AO, AT, AU, AZ, BA, BB, BG, BH, BR, BW, BY, BZ, CA, CH, CL, CN, CO, CR, CU, CZ, DE, DK, DM, DO, DZ, EC, EE, EG, ES, FI, GB, GD, GE, GH, GM, GT, HN, HR, HU, ID, IL, IN, IS, JP, KE, KG, KM, KN, KP, KR, KZ, LA, LC, LK, LR, LS, LT, LU, LY, MA, MD, ME, MG, MK, MN, MW, MX, MY, MZ, NA, NG, NI, NO, NZ, OM, PE, PG, PH, PL, PT, QA, RO, RS, RU, RW, SC, SD, SE, SG, SK, SL, SM, ST, SV, SY, TH, TJ, TM, TN, TR, TT, TZ, UA, UG, US, UZ, VC, VN, ZA, ZM, ZW.

(84) Designated States (unless otherwise indicated, for every kind of regional protection available): ARIPO (BW, GH, GM, KE, LR, LS, MW, MZ, NA, RW, SD, SL, SZ, TZ, UG, ZM, ZW), Eurasian (AM, AZ, BY, KG, KZ, MD, RU, TJ, TM), European (AL, AT, BE, BG, CH, CY, CZ, DE, DK, EE, ES, FI, FR, GB, GR, HR, HU, IE, IS, IT, LT, LU, LV, MC, MK, MT, NL, NO, PL, PT, RO, RS,

[Continued on next page]

(54) Title: METHODS AND SYSTEMS FOR PRODUCING COMPOUNDED ULTRASOUND IMAGES

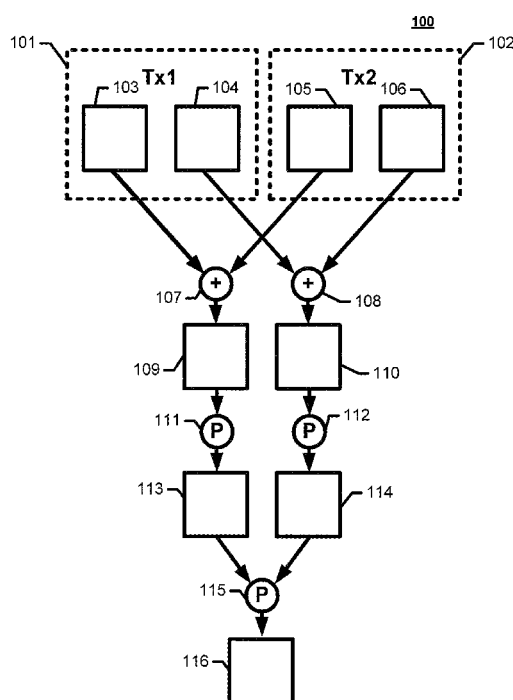


Fig.1

(57) Abstract: Disclosed is a method for producing compounded ultrasound images by beamforming a first and a second low-resolution image using data from a first ultrasound emission, beamforming a third and a fourth low-resolution image using data from a second ultrasound emission, summing said first and said third low-resolution image creating a first high-resolution image and said second and said fourth low-resolution image creating a second high-resolution image, wherein the method further comprises computing a first envelope image for said first high-resolution image and a second envelope image for said second high-resolution image, and processing said first envelope image and said second envelope image creating in a first compounded high-resolution image.



SE, SI, SK, SM, TR), OAPI (BF, BJ, CF, CG, CI, CM, GA, GN, GQ, GW, ML, MR, NE, SN, TD, TG).

Published:
— *without international search report and to be republished
upon receipt of that report (Rule 48.2(g))*

Title *Methods and systems for producing compounded ultrasound images***Field**

- 5 This invention generally relates to ultrasound imaging, more particular to methods for producing compounded ultrasound images.

Background

- 10 A major benefit of clinical ultrasound is the ability to capture the dynamic anatomy in real time. The diagnostic capability of ultrasound imaging is dependent on the properties of the imaging system in terms of resolution, contrast, suppression of speckle noise, and frame rate. Improving diagnostic capabilities is challenging since these properties are in essence of conflicting
15 nature.

Compounding may be used for speckle suppression. In clinical ultrasound imaging the displayed images have an image overlay with a grainy appearance called speckle. Speckle does not represent physical structure
20 but is a result of diffuse backscattering from tiny tissue structures much smaller than the wavelength of the ultrasound pulse. Since speckle is not assigned a clinical diagnostic value and only perceived as an unwanted imaging artifact speckle is often denoted as speckle-noise. The appearance of speckle makes it difficult to resolve small differences in echogenecity and
25 thus reduces the contrast and limits the ability to display cysts. Different ways of eliminating speckle has been proposed, and one method is compounding. Speckle patterns are related to the viewing angle, at which a given region of tissue is scanned, and the most common method for speckle reduction is to use angular compounding. An image is created by transmitting and receiving
30 beams perpendicular to the transducer surface. Each beam is created by exciting a sub-set of transducer elements to create a transmit beam. The

echoes are received with the same or another subset of transducer elements, and an image line is formed along the propagation direction of the transmit beam. After a line has been beamformed, adjacent transmit elements are excited to create a new transmit beam, and a new receive beam is formed in
5 the same direction. The process is repeated till an image is scanned. Then a new image is created in the same sequential manner. The beams are this time steered at an angle. A number of such images are scanned sequentially. The beams from the images are envelope detected and scan-converted. The envelope detected and scan converted images are combined together to
10 suppress speckle. The process is known as spatial compounding or angular compounding.

US4604697 discloses synthetic transmit aperture imaging. The principle of synthetic transmit aperture imaging is to acquire backscattered data with
15 different phase and amplitude information which will allow to reconstruct the image using, for example, delay-and-sum beamforming. Spherical waves are used to scan the region. First a spherical wave is created such as its origin is at the one end of the transducer. The wave propagates in the whole region under investigation and is back scattered to the transducer. Then the
20 acquisition is repeated, but this time the origin of the spherical wave is positioned at another spatial location. The process is repeated until the whole transmit aperture is spanned by the centers of origin of the spherical waves. At every emission a full image is created by delay and sum beamforming. These images have a low resolution since beamforming is performed only in
25 receive. By combining the individual images a resulting image having a high-resolution is created. This proposed method improves the resolution but does not solve the problem of speckle suppression.

US6508770 discloses a method for speckle suppression which is called
30 aperture compounding. In this method a beam is transmitted and received along a scan line. The acquisition is done sequentially with first and second

apertures, where the center of first aperture is different from the center of second aperture. The compounding effect is achieved by adding the envelope-detected data from first and second aperture. The method cannot achieve the full potential of compounding for the whole line, and the frame rate is limited by the sequential nature of the acquisition.

US20090069693 suggest the use of the principles of retrospective dynamic focusing for spatial compounding. In their work a line is illuminated by a small set of transmissions. The data is processed to achieve retrospective dynamic transmit focusing. The compound effect in this approach is limited because of the focused transmissions and the line-based beamforming. Further the frame rate is limited by the sequential nature of line-based acquisition.

It remains thus a problem to provide an improved method and/or system for reducing the unwanted effects of speckle in ultrasound images.

Summary

According to a first aspect, there is provided a method of producing compounded ultrasound images by beamforming a first and a second low-resolution image using data from a first ultrasound emission, beamforming a third and a fourth low-resolution image using data from a second ultrasound emission, summing said first and said third low-resolution image creating a first high-resolution image and said second and said fourth low-resolution image creating a second high-resolution image, wherein the method further comprises computing a first envelope image for said first high-resolution image and a second envelope image for said second high-resolution image, and processing said first envelope image and said second envelope image creating in a first compounded high-resolution image.

Consequently, there is provided a method capable of producing high quality ultrasound images with a high frame rate. By beamforming two images for each ultrasound emission and further combining images from different emissions, resulting images with both a high resolution and reduced
5 unwanted speckle effects may be provided.

Each low-resolution image may have any size; e.g. it may comprise a single image line or a plurality of image lines. In some embodiments, each low-resolution image comprises at least 2, 5, 10, 20, 50, 100, or 500 image lines.
10 A low-resolution image may be defined as an ultrasound image created by processing data originating from a single ultrasound transmission. The first and the second low-resolution image may be created by using any beamforming method, e.g. a conventional delay and sum beamformer. A high-resolution image may be defined as an ultrasound image created by
15 processing data from a plurality of emissions.

The ultrasound emissions may be focused emissions where the ultrasound wave front converges towards a focus point positioned in front of the ultrasound transducer, e.g. by transmitting an ultrasound signal from a group
20 of transducer elements where the ultrasound signals transmitted from the transducer elements of the central part of the group are delayed relative to the ultrasound signals transmitted from transducer elements of the outer part of the group, an unfocused ultrasound emission where an approximately plane wavefront is created, e.g. by transmitting from a plurality of transducer
25 elements coherently, or a defocused ultrasound emission where an ultrasound wavefront is created that converges away from a point positioned at or behind the ultrasound transducer, e.g. by transmitting an ultrasound signal from a group of transducer elements where the ultrasound signal transmitted from the transducer elements of the outer part of the group is
30 delayed relative to the ultrasound signal transmitted from transducer elements of the central part of the group.

The transmitted ultrasound beam for the first ultrasound emission may differ from the transmitted ultrasound beam for the second ultrasound emission with respect to its geometrical position and/or shape and/or frequency content. Transmitted ultrasound beams at different geometrical positions and/or different shapes and/or with different frequency content may be generated by selecting different sub groups of transducer elements and/or using different apodization functions and/or using different excitation signals having different frequency contents.

10

The low-resolution images may be weighted before they are summed into high-resolution images. The weight may be a single weight for all image points in a low-resolution image or a particular weight for each image point in a low-resolution image may be used. The weights may have any value including zero.

15

More than two low-resolution images may be beamformed for each ultrasound emission, e.g. at least 3, 4, 5, 6, or 10 low-resolution images may be created for each ultrasound emission, thus resulting in at least 3, 4, 5, 6, or 10 high-resolution images. More than two emissions may be used to create the high-resolution images, e.g. at least 3, 4, 5, 8, 16, 32, 64, 128, 192 ultrasound emissions, e.g. each high-resolution image may be created by summing at least 3, 4, 5, 8, 16, 32, 64, 128, 192 low-resolution images.

20

A compounded image may be defined as an image created by processing at least two envelope detected images for reducing the effect of speckle in the envelope detected images. The processing may be performed by summing the envelope detected images and/or by multiplying the envelope detected images by each other and/or by performing another mathematical operation between the at least two envelope detected images. A compounded image may also be created using nonlinear operations, e.g. creating a compounded

25

30

image comprising for each image point, the maximum or minimum value of the image point in any of the envelope detected images.

5 Low-resolution images for an emission may differ with respect to the steering angle thus resulting in angular compounding. Additionally or alternatively different frequency intervals may be used to beamform low-resolution images for an emission thus resulting in angular and frequency compounding or frequency compounding. Low-resolution images for an emission may be created with a desired frequency interval by filtering data from an ultrasound
10 emission with a band-pass filter having a passband corresponding to the desired frequency interval, prior to beamforming the data.

Envelope images may also be known as envelope detected images. The process of determining the envelope of a beamformed ultrasound image is
15 commonly performed in ultrasound systems.

Envelope images may be computed by processing for each image line in a high-resolution image processing beamformed or RF data. For narrow band signals with no DC component, the ideal envelope detection can be done by
20 computing the absolute value of the analytic signal. Different realizations of approximations to the ideal envelope detection exist. One solution is to use a single rectifier component or a rectifier bridge followed by a low-pass filter. A precision rectifier is another, more advanced solution where a circuit comprising an operational amplifier is configured to act as a more ideal
25 rectifier for a detection closer to the ideal detection.

In some embodiments, the method comprises transmitting a first ultrasound signal into a physical medium using an ultrasound transducer, receiving a first data signal using said ultrasound transducer said first data signal being
30 indicative of the acoustic properties of said physical medium, creating a first low-resolution image by beamforming data comprising said first data signal

using a first set of apodization functions, creating a second low-resolution image by beamforming data comprising said first data signal using a second set of apodization functions,

- 5 In some embodiments, the method comprises transmitting a second ultrasound signal into a physical medium using said ultrasound transducer, receiving a second data signal using said ultrasound transducer said second data signal being indicative of the acoustic properties of said physical medium, creating a third low-resolution image by beamforming data
- 10 comprising said second data signal using a third set of apodization functions, creating a fourth low-resolution image by beamforming data comprising said second data signal using a fourth set of apodization functions.

- In some embodiments, the method comprises summing said first and said
- 15 third low-resolution image creating a first high-resolution image and said second and said fourth low-resolution image creating a second high-resolution image.

- In some embodiments, the method comprises computing a first envelope
- 20 image for said first high-resolution image and a second envelope image for said second high-resolution image, and processing said first envelope image and said second envelope image resulting in a first compounded high-resolution image.

- 25 The ultrasound transducer may be a single element transducer or an array transducer comprising a plurality of transducer elements arranged in an array. The ultrasound transducer may be a one-dimensional array transducer or a two-dimensional array transducer. The array transducer may be arranged in a linear array, a convex array or a concave array. The array
- 30 transducer may be a phased array transducer, where the transducer

elements are spaced with a pitch not above half the centre frequency of the ultrasound transducer.

In some embodiments, the ultrasound transducer comprises a plurality of transducer elements, and wherein the first and the second data signal
 5 comprise a plurality of RF signals recorded by a subset of said plurality of transducer elements, and where the step of beamforming a low-resolution image comprises, for each point in the low-resolution image, delaying, apodizing, and summing RF signals recorded by said subset of said plurality
 10 of transducer elements.

Each set of apodization functions may comprise a plurality of apodization functions, each apodization function comprising a plurality of apodization values. An apodization value is a value used to weight an RF signal recorded
 15 by a specific transducer element when beamforming an image point in an image. Each set of apodization functions may comprise a specific apodization function for a given image point in a given low-resolution image, and each apodization function may comprise an apodization value for each transducer element used to beamform a given image point of a given low-
 20 resolution image, thus an apodization value for an RF signal recorded by a specific transducer element may be dependent on the specific low-resolution image being beamformed, and the index of the image point in the specific low-resolution image being beamformed.

25 The subset may comprise at least two transducer elements and/or not all transducer elements and/or all transducer elements of the ultrasound transducer. For a given image point in a low-resolution image corresponding to a spatial position relative to the ultrasound transducer, the beamformed value may be given by the following equation:

$$low_res_im_k(x, y) = \sum_{n=1}^N a_{x,y,k,n} \cdot S_n(t - t_f)$$

where $low_res_im_k(x, y)$ is the value of the k'th low-resolution image at an image point with index x and y, N is the number of transducer elements of the subset, $a_{x,y,k,n}$ is the apodization value for the image point with index x and y in the k'th low-resolution image for transducer element n, $S_n(t)$ is the RF
5 signal recorded by the n'th transducer element of the subset of transducer elements, and t_f is a delay value corresponding to an estimated total time of flight for the ultrasound signal transmitted from the transducer to the spatial point corresponding to the image point with index x and y and back to the n'th transducer element. t_f may be estimated by estimating the distance the
10 ultrasound signal must travel and combining that estimated distance with an estimated average speed of sound in the physical medium. The above described beamforming method may be known as a kind of delay and sum beamformer, however beamforming may be performed in a variety of ways, e.g. beamforming may be performed in the frequency domain and/or using
15 adaptive algorithms.

In some embodiments, the ultrasound transmissions are low-focused transmissions.

20 A low-focused ultrasound transmission may be a transmission that does not converge towards a focus point within at least a distance of 2 cm, 3 cm, 5 cm, 10 cm, 20 cm, 30 cm, 40 cm or 50 cm from the ultrasound transducer. The low-focused transmission may be an emission from a single ultrasound transducer element or a group of transducer elements, e.g. a defocused
25 ultrasound emission emitted from a group of transducer elements where an ultrasound wavefront is created that converges away from a point positioned at or behind the ultrasound transducer, e.g. by transmitting an ultrasound signal from the group of transducer elements where the ultrasound signal transmitted from the transducer elements of the outer part of the group is
30 delayed relative to the ultrasound signal transmitted from transducer elements of the central part of the group.

By using a low-focused transmission, a more precise estimation of the time of flight for the ultrasound signal from the ultrasound transducer to points in space may be estimated as a more simple transmit wave is generated.

- 5 Thereby low-resolution image may be beamformed with a more even resolution for all image points. This will further result in high-resolution images with increased resolution.

10 In some embodiments, said first transmitted ultrasound signal is transmitted with a first subset of ultrasound transducer elements, and said second transmitted ultrasound signal is transmitted with a second subset of ultrasound transducer elements, said first and said second subset of transducer elements differing with at least one transducer element.

- 15 In some embodiments, said second transmitted ultrasound signal is directly consecutive of said first transmitted ultrasound signal e.g. there is no ultrasound signals transmitted between said first transmitted ultrasound signal and said second transmitted ultrasound signal.

20 By combining low-resolution images beamformed from data resulting from ultrasound emissions from different parts of the ultrasound transducer array, high-resolution images may be created with an increased resolution.

25 In some embodiments, said first data signal is recorded by a third subset of ultrasound transducer elements, and said second data signal is recorded by a fourth subset of transducer elements, said third and said fourth subset differing with at least one transducer element.

30 By combining low-resolution images beamformed from data recorded by different parts of the ultrasound transducer array, high-resolution images may be created with an increased resolution.

In some embodiment, said first data signal is recorded by a third subset of ultrasound transducer elements, and said second data signal is recorded by a fourth subset of transducer elements, said third and said fourth subset being identical.

5

In some embodiments, the first set of apodization functions comprises an apodization function for each image point in the first low-resolution image, the second set of apodization functions comprises an apodization function for each image point in the second low-resolution image, the third set of

10 apodization functions comprises an apodization function for each image point in the third low-resolution image, the fourth set of apodization functions comprises an apodization function for each image point in the fourth low-resolution image.

15 The apodization functions may comprise an apodization value for each transducer element used to beamform a particular image point in a particular low-resolution image, e.g. an apodization function of the first set of apodization functions may comprise an apodization value for each RF signal recorded by each transducer element used to beamform a particular image

20 point in the first low-resolution image, an apodization function of the second set of apodization functions may comprise an apodization value for each RF signal recorded by each transducer element used to beamform a particular image point in the second low-resolution image, etc.

25 In some embodiments, a set of apodization functions is configured to rotate the resulting point spread function for each image point in a low-resolution image with a predetermined angle so that low-resolution images having point spread functions rotated with different angles may be created.

30 The point spread function is a measure of the performance of an ultrasound system. It defines the resolution of the system. An estimate of the point

spread function of an ultrasound system may be measured by imaging an ultrasound reflector submerged in water e.g. a wire phantom submerged in water. By varying the used apodization functions, the point spread function may be rotated, e.g. by primarily using data recorded by transducer elements positioned in either a first side or a second side of the ultrasound transducer, wherein the point spread function may be rotated in a first or a second direction, respectively.

In some embodiments, a set of apodization functions configured to rotate the resulting point spread function for each image point in a particular low-resolution images with an angle is computed by generating a first line orthogonal to a line having a predetermined angle relative to the ultrasound transducer, wherein the first line intersects a particular image point., placing a first apodization window centred at the particular image point on this first line, generating a second line with an angle relative to the ultrasound transducer equal to the predetermined angle, wherein the second line intersects the centre of emission of the emission used to create the particular low-resolution image. A first part of the apodization value for a particular transducer element, which data are used to beamform the particular image point in the particular low-resolution image, is given as the value of the first apodization window at which the second line and the first apodization window intersects. Similarly, a second part of the apodization value for the particular transducer element, which recorded data are used to beamform the particular image point in the particular low-resolution image, is computed by placing a second apodization window centered at the particular image point on the first line. The second apodization window may be equal to the first apodization window or different from the first apodization window, generating a third line with an angle relative to the ultrasound transducer equal to the predetermined angle, wherein the third line intersects the particular transducer element. The second part of the apodization value is given as the value of the second apodization window at which the third line and the second apodization

window intersect. The final apodization value is given by multiplying the first part of the apodization value by the second part of the apodization value. By repeating the above steps for all transducer elements which recorded data are used to beamform the particular image point in the particular low-resolution image, an apodization function for beamforming the particular image point in the particular low-resolution image may be generated. By repeating the above steps for all image points in a particular low-resolution image, a set of apodization functions configured to rotate the resulting point spread function for each image point in the particular low-resolution images with an angle may be generated.

The length of the apodization window(s) may be adjusted as a function of the distance between the image point and the centre of transmission and/or or as a function of the distance between the image point and the receiving transducer element.

Thereby the resolution may be evened out over a range of depths to maintain a constant resolution by realizing a fixed F-number using one or more expanding or contracting apodization window(s).

In some embodiments, the first low-resolution image comprises image data beamformed at a first set of spatial positions, the second low-resolution image comprises image data beamformed a second set of spatial positions, wherein the first and the second set of spatial positions are identical.

In some embodiments, all the low-resolution images comprise image data beamformed at a single set of spatial positions so that all low-resolution images comprise image data from the same spatial positions.

In some embodiments, all the high-resolution images comprises image data from the same set of spatial positions.

All spatial positions may be calculated relative to the position of the ultrasound transducer.

- 5 Consequently, compounded images may easily be made without the need or complex re-sampling, e.g. complex scanline conversion.

In some embodiments, the apodization function used to beamform a particular image point in the first low-resolution image has a centre of mass in
10 a first side of the receiving aperture, and the apodization function used to beamform the corresponding image point in the second low-resolution image (e.g. the image point having the same spatial position) has a centre of mass in a second side of the receiving aperture, thus the point spread function of said particular image point has a different orientation in said first and said
15 second low-resolution image.

The receiving aperture for a low-resolution image may be defined as the transducer elements providing the RF signals used to beamform the low-resolution image.

20

In some embodiments, the apodization function used to beamform a particular image point in the first low-resolution image has a maximum value in a first side of the receiving aperture, and the apodization function used to beamform the corresponding image point in the second low-resolution image
25 (e.g. the image point having the same spatial position) has a maximum value in a second side of the receiving aperture.

In some embodiments, the method further comprises creating a second compounded high-resolution image by combining low-resolution images
30 beamformed using data from at least two ultrasound emissions into at least two high-resolution images, computing at least two envelope images from

said at least two high-resolution images and processing said at least two envelope images creating a second compounded high-resolution image, wherein the method further comprises: processing said first and said second compounded high-resolution image creating a combined compounded high-resolution image.

The at least two ultrasound emissions used to create the second compounded high-resolution image may differ with at least one emission from the emissions used to create the first compounded high-resolution image, e.g. at least one emission used to create the second compounded high-resolution image may not be used to create the first compounded high-resolution image. Any method steps used to create the first compounded high-resolution image may equally be used to create the second compounded high-resolution image. The processing of the first and the second compounded high-resolution image may be performed by summing the compounded high-resolution images and/or by multiplying the compounded high-resolution images by each other and/or by performing another mathematical operation between the at least two compounded high-resolution images.

In some embodiments, the method further comprises the step of: providing a user with means to select a contrast/resolution ratio, wherein a compounded image with the selected contrast/resolution ratio is generated.

In some embodiments, the method further comprises the step of: providing a user with means for selecting a contrast/resolution ratio, wherein a compounded image with the selected contrast/resolution ratio is created by:

- configuring the sets of apodization functions so that a high contrast/resolution ratio result in an apodization function for a particular image point in a low-resolution image having an effective width that is less than the effective width of the apodization function for said

particular image point in said low-resolution image when a low contrast/resolution ratio is selected, and/or

- applying a set of weights to a set of low-resolution images forming a high-resolution image, said set of weights being configured to decrease the resolution of the high-resolution images when a high contrast/resolution ratio is selected compared to the resolution of the high-resolution image when a low contrast/resolution ratio is selected.

The effective width of an apodization function may be defined as the length of a particular part of the apodization function comprising a particular percentage of the total energy of the apodization function, e.g. 30%, 40%, 50%, 60% or 80% of the total energy of the apodization function, where the particular part is chosen so that its length is minimized.

The means for selecting a contrast/resolution ratio may be any user input means, e.g. a button, a slider, a voice command system or the like.

The resolution of a high-resolution image may be lowered by applying weights to the low-resolution images summed to give the high-resolution image so that a particular image point in a particular high-resolution image is more influenced by one low-resolution image than another low-resolution image. By primarily using low-resolution images beamformed from ultrasound emissions emitted from a first side of the ultrasound transducer to create a high-resolution image (by applying weighting to the low-resolution image before they are summed into a high-resolution image), high-resolution images may be created having a lower resolution and a point spread function being more rotated. The lower resolution will result in a lower resolution in the compounded ultrasound image; however, the increased rotation will increase the compounding effect increasing the contrast, thus increasing the contrast/resolution ratio.

Contrast influences the ability of the observer to detect small differences in echogenicity of the imaged tissue. A common measure is the contrast-to-noise ratio defined as

$$CNR = \frac{\mu_A - \mu_B}{\sqrt{\sigma_A^2 + \sigma_B^2}}$$

where μ_A is the mean value of the envelope in a region of interest, μ_B is the
5 mean value of the envelope of the background. The variances σ_A^2 and σ_B^2 are measures of the variations of the amplitude of the envelope in the region of interest, and in the background, respectively.

Resolution is a measure of the ability of a system to resolve small structures. It is commonly defined as the full-width at half maximum of the point spread
10 function of the imaging system.

In some embodiments, the method further comprises the step of determining automatically a contrast/resolution ratio based on coherence estimation
15 between low-resolution image from different emissions, so that a high contrast/resolution ratio is chosen when a low coherence is detected (indicative of high motion of the ultrasound transducer and/or the tissue being scanned), and a low contrast/resolution ratio is chosen when a high coherence is detected (indicative of low motion of the ultrasound transducer
20 and/or the tissue being scanned), wherein a compounded image with the selected contrast/resolution ratio is created by:

- configuring the sets of apodization functions so that a high
contrast/resolution ratio result in an apodization function for a particular
image point in a low-resolution image having an effective width that is
25 less than the effective width of the apodization function for said
particular image point in said low-resolution image when a low
contrast/resolution ratio is selected, and/or
- applying a set of weights to a set of low-resolution images forming a
high-resolution image, said set of weights being configured to decrease

the resolution of the high-resolution images when a high contrast/resolution ratio is selected compared to the resolution of the high-resolution image when a low contrast/resolution ratio is selected.

- 5 In some embodiments, a first compounded high-resolution image is generated with a first contrast/resolution ratio, and a second compounded high-resolution image is generated with a second contrast/resolution ratio different from the first contrast/resolution ratio, wherein the first compounded high-resolution image and the second compounded high-resolution image
10 are displayed on a display simultaneously.

The first and the second compounded high-resolution image may be generated using the same data.

- 15 In some embodiments, for a transmission at least a part of the received data signal is shifted in phase, yielding a phase-shifted data signal, where the data signal and the phase-shifted data signal is combined into a complex data signal where the data signal constitutes the real part and the phase-shifted data signal constitutes the imaginary part, resulting in complex low-resolution
20 images and complex high-resolution images, and wherein an envelope image for a high-resolution image is computed by for an image point calculating:

$$E_n(x, y) = \sqrt{I_n(x, y)^2 + R_n(x, y)^2}$$

- where $E_n(x, y)$ is the value of the n'th envelope image at image point index x,y, $I_n(x, y)$ is the imaginary part of the n'th complex high-resolution image
25 at image point index x,y, and $R_n(x, y)$ is the real part of the n'th complex high-resolution image at image point index x,y.

- All data signals may be shifted in phase, e.g. all RF signals recorded by all receiving transducer elements. The RF signals are shifted in phase on a pr.
30 element basis. The data signals may be shifted approximately 90 degrees in

phase. This may be achieved using the Hilbert transformation or approximations to the Hilbert transformation. The complex signals may be beamformed as normal signals, e.g. both the real part and the imaginary part of the complex signals may be delayed and summed resulting in complex
5 beamformed images.

Consequently, envelope images may be created for images beamformed below the Nyquist sampling limit of the RF signals. This greatly lowers the memory and processing requirements of the method decreasing the cost of
10 implementing the method.

According to a second aspect, there is provided an ultrasound system configured to produce compounded ultrasound images by beamforming a first and a second low-resolution image using data from a first ultrasound
15 emission, beamforming a third and a fourth low-resolution image using data from a second ultrasound emission, summing said first and said third low-resolution image creating a first high-resolution image and said second and said fourth low-resolution image creating a second high-resolution image, wherein the ultrasound system further is configured to compute a first
20 envelope image for said first high-resolution image and a second envelope image for said second high-resolution image, and process said first envelope image and said second envelope image creating in a first compounded high-resolution image.

25 The different aspects of the present invention can be implemented in different ways including the methods of producing compounded ultrasound images and the ultrasound systems described above and in the following, each yielding one or more of the benefits and advantages described in connection with at least one of the aspects described above, and each having one or
30 more preferred embodiments corresponding to the preferred embodiments described in connection with at least one of the aspects described above

and/or disclosed in the dependent claims. Furthermore, it will be appreciated that embodiments described in connection with one of the aspects described herein may equally be applied to the other aspects.

5 **Brief description of the drawings**

The above and/or additional objects, features and advantages of the present invention, will be further elucidated by the following illustrative and non-limiting detailed description of embodiments of the present invention, with
10 reference to the appended drawings, wherein:

Fig. 1 shows a flowchart of a method of producing compounded ultrasound images according to an embodiment of the present invention.

15 Fig. 2 shows a flowchart of a method of producing compounded ultrasound images according to an embodiment of the present invention.

Fig. 3 illustrates a method of producing compounded ultrasound images according to an embodiment of the present invention.

20

Fig. 4 illustrates a method of producing compounded ultrasound images, according to an embodiment of the present invention.

Fig. 5 shows how an apodization value may be determined according to an
25 embodiment of the present invention.

Fig. 6a-d show examples of apodization functions generated according to an embodiment of the present invention.

30 **Detailed description**

In the following description, reference is made to the accompanying figures, which show by way of illustration how the invention may be practiced.

Fig. 1 shows a schematic drawing of a method of producing compounded
5 ultrasound images 100 according to an embodiment of the present invention. A first low-resolution image 103 and a second low-resolution image 104 are beamformed using data from a first ultrasound transmission 101. A third low-resolution image 105 and a fourth low-resolution image 106 are beamformed using data from a second ultrasound emission 102. Each low-resolution
10 image comprises image data beamformed at identical spatial positions relative to the ultrasound transducer so that they may be easily processed together without the need for complex re-sampling. The first and the third low-resolution image 103 105 are added 107 forming a first high-resolution image 109. Correspondingly, the second and the fourth low-resolution image
15 104 106 are added 108 forming a second high-resolution image 110. The first high-resolution image 109 is processed 111 to obtain a first envelope image 113, and the second high-resolution image 110 is processed 112 to obtain a second envelope image 114. The first and the second envelope image 113 114 are processed together 115 to obtain a first compounded high-resolution
20 image 116 having a high resolution in all image points and a reduced speckle effect.

Beamforming of low-resolution images may be done directly on the RF signals recorded by a plurality of transducer elements making up the
25 receiving aperture. Alternatively, beamforming may be done on the complex analytical counterpart of the RF signals which has both in-phase and quadrature components. The RF data signals are shifted in phase yielding phase-shifted data signals, where the data signals and the phase-shifted data signals are combined into complex data signals where the data signals
30 constitute the real part and the phase-shifted data signals constitute the imaginary part. Finding the imaginary part of the complex analytical

counterpart of the RF signals can be done by computing the Hilbert Transform of the RF signals. When the process of beamforming uses complex signals, the result is complex low-resolution images and complex high-resolution images from which envelope detection is computed.

5

Every low-resolution image consists of a number of points. If beamforming is based on RF signals as input signals, the points may be placed in lines making up image lines and where the distance between image lines and the distance between points in an image line are determined by the Nyquist sampling criterion for the RF signals. Working with complex in-phase and quadrature data makes it possible to beamform only those points in which the envelope detected value is needed. The bandwidth of the detected signal is much lower than the RF signals, and the points making up the low-resolution images may be placed in a less dense grid than when working with RF signals in the beamformer.

10
15

Fig.2 shows a flowchart of a method of producing compounded ultrasound image according to an embodiment of the present invention.

First, a first ultrasound signal is emitted from an ultrasound transducer in step 201. Using a receiving aperture of the ultrasound transducer, the reflected echoes of the emitted ultrasound signal are recorded resulting in a first data signal, e.g. a plurality of RF signals one for each transducer element of the receiving aperture. Then, to beamform a particular low-resolution image, a specific set of apodization functions is chosen in step 202 dependent on the specific low-resolution image. In step 203 the chosen set of apodization functions is used to beamform a specific low-resolution image by processing the first data signal. In step 204 the method determines if all low-resolution images for the specific ultrasound emission have been beamformed. If the method determines that not all low-resolution images have been beamformed, it returns to step 202 and selects a new set of apodization functions and uses the set of apodization functions to beamform a new low-

20

25

30

resolution image using the first data signal. The different low-resolution images for a specific ultrasound emission may differ with respect to the orientation of the point spread function. The point spread function may be rotated by primarily using data recorded by a particular side of the receiving aperture when beamforming a low-resolution image. This may be achieved by using specially designed apodization functions, e.g. as described in relation to Fig. 5. On the other hand, if the method determines that all low-resolution images for the specific ultrasound emission have been beamformed, it proceeds to step 206 where the method determines if all ultrasound emissions have been emitted. If the method determines that not all ultrasound emissions have been emitted, it returns to step 201, emits a new ultrasound emission records a new data set, and beamforms a number of low-resolution images using different sets of apodization functions. If the method, however, determines that all ultrasound emissions have been emitted, it proceeds to step 208 where a high-resolution image is generated by summing a number of low-resolution images, e.g. summing the first low-resolution image beamformed for each ultrasound emission. By processing the generated high-resolution image, the method creates an envelope image, in step 209. In step 210, the method determines if all envelope images have been created. If the method determines that not all envelope images have been created, it returns to step 208 where a new high-resolution image is created by summing low-resolution images, e.g. summing the second low-resolution image beamformed for each ultrasound emission. However, if the method determines that all envelope images have been created, it continues to step 212 where the envelope images are processed together, as described above or below, resulting in a compounded high-resolution image 213.

Fig. 3 illustrates a method of producing compounded ultrasound images according to an embodiment of the present invention. The acquisition is performed by use of an array of ultrasound elements 301. First a defocused wave is transmitted with a center of emission 302. The defocused wave may

be transmitted by a single transducer element or a group of transducer elements where the ultrasound signal transmitted from the transducer elements of the outer part of the group is delayed relative to the ultrasound signal transmitted from transducer elements of the central part of the group.

- 5 The wave propagates in the whole region of investigation. The back scattered signal is recorded using a receive aperture 305. Recorded channel data are used to generate three low-resolution images 318 319 320 using delay-and-sum beamforming. The delays and apodization coefficients vary from image point to image point in the image. Shown are three apodization
- 10 functions 308 309 310, used to beamform the centre image point 326 327 328 of the three low-resolution image 318 319 320, respectively. The apodization function 308 has a centre of mass in the left part of the receiving aperture and as a result the point spread function for the centre point 326 in the low-resolution image 318 is rotated to the left with respect to the receiving
- 15 aperture. The apodization function 309 has a centre of mass in the centre of the receiving aperture. Consequently the point spread function for the centre point 327 in the low-resolution image 319 is not rotated with respect to the receiving aperture. The apodization function 310 has a centre of mass in the right part of the receiving aperture. As a result the point spread function for
- 20 the centre point 328 in the low-resolution image 320 is rotated to the right with respect to the receiving aperture. It can further be observed that the height of the apodization function 308 is higher than the apodization functions 309 310, and the height of the apodization function 309 is higher than the height of the apodization function 310. The apodization functions for the
- 25 majority of the remaining points in each of the low-resolution images 318 319 320 may be similar to the apodization function of the centre point, thus the low-resolution image 318 is angled to the left, the low-resolution image 319 is not angled, and the low-resolution image 320 is angled to the right. As the height of the apodization functions used to beamform the low-resolution
- 30 image 318 are higher than the height of the apodization functions used to beamform the low-resolution images 319 320, the low-resolution image 318

generally comprises larger values (possibly positive and negative) compared to the low-resolution images 319 320. Correspondingly, as the heights of the apodization functions used to beamform the low-resolution image 319 are higher than the heights of the apodization functions used to beamform the
5 low-resolution image 320, the low-resolution image 319 generally comprises larger (possibly positive and negative) values compared to the low-resolution images 320.

The acquisition using a defocused transmission is repeated with another
10 center of emission 303. The wave propagates in the whole region of interest. The back scattered signal is recorded using a receive aperture 306. Recorded channel data are used to generate three low-resolution images 321, 322 and 323 using delay-and-sum beamforming. The delays and apodization functions vary from image point to image point in the image.
15 Shown are three apodization functions 311 312 313 used to beamform the centre image point 329, 330 331 of the three low-resolution images 321 322 323, respectively. The apodization function 311 has a centre of mass in the left part of the receiving aperture, and as a result the point spread function for the centre point 329 in the low-resolution image 321 is rotated to the left with
20 respect to the receiving aperture. The apodization function 312 has a centre of mass in the centre of the receiving aperture. Consequently the point spread function for the centre point 330 in the low-resolution image 322 is not rotated with respect to the receiving aperture. The apodization function 313 has a centre of mass in the right part of the receiving aperture. As a result the
25 point spread function for the centre point 331 in the low-resolution image 323 is rotated to the right with respect to the receiving aperture. It can further be observed that the height of the apodization function 312 is higher than the apodization functions 311 313, and the heights of the apodization functions 311 313 are the same. The apodization functions for the majority of the
30 remaining points in each of the low-resolution images 321 322 323 may be similar to the apodization function of the centre point, thus the low-resolution

image 321 is angled to the left, the low-resolution image 322 is not angled, and the low-resolution image 323 is angled to the right. As the heights of the apodization functions used to beamform the low-resolution image 322 are higher than the heights of the apodization functions used to beamform the
5 low-resolution images 321 323, the low-resolution image 322 generally comprises larger values (possibly positive and negative) compared to the low-resolution images 321 322. Correspondingly as the heights of the apodization functions used to beamform the low-resolution images 321 323 are the same, the low-resolution images 321 323 generally comprise values
10 of equal size.

The acquisition using a defocused transmission is repeated with another center of emission 304. The wave propagates in the whole region of interest. The back scattered signal is recorded using a receive aperture 307.
15 Recorded channel data are used to generate three low-resolution images 324 325 335 using delay-and-sum beamforming. The delays and apodization functions vary from image point to image point in the images. Shown are three apodization functions 314 315 316 used to beamform the centre image point 332, 333 334 of the three low-resolution images 324 325 335,
20 respectively. The apodization function 314 has a centre of mass in the left part of the receiving aperture, and as a result the point spread function for the centre point 332 in the low-resolution image 324 is rotated to the left with respect to the receiving aperture. The apodization function 315 has a centre of mass in the centre of the receiving aperture. Consequently the point
25 spread function for the centre point 333 in the low-resolution image 325 is not rotated with respect to the receiving aperture. The apodization function 316 has a centre of mass in the right part of the receiving aperture. As a result the point spread function for the centre point 334 in the low-resolution image 335 is rotated to the right with respect to the receiving aperture. It can further be
30 observed that the height of the apodization function 316 is higher than the apodization functions 314 315, and the height of the apodization function 315

is higher than the height of the apodization function 314. The apodization functions for the majority of the remaining points in each of the low-resolution images 324 325 335 may be similar to the apodization function of the centre point. Thus the low-resolution image 324 is angled to the left, the low-resolution image 325 is not angled and the low-resolution image 335 is angled to the right. As the height of the apodization functions used to beamform the low-resolution image 335 are higher than the height of the apodization functions used to beamform the low-resolution images 325 324, the low-resolution image 335 generally comprises larger values (possibly positive and negative) compared to the low-resolution images 324 325. Correspondingly as the height of the apodization functions used to beamform the low-resolution image 325 are higher than the height of the apodization functions used to beamform the low-resolution image 324, the low-resolution image 325 generally comprises larger (possibly positive and negative) values compared to the low-resolution images 324.

The low-resolution images 318 321 324 angled to the left by the used apodization functions, e.g. apodization functions 308 311 314, are summed 336 into high-resolution image 339 correspondingly angled to the left. The heights of the apodization functions used to beamform the low-resolution image 318 are generally higher than the heights of the apodization functions used to beamform the low-resolution images 321 324. The low-resolution image 318 therefore generally comprises larger values (possibly positive and negative) compared to the low-resolution images 321 324. Correspondingly, the heights of the apodization functions used to beamform the low-resolution image 321 are generally higher than the heights of the apodization functions used to beamform the low-resolution image 324. The low-resolution image 321 therefore generally comprises larger values (possibly positive and negative) compared to the low-resolution image 324. As a result, the high-resolution image 339 is more influenced by the low-resolution images beamformed from emissions from the left part of the array. Thereby, a

transmit apodization is synthesized, further rotating the point spread functions of the image points in the high-resolution image 339 to the left.

The low-resolution images 319 322 325 not angled by the used apodization functions, e.g. apodization functions 309 312 315, are summed 337 into high-resolution image 340 correspondingly not angled. The heights of the apodization functions used to beamform the low-resolution image 322 are generally higher than the heights of the apodization functions used to beamform the low-resolution images 319 325. The low-resolution image 322 therefore generally comprises larger values (possibly positive and negative) compared to the low-resolution images 319 325. As a result, the high-resolution image 340 is more influenced by the low-resolution images beamformed from emissions from the centre part of the array. Thereby a transmit apodization is synthesized not rotating the point spread functions of the image points in the high-resolution image 340.

The low-resolution images 320 323 335 angled to the right by the used apodization functions, e.g. apodization functions 310 313 316, are summed 338 into high-resolution image 341 correspondingly angled to the right. The height of the apodization functions used to beamform the low-resolution image 335 are generally higher than the height of the apodization functions used to beamform the low-resolution images 320 323. The low-resolution image 335 therefore generally comprises larger values (possibly positive and negative) compared to the low-resolution images 320 323. Correspondingly, the heights of the apodization functions used to beamform the low-resolution image 323 are generally higher than the heights of the apodization functions used to beamform the low-resolution image 320. The low-resolution image 323 therefore generally comprises larger values (possibly positive and negative) compared to the low-resolution image 320. As a result the high-resolution image 341 is more influenced by the low-resolution images beamformed from emissions from the right part of the array. Thereby a

transmit apodization is synthesized, further rotating the point spread functions of the image points in the high-resolution image 341 to the right.

The envelope of each image lines of the high-resolution image angled to the left 339 is computed 342 to produce an envelope image correspondingly angled to the left, the envelope of each image lines of the high-resolution image not angled 340 being computed 343 to produce an envelope image correspondingly not angled, and the envelope of each image lines of the high-resolution image angled to the right 341 being computed 344 to produce an envelope image 344 correspondingly angled to right. By processing 345 the envelope images at the output of 342 343 344, e.g. summing them, multiplying them by each other, or performing other linear or nonlinear operations, a compounded high-resolution image 346 is created having a high resolution in all image points and being suppressed for speckle. It should be understood that more or less all ultrasound emissions may be used, e.g. at least 2, 4, 5, 8, 16, 32, 64, 128, or 192 ultrasound emissions and/or more or less low-resolution images, e.g. at least 2, 4, 5, 6, 8, 10, or 20 low-resolution images.

Figure 5 shows how an apodization value used to weight the output of a particular receive transducer element 507 when beamforming a particular image point 502 in a particular low-resolution image may be generated according to an embodiment of the present invention. Shown is a transducer array 501 comprising a plurality of transducer elements. First, a first line 503 is generated orthogonal to a line having predetermined angle θ relative to the ultrasound transducer, wherein the angle θ is related to a desired angling of the point spread function of the particular low-resolution image. The first line 503 is positioned so that it intersects the particular image point 502. On the first line 503 is placed a first apodization window 504, in this example a Hanning window; however, other window functions may be used, e.g. a boxcar or Hamming etc. The first apodization window 504 is centred around

the particular image point 502. To calculate a first part of the apodization value 505 for a particular receive transducer element 507, which data are used for beamforming, the particular image point 502 of the particular low-resolution image, the first apodization window 504 is projected onto the
5 centre of emission 508 for the particular emission used to generate the particular low-resolution image. This is done by generating a second line 509 which is orthogonal to the first line 503 and intersecting the centre of emission 508. The first part of the apodization value 505 is given as the value of the first apodization window 504 at which the second line 509 and the first
10 apodization window 504 intersect.

Similarly, a second part of the apodization value 506 for the particular transducer element 507, which recorded data are used to beamform the particular image point 502 in the particular low-resolution image, is computed
15 by placing a second apodization window 511 centered at the particular image point 502 on the first line 503. The second apodization window 511 is, in this embodiment, equal to the first apodization window 504; however, in other embodiments they may differ. To calculate the second part of the apodization value for a particular receive transducer element 507, which data are used
20 for beamforming the particular image point 502 of the particular low-resolution image, the second apodization window 511 is projected onto the particular receive transducer element 507. This is done by generating a third line 510 which is orthogonal to the first line 503, wherein the third line intersects the particular receive transducer element 507. The second part of
25 the apodization value 506 is given as the value of the second apodization window 511 at which the third line 510 and the second apodization window 511 intersect. The final apodization value is given by multiplying the first part of the apodization value 505 by the second part of the apodization value 506. By repeating the above steps for all transducer elements, which recorded
30 data are used to beamform the particular image point 502 in the particular low-resolution image, an apodization function 512 for beamforming the

particular image point 502 in the particular low-resolution image may be generated. By repeating the above steps for all image points in a particular low-resolution image, a set of apodization functions configured to rotate the resulting point spread function for each image point in the particular low-resolution images with an angle may be generated.

Fig 6a-d show examples of apodization functions for image points generated using the method described in relation to Fig. 5.

Fig. 6a shows the resulting apodization function 601 for image point 602 in a particular low-resolution image when it is desired to rotate the resulting point spread function to the left. The transducer element 605 shows the centre of emission for the ultrasound emission used to generate the particular low-resolution image. The resulting apodization function 601 is generated by projecting the apodization window 604 onto the transducer elements used to beamform the image point 602 and scaling the projected preliminary apodization function with the value 606 corresponding to the value of the apodization window 604 projected onto the centre of emission 605 for the ultrasound emission used to generate the particular low-resolution image.

Fig. 6b shows the resulting apodization function 601 for image point 602 in a particular low-resolution image when it is desired to rotate the resulting point spread function to the left. The transducer element 605 shows the centre of emission for the ultrasound emission used to generate the particular low-resolution image. The resulting apodization function 601 is generated by projecting the apodization window 604 onto the transducer elements used to beamform the image point 602 and scaling the projected apodization window with the value 606 corresponding to the value of the apodization window 604 projected onto the centre of emission 605 for the ultrasound emission used to generate the particular low-resolution image.

Fig. 6c shows the resulting apodization function 601 for image point 602 in a particular low-resolution image when it is desired to rotate the resulting point spread function to the right. The transducer element 605 shows the centre of emission for the ultrasound emission used to generate the particular low-resolution image. The resulting apodization function 601 is generated by projecting the apodization window 604 onto the transducer elements used to beamform the image point 602 and scaling the projected apodization window with the value 606 corresponding to the value of the apodization window 604 projected onto the centre of emission 605 for the ultrasound emission used to generate the particular low-resolution image.

Fig. 6d shows the resulting apodization function 601 for image point 602 in a particular low-resolution image when it is desired to rotate the resulting point spread function to the right. The transducer element 605 shows the centre of emission for the ultrasound emission used to generate the particular low-resolution image. The resulting apodization function 601 is generated by projecting the apodization window 604 onto the transducer elements used to beamform the image point 602 and scaling the projected preliminary apodization function with the value 606 corresponding to the value of the preliminary apodization window 604 projected onto the centre of emission 605 for the ultrasound emission used to generate the particular low-resolution image.

Fig. 4 shows a method of producing a combined compounded high-resolution image according to an embodiment of the present invention. A number of sequential emissions (N_e) 401-407 are used to process a single combined compounded high-resolution image 458. In this embodiment, N_e is 7, but it may be higher or lower. Each of the N_e emissions may be a focused emission, an unfocused emission, a plane wave emission, a defocused emission, or a spherical wave emission from a single element. The transmit apertures 401-407 indicate the origins of the different emissions. N_e different

origins are used for the Ne emissions and these Ne origins may be distributed equally over the entire transducer.

For each emission, the ultrasound transducers comprising a plurality of
5 transducer elements are used to record a set of RF channel data from all transducer elements as in this embodiment or from a subset of the plurality of transducer elements if the number of receiving channels in the ultrasound system is limited to a number less than the number of transducer elements.

10 For the emission 401, a set of RF signals is recorded by the plurality of transducer elements making up the receiving aperture 408. These data are used for beamforming a number of low-resolution images 415, 425, 435, by for each point in the resolution image delaying, apodizing, and summing RF signals recorded by the plurality of transducer elements making up the
15 receiving aperture 408. The number of low-resolution images being beamformed for each emission is 3 in this embodiment, but it may be higher (or lower) for a larger suppression of speckle thus improving contrast.

Beamforming of low-resolution images can be done directly on the RF
20 signals recorded by the plurality of transducer elements making up the receiving aperture 408. Beamforming can also be done on the complex analytical counterpart of the RF signals which has both in-phase and quadrature components. The RF data signals are shifted in phase yielding phase-shifted data signals, where the data signals and the phase-shifted
25 data signals are combined into complex data signals where the data signals constitute the real part and the phase-shifted data signals constitute the imaginary part. Finding the imaginary part of the complex analytical counterpart of the RF signals can be done by computing the Hilbert Transform of the RF signals. When the process of beamforming uses
30 complex signals, the result is complex low-resolution images and complex high-resolution images from which envelope detection is computed.

Every low-resolution image consists of a number of points. If beamforming is based on RF signals as input signals, the points may be placed in lines making up image lines and, where the distance between image lines and the distance between points in an image line are determined by the Nyquist sampling criterion for the RF signals. Working with complex in-phase and quadrature data makes it possible to beamform only those points in which the envelope detected value is needed. As the bandwidth of the detected signal may be lower than the bandwidth of the RF signals, the points making up the low-resolution images may be placed in a less dense grid than when working with RF signals in the beamformer. In the embodiment described, beamforming is done on complex data and every low-resolution image beamformed from every emission comprises beamformed samples at identical spatial positions. However, beamforming may also be done directly on RF signals.

Each of the low-resolution images 415, 425, 435 is beamformed using the same set of delay profiles. A set of delay profiles comprises a delay profile for each point in the low-resolution image. A delay profile comprises a set of delay values, one delay value for each of the plurality of transducer elements making up the receiving aperture 408. A delay value for a given receiving element corresponds to an estimated total time of flight for the ultrasound signal transmitted from the transmit aperture origin 401 to the spatial point corresponding to a given point in the low-resolution image and back to the given receiving element. The time of flight may be estimated by estimating the distance the ultrasound signal must travel and dividing that estimated distance by an estimated average speed of sound in the physical medium. This beamforming process of the embodiment may be characterized as time domain delay and sum beamforming. Other beamforming techniques can be utilized here as a replacement of time domain delay and sum beamforming,

such as frequency domain delay and sum beamforming, or adaptive beamforming algorithms.

The low-resolution images 415, 425, 435 are beamformed using different
5 sets of apodization functions emulating different steering directions. Each set of apodization functions may comprise a plurality of apodization functions, and in one embodiment there is one apodization function for each point in the low-resolution image, and wherein each apodization function comprises a plurality of apodization values and, in one embodiment, one value for each of
10 the plurality of transducer elements making up the receiving aperture 408. An apodization value is a value used to weight an RF signal when beamforming a given point in a given low-resolution image for a given steering direction; thus, an apodization value for an RF signal recorded by a specific transducer element may be dependent on the specific low-resolution image being
15 beamformed and the index of the image point in the specific low-resolution image being beamformed. An apodization value may comprise a first part determined by the centre of emission for the ultrasound emission and a desired angling of the point spread function, and a second part determined by the position of the receiving transducer element and the desired angling of
20 the point spread function. The apodization value may effectively be the product of the two parts.

The principle of computation of the apodization value is illustrated in figure 5. The steps of beamforming a low-resolution image thus comprise for each
25 point in the low-resolution image delaying, apodizing, and summing RF signals recorded by the plurality of transducer elements.

The beamformed low-resolution images 415, 425, 435 are stored in a number of buffers, the number being equal to the number of steering angles
30 or a number being equal to the total number of low-resolution images that are created in the process of creating a combined compounded high-resolution

image 458, or a number in between. If the number of buffers is equal to the number of steering angles, each buffer serves as a storage for accumulated low-resolution images from a given steering angle. If the number of buffers is larger, it yields a more flexible system, but requires a larger memory for data storage.

For the emission 402, a set of RF signals is recorded by the plurality of transducer elements making up the receiving aperture 409. These data are used for beamforming a number of low-resolution images 416, 426, 436, and it comprises, for each point in the low-resolution image, delaying, apodizing, and summing RF signals recorded by the plurality of transducer elements making up the receiving aperture 409.

The beamformed low-resolution images 416, 426, 436 from the emission 402 are beamformed using different sets of apodization functions emulating different steering directions and are stored in buffers.

For the emission 403 a set of RF signals is recorded by the plurality of transducer elements making up the receiving aperture 410. These data are used for beamforming a number of low-resolution images 417, 427, 437 by for each point in the low-resolution image, delaying, apodizing, and summing RF signals recorded by the plurality of transducer elements making up the receiving aperture 410.

The beamformed low-resolution images 417, 427, 437 from the emission 403 are beamformed using different sets of apodization functions emulating different steering directions and are stored in buffers.

The low-resolution images 415, 416, 417 comprise beamformed image points with the same spatial positions. They are beamformed with a first steering direction using RF data acquired from 3 different emission with 3 different

transmit apertures 401, 402, 403 having 3 different positions of the transmit origins. Coherently adding the complex in-phase and quadrature low-resolution images 415, 416, 417 in the adder 422 yields a high-resolution image with a first steering direction and with a synthesized transmit aperture
5 that is larger than the individual transmit apertures 401, 402, 403 thus yielding an improved resolution. Adding the low-resolution images 415, 416, 417 in the adder 422 may comprise a weighting of the low-resolution images 415, 416, 417 before they are added in 422.

10 Similarly the low-resolution images 425, 426, 427 comprise beamformed image points with the same spatial positions, and further with the same spatial positions as the low-resolution images 415, 416, 417. The low-resolution images 425, 426, 427 are beamformed with a second steering direction using RF data acquired from 3 different emission with 3 different
15 transmit apertures 401, 402, 403 having 3 different positions of the transmit origins. Coherently adding the complex in-phase and quadrature low-resolution images 425, 426, 427 in the adder 432 yields a high-resolution image with a second steering direction and with a synthesized transmit aperture that is larger than the individual transmit apertures 401, 402, 403
20 thus yielding an improved resolution. Adding the low-resolution images 425, 426, 427 in the adder 432 may comprise a weighting of the low-resolution images 425, 426, 427 before they are added in 432.

Similarly the low-resolution images 435, 436, 437 comprise beamformed
25 image points with the same spatial positions and further with the same spatial positions as the low-resolution images 415, 416, 417, 425, 426, 427. The low-resolution images 435, 436, 437 are beamformed with a third steering direction using RF data acquired from 3 different emission with 3 different transmit apertures 401, 402, 403 having 3 different positions of the transmit
30 origins. Coherently adding the complex in-phase and quadrature low-resolution images 435, 436, 437 in the adder 442 yields a high-resolution

image with a third steering direction and with a synthesized transmit aperture that is larger than the individual transmit apertures 401, 402, 403 thus yielding an improved resolution. Adding the low-resolution images 435, 436, 437 in the adder 442 may comprise a weighting of the low-resolution images
5 435, 436, 437 before they are added in 442.

The number of low-resolution images being added in the adders 422, 432, 442 is 3 in this embodiment. This number may be higher for an extended synthesized aperture yielding an improved resolution. The number is
10 determined by the desired contrast/resolution ratio and may depend on whether the image medium is stationary or moving. For an image medium that moves, it may be desirable to keep this number low to ensure a coherent summation.

15 Consider a high-resolution image with a given steering direction comprising a grid of beamformed points created from beamforming low-resolution images using complex in-phase and quadrature RF signals and finally adding low-resolution images. The delay and apodization functions applied in the beamforming process are configured such that the point spread function at a
20 given point in the high-resolution image corresponds to the point spread function at the same spatial position of an image constructed by having steered and focused emissions and steered beams beamformed in the direction of the said steering direction.

25 The complex in-phase and quadrature high-resolution images at the output of the adders 422, 432, 442 are envelope detected in 445, 446, 447. The detection is computed as the magnitude of the complex image.

The envelope detected high-resolution images at the output of the envelope
30 detectors 445, 446, 447 comprises beamformed image points with the same spatial positions, but with a first, a second, and a third steering direction. The

envelope detected high-resolution images are processed together, e.g. by adding these images and creating a compounded high-resolution image comprising, for each image point, e.g. an addition of image points constructed as if they were observed from a first, and a second, and a third
5 observation angle suppressing the speckle and improving the contrast of the compounded high-resolution image.

The above process of constructing a first compounded high-resolution image based on the emissions 401, 402, 403 is repeated for the emissions 403,
10 404, 405 constructing the second compounded high-resolution image, and is repeated for the emissions 405, 406, 407 constructing the third compounded high-resolution image. In this embodiment emission 403 is used for constructing both the first and the second compounded high-resolution image, and emission 405 is used for constructing both the second and the
15 third compounded high-resolution image; however, in other embodiments there may be no overlap between the emissions used to create the different compounded high-resolution images, e.g. emissions 401 402 403 may be used to create a first compounded high-resolution image, and emissions 404 405 406 may be used to create a second compounded high-resolution
20 image, or there may be an increased overlap, e.g. emissions 401 402 403 may be used to create a first compounded high-resolution image and emission 402 403 404 may be used to create a second compounded high-resolution image.

25 The final combined compounded high-resolution image 458 is constructed by processing the compounded high-resolution images, e.g. by adding them. The compounded high-resolution image may be weighted before they are processed, e.g. they may be weighted before they are added.

30 Although some embodiments have been described and shown in detail, the invention is not restricted to them, but may also be embodied in other ways

within the scope of the subject matter defined in the following claims. In particular, it is to be understood that other embodiments may be utilised and structural and functional modifications may be made without departing from the scope of the present invention.

5

In device claims enumerating several means, several of these means can be embodied by one and the same item of hardware. The mere fact that certain measures are recited in mutually different dependent claims or described in different embodiments does not indicate that a combination of these
10 measures cannot be used to advantage.

It should be emphasized that the term "comprises/comprising" when used in this specification is taken to specify the presence of stated features, integers, steps or components but does not preclude the presence or addition of one
15 or more other features, integers, steps, components or groups thereof.

Claims:

1. A method for producing compounded ultrasound images by beamforming a first and a second low-resolution image using data from a first ultrasound emission, beamforming a third and a fourth low-resolution image using data from a second ultrasound emission, summing said first and said third low-resolution image creating a first high-resolution image and said second and said fourth low-resolution image creating a second high-resolution image, wherein the method further comprises computing a first envelope image for said first high-resolution image and a second envelope image for said second high-resolution image, and processing said first envelope image and said second envelope image creating in a first compounded high-resolution image.
2. A method according to any of the above claims, where the method comprises transmitting a first ultrasound signal into a physical medium using an ultrasound transducer, receiving a first data signal using said ultrasound transducer said first data signal being indicative of the acoustic properties of said physical medium, creating a first low-resolution image by beamforming data comprising said first data signal using a first set of apodization functions, creating a second low-resolution image by beamforming data comprising said first data signal using a second set of apodization functions.
3. A method according to any of the above claims, where the method comprises transmitting a second ultrasound signal into a physical medium using said ultrasound transducer, receiving a second data signal using said ultrasound transducer said second data signal being indicative of the acoustic properties of said physical medium, creating a third low-resolution image by beamforming data comprising said second data signal using a third set of apodization functions, creating a fourth low-resolution image by

beamforming data comprising said second data signal using a fourth set of apodization functions.

4. A method according to any of the above claims, where the method
5 comprises summing said first and said third low-resolution image creating a first high-resolution image and said second and said fourth low-resolution image creating a second high-resolution image and wherein the method further comprises computing a first envelope image for said first high-resolution image and a second envelope image for said second high-resolution image, and processing said first envelope image and said second
10 envelope image resulting in a first compounded high-resolution image.
5. A method according to any of the above claims, where the ultrasound transducer comprises a plurality of transducer elements, and wherein the first
15 and the second data signal comprise a plurality of RF signals recorded by a subset of said plurality of transducer elements, and where the step of beamforming a low-resolution image comprises, for each point in the low-resolution image, delaying, apodizing, and summing RF signals recorded by said subset of said plurality of transducer elements.
20
6. A method according to any of the above claims, where a set of apodization functions is configured to rotate the resulting point spread function for each image point in a low-resolution image with a predetermined angle so that low-resolution images having point spread functions rotated with different angles
25 may be created.
7. A method according to any of the above claims, where , the method further comprises creating a second compounded high-resolution image by combining low-resolution images beamformed using data from at least two
30 ultrasound emissions into at least two high-resolution images, computing at least two envelope images from said at least two high-resolution images and

processing said at least two envelope images creating a second compounded high-resolution image, wherein the method further comprises: processing said first and said second compounded high-resolution image creating a combined compounded high-resolution image.

5

8. A method according to any of the above claims, where the method further comprises the step of: providing a user with means to select a contrast/resolution ratio, wherein a compounded image with the selected contrast/resolution ratio is generated.

10

9. A method according to any of the above claims, where for a transmission at least a part of the received data signal is shifted in phase, yielding a phase-shifted data signal, where the data signal and the phase-shifted data signal is combined into a complex data signal where the data signal

15 constitutes the real part and the phase-shifted data signal constitutes the imaginary part, resulting in complex low-resolution images and complex high-resolution images, and wherein an envelope image for a high-resolution image is computed by for an image point calculating:

$$E_n(x, y) = \sqrt{I_n(x, y)^2 + R_n(x, y)^2}$$

20 where $E_n(x, y)$ is the value of the n'th envelope image at image point index x,y, $I_n(x, y)$ is the imaginary part of the n'th complex high-resolution image at image point index x,y, and $R_n(x, y)$ is the real part of the n'th complex high-resolution image at image point index x,y.

25 10. An ultrasound system configured to produce compounded ultrasound images by beamforming a first and a second low-resolution image using data from a first ultrasound emission, beamforming a third and a fourth low-resolution image using data from a second ultrasound emission, summing said first and said third low-resolution image creating a first high-resolution
30 image and said second and said fourth low-resolution image creating a

second high-resolution image, wherein the ultrasound system further is configured to compute a first envelope image for said first high-resolution image and a second envelope image for said second high-resolution image, and process said first envelope image and said second envelope image
5 creating in a first compounded high-resolution image.

| _____

1/5

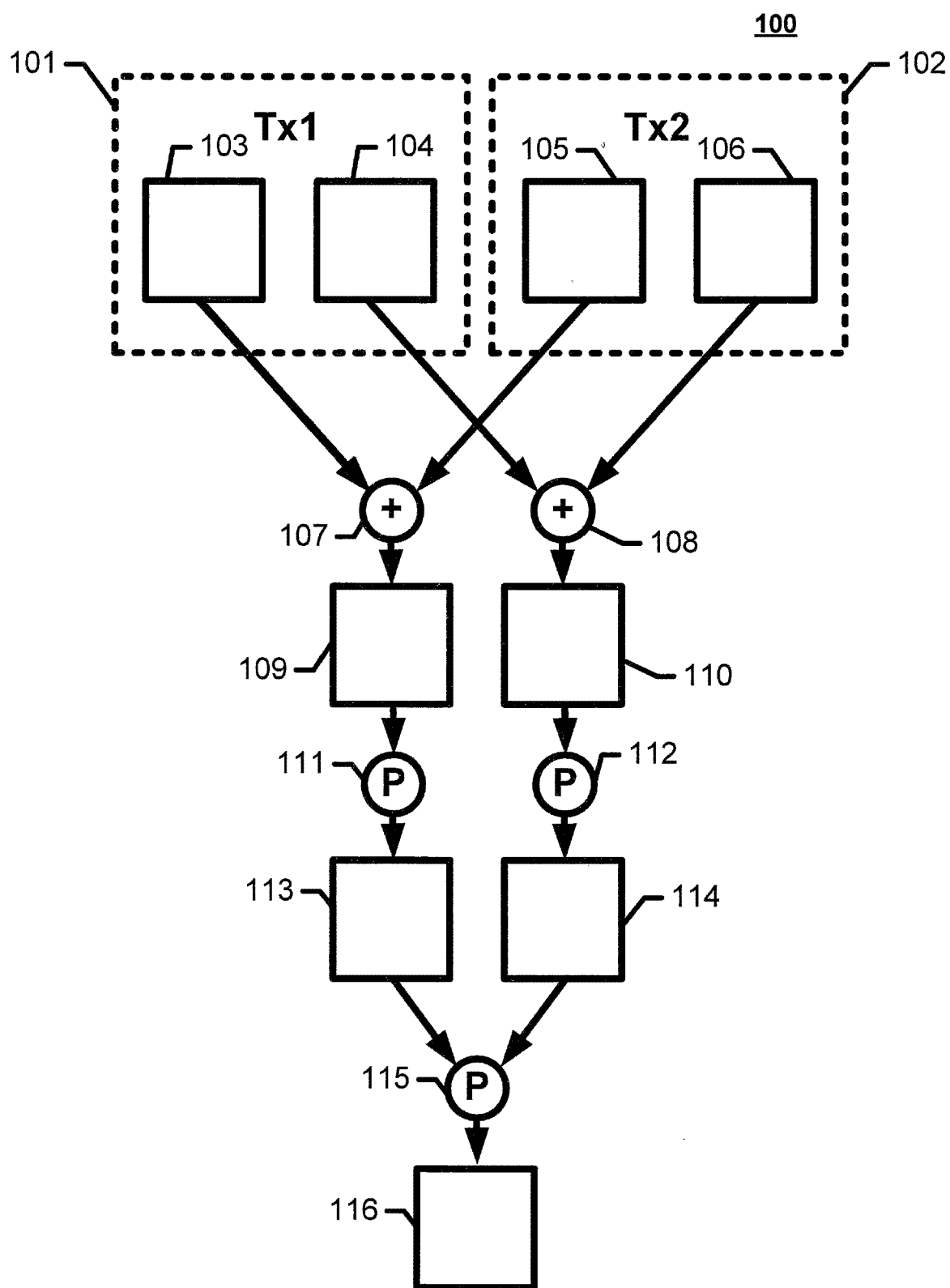


Fig.1

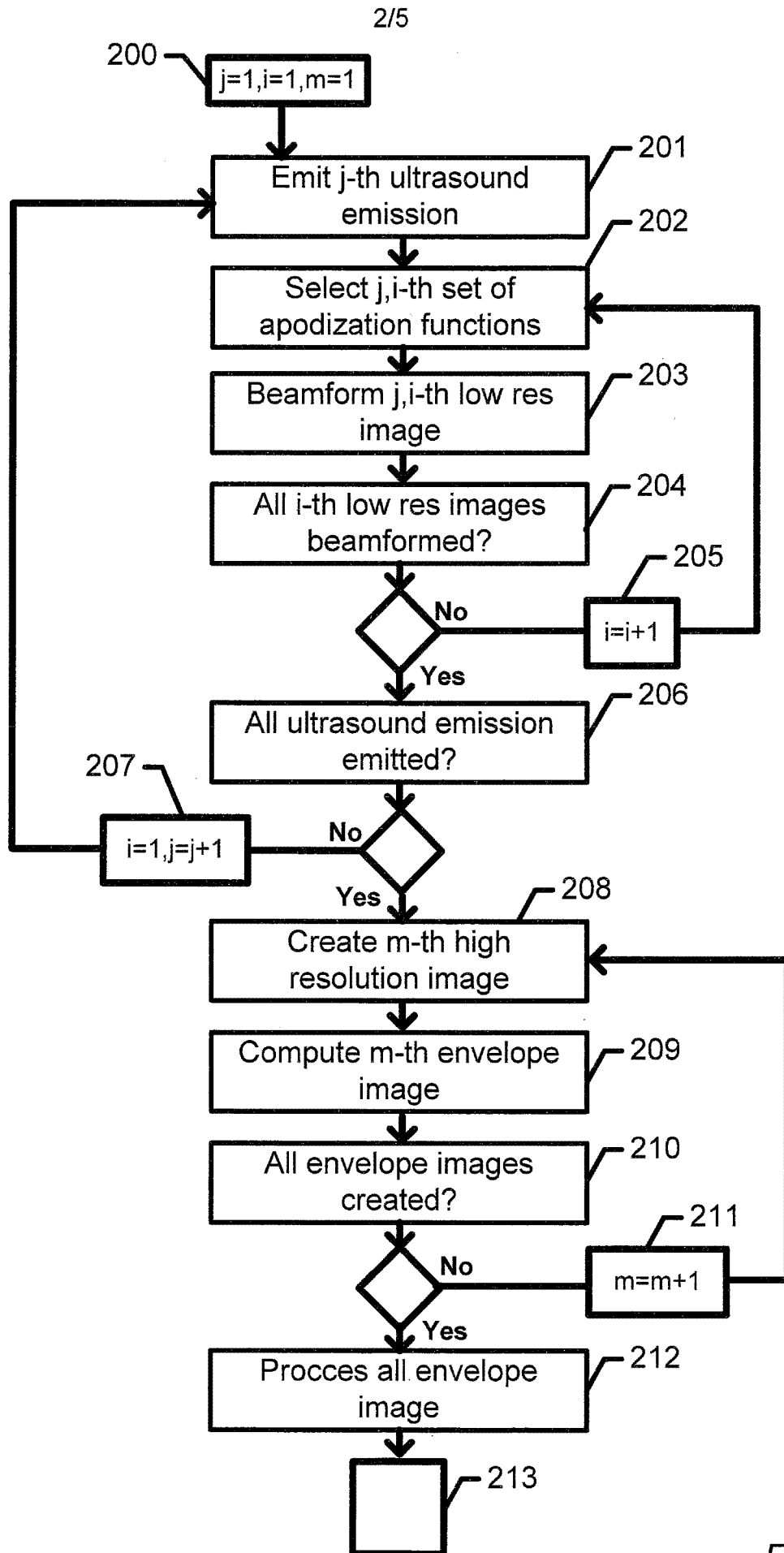


Fig.2

3/5

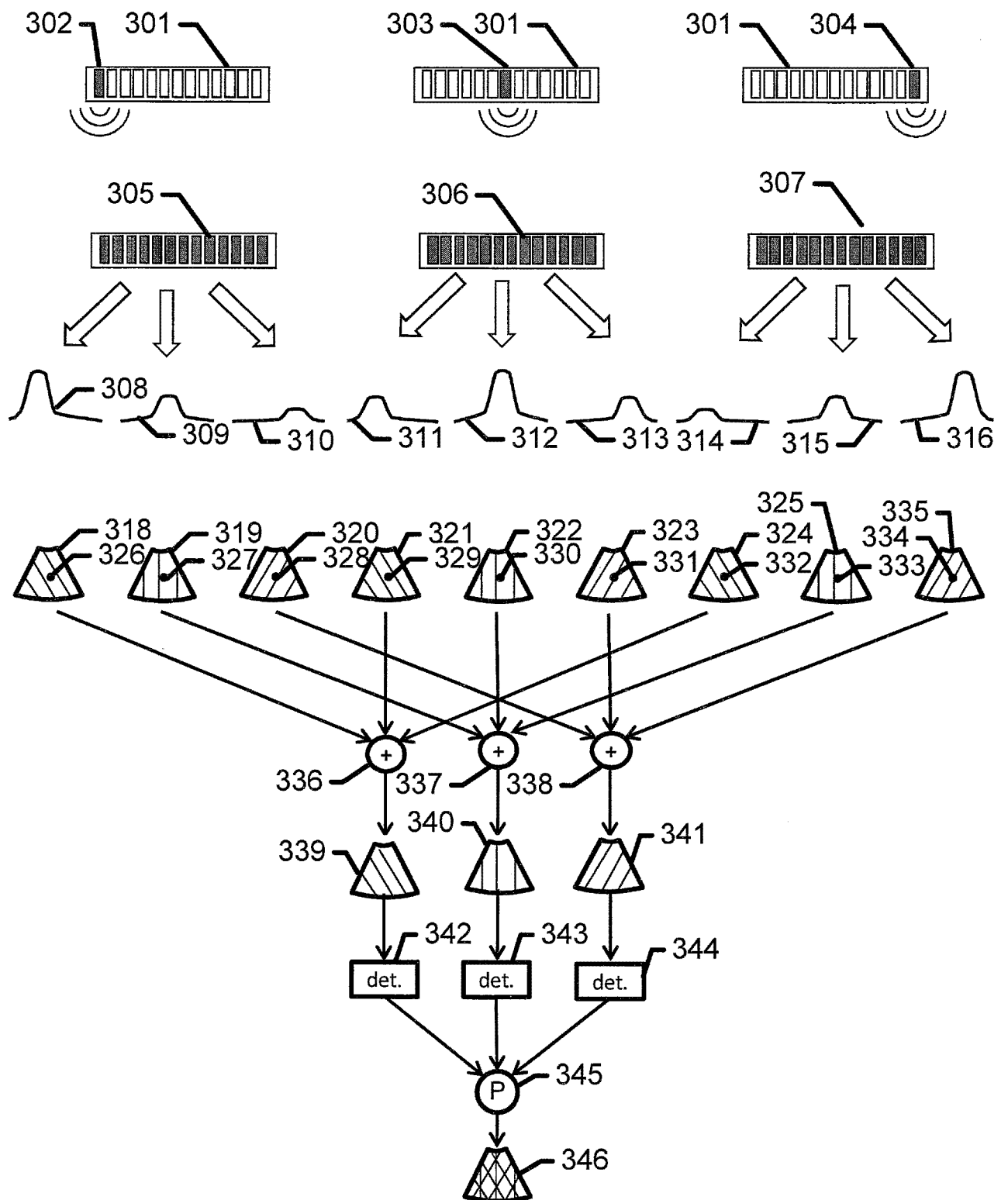


Fig.3

4/5

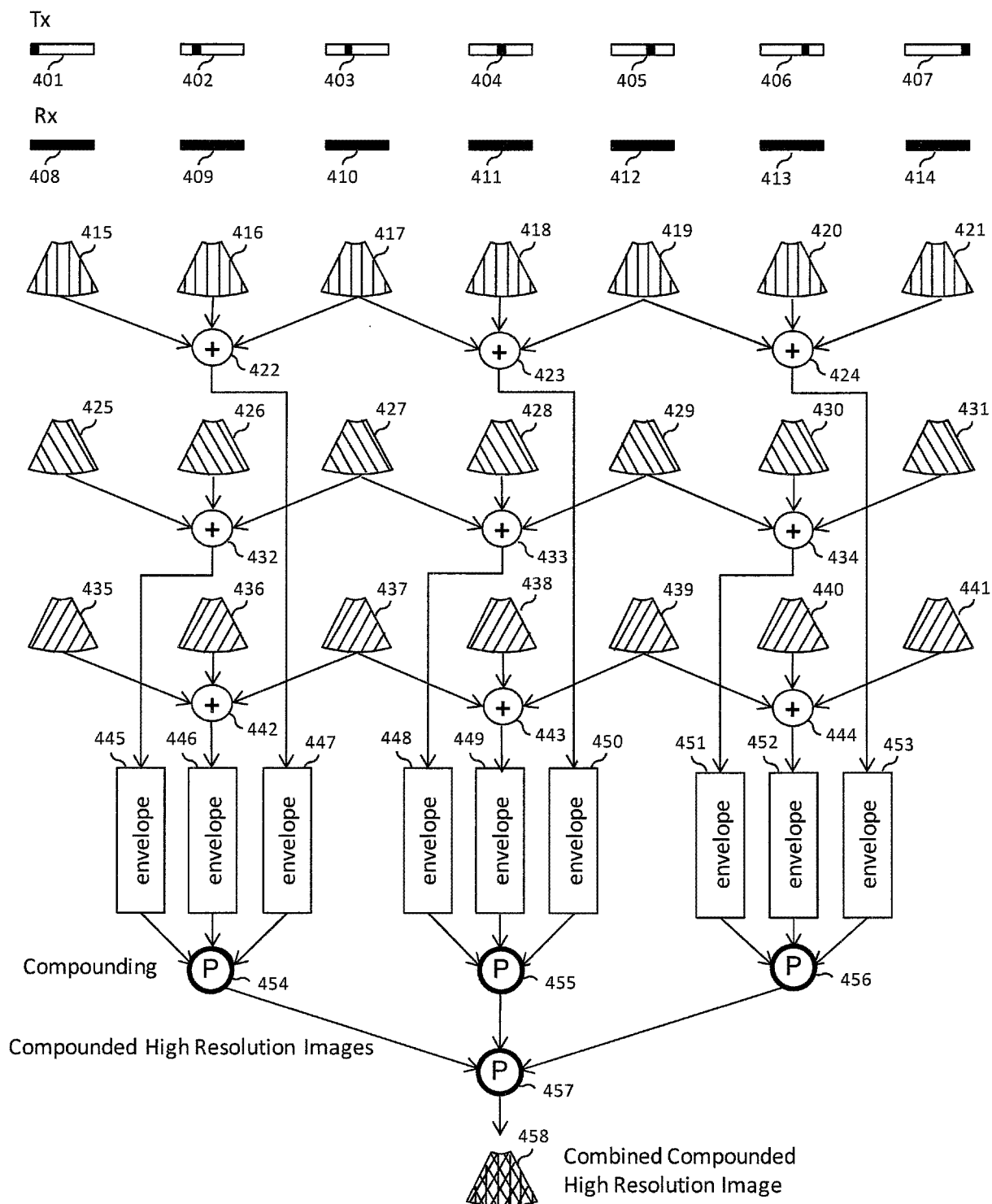


Fig.4

5/5

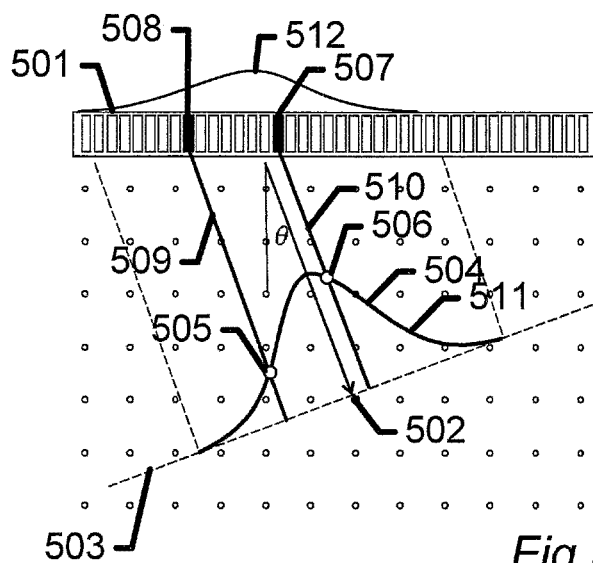


Fig. 5

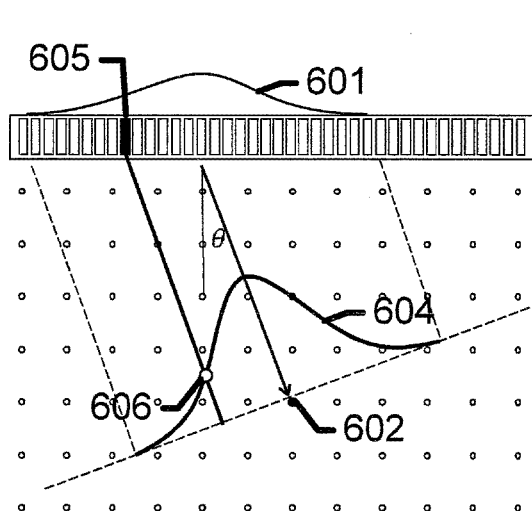


Fig. 6a

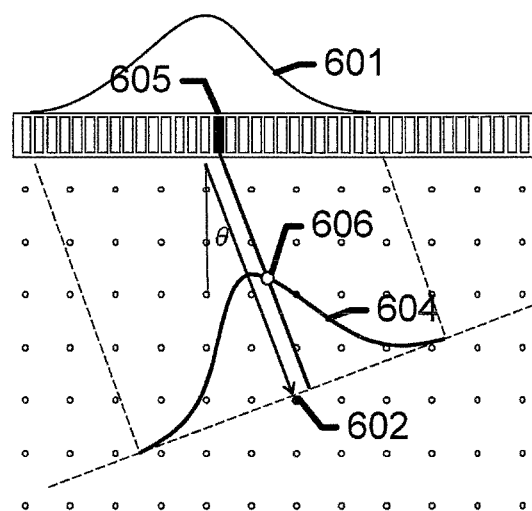


Fig. 6b

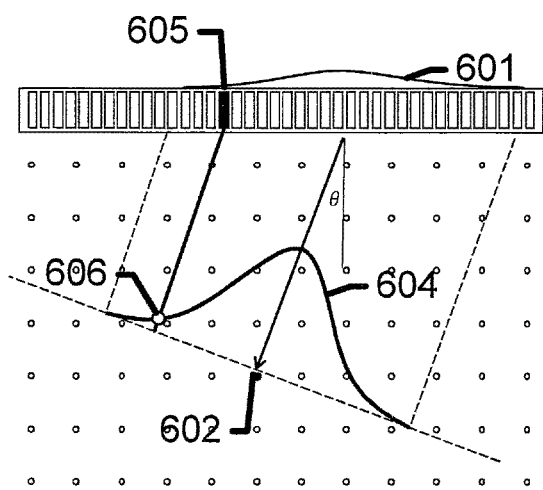


Fig. 6c

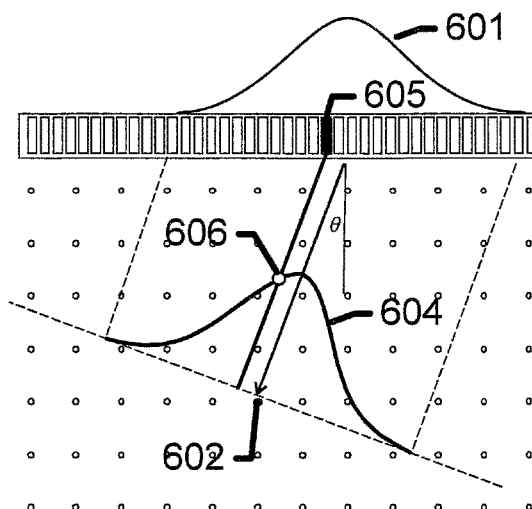


Fig. 6d

A.4 Performance of Synthetic Aperture Compounding for *in-vivo* Imaging

- **J. M. Hansen** and J. A. Jensen: Performance of Synthetic Aperture Compounding for *in-vivo* Imaging. Proceedings of the IEEE Ultrasonics Symposium, October, 2011.

Performance of Synthetic Aperture Compounding for *in-vivo* imaging

Jens Munk Hansen and Jørgen Arendt Jensen

Center for Fast Ultrasound Imaging, Dept. of Elec. Eng. Bldg. 349,
Technical University of Denmark, DK-2800 Kgs. Lyngby, Denmark

Abstract—A method for synthetic aperture compounding (SAC) is applied to data from water tank measurements, data from a tissue-mimicking phantom, and clinical data from the abdomen of a healthy 27 year old male. Further, using this method compounding can be obtained without any loss in temporal resolution. The water tank measurements reveal an improved detail resolution of 45% when comparing SAC to conventional compounding and an improvement of 22%, when comparing to synthetic aperture (SA) imaging. The cystic resolution at 12 dB is improved by 50% and 12% when comparing SAC to conventional compounding and SA imaging respectively. The tissue phantom measurements show a 3.2 dB improvement of the normalized information density (NID) when comparing images formed using SAC to conventional compound images and an improvement of 2 dB for a comparison between SAC imaging and SA imaging. For the clinical images, contrast ratios (CR) are computed between regions in the portal and hepatic veins and the surrounding tissue. An average improvement of 15% is obtained when comparing SAC images to SA images without compounding.

I. INTRODUCTION

Medical ultrasound imaging is used for many purposes, e.g. for localizing and classifying cysts, lesions, and other processes. Almost any mass is first observed using B-mode imaging and later classified using e.g. color flow, strain, or biopsies. It is therefore important that the B-mode images have high contrast. Like all imaging modalities, ultrasound is subject to a number of inherent artifacts that compromise image quality. The most prominent artifact is the degradation by coherent wave interference, known as 'speckle', which gives a granular appearance to an otherwise homogeneous region of parenchyma [1], [2]. The speckle reduces image contrast and diminishes the possibilities for detection of low-contrast regions.

A successful approach to remedy the speckle artifacts is spatial compounding, where images are acquired from a number of directions and combined after envelope-detection [3], [4]. Today, spatial compounding is implemented in all state of the art, high-end ultrasound systems and available when using a low pitch transducer with a fairly high number of independent channels. A drawback of conventional compounding is either a reduction of the frame rate or a reduction of the true temporal resolution. This paper investigates an approach based on synthetic aperture imaging, where compounding can be obtained without any loss in temporal resolution.

The organization of this paper is as follows: First, some performance measures for ultrasound imaging systems are defined. Next, spatial compounding is described as used

for images formed using dynamic receive focusing (DRF), which we will refer to as DRFC. After a brief introduction to synthetic aperture (SA) imaging, the synthetic aperture compounding (SAC) is described in full detail. In the results section, performance measures are extracted from water tank and phantom measurements and using a similar setup, the first clinical image obtained using SAC is presented. Finally, a discussion of the results and possibilities for improvements.

II. PERFORMANCE MEASURES

Development of new ultrasound imaging methods includes several quality and performance assessment stages. To assess the image quality both the detail and contrast resolution are studied. They can both be measured and quantized through a combination of water tank and phantom measurements, but often extensive clinical evaluations are also carried out to ensure that the desired clinical performance is met. In this paper, the main focus will be on the following measures, which can be obtained from water tank and phantom measurements alone.

a) Detail resolution: The *detail resolution* is the separation at which identically point targets can be distinguished. It is distinguished by the main lobe width of the point-spread-function (PSF) and the 6 dB axial pulse length, i.e. the lateral and axial full width at half maximum (FWHM) of the PSF.

b) Cystic resolution: The detail resolution alone is not appropriate for comparing the imaging performance of medical ultrasound systems, since it ignores what is outside the main lobe, which have a significant impact on the image of wide dynamic range systems. Acoustic clutter from surrounding objects fill-in images of anechoic objects such as cysts, or weakly echogenic objects such as blood vessels, and reduces their detectability. The ability to detect anechoic or weakly echogenic objects in the presence of strong surrounding objects is sometimes referred to as *contrast resolution* and was first introduced as "cystic resolution" [5]. The contrast resolution can be quantized by the clutter energy to total energy ratio (CTR). The CTR is defined as the ratio of the PSF energy outside a circular region with radius R to the total PSF energy. For a large ensemble of measurements, the CTR is also a measure of the difference between the average level of a cyst's center and the background. To get a single measure, one either measures the drop in brightness for a fixed radius R or the radius of a cyst, which can be observed at a fixed level, e.g. R_{12dB} .

c) *Tissue contrast resolution*: Most commonly, contrast resolution refers to the ability to distinguish echogenicity differences between a region of interest (ROI) and the background, *tissue contrast resolution*. Tissue contrast resolution is often quantified by either contrast ratio (CR) or contrast-to-noise ratio (CNR), which are both object dependent and where latter is improved on increasing object contrast as well as by lowering the variance.

d) *Normalized information density*: The primary source of contrast resolution loss is coherent wave interference also known as *speckle*. This artifact is reflected in the signal-to-noise ratio (SNR) at a point defined as the expectation value of the magnitude of the received signal, $\mu_V = \mathbb{E}(V)$ and in units of its standard deviation, σ_V . In the literature, this is referred to as the signal-to-noise ratio at a point SNR_0 , and if the envelope-detected signals, V follow Rayleigh statistics, then for a fully developed speckle, the theoretical value of SNR_0 is 1.91 [2]. This value is increased by spatial compounding [6] and an increase is associated with improved image contrast. SNR_0 is object independent, but theoretically it can be shown that the SNR for a difference signal scales with the square root of the number of independent speckle cells [7], so somehow it would be beneficial to incorporate speckle size. Such a measure was introduced by Ustuner et. al. referred to as normalized information density (NID), which reflects the ability of a system to distinguish 1 dB brightness differences in the presence of fully-developed speckle [8]

$$\text{NID} = \frac{\text{SNR}_0^2}{2S} = \frac{(\mu_V/\sigma_V)^2}{2S}, \quad (1)$$

where S is the average speckle size, which can be obtained from the auto-covariance function of the intensity.

III. METHODS

A. Compounding

For conventional spatial compounding, a low-pitch linear or convex array is used. A subset of the elements is selected as the current active aperture, and this aperture is used as a phased array to steer the beam in a direction making an angle θ with a normal to the transducer surface. The active aperture is then moved, until scan lines originating from the entire extent of the array are recorded. This procedure is repeated for angles θ_i , $i = 1, \dots, N_\theta$, where N_θ is the number of angles to be used for compounding. Next, the N_θ sub-images are envelope-detected and added using scan-line conversion. The resulting image has a reduced speckle appearance, a lower noise floor, grating lobes (if present) are lowered, and boundaries subject to non-normal incidence are more visible, and image shadowing is confined to a smaller triangular region behind the attenuating masses or boundaries. The region where all sub-images overlap is referred to as the fully-compounded region.

A drawback of conventional compounding is either a reduction of the frame rate or a reduction of the true temporal resolution. In the case of the latter, the temporal resolution is

reduced due to images being buffered to achieve an apparent high frame rate.

B. Synthetic Aperture

A typical setup for synthesizing both the transmit and receive aperture is to acquire data by emitting a spherical wave with a subaperture and receiving with all of the elements [9]. This procedure is then repeated for all emissions and a complete data set is acquired. Using this data set, any beam and focusing can be synthesized.

For transmit focusing, delays and apodizations are calculated for each point in the image to construct signals, which at each point sum up coherently. For receive focusing, another set of delays and apodizations are applied to the signals received from the individual transducer elements and then a weighted sum is performed. In addition, the apodization can be adjusted to even out the resolution over a range of depths to maintain a constant resolution by realizing a fixed F-number using an expanding or contracting aperture for transmit and receive beamformation, respectively. A major advantage of synthetic aperture imaging is the possibility to focus everywhere in the image resulting in a better resolution. Further, this can be achieved using the same amount of time for data acquisition as for conventional imaging. The price for the resolution though, is a huge increase in RF data processing - an increase by the number of lines to beamform for each pulse emission.

C. Synthetic Aperture Compounding

To perform compounding using synthetic aperture data, apodizations are calculated for each image point corresponding to imaging the point using a focused beam centered around the point and making an angle θ with a normal to the transducer surface. In Fig. 1, it is shown for a single point, how the transmit apodization for an emission with transmit origin \vec{x}_{origin} are calculated using the distance from the transmit origin \vec{x}_{xmt} to the “scan-line”. Similarly, receive apodizations

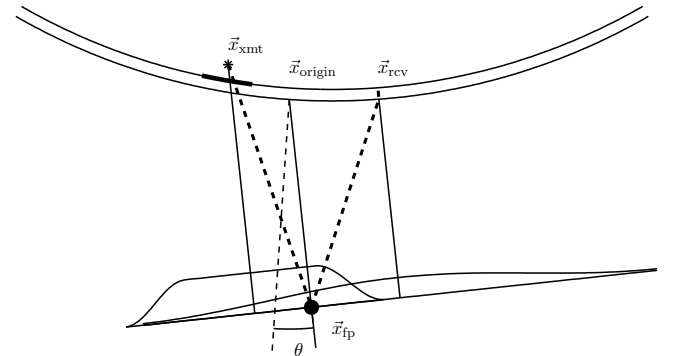


Figure 1. Wave propagation path (thick dashed line) for calculating time-of-flight for synthetic aperture focusing for an emission with origin \vec{x}_{origin} and data acquired with the element positioned at \vec{x}_{rcv} . The transmit and receive apodizations can be read-off the figure as the intersections of the scan line and the Tukey and Hamming profile respectively.

are calculated for each point and applied to the signals received

from the individual receiving elements of each transmission. The receive apodization values are likewise computed using the distance from the “scan-line” to now the position of the receiving elements. The delay calculation are identical to what is used for synthetic aperture imaging without compounding. The RF data are beamformed as in-phase and quadrature components, and the envelope computed as the absolute value. This rather complex procedure is repeated for angles θ_i , $i = 1, \dots, N_\theta$, where N_θ is the number of angles to be used for compounding. Finally, the compound image are constructed by addition or multiplication of the enveloped images. An implementation of this method uses a buffer for N_θ images and calculates the delays for each pixel only once. In this way, a compound image is ready immediately after the last emission and only the processing resources limits the number of angles used.

IV. RESULTS

To investigate the contrast and detail resolution for SAC a setup using a commercial 3 MHz, 192 element, λ pitch convex array (BK Medical) was used for water tank and tissue phantom measurements. The sampling was done using an experimental ultrasound scanning system, SARUS, capable of storing 12-bit individual channel data at 70 MHz [10]. For SA and SAC imaging, a 16 element subaperture was used for 192 unfocused emissions. For each emission, data from all 192 channels were stored. For comparison, for DRF and DRFC, a 64 element subaperture was used for 192 focused emissions for each compound angle. For each emission, data from all 192 channels were stored. For all emissions, a two-cycle sinusoid was used for excitation together with a Hamming apodization on the active subaperture. Compounding for DRF and SA data was done using 5 angles with an angular separation of 5 degrees.

For processing, a small parameter study was made to find the optimal F#’s for dynamic apodization to achieve the best R_{12dB} for wires at depths 15, 40, 65, and 90 mm.

A. Water phantom

In Table I, the detail resolution and contrast resolution (for anechoic objects) is measured for the wire at depth 65 mm, shown in Fig. 2 using the four imaging techniques. For both

Table I

	R_{12dB}	$FWHM_{lat}$	$FWHM_{ax}$ [mm]	$Area_{6dB}$ [mm ²]
DRF	1.25	1.41	0.70	3.08
DRFC	1.19	1.37	0.70	3.00
SA	0.68	1.13	0.59	2.10
SAC	0.60	0.83	0.63	1.65

the DRF and SA, compounding results in an improved lateral resolution, but only for SA this comes at the cost of a worse axial resolution. The cystic resolution, R_{12dB} is also improved.

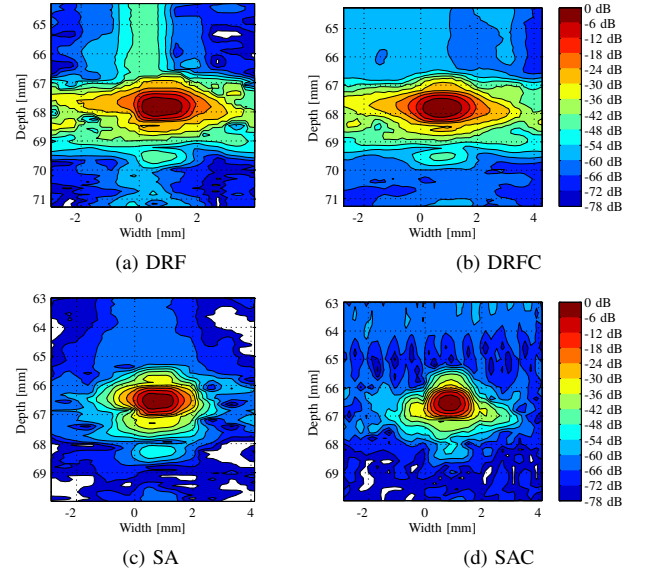


Figure 2. PSF images obtained using water tank phantom with wires.

Finally, we note that the CTR as well as the clutter ratio is much improved for both SA and SAC compared to DRF and DRFC.

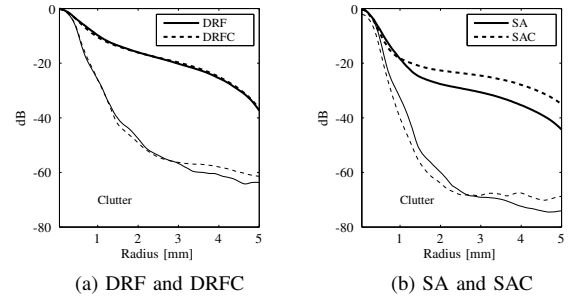


Figure 3. CTR for DRF and SA (thick dashed lines) and for DRFC and SAC (thick solid lines). Clutter levels are shown below as thin dashed and solid lines for the wire at 65 mm, for images with and without compounding respectively.

B. Tissue phantom

To obtain measures for tissue contrast resolution, a tissue mimicking phantom was scanned using the same configurations. In Fig. 4, the resulting images are presented and in Table II, SNR_0 , speckle size, and NID measures are presented computed as an average inside the regions shown in Fig. 4. A small increase in SNR_0 followed by an increase in speckle size is seen for DRFC, when compared to DRF. This is much less than anticipated and deserves future investigation. Consequently, only a 1% increase in NID is observed. For SA, no increase in SNR_0 is observed, a large decrease in speckle size is observed, and the NID is improved dramatically.

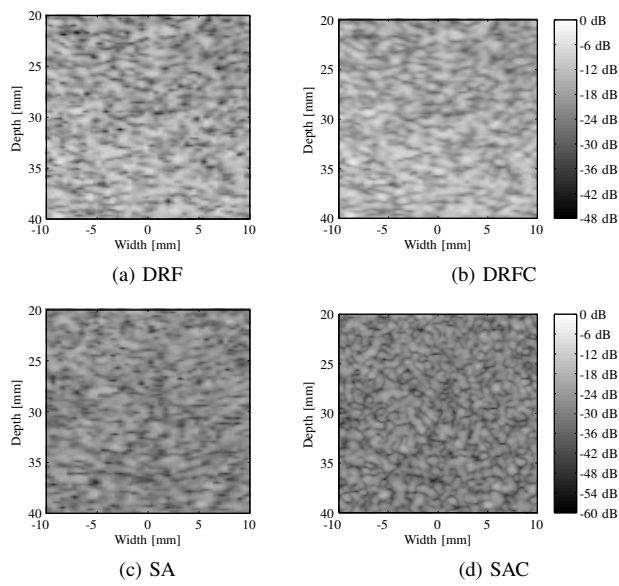


Figure 4. Speckle images obtained using a tissue-mimicking phantom.

Table II

	SNR ₀	Speckle size [mm ²]	NID [dBmm ⁻²]
DRF	1.88	0.66	4.29
DRFC	1.96	0.73	4.23
SA	2.01	0.57	5.50
SAC	1.95	0.34	7.45

C. Clinical images

The measurements for the clinical images were performed using an experimental ultrasound scanning system, RASMUS, capable of storing 12-bit individual channel data at 40 MHz. For imaging, an 11 element subaperture is used for each emission using a 20 μ s FM signal. For receiving 128 channels are sampled. The transducer used is a commercial 5.5 MHz, 128 element convex array with λ pitch (BK Medical) [11].

The data were processed exactly like for the water and tissue phantoms taking into account the different excitation. In Fig. 5, the first clinical image obtained using SAC is presented. The portal vein branch is in the center of the image and the hepatic veins are located to the left above. CR and CNR values are computed between regions in the portal and hepatic veins and the surrounding tissue. The resulting values are presented in Table III.

V. CONCLUSION

The water tank and tissue-mimicking phantom measurements show an improved lateral resolution and an improved NID for the suggested method for compounding using synthetic aperture data. An improved contrast resolution is also observed for the clinical data and it is definitely worth continuing studying this method for further evidence of its work

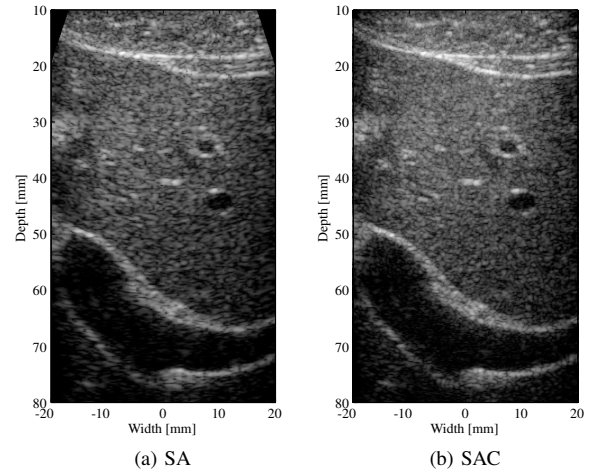


Figure 5. The images (a) and (b) show the abdomen of a healthy 27 year old male with and without compounding. Dynamic range is 60 dB.

Table III

	SA	SAC	
CR(dB)	-12.59	-13.07	portal
CNR	-1.34	-1.30	
CR(dB)	-16.77	-18.41	hepatic
CNR	-2.66	-2.88	

REFERENCES

- [1] C. Burckhardt, "Speckle in ultrasound B-mode scans," *IEEE Trans. Son. Ultrason.*, vol. SU-25, no. 1, pp. 1–6, Jan. 1978.
- [2] R. F. Wagner, S. W. Smith, J. M. Sandrick, and H. Lopez, "Statistics of speckle in ultrasound B-scans," *IEEE Trans. Son. Ultrason.*, vol. 30, pp. 156–163, 1983.
- [3] D. Shattuck and O. von Ramm, "Compounding scanning with a phased array," *Ultrason. Imaging*, vol. 4, pp. 93–107, 1982.
- [4] G. E. Trahey, S. W. Smith, and O. T. von Ramm, "Speckle pattern correlation with lateral aperture translation: Experimental results and implications for spatial compounding," *IEEE Trans. Ultrason., Ferroelec., Freq. Contr.*, vol. UFFC-33, pp. 257–264, 1986.
- [5] D. Vilkomerson, J. Greenleaf, and V. Dutt, "Towards a Resolution Metric for Medical Ultrasound Imaging," in *Proc. IEEE Ultrason. Symp.*, 1995, pp. 1405–1410.
- [6] S. K. Jespersen, J. E. Wilhjelm, and H. Sillesen, "Multi-angle compound imaging," *Ultrason. Imaging*, vol. 20, pp. 81–102, 1998.
- [7] S. W. Smith, R. F. Wagner, J. M. Sandrick, and H. Lopez, "Low contrast detectability and contrast/detail analysis in medical ultrasound," *IEEE Trans. Son. Ultrason.*, vol. 30, pp. 164–173, 1983.
- [8] K. F. Ustuner and G. L. Holley, "Ultrasound imaging system performance assessment," presented at 2003 AAPM Annual Meeting, 2003.
- [9] G. R. Lockwood, J. R. Talman, and S. S. Brunke, "Real-time 3-D ultrasound imaging using sparse synthetic aperture beamforming," *IEEE Trans. Ultrason., Ferroelec., Freq. Contr.*, vol. 45, pp. 980–988, 1998.
- [10] J. A. Jensen, S. Nikolov, B. Tomov, F. Gran, M. Hansen, and T. V. Hansen, "Specification of SARUS: the synthetic aperture real-time ultrasound scanner," Ørsted•DTU, Technical University of Denmark, Tech. Rep., 2006.
- [11] K. L. Gammelmark and J. A. Jensen, "Experimental study of convex coded synthetic transmit aperture imaging," in *Proc. IEEE Ultrason. Symp.*, 2002, pp. 1573–1576.

A.5 Compounding in Synthetic Aperture Imaging

- **J. M. Hansen** and J. A. Jensen: Compounding in Synthetic Aperture Imaging. IEEE Trans. Ultrason., Ferroelec., Freq. Contr., 2012, *In press*.

Compounding in Synthetic Aperture Imaging

Jens Munk Hansen and Jørgen Arendt Jensen

Center for Fast Ultrasound Imaging, Dept. of Elec. Eng. Bldg. 349,
Technical University of Denmark, DK-2800 Kgs. Lyngby, Denmark

Abstract—A method for obtaining compound images using synthetic aperture data is investigated using a convex array transducer. The new approach allows spatial compounding to be performed for any number of angles without reducing the frame rate or temporal resolution. This important feature is an intrinsic property of how the compound images are constructed using synthetic aperture data and an improvement compared to how spatial compounding is obtained using conventional methods. The synthetic aperture compound images are created by exploiting the linearity of delay-and-sum beamformation for data collected from multiple spherical emissions to synthesize multiple transmit and receive apertures corresponding to imaging the tissue from multiple directions. The many images are added incoherently, to produce a single compound image. Using a 192 element, 3.5 MHz, λ -pitch transducer, it is demonstrated from tissue-phantom measurements, how the speckle is reduced and the contrast resolution improved when applying synthetic aperture compound imaging. At a depth of 4 cm, the size of the synthesized apertures are optimized for lesion detection based on the *speckle information density*. This is a performance measure for tissue contrast resolution, which quantifies the trade-off between resolution loss and speckle reduction. The speckle information density is improved by 25 percent when comparing synthetic aperture compounding to a similar setup for compounding using dynamic receive focusing. The cystic resolution and clutter levels are measured using a wire phantom setup and compared to conventional application of the array, as well as to synthetic aperture imaging without compounding. If the full aperture is used for synthetic aperture compounding, the cystic resolution is improved by 41 percent, when compared to conventional imaging, and is at least as good to what can be obtained using synthetic aperture imaging without compounding.

I. BACKGROUND

A number of averaging techniques have been used to remedy speckle artifacts in medical ultrasound. The methods include temporal averaging, spatial compounding [1], [2], and frequency compounding [3]. They are all based on averaging multiple decorrelated frames [4] and decorrelation is obtained through tissue or probe motion in temporal averaging, by transmitting and receiving at different angles in spatial compounding, and image formation at different frequencies in frequency compounding. Decorrelated frames have different speckle patterns, but the same feature information, so speckle gets reduced and feature information is comparatively strengthened.

Today, in addition to temporal averaging, spatial compounding is implemented in all state of the art, high-end ultrasound systems and available when using a low pitch transducer with a fairly high number of independent channels [5]. Many variations of spatial compounding has been implemented and patented within the last decade. There is compound imaging, where the compound effect is obtained by imaging the same

line using different transmit apertures [6] and more interestingly compound imaging, where an adaptive synthesis selects whether the final image point should be made by compounding or be coherently adding the images [7]. A weakness of conventional compounding imaging is a reduction of the frame or at least a reduction of the true temporal resolution. The latter occurs when using a circular buffer and reusing old frames to achieve an apparently higher temporal resolution, a method sometimes referred to as recursive imaging. To remedy the drop in frame rate, methods have been developed, where only receive compounding is used [8] or where the number of scan-lines is reduced by using a more uniform scan-line density [9]. This paper suggests and investigates an approach based on synthetic aperture imaging, where transmit and receive compounding can be obtained without any loss in temporal resolution.

The organization of this paper is as follows: First, spatial compounding is described for images formed using dynamic receive focusing (DRF). When abbreviated, we will refer to this as DRFC. Next, a brief introduction to synthetic aperture (SA) imaging followed by a more detailed description of the approach used for synthetic aperture compounding (SAC). To evaluate the image quality, a number of performance measures for ultrasound imaging systems are defined. The performance measures are all be obtained using water tank measurements and by scanning a tissue mimicking phantom. Theoretical results are presented for how to tradeoff contrast and detail resolution for an improved lesion detection and results from earlier publications are discussed. In the results section, images obtained using dynamic receive focusing and synthetic aperture focusing are presented; both with and without compounding. Performance measures are extracted from the images, and the results are compared between the different methods used for imaging as well as to theoretical results.

II. METHODS

A. Compounding

For conventional spatial compounding, a low-pitch linear or convex array is used. A subset of the elements is selected as the current active aperture, and this aperture is used as a phased array to steer the beam in a direction making an angle θ with a normal to the transducer surface. The active aperture is then translated, until scan lines originating from the entire extent of the array are recorded. This procedure is repeated for angles θ_i , $i = 1, \dots, N_\theta$, where N_θ is the number of angles used for compounding. Next, the N_θ sub-images are envelope-detected and added during scan-line conversion. The resulting image has a reduced speckle appearance, a lower

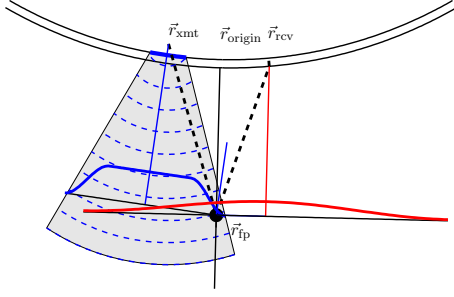


Figure 1: Wave propagation path (thick dashed line) for calculating time-of-flight for an emission with origin \vec{r}_{origin} and data acquired with the element positioned at \vec{r}_{rcv} . Transmit apodization can be read-off as the intersection of the Tukey profile (blue) and the line passing through the focal point, \vec{r}_{fp} and parallel to the center line of the emission. Receive apodization can be read-off as the intersection of the scan line and the Hamming profile (red).

noise floor, grating lobes (if present) are lowered, boundaries subject to non-normal incidence are more visible, and image shadowing is confined to a smaller triangular region behind the attenuating masses or boundaries. The region where all sub-images overlap is referred to as the fully compounded region.

As mentioned in the introduction, a drawback of conventional compounding is that it comes at the cost of a reduction of the frame rate by the number of angles used for compounding. An often used strategy to avoid too low a frame rate is to buffer images and display a new frame using just a single new image and $N_\theta - 1$ old images. In this way, an apparent high frame rate is achieved, but the true temporal resolution is still reduced.

B. Synthetic Aperture

A typical setup for synthesizing a full aperture is to acquire data by emitting a spherical wave with a subaperture and receiving with all or part of the elements [10], [11], [12]. This procedure is then repeated for all emissions such that a complete data set is acquired. Using this data set, any beam and focusing can be synthesized.

For transmit focusing, delays and apodization values are calculated for each point in the image to construct signals, which at each point sum up coherently. For receive focusing, another set of delays and apodizations are applied to the signals received from the individual transducer elements and then a weighted sum is performed. In addition, the apodization can be adjusted to maintain a constant resolution over a range of depths using a fixed F-number for an expanding or contracting aperture for transmit and receive beamforming. The F-number used for dynamic transmit apodization also limits the influence of a single emission and a suitable value can be derived from the acceptance angle of the transducer elements [13]. In Fig. 1, the time-of-flight and apodization calculation involved for a single emission and a single focal point are shown. It is very important to see that in addition to focusing, apodization must be applied, in particularly for

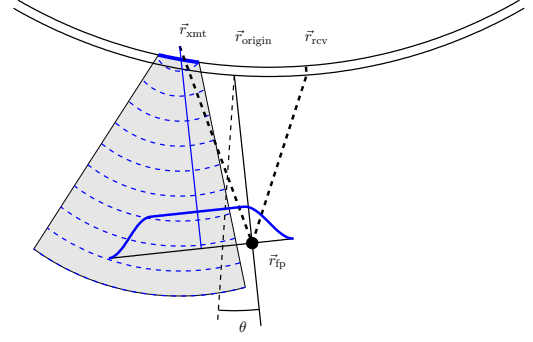


Figure 2: Transmit apodization calculation for a single image point \vec{r}_{fp} for an image angle θ . The apodization value can be read-off the figure as the intersection of the scan line and the apodization profile.

transmit. For the synthetic aperture images in this article, the transmit apodization for a single-emission is computed to be symmetric around the center line of the emission, sometimes also referred to as the line of fire.

A major advantage of synthetic aperture imaging is the possibility to focus everywhere in the image resulting in a better resolution. Further, this can be achieved using the same amount of time for data acquisition as for conventional imaging - or even less if fewer emissions are used. The price for the improved resolution is a huge increase in RF data processing - an increase by the number of lines in the resulting image, for each pulse emission.

C. Synthetic Aperture Compounding

To perform compounding using synthetic aperture data, the linearity of delay-and-sum beamformation is exploited to synthesize multiple transmit and receive apertures using data from part or all of the unfocused emissions. For each point in the image, transmit apodization values are calculated corresponding to insonifying the point using a focused beam centered around the point and making an angle θ with a normal to the transducer surface. In Fig. 2, it is shown for a single point, how the transmit apodization for an emission with origin \vec{r}_{xmt} is calculated using the distance from the transmit origin to the scan line. Similarly, receive apodizations are calculated for each point and applied to the signals received from the individual receiving elements of each transmission. The receive apodization values are likewise computed using the distance from the scan line to the position of the receiving elements as shown in Fig. 3. No special attention is paid to the fact that the transducer is convex. In particular, the transmit apodizations are not adjusted according to the acceptance angle and only a limitation of the angle, θ prevents an emission from contributing to the image outside the region insonified.

For each emission, this (rather complex) procedure is repeated for angles θ_i , $i = 1, \dots, N_\theta$ to update N_θ images used for compounding. To avoid the need for sampling according to the Nyquist criterion for the excitations used in all the

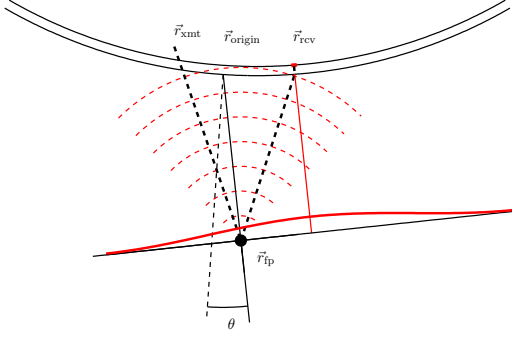


Figure 3: Receive apodization calculation for a single image point \vec{r}_{fp} for an image angle θ . The apodization values can be read-off the figure as the intersection of the scan line and the Hamming profile.

directions of the scan lines, the RF data are beamformed as in-phase and quadrature components, and the envelope for each angular image is simply computed as the absolute value. Finally, the compound image are constructed by adding the enveloped images. An implementation of this method uses a buffer for N_θ images and calculates the delays and accesses the RF data for each pixel only once. In this way, a compound image is ready immediately after the last emission and only the processing resources limits the number of angles used. Since the amount of memory IO for data access is much larger than what is used for accessing the image, the requirement for memory IO resources is comparable to what is required for synthetic aperture imaging without compounding.

In Section III-B, it will be explained why a set of N_θ images, each optimized to give the best possible detail resolution, results in a synthetic aperture compound image with none or very little speckle reduction. After optimizing the approach for synthetic aperture compounding to give the best possible detail resolution and produce images with almost no speckle reduction, in Section IV-C, it will be demonstrated how speckle reduction can be achieved by sacrificing some of the detail resolution.

III. IMAGE QUALITY

Development of new ultrasound imaging methods includes several quality and performance assessment stages. To assess the image quality both the detail and contrast resolution must be studied. They can both be measured and quantized through a combination of water tank and phantom measurements, but often extensive clinical evaluations are carried out to ensure that the desired clinical performance is met. In this paper, the main focus will be on the following measures, which can be obtained from water tank and phantom measurements alone.

A. Performance Measures

a) *Detail resolution*: The *detail resolution* is the separation at which identically point targets can be distinguished. It is distinguished by the main lobe width of the point-spread-function (PSF) and the 6 dB axial pulse length, i.e. the lateral and axial full width at half maximum (FWHM) of the PSF.

b) *Cystic resolution*: The detail resolution alone is not appropriate for comparing the imaging performance of medical ultrasound systems, since it ignores what is outside the main lobe, which has a significant impact on the images of wide dynamic range systems. Acoustic clutter from surrounding objects fill-in images of anechoic objects such as cysts, or weakly echogenic objects such as blood vessels, and reduces their detectability. The ability to detect anechoic or weakly echogenic objects in the presence of strong surrounding objects is sometimes referred to as contrast resolution and was first introduced as *cystic resolution* [14]. The cystic resolution can be quantized by the clutter energy to total energy ratio (CTR). The CTR is defined as the ratio of the energy outside a circular region \mathfrak{R} with radius R centered at the peak of the PSF to the total PSF energy

$$\begin{aligned} \text{CTR}_R(\vec{r}_0) &= 10 \log \left(\frac{\int_{\vec{r} \notin \mathfrak{R}} |h(\vec{r}, \vec{r}_0)|^2 dS}{\int |h(\vec{r}, \vec{r}_0)|^2 dS} \right), \\ &= 10 \log \left(1 - \frac{\int_{\vec{r} \in \mathfrak{R}} |h(\vec{r}, \vec{r}_0)|^2 dS}{\int |h(\vec{r}, \vec{r}_0)|^2 dS} \right), \end{aligned}$$

where $|h(\vec{r}, \vec{r}_0)|$ is the PSF at \vec{r}_0 . For a large ensemble of measurements, the CTR is also a measure of the difference between the average level of an anechoic cyst's center and the background. To get a single measure, one either measures the drop in brightness for a fixed radius R or the radius for which a cyst can be observed at a fixed level, e.g. $R_{20\text{dB}} \equiv \{R \mid \text{CTR}_R = -20\text{dB}\}$.

c) *Tissue contrast resolution*: Most commonly, contrast resolution refers to the ability to distinguish echogenicity differences between a region of interest (ROI) and the background (B) and is quantified by a signal-to-noise ratio for contrast [15]

$$C = \frac{|I_{\text{ROI}} - I_B|}{\sqrt{\sigma_{I_{\text{ROI}}}^2 + \sigma_{I_B}^2}} = \frac{\Delta I}{\sqrt{\sigma_{I_{\text{ROI}}}^2 + \sigma_{I_B}^2}}, \quad (1)$$

where I_{ROI} and I_B are the mean intensities of the ROI and background, and $\sigma_{I_{\text{ROI}}}^2$ and $\sigma_{I_B}^2$ are their corresponding variances. The contrast C is object dependent and is improved by increasing object contrast, ΔI as well as by lowering the variance in the ROI or the surrounding tissue. In [15], Smith et al. proposed a theoretical model of an ideal observer for the task of identifying a lesion within a uniform background, where the model quantifies the expected trade-off between resolution loss and speckle reduction. It assumes Rayleigh statistics, an elliptical speckle cell shape, and that the lesion is large compared to the speckle size. Using this model, the signal-to-noise ratio for lesion detection is [15]

$$\text{SNR}_{\Delta I} = \frac{C d N_{\text{eff}}^{1/2}}{(S_{\text{lat}} S_{\text{ax}})^{1/2}},$$

where C is the contrast of a circular lesion of diameter d , S_{lat} , and S_{ax} , are the lateral and axial speckle dimension, and N_{eff} is the number of independent images compounded. To improve detectability of a lesion with a given contrast, it is therefore of great interest to maximize the density

$$\rho_{\text{SID}} = \frac{N_{\text{eff}}}{(S_{\text{lat}} S_{\text{ax}})}, \quad (2)$$

which we will refer to as the *speckle information density*. The speckle information density is related to the signal-to-noise ratio when averaging over a disk target with area A compounded using N_{eff} independent images, through

$$\text{SNR}_I^2 = A \frac{N_{\text{eff}}}{(S_{\text{lat}} S_{\text{ax}})} = A \rho_{\text{SID}}. \quad (3)$$

Eq. (3) is consistent with the theory given in [15] and states that the signal-to-noise ratio, SNR_I is given by the square root of the number of independent speckle-cells within the disk. The speckle information density (2) is object independent and can be extracted from a tissue-phantom scan and used as a performance measure for lesion detection or tissue contrast resolution. Using this density, degradation of the images from unwanted blurring is penalized because longer correlations are introduced upon blurring. In general, this statement only applies near the focus point, where the speckle size reflects the resolution. For synthetic aperture imaging, however, focusing is done in both transmit and receive and the statement applies everywhere. The number of independent images, N_{eff} can be estimated by measuring the signal-to-noise ratio at a point SNR_0 and using that the enveloped signals follow Rayleigh statistics. The signal-to-noise ratio at point is defined as

$$\text{SNR}_0 \equiv \frac{\mu_V}{\sigma_V},$$

where μ_V and σ_V are the expectation value and standard deviation of the envelope-detected signals and using that the theoretical value of SNR_0 is 1.91, the number of independent images, N_{eff} can be found [16]

$$N_{\text{eff}} = \left(\frac{\text{SNR}_0}{1.91} \right)^2. \quad (4)$$

The speckle dimensions, S_{lat} and S_{ax} can be found from the correlation cell [17]

$$S_c = \int_{-\infty}^{\infty} \frac{C_I(\Delta\xi)}{C_I(0)} d(\Delta\xi), \quad (5)$$

where C_I is the spatial auto-covariance for the intensity and $\Delta\xi$ is the distance between image pixels. In order to apply (5), it is important to introduce some cutoff when performing the integration, because obviously negative correlations should never occur. Preferably, one can assume that the normalized auto-covariance is described by some exponential, apply a least-squares fit to part of the data, and integrate the fit.

B. Contrast - resolution tradeoff

The theoretical contrast of compound images can be computed by using the correlation function between pulse-echo measurements obtained at different spatial positions. This was first done by Burckhardt [18] and used by Shankar and Newhouse in an expression for the improvement of SNR_0 when compounding N images [19]

$$\text{SNR}_0 = 1.91 \sqrt{\frac{N}{1 + 2(N-1)\rho^2/N}}, \quad (6)$$

where ρ is the intensity correlation between two neighboring images. Using the result of Burckhardt, compounding every

0.5 aperture length, results in at most 2.25 independent images per aperture. In later publications, Wagner et al. [4] have shown through theoretical considerations, and Trahey et al. [2] through measurements that the approximate form for the correlation function presented by Burckhardt and used by Shankar and Newhouse is inaccurate in the sense that it overestimates the correlation. The measurements by Trahey et. al. show that translating the aperture by 0.4 times its length, results in about 3.2 independent images per aperture. In [20], an exact analytic expression for the pulse-echo correlation function was derived, and it is now well known that the conclusions made by Burckhardt are inaccurate. The analytic expression of [20] matches the measurements of Trahey et. al reasonably well and can be used for deriving the optimum aperture displacement for efficient compounding to be about half the aperture length. The displacement is computed based on a figure of merit for the task of lesion detection [15]

$$f_m = N_{\text{eff}} L_s / L, \quad (7)$$

where L and L_s are, respectively the length of the aperture and the length of the subaperture used for compounding. The fractional size of the subaperture, L_s/L is a measure for the lateral resolution of the imaging system and N_{eff} is a measure for the efficiency of compounding. Hence, there is a tradeoff between contrast and detail resolution. To conclude that the optimum displacement for efficient compounding should be about one-half the aperture length, O' Donnell et al. [20] show that using a fixed aperture of length L divided into N overlapping subarrays of length L_s with equal displacements, x_0 , the figure of merit, f_m is constant for a given relative aperture displacement, $x \equiv x_0/L_s$ and fractional size of the subaperture, L_s/L

Following the theory of O' Donnell, in Fig. 4, the values of f_m are plotted as a function of the relative aperture displacement, x , and the fractional size of the subaperture, L_s/L [20].

$$f_m(L_s/L, x) = N_{\text{eff}}(L_s/L, x) L_s/L = \text{const.} \quad (8)$$

The values of f_m can also be used for computing the maximum number of independent images, N_{eff} for a setup with a given relative aperture displacement, x and subaperture size, L_s .

Experimental results for SNR_0 and the correlation, ρ by Jespersen et al. [21] for compounding using a linear array with a subaperture of one third of the aperture, $N = 11$, and an angular separation of 5° , reveal values for N_{eff} of 6.75 and 7.47. The former value is obtained by using measurements of SNR_0 and the latter is obtained by using an experimental-determined correlation value, $\rho = 0.26$ together with (6). The theoretical expression from O' Donnell et al. states that with the setup of [21], the number of independent images, N_{eff} should be about 4.4. As also noted by Jespersen, the large result obtained using (6) is not surprisingly too large, because in deriving (6), an assumption is used, which states that only neighboring images are correlated and images separated by more than one 'angle-step' are uncorrelated. The experimentally-determined value for ρ obtained by Jespersen is

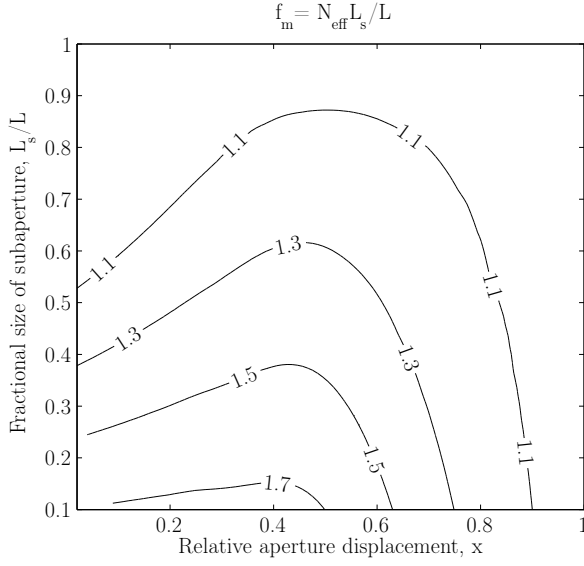


Figure 4: Contour plot of f_m vs. relative aperture displacement, x and fractional size of the subaperture, L_s/L .

in good agreement with theory and the experiments performed by Trahey et. al. The large result obtained using (4) however, cannot be due to successful compounding alone. Some reasons for obtaining too large a value of SNR_0 could be electronic noise, improper focusing, or high clutter levels, which all contribute to blurring the images. Also, the theoretical results of O' Donnell are derived by assuming focusing on both the transmit and the receive signals. For these reasons, the speckle information density (2) is a better performance indicator for tissue contrast resolution or lesion detection than the figure of merit, f_m , originally proposed by Smith et al. [15]. We will return to this in the discussion section.

In this paper, the detail resolution is measured using the axial and lateral FWHM of the PSF. The cystic resolution is measured using the CTR, represented by R_{20dB} . The number of independent images, N_{eff} are computed to compare values for f_m with the theory for a linear array described by O' Donnell [20]. For evaluating the tissue contrast resolution of the images however, the speckle information density, ρ_{SID} (2) is used rather than N_{eff} or the figure of merit, f_m (7).

IV. RESULTS

To investigate the performance of synthetic aperture compounding, a setup using a commercial 192 element, 3.5 MHz, λ -pitch transducer with a convex radius of 60 mm was used for water tank and tissue phantom measurements. The sampling was performed using an experimental ultrasound scanning system, SARUS, capable of storing 12-bits individual channel data at 70 MHz [22]. For SA and SAC imaging, a 16 element subaperture was used for 192 unfocused emissions. For each emission, data from all 192 channels were stored. For all emissions, a two-cycle sinusoid was used for excitation together with a Hamming apodization on the active subaperture. Compounding was done using 5 angles with an angular separation of 5° . For the transducer used and a point

imaged at a depth of 40 mm, this amounts to a relative aperture displacement between 5.5 and 5.7 percent along the transducer surface.

For comparison, for dynamic receive focusing, a 64 element subaperture was used for 192 focused emissions for each compound angle. The excitation used was the same as for the synthetic aperture setup. Compounding using dynamic receive focusing was made using 5 angles with an angular separation of 5° . The emissions for each subaperture was constructed using a focal distance of 42 mm and by steering the beam in directions relative to a normal on the active subaperture. By steering the beams this way, the compound images correspond to images obtained using a relative aperture displacement of around 10 percent of the active subaperture. Using that the active subaperture is 64 elements wide, this is less than what we have used for the synthetic aperture setup and much less than the 40-50 percent relative aperture displacement recommended for a linear array [20]. The very limited angular span was used to avoid grating lobes and avoid the need for receiving or transmitting signals with an angle of incidence outside the acceptance angle.

A. Water phantom measurements

The water tank phantom consists of 4 wires at depths of 15, 41, 66, and 90 mm. The temperature of the water was measured and delays for both the focused and the unfocused emissions computed. The transducer was then submerged into the water and data were collected using 5 times 192 focused emissions followed by 192 unfocused emissions. To obtain a constant lateral resolution across depth, an expanding and contracting aperture corresponding to a constant F-number was used for both dynamic receive focusing and the synthetic aperture methods. A small parameter study was made using the recorded data to find the optimal F-number, which gave the smallest values for R_{20dB} . For the methods using dynamic receive focusing, the problem is convex and the optimal F-number for a given depth can be used for estimating the size of the effective aperture. For the synthetic aperture methods, both a transmit and a receive F-number is applied for determining the width of respectively the transmit and receive apertures. The optimization problem is convex in both variables and a transmit and a receive F-number was found for each depth. For all studies, a Hamming function was used for the dynamic aperture. Using the optimal F-numbers (see Table I), images were beamformed and in Fig. 5, contour plots of the wire at a depth of 66 mm are shown.

In Table I, the detail resolution and cystic resolution have been measured for the wire at 66 mm using the four imaging techniques. For both DRF and SA, compounding results in an improved lateral resolution in terms of the full-width at half maximum. For synthetic aperture compounding, this is due to the nature of how the apodizations are calculated. For synthetic aperture, the transmit apodizations are always symmetric around the emissions, whereas for synthetic aperture compounding, they are not. In particular, the emissions may contribute to parts of the image outside their region of insonification determined by the acceptance angle of the elements. An

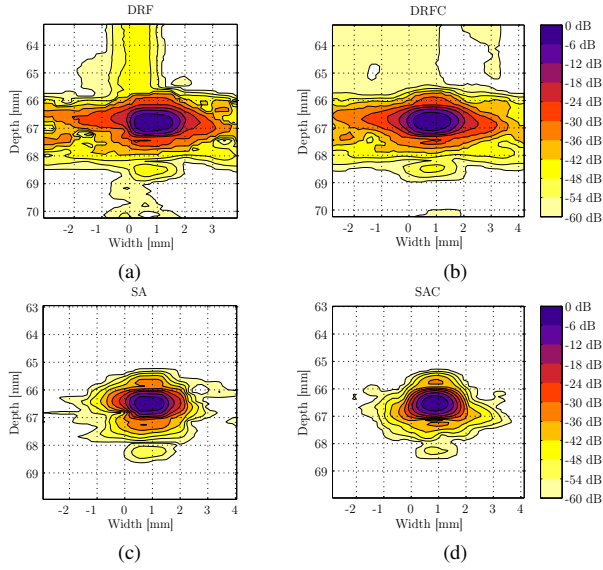


Figure 5: The PSF imaged at a depth of 66 mm obtained using a water tank phantom with wires. Figure (a) and (b) are made using dynamic receive focusing and figure (c) and (d) are made using synthetic aperture focusing. The figures to the right, (b) and (d) are compound images obtained using conventional compounding and synthetic aperture compounding, respectively.

Table I: Detail resolution, FWHM and cystic resolution, R_{20dB} extracted from the water tank measurements. The transmit F-numbers, F_{xmt} are the F-numbers used for beamformation not to be confused with the F-numbers determining the position of the focus points or virtual sources. The F-numbers used for the four imaging methods were selected to be the ones producing the smallest values for R_{20dB} at the depth of 66 mm.

	DRF	DRFC	SA	SAC
R_{20dB}	1.47	1.36	0.92	0.80
$FWHM_{lat}$	1.41	1.37	1.13	0.97
$FWHM_{ax}$ [mm]	0.70	0.70	0.59	0.59
$Area_{6dB}$ [mm ²]	0.77	0.75	0.53	0.45
F_{xmt}	-	-	1.2	1.15
F_{rcv}	1.2	1.2	0.8	1.10

example of this situation is shown in Fig. 2. Another difference is how the sizes of the dynamic apertures are calculated. For synthetic aperture focusing, the depth used for calculating the width of the receive aperture is the distance to the transducer surface, whereas for synthetic aperture compounding, the depth is computed as the distance from the focal point to the aperture along the scan line for the given angle. For synthetic aperture, the width of the transmit aperture is determined using the distance from the focal point to the plane containing the virtual source, whereas for synthetic aperture compounding, the distance used is simply the distance to the aperture along the scan line for the given angle. From the results in Table I, it follows that when applying compounding, the cystic resolution

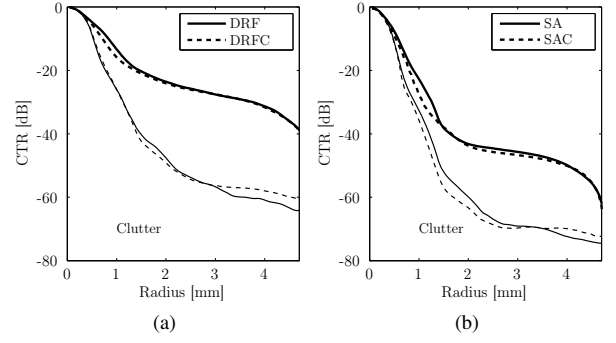


Figure 6: Clutter energy to total energy ratio (CTR) computed for the PSF at a depth of 66 mm. In (a), the CTR for DRF (thick solid line) and DRFC (thick dashed line) are shown and in (b), the CTR for SA (thick solid line) and SAC (thick dashed line) are shown. Clutter levels are shown below as thin dashed and solid lines for images with and without compounding, respectively.

Table II: Signal-to-noise ratio at a point, SNR_0 , speckle size and the speckle information density, ρ_{SID} computed using the same data as for creating the tissue phantom images in Fig. 7.

	DRF	DRFC	SA	SAC
SNR_0	2.19	2.28	2.11	1.97
Speckle size [mm ²]	0.50	0.54	0.51	0.32
ρ_{SID}	2.07	2.08	1.87	2.61

is improved for both DRF and SA. The most interesting figure in Table I is the fact that the cystic resolution is improved by 41 percent, when comparing R_{20dB} of SAC to that of DRFC. Recall that the cystic resolution reflects the ability to detect anechoic or weakly echogenic objects in the presence of strong surrounding objects. Finally, in Fig. 6, the CTR is plotted together with the clutter level for the wire at depth 66 mm using the four imaging techniques. We see that in general, the CTR for the compound images are better for any radius. Also, we see that both synthetic aperture methods perform better than the methods using dynamic receive focusing.

B. Tissue phantom measurements

To investigate the performance for lesion detection, a tissue mimicking phantom was scanned using the same configuration as was used for scanning the wire phantom in the previous section. The location and size of the region for extracting SNR_0 and the auto-covariance was directly in front of the transducer at a depth of 40 mm and 230x170 pixels corresponding to a region of 20x20 mm. In Fig. 7, the region is imaged using the four imaging techniques. The values for SNR_0 were calculated using the envelope detected images and the results are shown in Table II. As expected, almost no speckle reduction is observed for the image created using synthetic aperture compounding, the value for SNR_0 equals 1.97, which

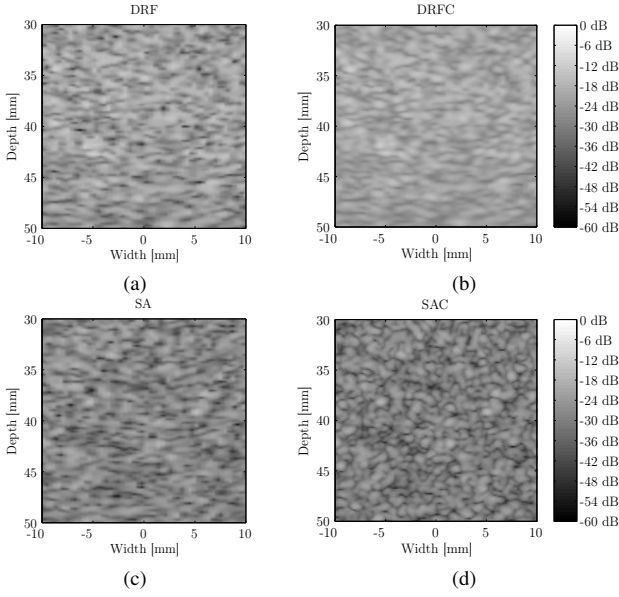


Figure 7: Speckle images obtained using a tissue-mimicking phantom. The figures (a) and (b) are made using dynamic receive focusing and the figures (c) and (d) are made using synthetic aperture focusing. The figures to the right, (b) and (d) are compound images obtained using conventional compounding and synthetic aperture compounding, respectively.

is very close to the theoretical value for a fully developed speckle. To get more representative numbers, a larger ensemble should be studied using different realizations of the tissue obtained by e.g. moving the transducer. A drawback of this approach though is that the contact between the transducer and the surface of the phantom may vary from measurement to measurement. A similar effect can be obtained by studying a larger region, but this is a delicate matter, since the pulse-echo-fields vary over the region. The region selected for this study is chosen big enough to contain 20 speckle correlation lengths in the lateral direction for the method with the largest speckle size, which is observed from compounding using dynamic receive focusing.

The number of independent frames, N_{eff} was computed from the signal-to-noise ratio at a point, SNR_0 and the speckle correlation cell was computed by fitting the normalized auto-covariance, $C_I(\Delta\xi)/C_I(0)$ to be described by a Gaussian and the integral was evaluated using the fit. For fitting the data, a least-squares fit was used together with a lower cutoff value of 0.3 for the auto-covariance. From the results in Table II, it follows that for compounding using dynamic receive focusing, the signal-to-noise ratio at a point, SNR_0 increases but it is also followed by an increase in the speckle size. This is a well known fact. When comparing SNR_0 and the speckle size to the numbers obtained using synthetic aperture, only a small difference is observed. This is expected, since the transmit focus for DRF, and DRFC was chosen at a depth of 42 mm. SNR_0 is probably slightly smaller for synthetic aperture because the average focusing for the ROI is better and improved focusing implies less blurring, which leads to

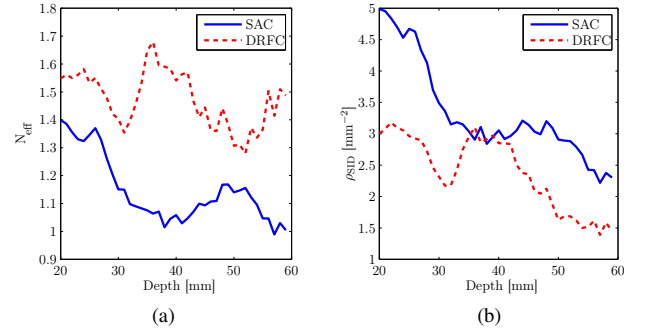


Figure 8: The number of independent images, N_{eff} and the speckle information density, ρ_{SID} as a function of depth for compounding using dynamic receive focusing and synthetic aperture focusing.

higher values for SNR_0 .

The explanation for why the value for SNR_0 is lower for SAC is due to the fact that the apodizations are calculated in a different way, causing more aperture to be used for both transmit and receive. The most interesting figures in Table II are the speckle information densities, ρ_{SID} , which reveals that SAC is superior to both SA and dynamic receive focusing with and without compounding. An improvement of 25 percent is seen, when comparing SAC to DRFC.

The same data were also beamformed using F-numbers optimized for a depth of 41 mm. For both dynamic receive focusing and synthetic aperture compounding, the optimal F-numbers were found to be around 0.8, implying larger apertures. The results for SNR_0 using this setup were all lower than the values in Table II because of better focusing. Using this setup, in Fig. 8, the number of independent images, N_{eff} and the speckle information density, ρ_{SID} are plotted as a function of depth. Fig. 8a shows that in general, the numbers of independent images, N_{eff} are larger for compounding using dynamic receive focusing than for synthetic aperture compounding. It is important to remember that this value is computed using the SNR_0 values and an increase is not necessarily associated with successful compounding. Instead of comparing N_{eff} , the speckle information densities, ρ_{SID} are compared in Fig. 8b and they show how synthetic aperture compounding outperforms compounding using dynamic receive focusing everywhere except at the focus point around 42 mm. The largest differences are found in the region near the transducer, since here it is much easier to do proper focusing using spherical waves than using emissions with foci far away. The randomness of the lines is reflecting the stochastic but fully deterministic structure of the speckle. The measurements were repeated 10 times for a fixed transducer position and the results were unchanged.

C. Contrast - resolution tradeoff

From the main results of the theory derived in [20], which is summarized in Fig. 4, it is clear that in order to obtain compounding, resolution must be sacrificed, i.e. for a fixed

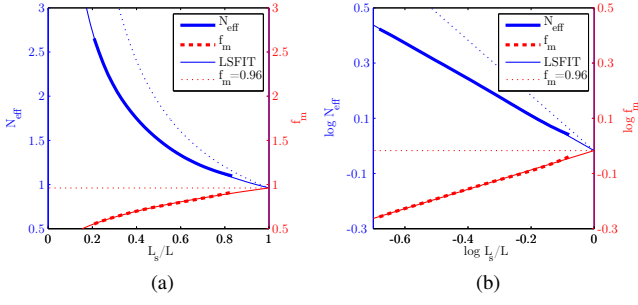


Figure 9: The number of independent images, N_{eff} (thick solid line) and the figure of merit, f_m (thick dashed line) plotted as a function of the fractional size of the synthesized apertures, L_s/L . The thin solid lines are least-squares fits using a function of the form, $N_{\text{eff}} = C(L_s/L)^p$. The dotted lines represent a situation, where the figure of merit, f_m remains constant.

aperture translation, x , by lowering L_s/L , the number of independent images, N_{eff} must go up. This fact also explains how N_{eff} varies as function of depth for synthetic aperture compounding, in Fig. 8a. Both F-numbers are fixed to 0.8 corresponding to an optimal cystic resolution at a depth of 41 mm. When imaging regions closer to the transducer, the apertures contract and the subapertures become less correlated resulting in an increase of N_{eff} . For regions further down, edge-artifacts appear because of limited aperture extent and hence also an increase should be observed. These two facts together with the fact that the fully compounded region is narrowing down as a function of depth explain how N_{eff} varies for different depths. For compounding using dynamic receive focusing, an opposite effect is expected close to the focal point because of how the focused emissions are constructed. Also, the effect should decrease as function of depth due to the narrowing down of the fully compounded region.

In Fig. 9, the values for N_{eff} and f_m are extracted from images created using 5 compound angles for different sizes of the synthesized apertures. The number of independent images, N_{eff} (thick solid line) is increasing, when reducing the size of the subaperture, which shows that the compound effect can be tuned for a given purpose. The figure of merit, f_m (thick dashed line) decreases when lowering the size of aperture, which is the opposite of what is predicted by the theory for a linear array. The reason for this behavior is obvious, since the theory assumes that the number of images, N is increasing when lowering the size of the subapertures for a fixed relative aperture translation, x , i.e. the number of images, N , must satisfy

$$N = 1 + (1 - L_s/L)/(xL_s/L).$$

The setup used in this paper corresponds to a fixed aperture translation, x and the same number of images, $N = 5$, irrespective of the size of the subapertures and the product, $f_m = N_{\text{eff}}L_s/L$ therefore decreases upon lowering the size of the subapertures and for small subapertures, only the center part of the transducer is used. By introducing more angles

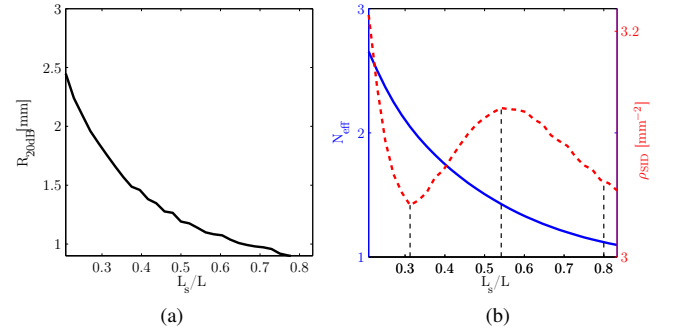


Figure 10: Cystic resolution, $R_{20\text{dB}}$, number of independent images, N_{eff} , and the speckle information density, ρ_{SID} for different sizes of the synthesized apertures.

or images, like the theory assumes, any part of the aperture is always in use for some subaperture. In this case, the measurements for N_{eff} and for the figure of merit, f_m should lie above the two dotted curves in Fig. 9a and Fig. 9b. For the λ -pitch convex array, it is not possible to have too large an angle separation nor use too many angles, since then either grating lobes are introduced or for the outermost elements, signals transmitted or received with an angle of incidence much larger than the acceptance angle are used. As a consequence of the fixed number of images or angles, fitting the N_{eff} using a function of the form

$$N_{\text{eff}} = D(L_s/L)^p,$$

reveals a value of p greater than -1. For a linear array, where images are created as dictated by the theory, the value of p should be less than -1. Fitting the data for the setup used for the convex transducer gives $p = -0.65$ and $D = 0.96$. The constant D should always be about one when averaged for a large ensemble of measurements reproducing the value for SNR_0 for a fully developed speckle. In Fig. 10, the cystic resolution, $R_{20\text{dB}}$, the number of independent images, N_{eff} , and the speckle information density, ρ_{SID} are plotted for different sizes of the synthesized apertures. The speckle information density peaks using an aperture size considerable less than using the full aperture and close to using half the aperture. Fig. 11 shows the speckle images constructed using the 3 different values for L_s/L corresponding to the dashed lines in Fig. 10b. It is interesting to see that in terms of the speckle information density, ρ_{SID} , the optimal image for lesion observation is not the image with the best cystic resolution nor the image with the largest compound effect, but a compromise. The optimal image in Fig. 11b is constructed by finding the size of the synthesized apertures, which give the highest speckle information density, ρ_{SID} in region where the speckle correlation lengths are not larger than twice the FWHM measured using a wire phantom. When using very small apertures, the blurring is no longer compensated for by an increased speckle size and the speckle information density cannot be used as a performance indicator.

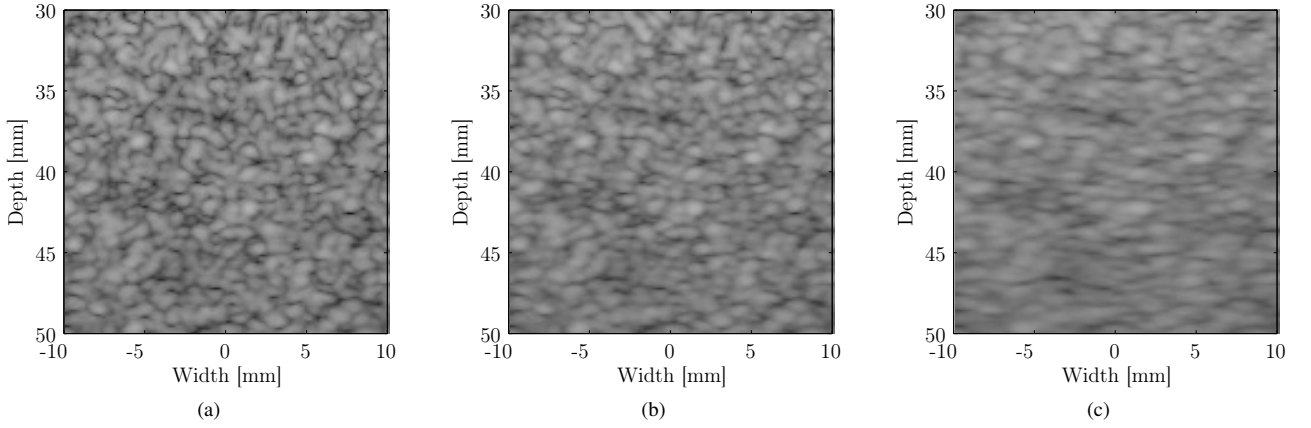


Figure 11: Speckle images for 3 different sizes of the synthesized apertures, L_s/L corresponding to the dashed lines in Fig. 10b: $L_s/L = 0.81$ (a), $L_s/L = 0.54$ (b), and $L_s/L = 0.31$ (c). The dynamic range used for all images is 60 dB.

V. CONCLUSION

A method for obtaining compound images using synthetic aperture data and a convex array has been presented. The suggested approach allows spatial compounding to be performed for any number of angles without reducing the frame rate or temporal resolution. It was demonstrated how resolution must be sacrificed to achieve compounding and the compound effect can be adjusted by scaling the size of the synthesized apertures. In terms of the speckle information density, the compound images obtained using synthetic aperture imaging was shown to be superior to images obtained using a similar setup using dynamic receive focusing. Further, it was demonstrated, how an optimal aperture size can be found by scanning a tissue-mimicking phantom and computing the speckle information density. When comparing synthetic aperture compounding to conventional spatial compounding, it was demonstrated that synthetic aperture compounding has an improved depth of field. Also the results and theory discussed in this paper states and suggest that compounding should be obtained from decorrelation of subapertures, which necessitates steering. Therefore, it will be very interesting to see how this method performs using a better transducer with $\lambda/2$ -pitch or a flat phased-array transducer, where the beam can be steered without having to worry about grating lobes or signals transmitted or received at large angles. For *in-vivo* studies, a potential problem could be tissue motion corrupting the data resulting in lack of coherence of signals from different emissions. It is a problem, but it can successfully be compensated for using motion compensation as shown in [23].

REFERENCES

- [1] D. Shattuck and O. von Ramm, "Compounding scanning with a phased array," *Ultrason. Imaging*, vol. 4, pp. 93–107, 1982.
- [2] G. E. Trahey, S. W. Smith, and O. T. von Ramm, "Speckle pattern correlation with lateral aperture translation: Experimental results and implications for spatial compounding," *IEEE Trans. Ultrason., Ferroelec., Freq. Contr.*, vol. UF33-33, pp. 257–264, 1986.
- [3] P. A. Magnin, O. T. von Ramm, and F. L. Thurstone, "Frequency compounding for speckle contrast reduction in phased array images," *Ultrasonic Imaging*, vol. 4, no. 3, pp. 267 – 281, 1982.
- [4] R. F. Wagner, M. F. Insana, and S. W. Smith, "Fundamental correlation lengths of coherent speckle in medical ultrasonic images," *IEEE Trans. Ultrason., Ferroelec., Freq. Contr.*, vol. 35, pp. 34–44, 1988.
- [5] R. Entekin, P. Jackson, and B. Porter, "Real time spatial compound imaging in breast ultrasound: technology and early clinical experience," *medicamundi*, vol. 43, pp. 35–43, September 1999.
- [6] S. J. C. Anming He Cai, "Aperture compounding for medical imaging," Patent, 01 2003, US 6508770.
- [7] M. V. C. Kutay F. Ustuner, P. V. C. Mirsaid S. Bolorforosh, and L. A. C. Albert Gee, "Medical ultrasonic imaging with adaptive synthesis and compounding," Patent, 08 2002, US 6432054.
- [8] M. V. C. Kutay F. Ustuner, B. C. Charles E. Bradley, and M. V. C. Daniel E. Need, "Medical ultrasonic imaging method and system for spatial compounding," Patent, 03 2003, US 6527720.
- [9] S. J. C. Anming He Cai and M. V. C. Rickard C. Loftman, "Overlapped scanning for multi-directional compounding of ultrasound images," Patent, 09 2004, US 6790181.
- [10] L. F. Nock and G. E. Trahey, "Synthetic aperture imaging in medical ultrasound with correction for motion artifacts," in *Proc. IEEE Ultrason. Symp.*, 1990, pp. 1597–1601.
- [11] G. R. Lockwood, J. R. Talman, and S. S. Brunke, "Real-time 3-D ultrasound imaging using sparse synthetic aperture beamforming," *IEEE Trans. Ultrason., Ferroelec., Freq. Contr.*, vol. 45, pp. 980–988, 1998.
- [12] C. R. Hazard and G. R. Lockwood, "Theoretical assessment of a synthetic aperture beamformer for real-time 3-D imaging," *IEEE Trans. Ultrason., Ferroelec., Freq. Contr.*, vol. 46, pp. 972–980, 1999.
- [13] N. Oddershede and J. A. Jensen, "Effects influencing focusing in synthetic aperture vector flow imaging," *IEEE Trans. Ultrason., Ferroelec., Freq. Contr.*, vol. 54, no. 9, pp. 1811–1825, 2007.
- [14] D. Vilkomerson, J. Greenleaf, and V. Dutt, "Towards a Resolution Metric for Medical Ultrasound Imaging," in *IEEE Ultrasonics Symposium*, 1995, pp. 1405–1410.
- [15] S. W. Smith, R. F. Wagner, J. M. Sandrik, and H. Lopez, "Low contrast detectability and contrast/detail analysis in medical ultrasound," *IEEE Trans. Son. Ultrason.*, vol. 30, pp. 164–173, 1983.
- [16] R. F. Wagner, S. W. Smith, J. M. Sandrick, and H. Lopez, "Statistics of speckle in ultrasound B-scans," *IEEE Trans. Son. Ultrason.*, vol. 30, pp. 156–163, 1983.
- [17] J. W. Goodman, "Statistical properties of laser speckle patterns," *Stanford Electron. Lab. Tech. Rep.*, no. 2303-1, 1963.
- [18] C. Burckhardt, "Speckle in ultrasound b-mode scans," *IEEE Trans. Son. Ultrason.*, vol. SU-25, no. 1, pp. 1–6, Jan. 1978.
- [19] P. M. Shankar and V. L. Newhouse, "Speckle reduction with improved resolution in ultrasound images," *IEEE Trans. Son. Ultrason.*, vol. 32, pp. 537–543, 1985.
- [20] M. O'Donnell and S. D. Silverstein, "Optimum displacement for compound image generation in medical ultrasound," *IEEE transactions on ultrasonics, ferroelectrics, and frequency control*, vol. 35, no. 4, pp. 470–476, 1988.
- [21] S. K. Jespersen, J. E. Wilhjelm, and H. Sillesen, "Multi-angle compound imaging," *Ultrason. Imaging*, vol. 20, pp. 81–102, 1998.

- [22] J. A. Jensen, H. Holten-Lund, R. T. Nielson, B. G. Tomov, M. B. Stuart, S. I. Nikolov, M. Hansen, and U. D. Larsen, "Performance of SARUS: A Synthetic Aperture Real-time Ultrasound System," in *Proc. IEEE Ultrason. Symp.*, Oct. 2010, pp. 305–309.
- [23] K. L. Gammelmark and J. A. Jensen, "Duplex synthetic aperture imaging with tissue motion compensation," in *Proc. IEEE Ultrason. Symp.*, 2003, pp. 1569–1573.

A.6 Synthetic Aperture Compounding using a Phased-array Transducer

- **J. M. Hansen** and J. A. Jensen: Synthetic Aperture Compounding using a Phased-array Transducer. JASA, (*Submitted*).

Synthetic Aperture Compounding using a Phased-array Transducer

Jens Munk Hansen and Jørgen Arendt Jensen

*Department of Electrical Engineering, Technical University of Denmark.
Center for Fast Ultrasound Imaging, Bldg. 349,
DK-2800 Kgs. Lyngby, Denmark*

(Dated: June 8, 2012)

Compound images are constructed using synthetic aperture data for a linear phased-array transducer. The images are constructed using receive and transmit aperture compounding using a method that allows compounding to be performed using any number of apertures without reducing the frame rate or temporal resolution. This important feature is an intrinsic property of how compound images are constructed using synthetic aperture data and is an improvement compared to how spatial compounding is obtained using conventional methods. Using an experimental ultrasound scanner with 1024 channels, SARUS, and a 128-element, 3.5 MHz, phased-array transducer, it is demonstrated how synthetic aperture compounding can be used to reduce speckle appearance and improve the contrast of cysts. By synthesizing three apertures of about half the size of the transducer, it is demonstrated how the signal-to-noise ratio associated with lesion detection is improved by 6 dB for a cyst at a depth of 50 mm. The increased contrast resolution comes at the cost of a reduced detail resolution and a tradeoff between detail resolution and contrast can be made, which optimizes the detectability of cysts based on a theory, which relates the lateral correlation of images to the size and positions of the subapertures used for compounding. The optimal configuration is based on a performance indicator, which can be found by scanning a speckle phantom without cysts. The measured values for the performance indicator are shown to be in good agreement with the theory and when comparing the contrast for a cyst with the performance indicator for 154 aperture configurations a correlation $R = 0.81$ is observed with a p-value of less than 0.0001.

PACS numbers: 43.35.Yb

I. INTRODUCTION

In ultrasound images, almost any mass is first observed using B-mode imaging and later classified using either doppler, color flow, or biopsies. It is therefore important that the B-mode images have high resolution and contrast. Speckle reduces image contrast and diminishes the possibilities for detection of low-contrast regions. To reduce the speckle appearance, a number of averaging techniques have been implemented. The methods include temporal averaging, spatial compounding^{1,2}, and frequency compounding³. They are all based on averaging multiple decorrelated frames⁴. Decorrelation is obtained through tissue or probe motion in temporal averaging, by transmitting and receiving at different angles or using different subapertures in spatial compounding, and image formation at different frequencies in frequency compounding. Decorrelated frames have different speckle patterns, but the same feature information, so speckle gets reduced and feature information is comparatively strengthened. Today, in addition to temporal averaging, spatial compounding is implemented in all state-of-the-art, high-end ultrasound systems and available when using a low pitch transducer with a fairly high number of independent channels⁵. A drawback of conventional compounding is a reduction of the frame rate or at least a reduction of the true temporal resolution. In the last case, the temporal resolution is lowered because of reuse of old frames to achieve an apparently higher frame rate.

An approach for compounding using synthetic aperture is in this paper applied to a phased-array transducer and the degree of compounding is shown to be

very close to what theoretically can be achieved. The authors Hansen and Jensen⁶, introduced in a recent paper a similar approach for angle compounding using synthetic aperture data and this was applied to a λ -pitch convex array transducer. The degree of compounding was limited due to restrictions from grating lobes as the array had λ pitch. The approach used in this paper uses aperture compounding instead of angle compounding to better control the decorrelation of the apertures required for efficient compounding.

The organization of this paper is as follows: First, two conventional approaches for spatial compounding are described. Next, the method for synthetic aperture compounding is presented and a number of performance measures are defined to evaluate synthetic aperture compounding. Theoretical results are presented for how to tradeoff contrast and detail resolution for an improved lesion detection and results from earlier publications are discussed. In the results section, performance measures are extracted from images acquired by the research scanner SARUS⁷ and compared to theoretical results with excellent agreement. Cyst images are shown with different degree of compounding and the contrast measured for a cyst at a depth 50 mm is correlated with a performance indicator, which can be obtained by scanning a tissue-mimicking phantom without cysts.

II. METHODS

As mentioned in the introduction, spatial compounding as implemented in the majority of scanners today has

its drawbacks. In this section, two different approaches are described, which both suffers from a reduction of the frame rate or at least a reduction of the temporal resolution. Next, the new approach for compounding using synthetic aperture data is described with the advantages of an improved resolution due better focusing and equally important no reduction of the temporal resolution.

A. Angle Compounding

For conventional spatial compounding, a low-pitch linear or convex array is used. A subset of the elements is selected as the current active aperture, and this aperture is used as a phased array to steer the beam in a direction making an angle θ with a normal to the transducer surface. The active aperture is then translated, until scan lines originating from the entire extent of the array are recorded. This procedure is repeated for angles θ_i , $i = 1, \dots, N_\theta$, where N_θ is the number of angles used for compounding. Next, the N_θ sub-images are envelope-detected and added during scan-line conversion. This method is in the literature referred to as multi-angle compound imaging (MACI)⁸.

B. Aperture compounding

Another approach uses instead multiple transmit-receive apertures, where the decorrelation of the apertures is controlled by imaging the same line using N_s subapertures. The subapertures are often selected to be of the same size and displaced using a fixed relative aperture translation, such that they overlap equally. Hereby, the lateral correlation of the sub-images can be related to the correlation of the apertures through a Fourier relation at the focus⁹.

For images formed using spatial compounding - angle compounding or aperture compounding, the resulting images have a reduced speckle appearance, a lower noise floor, grating lobes (if present) are lowered, boundaries subject to non-normal incidence are more visible, and image shadowing is confined to a smaller triangular region behind the attenuating masses or boundaries.

As mentioned in the introduction, a drawback of conventional compounding is a reduction of the frame rate by the number of angles or subapertures used for compounding. An often used strategy to avoid low frame rates is to buffer images and display a new frame using just a single new image and $(N_\theta - 1)$ or $(N_s - 1)$ old images. Hereby, an apparent high frame rate is achieved, but the true temporal resolution is still reduced.

C. Synthetic Aperture Compounding

To perform aperture compounding using synthetic aperture data, the linearity of delay-and-sum beamformation is exploited to synthesize multiple transmit and receive apertures using data from part of or all of a number of unfocused emissions¹⁰⁻¹³. For each point in the

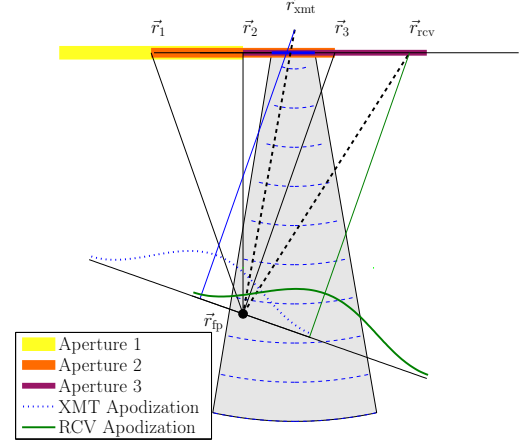


Figure 1. Transmit and receive apodization calculation for a single image point \vec{r}_{ip} for a sub-image using an aperture located at \vec{r}_3 . The apodization values can be read-off the figure as the intersection of the scan line and the apodization profiles. The shaded region is the region insonified by the active elements used for the unfocused emission with origin \vec{r}_{xmt} .

image, transmit apodization values are calculated corresponding to insonifying the point using focused beams from a number of synthetic apertures with different locations. In Fig. 1, it is shown for a single point, \vec{r}_{ip} , how the transmit apodization for an emission with origin \vec{r}_{xmt} is calculated using the distance from the transmit origin, \vec{r}_{xmt} to the “scan line” - the line connecting the point, \vec{r}_{ip} with center of a synthetic aperture, the aperture located at \vec{r}_3 . Similarly, receive apodizations are calculated for each point and applied to the signals received from the individual receiving elements of each transmission. The receive apodization values are likewise computed using the distance from the scan line to the position of the receiving elements as shown in Fig. 1.

For the specific setup used in this paper, the apertures are selected such that they overlap equally and are distributed symmetrically around the image point. In Fig. 1, three apertures are used, $N_s = 3$, and they are translated by half the aperture length and the apodizations for the situation in Fig. 1 are used for the third image.

For each emission, this procedure is repeated for a number of subapertures $i = 1, \dots, N_s$ to update N_s images used for compounding. To avoid the need for sampling according to the Nyquist criterion for the excitations used in all the directions of the scan lines, the RF data are beamformed as in-phase and quadrature components, and the envelope for each angular image is simply computed as the absolute value¹⁴. Finally, the compound image are constructed by adding the enveloped images. An implementation of this method uses a buffer for N_s images and calculates the delays and accesses the RF data for each pixel only once. In this way, a compound image is ready immediately after the last emission and only the processing resources limits the number of angles used. Since the RF data access is randomly shifted and

image data access is contiguous, the amount of memory IO for data access is much larger than what is used for accessing the image. This means that the requirement for memory IO resources is comparable to what is required for synthetic aperture imaging without compounding.

III. METHOD VALIDATION

Development of new ultrasound imaging methods includes several quality and performance assessment stages. To assess the image quality both the detail and contrast resolution must be studied. They can both be measured and quantized through a combination of water tank and phantom measurements, but often extensive clinical evaluations are carried out to ensure that the desired clinical performance is met.

A. Performance Measures

In this paper, the main focus will be on the following measures: FWHM, cystic resolution, speckle information density, and the number of independent images used for compounding.

a. Detail resolution The *detail resolution* is the separation at which identically point targets can be distinguished. It is distinguished by the main lobe width of the point-spread-function (PSF) and the 6 dB axial pulse length, i.e. the lateral and axial full width at half maximum (FWHM) of the PSF.

b. Cystic resolution The detail resolution alone is not appropriate for comparing the imaging performance of medical ultrasound systems, since it ignores what is outside the main lobe, which has a significant impact on the images of wide dynamic range systems. Acoustic clutter from surrounding objects fill-in images of anechoic objects such as cysts, or weakly echogenic objects such as blood vessels, and reduces their detectability. The ability to detect anechoic or weakly echogenic objects in the presence of strong surrounding objects is sometimes referred to as contrast resolution and was first introduced as *cystic resolution*¹⁵. The cystic resolution can be quantized by the clutter energy to total energy ratio (CTR). The CTR is defined as the ratio of the energy outside a circular region \mathfrak{R} with radius R centered at the peak of the PSF to the total PSF energy

$$\text{CTR}_R(\vec{r}_0) = 10 \log \left(1 - \frac{\int_{\vec{r} \in \mathfrak{R}} |h(\vec{r}, \vec{r}_0)|^2 dS}{\int |h(\vec{r}, \vec{r}_0)|^2 dS} \right),$$

where $|h(\vec{r}, \vec{r}_0)|$ is the PSF at \vec{r}_0 . For a large ensemble of measurements, the CTR is also a measure of the difference between the average intensity level of an anechoic cyst's center and the surrounding tissue. To get a single measure, one either measures the drop in brightness for a fixed radius R or the radius for which a cyst can

be observed at a fixed level, e.g. $R_{20\text{dB}} \equiv \{R | \text{CTR}_R = -20\text{dB}\}$.

c. Image contrast Most commonly, contrast resolution refers to the ability to distinguish echogenicity differences between a region of interest (ROI) and the background (B) and is quantified by a signal-to-noise ratio for contrast¹⁶

$$C = \frac{|\mu_{I_{\text{ROI}}} - \mu_{I_{\text{B}}}|}{\sqrt{\sigma_{I_{\text{ROI}}}^2 + \sigma_{I_{\text{B}}}^2}} = \frac{\Delta I}{\sqrt{\sigma_{I_{\text{ROI}}}^2 + \sigma_{I_{\text{B}}}^2}}, \quad (1)$$

where $\mu_{I_{\text{ROI}}}$ and $\mu_{I_{\text{B}}}$ are the mean intensities of the ROI and background, and $\sigma_{I_{\text{ROI}}}^2$ and $\sigma_{I_{\text{B}}}^2$ are their corresponding variances. The contrast C is object dependent and is improved by increasing object contrast, ΔI as well as by lowering the variance in the ROI or the surrounding tissue. In¹⁶, Smith et al. proposed a theoretical model of an ideal observer for the task of identifying a lesion within a uniform background, where the model quantifies the expected trade-off between resolution loss and speckle reduction. It assumes Rayleigh statistics, an elliptical speckle cell shape, and that the lesion is large compared to the speckle size. Using this model, the signal-to-noise ratio for lesion detection is¹⁶

$$\text{SNR}_{\Delta I} = \frac{C d N_{\text{eff}}^{1/2}}{(S_{\text{lat}} S_{\text{ax}})^{1/2}}, \quad (2)$$

where C is the contrast of a circular lesion of diameter d , N_{eff} is the number of independent images compounded, and S_{lat} , and S_{ax} , are the lateral and axial speckle dimension. To improve detectability of a lesion with a given contrast, it is therefore of great interest to maximize the density

$$\rho_{\text{SID}} = \frac{N_{\text{eff}}}{(S_{\text{lat}} S_{\text{ax}})}, \quad (3)$$

which we will refer to as the *speckle information density*. The speckle information density is related to the signal-to-noise ratio when averaging over a disk target with area A compounded using N_{eff} independent images, through¹⁶

$$\text{SNR}_I^2 = A \frac{N_{\text{eff}}}{(S_{\text{lat}} S_{\text{ax}})} = A \rho_{\text{SID}}. \quad (4)$$

Eq. (4) states that the signal-to-noise ratio, SNR_I is given by the square root of the number of independent speckle-cells of size $\pi(S_{\text{lat}}/2)(S_{\text{ax}}/2)$ within the disk. When applying the model of an ideal observer, it is important to distinguish the contrast C appearing in (2) from a measurement of the contrast, where the means and variances are replaced by their corresponding sample means, \bar{I} and sample variances, s^2

$$\bar{C} = \frac{|\bar{I}_{\text{ROI}} - \bar{I}_{\text{B}}|}{\sqrt{s_{I_{\text{ROI}}}^2 + s_{I_{\text{B}}}^2}}. \quad (5)$$

If an image setup yields great contrast in terms of a high value for N_{eff} and small speckle size, the theory of an ideal

observer states that a measure of the contrast is also improved. A small speckle size give rise to more independent measurements of the intensity and hence a better estimate for the difference. Likewise, a high value for N_{eff} gives an estimate with lower variance due to higher decorrelation. Contrary, if the underlying object contrast, ΔI is low or the variances $\sigma_{I_{\text{ROI}}}^2$ and $\sigma_{I_{\text{B}}}^2$ are high, a measurement of the contrast is low and it is important to have a high speckle information density in order to see the object.

The speckle information density (3) is object independent and can be extracted from a tissue-phantom scan and used as a performance measure for lesion detection. The number of independent images, N_{eff} can be estimated by measuring the correlation between the sub-images or by measuring the signal-to-noise ratio at a point SNR_0 ¹⁷ and using that the enveloped signals follow Rayleigh statistics¹⁸

$$N_{\text{eff}} = \left(\frac{\text{SNR}_0}{1.91} \right)^2. \quad (6)$$

The signal-to-noise ratio at a point is defined as

$$\text{SNR}_0 \equiv \frac{\mu_V}{\sigma_V},$$

where μ_V and σ_V are the expectation value and standard deviation of the envelope-detected signals. The speckle dimensions, S_{lat} and S_{ax} can be found from the correlation cell¹⁹

$$S_c = \int_{-\infty}^{\infty} \frac{C_I(\Delta\xi)}{C_I(0)} d(\Delta\xi), \quad (7)$$

where C_I is the spatial auto-covariance for the intensity and $\Delta\xi$ is the distance between image pixels.

B. Contrast or resolution

The theoretical contrast or more precisely, the number of independent images N_{eff} can be computed by using the correlation function between pulse-echo measurements at different spatial positions. The correlation function can be derived from the correlation of apertures and this was first done by Burckhardt⁹ and it was shown that compounding every 0.5 aperture length, results in at most 2.25 independent images per aperture. In later publications, Wagner et al.⁴ have shown through theoretical considerations, and Trahey et al.² through measurements that the approximate form for the correlation function presented by Burckhardt is inaccurate in the sense that it overestimates the correlation. The measurements by Trahey et. al. show that translating the aperture by half its length, results in about 3.2 independent images per aperture and even closer spacing allows more effective compounding. O' Donnell derived an exact analytic expression for the pulse-echo correlation function²⁰, and it is now well known that the conclusions made by Burckhardt are inaccurate. The analytic expression²⁰ matches the measurements of Trahey et. al reasonably well and

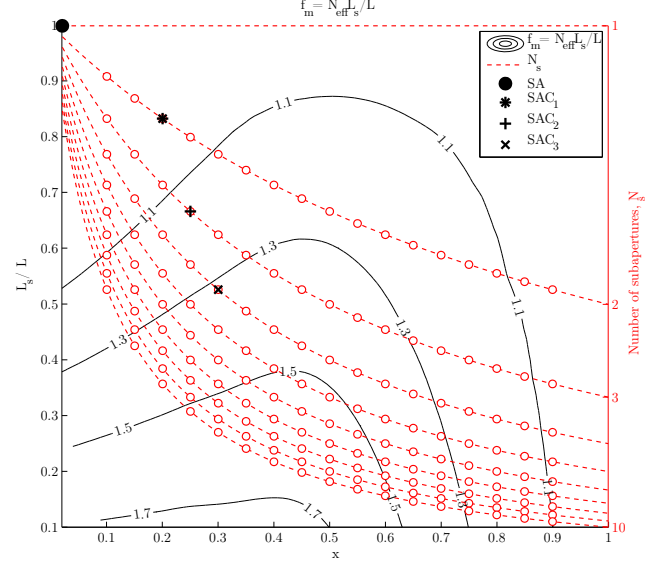


Figure 2. Contour lines of the figure of merit, f_m vs. relative aperture displacement, x and fractional size of the subaperture, L_s/L . The dashed lines represent configurations with an integral number of subapertures and the configurations used in this paper are shown using circular markers. The four configurations, SA, SAC₁, SAC₂, and SAC₃ are used for the images in Section IV.

can be used for deriving the optimum aperture displacement for efficient compounding to be about half the aperture length for $N_s = 3$ and smaller when using more compound apertures. The displacement is computed based on a figure of merit for the task of lesion detection¹⁶

$$f_m = N_{\text{eff}} L_s / L, \quad (8)$$

where L and L_s are, respectively the length of the aperture and the length of the subaperture(s) used for compounding. The fractional size of the subaperture, L_s/L is a measure for the lateral resolution of the imaging system and N_{eff} is a measure for the efficiency of compounding. By studying the product (8), decorrelation through N_{eff} and resolution through L_s/L are weighted equally to find an optimal compound configuration. To conclude that the optimum displacement for efficient compounding should be about half the aperture length, O' Donnell et al.²⁰ show that using a fixed aperture of length L divided into N overlapping subarrays of length L_s with equal displacements, x_0 , the figure of merit, f_m , is constant for a given relative aperture displacement, $x \equiv x_0/L_s$ and fractional size of the subaperture, L_s/L

$$f_m(L_s/L, x) = N_{\text{eff}}(L_s/L, x) L_s/L = \text{const.} \quad (9)$$

Following the theory of O' Donnell, in Fig. 2, contour lines of the figure of merit, f_m are plotted as a function of the relative aperture displacement, x , and the fractional size of the subaperture, L_s/L . The dashed lines represent configurations with an integral number of subapertures, N_s ranging from $N_s = 1$ to $N_s = 10$. In Section IV, the theoretical values for f_m will be compared with

Table I. Selected aperture configurations: x is the relative aperture displacement, N is the number of subapertures, and L_s/L is the fractional size of a subaperture.

	x	N	L_s/L
SA	-	1	1.00
SAC ₁	0.20	2	0.83
SAC ₂	0.25	3	0.67
SAC ₃	0.30	4	0.63

measurements corresponding to the subset with circular markers and the configurations listed in Table I are used for the sample images shown. Finally, the contour lines in Fig. 2 can also be used for computing the maximum number of independent images, N_{eff} for a setup with a given relative aperture displacement, x and subaperture size, L_s .

Experimental results by Jespersen et al.⁸ for SNR_0 and the correlation between two neighbouring sub-images for compounding using a linear array with a subaperture of one third of the aperture, $N_\theta = 11$, and an angular separation of 5° , reveal values for N_{eff} of 6.75 and 7.47. The former value is obtained by measurements of SNR_0 and using (2). The latter value is obtained by using an experimentally determined correlation value, $\rho = 0.26$ together with the expression²¹

$$\text{SNR}_0 = 1.91 \sqrt{\frac{N}{1 + 2(N-1)\rho^2/N}}, \quad (10)$$

where ρ is the intensity correlation between two neighboring images and N is the number of images used for compounding. The theoretical expression by O' Donnell et al. states that with the setup used by Jespersen⁸, the number of independent images, N_{eff} should be about 4.4. As also noted by Jespersen, the large result obtained using (10) is not surprisingly too large, because in deriving (10), an assumption is used, which states that only neighboring images are correlated and images separated by more than one 'angle-step' are uncorrelated. The experimentally-determined value for ρ obtained by Jespersen is in good agreement with theory and the experiments performed by Trahey et. al. The large results for N_{eff} obtained using (6) however, cannot be due to successful compounding alone. Some reasons for obtaining too large a value of SNR_0 are electronic noise, improper focusing, or high clutter levels, which all contribute to blurring the images. Also, the theoretical results of O' Donnell are derived by assuming focusing on both the transmit and the receive signals and it is a one-dimensional model, whereas real measurements are three dimensional including the effects of transducer bandwidth and out of plane focusing.

In this paper, synthetic aperture focusing is used for transmit and receive focusing and the number of independent images, N_{eff} , are computed to compare values for f_m with the theoretical results for a linear array described by O' Donnell²⁰ and illustrated in Fig. 2. The

Table II. Synthetic aperture compound setups used.

Setup	Apodization	L_s
I	Hamming	unchanged
II	Hamming	$L_s \mapsto D/f_{\text{xmt/rcv}}$, $f_{\text{xmt/rcv}} = 2.0$
III	Hamming	$L_s \mapsto L_s D/D_0$, $D_0 = 40\text{mm}$

detail resolution is measured using the axial and lateral FWHM of the PSF. The cystic resolution is measured using the CTR, represented by $R_{20\text{dB}}$. For evaluating the tissue contrast, the speckle information density, ρ_{SID} (3) is measured as well as the contrast for a cyst at a depth of 50 mm.

IV. RESULTS

To investigate the performance of synthetic aperture compounding, a setup using a commercial 128-element, 3.5 MHz linear phased-array transducer was used for water tank, tissue phantom, and cyst phantom measurements. The sampling was performed using an experimental ultrasound scanning system, SARUS, capable of storing 12-bit individual channel data at 70 MHz⁷. For synthetic aperture imaging, a 16 element subaperture was used for 128 unfocused emissions with an f-number of -0.5. For each emission, data from all 128 channels were stored. For all emissions, a two-cycle sinusoid was used for excitation together with a Hamming apodization on the active subaperture. Compounding is achieved by synthesizing $N_s = 2, \dots, 10$ transmit and receive apertures and relative aperture translations, $x = 0.10, 0.15, \dots, 0.90$ making a total of 153 different configurations for compounding. The number of configurations used for compounding together with a synthetic aperture configuration are shown in Fig. 2. For a given N_s and a given relative translation, x , the fractional size of the subaperture, L_s/L can be computed using $L_s/L = 1/(1 + x(N_s - 1))$. To experimentally verify the theory of O' Donnell, the transmit and receive apodizations were initially computed both to be of size L_s . A necessary Hamming apodization was applied to avoid edge artifacts, which otherwise give rise to a higher value for N_{eff} . This initial setup is referred to as Setup I in the following. A more useful setup, where the locations of the subapertures are unchanged, but the individual apertures are scaled to maintain a constant f-number across depth was also examined, Setup II in Fig 3 and in Table II. Note, how the effective aperture is smaller compared to that of Setup I. Finally, a setup where the apodization were designed to give apertures of size L_s for a certain depth, D_0 and then scaled using an f-number derived from L_s , i.e. $f = D_0/L_s$. In Fig 3, the last setup is shown using a depth $D_0 = 40\text{ mm}$. In Table II, the three setups are listed together with the formulas for computing the size of the apodization windows. The apodization in transmit is handled in the same way. For the last setup, the detail resolution will be reduced dramat-

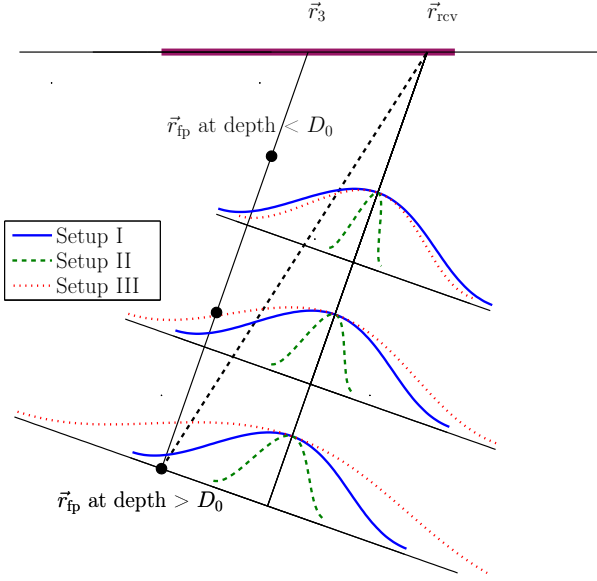


Figure 3. Receive apodizations for the three different setups used for compounding. For Setup I, the subapertures are exactly the same size as was used for the theoretical results of Section III. Setup II is using an f-number of 2.0 to dynamically scale the aperture. Finally, when using Setup III, the apertures are scaled to have the size used for Setup I for a depth of 40 mm.

ically for large values of x as apposed to using the same f-number for all combinations of N_s and x . The setups investigated in this article do not even closely cover all configurations that can be established for synthetic aperture compounding. The idea is to investigate a subset of configurations, which illustrate the tradeoff between contrast and detail resolution.

A. Water phantom measurements

The water tank phantom consists of 4 wires at depths of 8, 34, 59, and 83 mm. The transducer was submerged into the water and data were collected using 128 unfocused emissions. The data were downsampled to 35 MHz using a mean filter of width 2. In addition to the apodizations illustrated in Fig. 1, transmit and receive apodizations were applied to ensure that no signals arrived or transmitted with an angle of incidence larger than 45° contributed to the image. The axial and lateral FWHM together with the CTR, represented by R_{20dB} were measured using the wire at the depth of 34 mm. The results for the four configurations, SA, SAC₁, SAC₂, and SAC₃ are given in Table III and in Fig. 4b, the full CTR is plotted together with the clutter levels. In Fig. 4a, the CTR represented by R_{20dB} is shown for all 154 configurations. Note how the cystic resolution is degraded when introducing compounding. This clearly shows, how the introduction of compounding requires a sacrifice of aperture and thereby resolution. In a clinical setup, where the object is less homogeneous, one should expect that it

Table III. Detail resolution, FWHM and cystic resolution, R_{20dB} extracted from the water tank measurements for the wire at depth 34 mm.

	R_{20dB}	FWHM _{lat}	FWHM _{ax} [mm]	Area _{6dB} [mm ²]
SA	0.96	1.09	0.62	0.54
SAC ₁	1.01	1.20	0.62	0.59
SAC ₂	1.17	1.53	0.64	0.78
SAC ₃	1.40	1.86	0.64	0.94

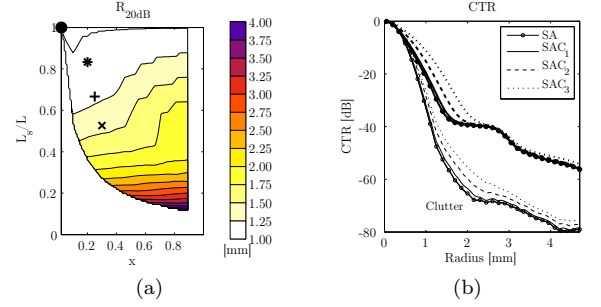


Figure 4. The CTR represented by R_{20dB} is shown in (a), and in (b), the full CTR is plotted together with the clutter levels for the four the configurations, SA, SAC₁, SAC₂, and SAC₃ using Setup I.

is a lot harder to do proper focusing and if the inclusion of more elements by enlarging the aperture does not improve on the resolution, compounding should be used to increase the contrast. In Fig. 5, the PSF is imaged using a wire at the depth of 34 mm using Setup I, where the size and positions of the subapertures are as in the theory. The four images are made using the configurations, SA, SAC₁, SAC₂, and SAC₃ listed in Table I. From the figures, it is clear that the detail resolution is degraded when applying compounding, but as the theory states, this is a necessary sacrifice for obtaining speckle reduction. In the next section, the compound effect is studied by studying images of a tissue-mimicking phantom.

B. Tissue phantom measurements

The speckle artifact appears when imaging a target with a finer structure than the detail resolution. The speckle artifact is deterministic in the sense that the same image are seen for repeated measurements of a fixed target. As mentioned in the introduction, for spatial compounding, the speckle is reduced by adding decorrelated images obtained with decorrelated apertures. To study the effect of compounding, a tissue-mimicking phantom with a speed-of-sound of 1540 m/s was scanned using the same setup as was used for scanning the wire phantom. The location and size of the region for extracting SNR₀ and the auto-covariance was directly in front of the transducer at a depth of 40 mm and 182x256 pixels corresponding to a region of 20x20 mm. Images were

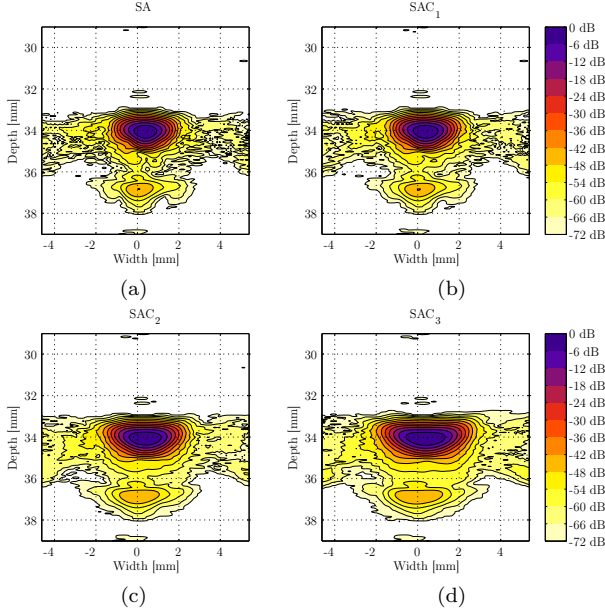


Figure 5. The PSF imaged at a depth of 34 mm using the four special configurations, SA (a), SAC_1 (b), SAC_2 (c), and SAC_3 (d) using Setup I.

created for all 154 configurations using the size and positions of the subapertures from the theory, i.e. Setup I in Table II. In Fig. 6a and 6b, the theoretical and the measured values for f_m are shown. The measured values are a little smaller than the theoretical ones and the maximum is located at a position with larger and more overlapping subapertures. This can be explained by the fact that a necessary Hamming apodization was applied and then of course, the theory is inherently one-dimensional and therefore only an approximate model. If no requirements are given for the detail resolution, an upper limit for R_{20dB} , the measurements show that a setup with many subapertures with a relative aperture translation of about 0.3 should be the ideal imaging configuration. However, as we have seen earlier in Fig. 4a, the detail resolution is quite poor for those configurations, so some other compromise should be made. So far, only apertures of fixed size have been considered. In an imaging system, it is desirable to maintain a constant resolution across depth and this can be achieved by using a constant f-number. In Fig. 6c, the value for the figure of merit, f_m , are calculated for a common f-number of 2.0 for transmit and receive. This translates into that the size of the subapertures are changed according to, $L_s \mapsto D/2.0$. Fig. 6c shows that by maintaining the positions and number of apertures, but at the same time increasing their size, the effect of compounding is diminished for configuration with large values of N_s . The apertures become larger and less decorrelated and the maximum moves closer to the synthetic aperture configuration without compounding. In Fig. 6d, the size of the subapertures are tuned to be of their original size at a depth of 40 mm and using the f-number, $f = L_s/40\text{mm}$, they are scaled to maintain a

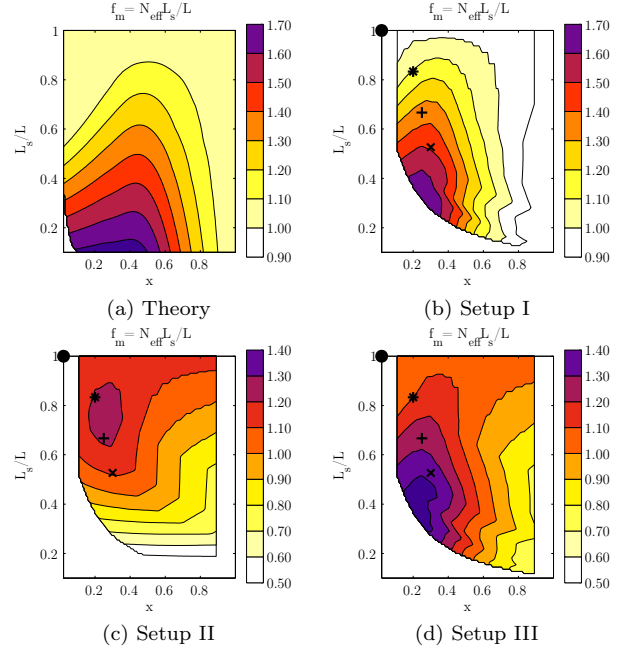


Figure 6. Theoretical and measured values for the figure of merit, f_m . In (a), the theoretical values are shown and in (b), the measured values are shown using a similar aperture configuration, i.e. Setup I. In (d) and (c), values are measured when using Setup II and Setup III.

Table IV. The effective number of images, N_{eff} , the speckle size, and the speckle information density, ρ_{SID} extracted from images of speckle obtained using the four aperture configurations in Table I and the three setups in Table II. For all imaging configurations, the contrast, \bar{C} of a cyst at a depth of 50 mm is measured using (5).

		N_{eff}	Speckle [mm^2]	ρ_{SID} [mm^{-2}]	\bar{C}
Setup I	SA	0.96	0.40	1.90	1.03
	SAC_1	1.33	0.47	2.24	1.50
	SAC_2	2.03	0.58	2.75	2.53
	SAC_3	2.82	0.69	3.21	3.55
Setup II	SA	1.06	0.44	1.89	1.04
	SAC_1	1.32	0.48	2.15	1.45
	SAC_2	1.91	0.61	2.44	2.44
	SAC_3	2.58	0.74	2.74	3.51
Setup III	SA	1.14	0.52	1.72	0.98
	SAC_1	1.46	0.54	2.14	1.57
	SAC_2	1.83	0.58	2.46	2.33
	SAC_3	2.11	0.59	2.82	2.80

constant resolution. In this way, the values for f_m are almost unchanged. This is the expected outcome, since the region examined is at a depth of 40 mm. In Table IV, the effective number of images, N_{eff} , the speckle size, and the speckle information density, ρ_{SID} are shown for the four selected configurations. In the next section, a cyst phantom is measured to show how the figure of merit,

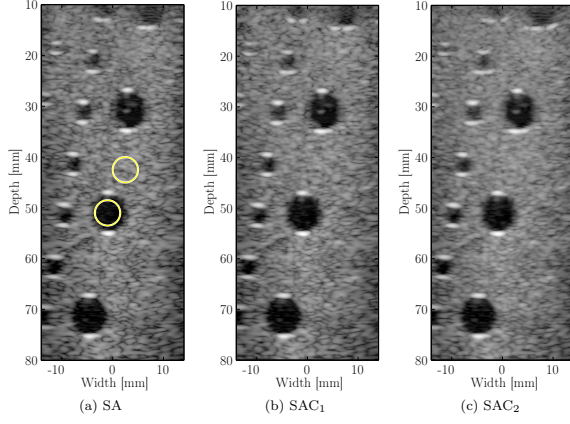


Figure 7. Synthetic aperture compound images created using Setup II. An image without compounding, (a) and two compound images (b), and (c) created using aperture configuration SAC_1 and SAC_2 respectively. All images are displayed using a dynamic range of 60 dB.

f_m , and speckle information density, SID relate to the detectability of a cyst.

C. Cyst phantom measurements

It has been demonstrated through wire and tissue phantom measurements how compounding reduces the appearance of speckle at the cost of a reduced detail resolution. A performance measure for lesion detection, the speckle information density, ρ_{SID} has been extracted. In this section, the same aperture configurations and setups are applied for scanning a cyst-phantom with a speed-of-sound of 1540 m/s corresponding to human tissue. In Fig. 7, images are created using a fixed f-number of 2.0, Setup II, and 3 of the 4 aperture configurations in Table I. In Fig. 8, the cyst at the depth 50 mm is imaged using Setup I, where the size of the subapertures is kept unchanged and the compound effect is more prominent.

The absolute contrast \bar{C} defined in (5) was measured for the cyst at a depth of 50 mm for the 3 setups in Table II using the 4 aperture configurations of Table I. The ROI and background regions were selected as shown in Fig. 7a. The values obtained for the contrast are shown in Table IV and put next to the values obtained for the speckle information density, ρ_{SID} . For all configurations, an increase of the speckle information density extracted from a tissue phantom is associated with an increased contrast measured for the cyst.

More interestingly, the contrast was measured for all aperture configurations for the three setups and in Fig. 9, the measured contrast is shown relative to a contrast achieved using a synthetic aperture configuration without compounding. The measured contrast in Fig. 9a follows the theoretical and the measurements of the figure of merit, f_m , in Figs. 6a and Fig. 6b, respectively. In Fig. 9b, the contrast is measured for a setup, where the resolution is maintained across depth by using a constant f-number, i.e. Setup II. The increase in contrast for this

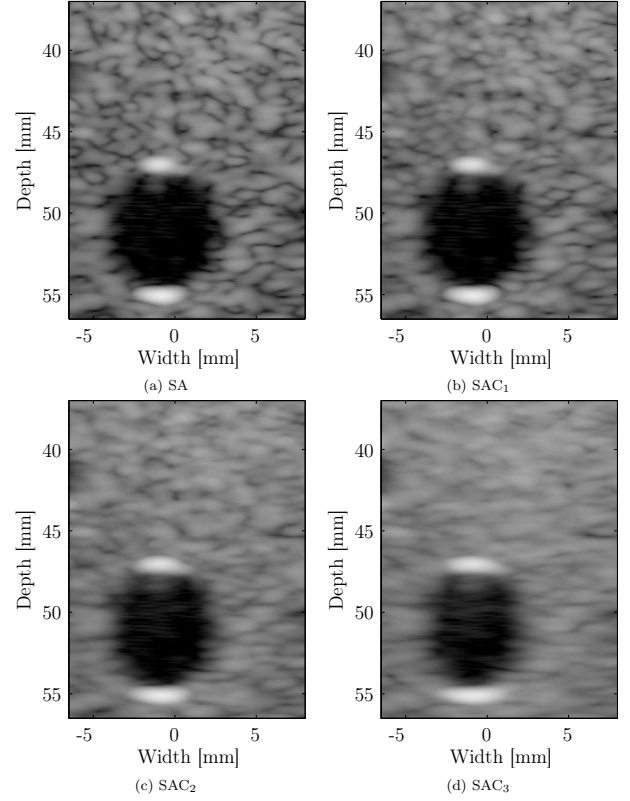


Figure 8. Cyst at the depth of 50 mm. imaged using Setup I and the four configurations in Table I. All images are displayed using a dynamic range of 60 dB.

setup is in general much less and a large fraction of the possible increase is obtained by replacing the SA configuration (marked with \bullet) with the compound configuration SAC_2 (marked with $+$). This setup is of particular interest in the sense that by requiring a fixed resolution across depth, a configuration which maximizes the contrast can be found. Finally, in Fig. 9c, the contrast is measured for Setup III, where the sizes of the subapertures are adjusted to their theoretical size at the depth 40 mm. The results are almost similar to the results obtained using Setup I. The small difference can be explained like this. Using Setup III, an f-number is used for obtaining aperture sizes equal to L_s at a depth of 40 mm. Further away from the transducer, the synthetic apertures must expand out of physical aperture and this causes an additional blurring. In Fig. 9d, the contrast measured using Setup I is compared to the values for the figure of merit, f_m , i.e. Fig 9a is compared to Fig 6b. A correlation coefficient of $R = 0.81$ with a p-value $p < 0.0001$ is obtained.

V. CONCLUSION

It has been demonstrated that spatial compounding can be obtained using synthetic aperture data and using the approach described, compounding can be achieved without reducing the frame rate or temporal resolution. In addition, the degree of compounding measured is close

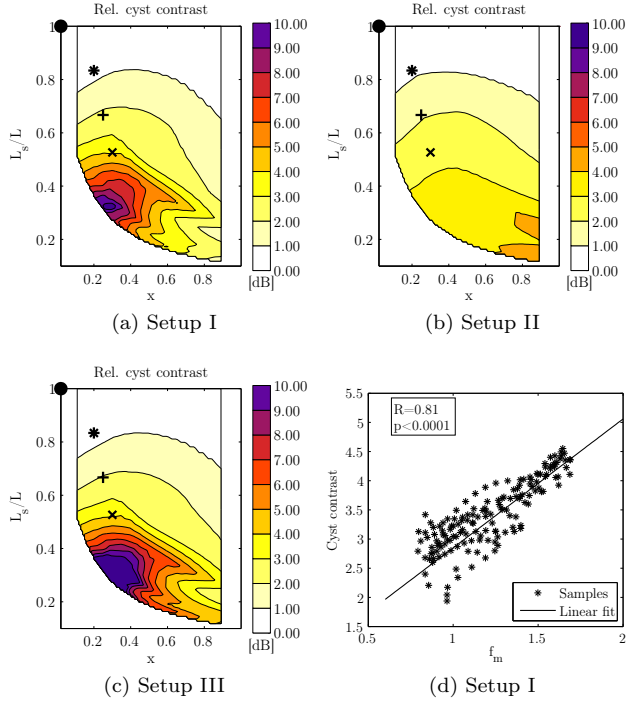


Figure 9. Contrast measured for the cyst at depth 50 mm measured using Setup I (a), Setup II, and Setup III (c). Scatter plot of the measured contrast vs. the figure of merit, f_m , for Setup I (d).

to a theoretical expression for the maximum compounding possible. Aspects of the necessary tradeoff between contrast and resolution was demonstrated by studying different aperture configurations with more or less compounding. A clear correlation was found between the measured contrast for a cyst and the figure of merit, f_m , for compound images created using Setup I. Further, it was demonstrated how an increase for the speckle information density was followed by an increased contrast for a cyst. This relationship was not studied in complete and deserves further investigation for how to relate ρ_{SID} to contrast in ultrasound images. Also, the method should be further developed and applied to e.g. a $\lambda/2$ -pitch convex array or a phased-array aperture of greater width.

- ¹ D. Shattuck and O. von Ramm, "Compounding scanning with a phased array", *Ultrason. Imaging* **4**, 93–107 (1982).
- ² G. E. Trahey, S. W. Smith, and O. T. von Ramm, "Speckle pattern correlation with lateral aperture translation: Experimental results and implications for spatial compounding", *IEEE Trans. Ultrason., Ferroelec., Freq. Contr.* **UFFC-33**, 257–264 (1986).
- ³ P. A. Magnin, O. T. von Ramm, and F. L. Thurstone, "Frequency compounding for speckle contrast reduction in phased array images", *Ultrason. Imaging* **4**, 267 – 281 (1982).
- ⁴ R. F. Wagner, M. F. Insana, and S. W. Smith, "Fundamental correlation lengths of coherent speckle in medical ultrasonic images", *IEEE Trans. Ultrason., Ferroelec., Freq. Contr.* **35**, 34–44 (1988).
- ⁵ R. Entekin, P. Jackson, and B. Porter, "Real time spatial compound imaging in breast ultrasound: technology and early clinical experience", *medicamundi* **43**, 35–43 (1999).
- ⁶ J. M. Hansen and J. A. Jensen, "Synthetic aperture compounding",

- IEEE transactions on ultrasonics, ferroelectrics, and frequency control* (2012).
- ⁷ J. A. Jensen, H. Holten-Lund, R. T. Nielson, B. G. Tomov, M. B. Stuart, S. I. Nikolov, M. Hansen, and U. D. Larsen, "Performance of SARUS: A Synthetic Aperture Real-time Ultrasound System", in *Proc. IEEE Ultrason. Symp.*, 305–309 (2010).
- ⁸ S. K. Jespersen, J. E. Wilhjelm, and H. Sillesen, "Multi-angle compound imaging", *Ultrason. Imaging* **20**, 81–102 (1998).
- ⁹ C. Burckhardt, "Speckle in ultrasound b-mode scans", *IEEE Trans. Son. Ultrason.* **SU-25**, 1–6 (1978).
- ¹⁰ M. Karaman, P. C. Li, and M. O'Donnell, "Synthetic aperture imaging for small scale systems", *IEEE Trans. Ultrason., Ferroelec., Freq. Contr.* **42**, 429–442 (1995).
- ¹¹ G. R. Lockwood, J. R. Talman, and S. S. Brunke, "Real-time 3-D ultrasound imaging using sparse synthetic aperture beamforming", *IEEE Trans. Ultrason., Ferroelec., Freq. Contr.* **45**, 980–988 (1998).
- ¹² C. R. Hazard and G. R. Lockwood, "Theoretical assessment of a synthetic aperture beamformer for real-time 3-D imaging", *IEEE Trans. Ultrason., Ferroelec., Freq. Contr.* **46**, 972–980 (1999).
- ¹³ K. L. Gammelmark and J. A. Jensen, "Multielement synthetic transmit aperture imaging using temporal encoding", *IEEE Trans. Med. Imag.* **22**, 552–563 (2003).
- ¹⁴ J. S. Hwang and T. K. Song, "A study of the display pixel-based focusing method in ultrasound imaging", *Ultrason. Imaging* **23**, 1–18 (2001).
- ¹⁵ D. Vilkomerson, J. Greenleaf, and V. Dutt, "Towards a Resolution Metric for Medical Ultrasound Imaging", in *Proc. IEEE Ultrason. Symp.*, 1405–1410 (1995).
- ¹⁶ S. W. Smith, R. F. Wagner, J. M. Sandrik, and H. Lopez, "Low contrast detectability and contrast/detail analysis in medical ultrasound", *Ultrason. Imaging* **30**, 164–173 (1983).
- ¹⁷ This signal-to-noise is an image property and should not be related or confused with the SNR used for electronic noise.
- ¹⁸ R. F. Wagner, S. W. Smith, J. M. Sandrick, and H. Lopez, "Statistics of speckle in ultrasound B-scans", *IEEE Trans. Son. Ultrason.* **30**, 156–163 (1983).
- ¹⁹ J. W. Goodman, "Statistical properties of laser speckle patterns", *Stanford Electron. Lab. Tech. Rep.* (1963).
- ²⁰ M. O'Donnell and S. D. Silverstein, "Optimum displacement for compound image generation in medical ultrasound", *IEEE transactions on ultrasonics, ferroelectrics, and frequency control* **35**, 470–476 (1988).
- ²¹ P. M. Shankar and V. L. Newhouse, "Speckle reduction with improved resolution in ultrasound images", *IEEE Trans. Son. Ultrason.* **32**, 537–543 (1985).

A.7 Synthetic Aperture Beamformation using the GPU

- **J. M. Hansen**, D. Schaa, and J. A. Jensen: Synthetic Aperture Beamformation using the GPU. Proceedings of the IEEE Ultrasonics Symposium, October, 2011.

Synthetic Aperture Beamformation using the GPU

Jens Munk Hansen[†], Dana Schaa^{*} and Jørgen Arendt Jensen[†].

[†]Center for Fast Ultrasound Imaging, Dept. of Elec. Eng,
Technical University of Denmark, DK-2800 Lyngby, Denmark

^{*} Dept. of Electrical and Computer Engineering,
Northeastern University, Boston, MA, USA

Abstract—A synthetic aperture ultrasound beamformer is implemented for a GPU using the OpenCL framework. The implementation supports beamformation of either RF signals or complex baseband signals. Transmit and receive apodization can be either parametric or dynamic using a fixed F-number, a reference, and a direction. Images can be formed using an arbitrary number of emissions and receive channels. Data can be read from Matlab or directly from memory and the setup can be configured using Matlab. A large number of different setups has been investigated and the frame rate measured. A frame rate of 40 frames per second is obtained for full synthetic aperture imaging using 16 emissions and 64 receive channels for an image size of 512x512 pixels and 4000 complex 32-bit samples recorded at 40 MHz. This amounts to a speed up of more than a factor of 6 compared to a highly optimized beamformer running on a powerful workstation with 2 quad-core Xeon-processors.

I. INTRODUCTION

Image quality and diagnostic capabilities of medical imaging depend on the inversion of the measured data for the given modality. For ultrasound imaging, the inversion is primarily made by delay-and-sum beamformation. This comprises computation and application of channel delays and apodization for both the emissions and the individual receiving elements. Ideally, one would like the result of the beamformation to approximate the true inverse of the forward model, which itself is a complex model of both time and space. A forward model or simulation model is described by the ultrasound simulation program Field II [1], [2]. This may sound like elements of the future, but the evolution of ultrasound beamformers moving from analog into digital implementations, described by Thomenius [3], has made it possible to implement more advanced beamformers and new and improved methods of beamformation are still emerging. At the moment, one of the more demanding methods is synthetic aperture (SA) imaging [4] and variations hereof. Even though computers today are fast, the limiting factor for a SA ultrasound system is still the memory IO resources available.

An equally high demand for memory throughput is found in the computer gaming industry, where hundreds of megabytes of data are processed every second for rendering a scene in a 3D computer game. The processing takes place on the graphics processing unit (GPU), which is a many-core massively parallel throughput-oriented execution unit. It contains a lot of arithmetic logic units (ALUs) and is suitable for single-instruction-multiple-data (SIMD) execution. Until the fourth generation of GPUs, the GPUs were all fixed-function,

but since then the vendors have introduced vertex-level and pixel-level programmability and several high-level graphics languages have been released, which allow programs written in C/C++ to use a runtime and load programs to be executed by the GPU. In this paper, the most recent framework, OpenCL [5] is used for SA beamformation of ultrasound data. Previous work has already been done using multiple GPUs for SA beamformation of ultrasound data [6]. This work is different in the way that a more advanced apodization is used and the beamformer can be configured using Matlab.

II. GPU HARDWARE

The GPUs consist of several compute units, which each can be thought of as (a collection of) multi-core processors sharing some local memory and a common pipeline. This means in particular that the groups of cores read and write data simultaneously and this should be kept in mind when implementing programs for the GPU to execute. Further, no caching or very little caching is done by the hardware, so memory handling is therefore more critical for GPU programs than for programs implemented for CPUs. The two manufacturers of GPUs, Nvidia and AMD/ATI have created two very different architectures for memory access on their devices. AMD operate with vectorized memory reads and writes and a uniform memory space exposition [7]. This is very similar to how SIMD is implemented on CPUs and the programmer has to think of organizing data as 128-bit vectors (4 floats) to achieve good performance. This makes the programming less flexible but potentially speed-up calculations involving vectorized input and output. Many programmers forget this and falsely arrive at a poor performance. Nvidia work instead with a two-level thread hierarchy and scalar memory addressing and does not take advantage of instruction level parallelism to the same extent as their rival [8]. The memory access pattern for synthetic aperture beamformation is randomly shifted and very few arithmetic operations are performed compared to load and store operations. It is therefore an advantage to have a large amount of L1 cache available for each compute unit. The latest generation of GPUs from Nvidia, Fermi, have up to 48 kB of L1 cache available for each compute unit, while the Evergreen family of their rival AMD, only has 8 kB. Further, since beamformation of a single pixel using linear interpolation involves only two consecutive values of RF data for each channel, you do not directly benefit from vectorized memory reads, but often more advanced interpolation is needed which can benefit

from this way of addressing memory. These considerations together with some initial performance measurements, made us focus on the Nvidia architecture.

A. SIMD cores

The GPU primarily used in this article is the GTX-580 from Nvidia. It has 16 compute units or streaming multiprocessors (SMs), each containing 2 groups of 16 streaming processors (SPs), 4 special function units (SFUs) and 16 load/store units. The SMs have a SIMD architecture. Scalar threads are grouped into SIMD groups called *warps*, with 32 scalar threads per warp. Each SP can execute a sequential thread, the SPs execute in what Nvidia calls SIMT (Single Instruction, Multiple Thread) fashion; all SPs in the same group execute the same instruction at the same time, much like classical SIMD processors. SIMT handles conditionals somewhat differently than SIMD, though the effect is much the same, where some cores are disabled for conditional operations.

The SM double pumps each group of 16 SPs to execute one instruction for each of two warps in two clock cycles, for integer or single-precision floating point operations. For double-precision instructions, the SM combines the two groups of cores to look like a single 16-core double-precision multiprocessor; this means the peak double-precision throughput is 1/2 of the single-precision throughput.

Another important feature of the GPUs is how multithreading is designed to hide memory and pipeline latencies. To facilitate low-cost context switching, all simultaneously running threads on an SM keep their register states in the same register file. The number of registers consumed by a thread depends on the program and it is possible to create more threads than what can fit simultaneously in the register file, but the user should avoid this. In addition to the register file and L1 cache, there is also a small local memory storage on each SM called shared memory that is partitioned among groups of threads called thread blocks. This can be used by the programmer for explicit caching of data.

The scheduling of the threads takes place by a dual warp scheduler that can occupy both 16-wide groups of SPs with separate warps via dual issue. Each SM can track a total of 48 warps simultaneously and schedule them pretty freely in intermixed fashion, switching between warps at will from one cycle to the next. Obviously, this should be a very effective means of keeping the execution units busy, even if some of the warps must wait on memory accesses, because many other warps are available to run. To give an idea of the scale involved, consider 32 threads times 48 warps per SM. This adds up to 25,576 concurrent threads in flight on the GPU.

This approach for keeping execution units busy is much simpler than what goes on in a modern CPU, where a larger instruction set is available, caching is done at multiple levels, and branch prediction is used to improve the flow in the instruction pipeline. In Fig 1, an illustration is given of how much area is used for control logic, ALUs, and caches in a GPU compared to what is used in a modern quad-core CPU.

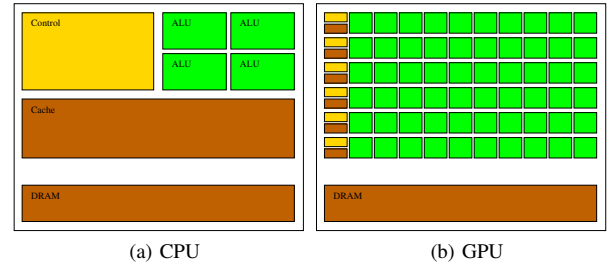


Figure 1. Simplified hardware layout for a quad-core CPU and a GPU with 60 SPs arranged in groups of 10.

Finally, we should mention that the previous Tesla generation has up to 30 SMs (GTX-285), but each SM contain only a single group of 8 SPs and the cores in this group are quad-pumped to execute one instruction for an entire warp, 32 threads, in four clock cycles. In addition to the 8 SP, each SM contains a shared SFU, which handle transcendentals and double-precision operations at 1/8 the compute bandwidth. This is four times slower than the new Fermi architecture.

B. Memory IO

As stated in the introduction, beamformation of ultrasound data comprises computation and application of channel delays and apodizations. The former also referred to as focusing amounts to massive distance calculations followed by memory look-ups. The apodization part consists of a weighting based on the pixel location and the origin of the ultrasound signals. The amount of calculations are massive, but the memory access pattern is randomly shifted. This is suboptimal for the current GPU architectures and the result is a heavily memory bound application. Because of this, to achieve a high performance, a high memory bandwidth as well as low latency for access to the global memory is preferable. The main memory on the GTX-580 delivers 192 gigabytes per second (GB/s). This is six times the bandwidth of a Core-i7 with triple-channel DDR3-1333 memory, delivering 32 GB/s. The memory speedup is obtained using multiple 64-bits interfaces (6 instead of 3) and higher clock values. The latency for accessing the global memory is several hundred clock cycles so a high bandwidth alone is not sufficient for a high performance. Multithreading and caching done by the programmer or by the hardware is used for hiding latency and keeping a high memory throughput. The Fermi also features a 768 kB unified L2 cache that services all load, store, and texture requests. The L2 provides efficient, high speed data sharing across the GPU. Algorithms for which data addresses are not known beforehand, like beamformation benefit from the cache hierarchy. Filter and convolution kernels that require multiple SMs to read the same data also benefit. Members of the AMD Evergreen family only contain 128 kB L2 cache.

III. DESIGN

To cover as many focusing strategies as possible and thereby be able to make important conclusion on processing capabilities and throughput, a full synthetic aperture (SA)

focusing system is implemented with possibilities for later simplifications to improve on the performance. In addition to this choice, the following decisions were made with respect to design and functionality of the beamformer:

- The implementation should support beamformation of either RF signals or complex base band signals.
- The input data should be read directly from memory or from .mat files supported by Matlab. In this way, data simulated with Field II as well as data acquired using our research scanner SARUS [9] can be processed.
- Support for full parametric or dynamic apodization using a fixed F-number, a reference point, and a direction.
- Beamformation should support an arbitrary number of emissions and receive channels.
- Parameters used for beamformation should be stored in configuration files, which are read once before processing starts with a given setup.
- The frame rate should be measured for continuous beamformation and display using a fixed setup.

IV. VALIDATION

To verify the correctness of the implementation, synthetic aperture RF data were simulated with Field II for 7 scatterers located on a line perpendicular to the transducer surface and passing through the center position of the transducer. IQ data were formed using Hilbert transformation and data were initially beamformed using BFT3 - a Matlab toolbox written in C++ [10]. The resulting image served as a reference for the output of the GPU beamformed. Next, the data were beamformed using a simple program written in ANSI-C, which later was used as a reference for debugging the GPU kernels. Initially, no apodization was included to focus only on the correctness of the delay calculation and interpolation. Later, dynamic receive apodization using a Hamming window and an F-number of 1.0 was introduced. The parameters used for the simulation and resulting image are shown in Fig 2

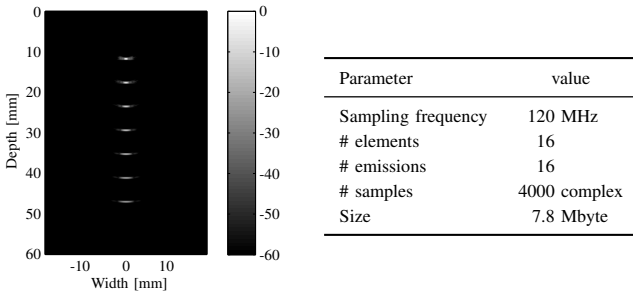


Figure 2. 7 scatter phantom image and parameters used for simulation. The image is beamformed using 1024 lines, each with 1024 samples.

V. IMPLEMENTATION

In the OpenCL framework, one operates with *work-groups* which are groups of threads associated with pixels in the resulting image. Several concurrent work-groups can reside on one compute unit depending on the work-group's memory

requirements and compute unit's memory resources. The optimal dimensions of the work-groups therefore depend on the registers and memory needed for the calculations, the amount of ALUs required for the calculations themselves, and the amount of IO to the global memory. The initial implementation was made by starting with an OpenCL kernel reproducing the results of the simple ANSI-C program applied to the RF data for the 7 scatter phantom. The dimension of the work-group was adjusted to achieve the best performance for this setup. Apodization was introduced and by experimenting with doing some calculations on a per work-item and some on a per work-group basis, no effect was seen on the performance confirming that the application is memory bound.

VI. OPTIMIZATION

Moving on to a larger dataset resembling what is actually acquired using a synthetic aperture approach. RF data for a cyst phantom was simulated for 192 channels and 16 emissions. The image and parameters used for simulation is given in Fig. 3 The total execution for synthetic aperture imaging

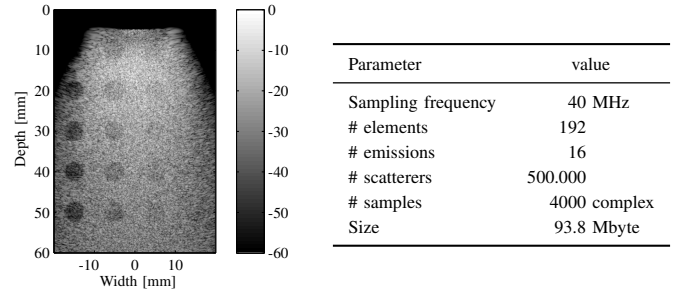


Figure 3. Cyst phantom image and parameters used for simulation. The image is beamformed using 1024 lines, each with 1024 samples.

of the 7 scatterers and cyst phantom using dynamic transmit and receive apodization is given in Table I. The execution time for beamformation using the BFT3 toolbox and a faster SIMD implementation on a dual CPU workstation is also included. We note that for this kernel, the GTX-285 is much faster than the more expensive GPU from AMD, HD 5870. Several

Table I

Phantom	GPU			2 × CPU, E5520, 2.26 GHz		
	GTX-580	GTX-480	GTX-285	HD 5870	SIMD	BFT3
7 scatter	0.087 sec	0.089 sec	0.28 sec	N/A	N/A	N/A
Cyst	0.46 sec	0.48 sec	0.92 sec	2.3 sec	5.48 sec	15.9 sec

attempts for optimization was made including:

- Using interleaved complex data rather than split format. In this way, the real and imaginary part of the relevant samples are next to each other memory-wise.
- Using the local memory for caching the samples used for beamformation the pixels in each work-group.
- Precalculating all delays and/or apodizations to keep calculations to an absolute minimum.

- Using the faster texture memory for loading a fraction of the RF data at a time for beamforming the image in multiple stages. The reason for this is that the texture is not big enough for data from 192 channels, each containing 4000 complex samples.

Using, the AMD HD 5870, we were only able to speed up the calculation by 15% and this was obtained by using interleaved data together with caching all samples used for a work-group in the local cache and accessing the samples using the faster cache rather than directly in the slower global memory. The precalculation of delays gave no speedup, which was expected since the application is heavily memory bound. We were not able to achieve any improvements using the local memory, but this deserves more attention.

VII. RESULTS

After having played around with different optimizations using the AMD HD 5870 and the GTX-285 from Nvidia, the latest generation of GPUs from Nvidia, here represented by GTX-480 and GTX-580 were tested. Using pinned or page-locked memory for the input data, it was possible to do overlapped IO such that while the GPU was busy beamforming data from one emission, data for the following emission was being copied. Since, a sum of contributions is computed from a number of emissions and for a set emissions the image is read back once or continuously imaged on the screen, this application is ideal for overlapped IO. Unfortunately more time is spent on beamforming than copying data from the CPU host to the GPU device, so only about a 50% speed up was achieved using overlapped IO. Moreover, since we are beamforming IQ data, it is sufficient beamforming a smaller image, since the frequency content of the enveloped signals is of lower values. Using the GTX-580 GPU, a work-group size of 32x32 pixels, the frame rates listed in Table II were obtained

Table II
FRAME RATES FOR AN IMAGE SIZE OF 512X512 PIXELS BEAMFORMED USING 4000 COMPLEX SAMPLES FOR EACH RECEIVE CHANNEL. THE FRAME RATES INCLUDE READING BACK EACH FRAME TO THE CPU.

		# emissions			
		4	8	16	32
# channels	192	42.8	23.7	12.5	7.2
	128	70.4	39.9	20.0	11.2
	96	77.6	44.8	23.8	13.3
	64	137.3	75.4	39.7	21.1
	48	171.3	80.5	49.7	26.2
	24	226.2	143.7	86.1	44.2

VIII. DISCUSSION

The motivation for the implementation of the SA beamformed for this article was to speed-up development of new beamformers rather than making a good enough solution which can easily be adopted for a commercial implementation.

However, the results show that even with a naive kernel, where only little work has been done for optimization, decent frame rates can be obtained. Later experiments, where 16-bit samples was used instead of 32-bit single precision floating point data, revealed an additional speed-up of a factor of two. Other attempts that could be made include; computing time-of-flight and apodization using look-up-tables combined with piecewise linear continuation.

Another way of speeding up the beamformation is to use multiple GPUs and this will obviously work, since the PCI-X 2.0 x16 delivers easily 5 GB/s and the data rate for the fastest setup in this article is still at least a factor of ten below this value.

IX. CONCLUSION

In this article, proof-of-concept is given for synthetic aperture beamformer running on the GPU supporting dynamic transmit and receive apodization. Experiments show that a naive beamformer performs much better on Nvidia Fermi GPUs than on the AMD Evergreen GPUs using the OpenCL 1.0 framework. Having studied the little information the vendors give on their hardware, the better performance on the Nvidia GPUs for naive kernels is most likely due to their two-level thread hierarchy and larger amount of L1 and L2 caches.

REFERENCES

- [1] J. A. Jensen and N. B. Svendsen, "Calculation of Pressure Fields from Arbitrarily Shaped, Apodized, and Excited Ultrasound Transducers," *IEEE Trans. Ultrason., Ferroelec., Freq. Contr.*, vol. 39, pp. 262–267, 1992.
- [2] J. A. Jensen, "Field: A Program for Simulating Ultrasound Systems," *Med. Biol. Eng. Comp.*, vol. 10th Nordic-Baltic Conference on Biomedical Imaging, Vol. 4, Supplement 1, Part 1, pp. 351–353, 1996.
- [3] K. E. Thomenius, "Evolution of ultrasound beamformers," in *Proc. IEEE Ultrason. Symp.*, vol. 2, 1996, pp. 1615–1621.
- [4] G. R. Lockwood, J. R. Talman, and S. S. Brunke, "Real-time 3-D ultrasound imaging using sparse synthetic aperture beamforming," *IEEE Trans. Ultrason., Ferroelec., Freq. Contr.*, vol. 45, pp. 980–988, 1998.
- [5] K. O. W. Group, *The OpenCL Specification, version 1.0.29*, 8 December 2008. [Online]. Available: <http://khronos.org/registry/cl/specs/opencl-1.0.29.pdf>
- [6] B. Y. S. Yiu, I. K. H. Tsang, and A. C. H. Yu, "Real-time GPU-based software beamformer designed for advanced imaging methods research," in *Proc. IEEE Ultrason. Symp.*, 2010, pp. 1920–1923.
- [7] A. M. Devices, "Heterogeneous computing. OpenCL™ and the ATI Radeon™ HD 5870 ("Evergreen") architecture," 2010.
- [8] *Whitepaper NVIDIA's Next Generation CUDA Compute Architecture: Fermi, v 1.1*.
- [9] H. Holten-Lund, I. Nikolov, and M. Hansen, "SARUS digital acquisition and ultrasound processing board, processing specification," Ørsted•DTU, Technical University of Denmark and Prevas A/S, Tech. Rep., 2007.
- [10] J. M. Hansen, M. C. Hemmsen, and J. A. Jensen, "An object-oriented multi-threaded software beam formation toolbox," in *Proc. SPIE - Medical Imaging - Ultrasonic Imaging and Signal Processing*, vol. 7968, 2011, p. 79680Y.

